Designing New Catalysts To Control Atmospheric Emissions Of Volatile Organic Pollutants

Thesis submitted in accordance with the requirement of
Cardiff University for the degree of Doctor of Philosophy

Kieran J. Aggett

2022

Summary of Thesis

The design of metal oxide and novel supported precious metal catalysts were investigated for the control of volatile organic pollutants, by method of total oxidation. CeO_2 based metal oxide catalysts were prepared by a precipitation method to assess the influence of cerium precursor on resultant catalyst characteristics. The precipitate formation was related to varying physiochemical properties of the catalyst, which was then associated to the catalytic activity for the total oxidation of model VOCs. Catalytic activity for propane and naphthalene total oxidation was shown to improve when a $CeO_2.H_2O$ precipitate was formed. The investigation of catalyst testing conditions was also carried out.

Following this, the improvement of catalytic activity was investigated by producing mixed metal oxide catalysts containing CeO_2. $CeFeO_x$ mixed metal oxide catalysts were prepared and the impact of cerium precursor, in addition to the ratio of the metals, was assessed for propane and naphthalene total oxidation. Concurrent trends were identified when using the different cerium precursors; however, the production of the mixed metal oxide system showed limited activity compared to the single metal oxide catalysts. The addition of dopants to a $CeZrO_x$ based catalyst was also investigated, to assess the impact on the total oxidation of propane and naphthalene VOCs. The addition of small quantities of transition metal dopants improved activity for both VOCs, with Fe and Cu dopants presenting the best activity.

The preparation of precious metal catalysts, supported on a novel silica support were investigated for the simultaneous total oxidation of a VOC mixture, commonly used to simulate ‘cold start pollutants’ in engines. The increased concentration of Pt nanoparticles on the catalyst surface were correlated with enhanced oxidation for propene, toluene and CO pollutants.

Acknowledgements

Firstly, I would like to extend my deepest gratitude to Professor Stuart Taylor for not only giving me the opportunity to undertake a PhD within the Cardiff Catalysis Institute, but also for the guidance and support he offered throughout the entire process, and the many additional opportunities he provided.

I would also like to extend my gratitude to Dr Tomás García and Dr Benjamin Solsona, along with the research teams at the Instituto de Carboquímica, University of Zaragoza and University of Valencia for allowing me to participate in the ongoing collaboration work. From Cardiff University, I would like to give a massive thank you to Dr Tom Davies for his help with electron microscopy analysis and Dr David Morgan for his assistance with XPS analysis. I owe a huge thanks to Dr Greg Shaw and Dr Nia Richards for their help and expertise when fixing the numerous technical issues throughout my PhD. Furthermore, I would like to thank Steve Morris and Lee Wescombe from the workshop for helping to manufacture parts for my reactors. I would also like to thank Dan Hewes for his help with the SEM analysis for my first publication.

From the CCI, I would like to extend my gratitude to all the postdocs who have contributed to my work in some way, whether it be offering training in analysis techniques or advice on catalyst synthesis. I would like to give a special thanks to Dr Parag Shah for his supervision and advice in the early part of my PhD, as well as welcoming me into the group. I am grateful to all members of the CCI, past and present, for making the last three years memorable. Particular thanks go to Owen, Joe, Matt and Dave for keeping me entertained in the office. A massive thanks goes to Dr Louise Smith for the constant advice and help throughout my PhD. I am extremely grateful to Annie Cooper and Liam Bailey for their continuous support, friendship and all the laughs along the way.

I would like to thank all my friends outside of Cardiff University for their encouragement throughout the last three years, particularly to Cam, Connor, Georgia, Etty, Patch, Bevan and Sam for helping me through the difficult times. Finally, I would like to thank my family, who have been so supportive of me over the course of my PhD. Especially mum and dad, thank you for everything. I would not have been able to do this without your love and support. I am forever grateful for all you have done and continue to do for me.

Abstract

The preparation and analysis of cerium oxide (CeO_2) based metal oxide catalysts, and novel supported precious metal catalysts were investigated for the total oxidation of volatile organic compounds (VOCs). The influence of the cerium precursor on the physiochemical properties of the resulting CeO_2 catalyst was determined, and how these properties were then related to the catalytic performance for propane and naphthalene total oxidation. The synthesis method was optimised to further understand the impact of precipitate formation and how this resulted in the characteristics observed. Catalysts that formed the hydrated $CeO_2.H_2O$ precipitate were shown to be more active for the total oxidation of VOCs. The application of 'real world' testing conditions was used to assess the catalytic activity under conditions required for industrial uses, with these conditions inhibiting catalyst performance.

The addition of iron (Fe), a cheap and abundant metal, to the CeO_2 catalysts was carried out to determine the impact on catalytic activity. Similar effects of the cerium precursor were observed in the mixed metal oxide catalysts for propane and naphthalene total oxidation. The mixture of Ce and Fe species was overall shown to inhibit the catalytic activity for the oxidation of both VOCs. For propane, this was a result of the supressed reducibility of Fe_2O_3 by Ce addition; whereas for naphthalene, the addition of Fe species inhibited CeO_2 catalytic activity. Propane and naphthalene total oxidation were also assessed over a range of doped ceria-zirconia ($CeZrO_x$) catalysts, using small quantities of abundant transition metals as dopants. The incorporation of copper (Cu) and Fe increased catalytic activity for the total oxidation of both VOCs, with enhanced surface area, increased oxygen mobility and decreased residual sodium (Na) species attributed to the improved activity measured.

Precious metal catalysts, containing mono or bimetallic gold (Au) and platinum (Pt) nanoparticles, supported on a novel porous silica structure, were investigated for the simultaneous total oxidation of three model VOCs, commonly used to simulate 'cold start pollutants' in engines. Pt nanoparticles were identified as the active catalyst component, with Au species inhibiting activity. The order of metal deposition was found to be influential, with depositing Au and Pt sequentially resulting in surface enrichment of either metal nanoparticle. In the case of depositing Au first, this enriched the surface with Pt nanoparticles leading to improved catalytic activity.

Publication List

- **Aggett, K**.; Davies, T.E.; Morgan, D.J.; Hewes, D.; Taylor, S.H. The Influence of Precursor on the Preparation of CeO_2 Catalysts for the Total Oxidation of the Volatile Organic Compound Propane. *Catalysts* **2021**, *11*, 1461. https://doi.org/10.3390/catal11121461

Contents

1. Introduction

1.1 Catalysis introduction

Catalysis as an unknown concept has been utilised for thousands of years in various processes, including fermentation. However, the first definition of the chemical process involved was identified by Berzelius in 1836 as a catalytic force that drove the reaction [1]. The term 'catalytic force' was used to provide a general description of the process but did not provide an explanation on the understanding of the effect the catalyst had in a reaction. An explanation was later provided by Ostwald, who defined catalysis as the acceleration of a reaction by a foreign body [2]. This explanation is commonly accepted, resulting in a modern-day interpretation of the definition to be a substance which increases the rate of reaction, without being consumed in the process.

It is important to note that a catalyst does not alter the thermodynamic equilibrium of a reaction, just enable the rate of reaction to be increased. In keeping with the conservation of the thermodynamics, the energy of the initial and final states cannot change. In contrast, the increase to the rate constant is a result of the reduction of the activation energy (E_a) for a given reaction [3]. This occurs as the catalyst provides different pathways for the reaction to proceed, with the new pathways being more energetically favourable when compared to the un-catalysed reaction.

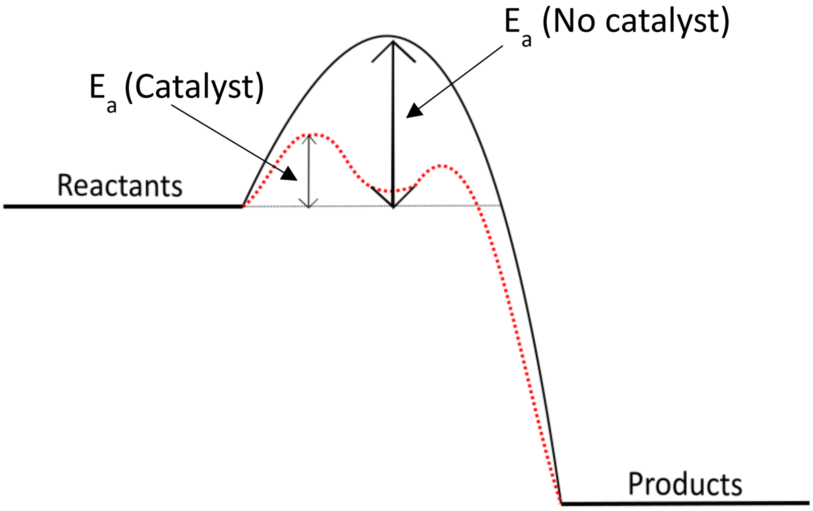

Figure 1: Energy level diagram depicting the differences in activation energy (E_a) with and without the use of a catalyst.

The development of catalysis as a discipline can be defined by certain periods of time which saw the demand grow, as a result of viable industrial processes. Some of the most influential periods included the demand for bulk chemicals during WW1, which saw the growth of catalysis in industrial processes. This was followed by the dominating role of the petrochemical industry and the use of catalysts for the synthesis of fuels and polymers. Environmental catalysis emerged in the 1970s as a result of increased environmental awareness, paving the way for the use of catalysis in most modern day industrial processes [4]. It is thought that over 90% of industrial chemicals are made using catalysis, with the total value of those chemicals being $900 billion per year in 1991 [5].

There are three main class of catalysts, these being: homogeneous, heterogeneous and biological catalysts. Enzymes can be used as biological catalysts, which are very active for specific reactions. However, these catalysts suffer from poor stability and, upon variation of reaction conditions, can deactivate very quickly. Homogeneous catalysts are catalysts which are in the same state as the reactants. For example, if the reactants are in the liquid phase then the catalyst will also be in the liquid phase. Heterogeneous catalysts are in a different phase to the reactants, with many industrial examples of heterogeneous catalysis relating to gas phase reactions using solid catalysts. It has been stated that heterogeneous catalysts make up 80% of industrial catalytic processes [6].

For a catalyst to be effective, factors such as activity, selectivity and stability should be considered. Catalytic activity can be defined by the promotion of a reaction by the catalyst, with a more active catalyst displaying an increased rate of reaction in terms of product produced per volume of catalyst in the reactor. The term selectivity refers to the production of desired product from consumed reactants [7]. A combination of these two factors can be important when assessing the effectiveness of a catalyst for certain situations. For example, a highly selective catalyst that has low activity would not be efficient for producing large quantities of cheap chemicals, whereas, a highly selective catalyst would be beneficial for producing products which are not the most thermodynamically stable. Stability of a catalyst is key for commercial use, as it refers to how long a catalyst will maintain its activity before deactivating [8]. A catalyst with slightly lower activity but higher stability can sometimes be more economically beneficial for a commercial process.

1.2 Volatile Organic Compounds (VOCs)

A Volatile Organic Compound (VOC) can be defined in various ways. The 2004/42/CE EU directive states that a VOC is defined as ‘any organic compound that has a boiling point less than or equal to 250°C, measured at standard pressure’ [9]. In comparison to this, the US Environmental Protection Agency (EPA) identifies a VOC as ‘any compound of carbon, excluding carbon monoxide, carbon dioxide, carbonic acid, metallic carbides or carbonates, and ammonium carbonate, which participates in atmospheric photochemical reactions’ [10]. As a result of the poor quantitative definition of a VOC, a more general interpretation can be used. This being that, an organic compound is considered a VOC if it can be identified by these characteristics: having a vapour pressure greater than 10 Pa at 25°C, having a boiling point equal to or less than 260°C at standard atmospheric pressure and containing 15 or less carbon atoms [11]. The broad and varying definition of a VOC enables the division of compounds into sub-categories, which can be linked by certain chemical properties, such as Semi-Volatile Organic Compounds (SVOCs) or Very Volatile Organic Compounds (VVOCs).

The source of a VOC can be divided into two main categories; these being, biogenic and anthropogenic sources. Biogenic, also known as natural sources, mostly originate from areas of vegetation, soils, oceans and volcanic activity. The emission of these types of VOCs are associated with plant metabolism, regulating plant growth and are dominant in the troposphere, strongly affecting the climate [12,13]. It has been stated that of all VOCs emitted into the atmosphere, biogenic VOCs can account for 90% of global emissions [14]. Of the varying biogenic VOCs, isoprene is noted as representing a large portion of global VOC emissions in the atmosphere [15]. As biogenic VOCs are emitted naturally and can vary depending on conditions, it is difficult to limit their impact on the environment.

Anthropogenic VOCs originate from man-made activities, which can be at either large industrial scale or on a small domestic scale. Solvents in house-hold products, such as paints and adhesives, are attributed with domestic VOC emissions, in addition to gas cooking equipment and building materials [16]. Emission of VOCs at an industrial scale can be linked to the manufacture of pharmaceutical products and biomass burning from agricultural practices. However, the largest proportion of anthropogenic VOCs emitted are from the burning or production of fossil fuels [17]. Discussed in Section 1.3, VOCs can cause an array of issues relating to environmental degradation and human health. VOCs emitted from anthropogenic sources have been targeted by numerous legislations worldwide in order to reduce the quantity in the atmosphere. This is being achieved by developing various technologies, including research and improvement of catalytic technologies, and implementing ‘green’ processes.

1.3 Environmental impact of VOCs

Ozone (O_3) concentrations in the atmosphere are dependent on the emission of VOCs. O_3 in the stratosphere (ozone layer) is naturally occurring and protects the earth’s surface from harmful solar UV radiation. Certain types of VOCs, such as aromatic and chlorinated VOCs, are able to deplete this layer allowing an increased amount of UV radiation to enter the atmosphere [18]. This can lead to adverse health effects, with increased UV exposure linked to skin cancer. In addition to the depletion of the ozone layer, VOCs are key precursors to the formation of tropospheric (ground-level) O_3. The combination of VOCs and NO_x species, released into the atmosphere, causes the formation of tropospheric ozone following the mechanism:

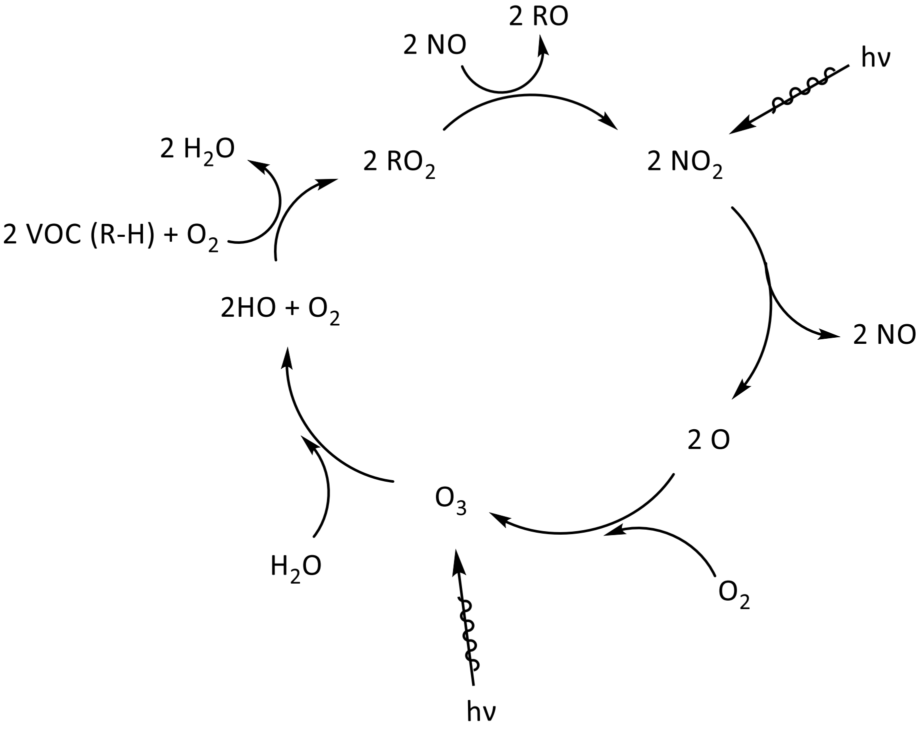

Figure 2: Mechanism for the formation of tropospheric O_3 from the reaction between VOC and NO_x species.

Tropospheric ozone is one of several important air pollutants which can severely affect human health and vegetation. An increase in respiratory disease, cardiovascular disease and cancer have been associated with increased exposure to ozone [19,20]. Furthermore, negative effects on vegetation can be highlighted, with a decrease in crop yield and quality [21]. Models have been used to indicate that the increasing emission of VOCs and NO_x

would result in an increase in ozone concentration, thus leading to more detrimental health effects [22]. The issue of ozone is also two-fold, in that increased VOC emission can deplete stratospheric ozone, allowing more UV radiation to enter the atmosphere, whilst the mechanism for tropospheric ozone can depend on the intensity of the UV radiation, leading to a higher concentration [23,24].

As previously mentioned, the emission of VOCs into the atmosphere can result in an indirect negative effect on human health through the production of tropospheric ozone. However, it is of concern that certain VOCs can have a direct negative effect on human health. Exposure to VOCs present in an indoor setting have been linked with reduced lung function in young people, which supports further epidemiological studies relating the prevalence of asthma in children with increased concentration of indoor VOCs [25]. Furthermore, even at low concentrations, many VOCs can have carcinogenic or mutagenic effects with prolonged exposure [26].

Another indirect effect of VOC emissions on the environment is the impact it has on climate change. The term climate change is defined by the long-term change in global or regional climate by natural or anthropogenic activity. Recently, it has been attributed to the change in the global climate from anthropogenic activity, termed global warming, that has seen an increase in the earth’s surface temperature from the emission of greenhouse gases. Greenhouse gases are compounds that absorb infrared radiation, thus enforcing the greenhouse effect of heating the earth’s surface [27]. This is a natural process which is kept in balance; however, emission of anthropogenic greenhouse gases can further enhance this process, therefore resulting in global warming. Global warming can have detrimental effects on the way humans live as it can cause more frequent severe weather occurrences, rising sea levels and affect food supplies [28]. Many VOCs have been classified as contributing to the greenhouse effect, making the emission of these compounds important to control [29]. A way to identify how harmful a VOC can be is to look at its global warming potential (GWP). This is a measure of the direct and indirect effect a VOC has on the atmosphere by encompassing its time-integrated radiative force upon release of a set quantity, compared with CO_2. CO_2 is used as a reference compound, as it is largely responsible for the natural greenhouse effect. Some aliphatic and aromatic VOCs have been shown to have GWPs of up to ten times that of the of the reference [30,31], with halogenated VOCs presenting GWPs over a thousand times higher.

Secondary Organic Aerosols (SOA) can be formed from aromatic VOC precursors, most commonly associated with fuel combustion, when reacted with atmospheric oxidants such as hydroxyl radicals, NO_x and ozone [32,33]. The oxidation products of aromatic VOCs lead to larger molecular weight compounds, which lowers their vapour pressure. These compounds can then form SOAs, either by partitioning into a particulate phase through condensation, or undergo nucleation to create new aerosols [34]. These SOAs can influence the production of particulate matter, such as soot and $PM_{2.5}$, and account for a large portion of the organic species in these systems [35]. Increases in biogenic SOAs can also be linked to increased anthropogenic emissions, leading to further issues caused by particulate formation [36]. Exposure to particulate matter from SOAs can lead to a multitude of health conditions, including respiratory problems, increased likelihood of a stroke and increased mortality for diseases such as cancer [20,37–39].

As discussed, VOC emission from anthropogenic activities cause an abundance of direct and indirect issues that negatively impact human health and the environment. In response to these problems, global legislations, such as The Montreal Protocol, Kyoto Protocol and Gothenburg Protocol, were adopted to reduce the emission of pollutants. More recently, legislation has gone further, with agreements like The Paris Agreement 2015 and EURO 7 regulations, targeting the reduction of pollutants associated with fossil fuel use. Ways to avoid and abate these emissions are constantly being improved upon, with advancement of technologies and implementing ‘greener’ processes, including further development of catalytic processes.

1.3.1 Propane and naphthalene as model aliphatic and polyaromatic VOCs

As mentioned in Section 1.2, VOCs can be divided into sub-categories to better identify their characteristics. Short chain alkanes are categorised as aliphatic VOCs, with propane often studied as a model compound for aliphatic VOCs due to its simplistic nature. Furthermore, it is well established that short chain alkanes are less reactive, making them difficult to remove from the atmosphere, therefore making propane an excellent model compound to study [40].

Aliphatic VOC emissions are predominantly generated by the petroleum refining and petrochemical industries [41]. Additionally, alkane emissions can be strongly associated with vehicle exhaust emissions, accounting for approximately 40% of all chemicals measured [42]. The increased use of liquified petroleum gas (LPG) as a fuel has led to an increase in propane emissions specifically [43]. LPG is made from a mixture of alkanes, usually consisting of a ratio of propane and butane and is thought to be more economically viable compared with standard petrol [44].

Whilst propane itself is a non-toxic VOC, emission of the compound can result in negative effects for the environment and human health. The emission of propane can result in the formation of tropospheric ozone from the reaction with NO_x, as mentioned in Section 1.3. In addition to this, previous studies have shown propane to have a global warming potential (GWP) of 9.5 [30]. Furthermore, short chain alkanes like propane have been identified as difficult to remove from the atmosphere owing to their chemical stability [45], causing concern for longevity in the atmosphere. This fact also makes propane an excellent model compound to assess the removal of VOCs by catalytic methods.

Naphthalene is the simplest polyaromatic hydrocarbon (PAH) and is another compound that can be used as an appropriate and contrasting model compound. Naphthalene can be categorised as an aromatic VOC, with emission sources linked to several combustion processes such as coal, diesel and biomass burning [46]. It can also be found from domestic sources, including fumigants and cigarette smoke [47]. In contrast to propane, it is a known carcinogenic compound with severe health impacts [48]. Prolonged exposure can lead to liver and kidney damage, nasal tumours, and cancer [47,49]. In addition to the direct impacts, naphthalene emission can contribute to the indirect environmental effects mentioned throughout Section 1.3.

1.3.2 Carbon monoxide, propene, and toluene as a model VOC mixture for vehicle emissions

The release of pollutants from vehicle emissions is becoming increasingly regulated with the introduction of new legislation, such as EURO 7, which will replace the current EURO 6 regulations. This legislation aims to reduce the emission of VOCs, NO_x and particulate matter from vehicle exhausts. To do this, new technologies are required to remove pollutants simultaneously. The combination of carbon monoxide (CO) and unburnt hydrocarbons, emitted during cold start in engines, have been targeted in previous research [50,51]. Of the unburnt hydrocarbons emitted, aromatic VOCs such as toluene and lighter hydrocarbons such as propane, ethene and propene have been shown to be the most abundant [52]. Therefore, the use of CO, propene and toluene is an excellent model for assessing VOC emission from vehicle exhausts.

Although not classified as a VOC, CO emissions can have detrimental effects for human health. CO is mainly emitted from petrol engines, compared to diesel engines, in addition to unburnt hydrocarbons and NO_x species [53]. Prolonged exposure of CO can lead to a range of health issues, including myocardial injury due to lack of oxygen, impaired neurodevelopment and tissue hypoxia, leading to severe damage of critical organs [54–56]. Toluene and propene have been identified as highly polluting compounds due to their high Photochemical Ozone Creativity Potential (POCP) [57,58]. Furthermore, toluene is a toxic VOC, with inhalation of low concentrations linked to decreased brain function and adverse nervous system issues [59].

1.4 Methods to remove VOCs

As discussed in Section 1.3, VOC emissions can result in negative impacts for human health and the environment. This has led to a plethora of technologies invented to abate these emissions. Technologies can be categorised into two main types, those being recovery methods or destructive methods. Recovery methods focus on the removal of VOCs from waste streams and recycle them into useful products. Whereas destructive methods completely remove VOCs, mainly by converting them into CO_2 and H_2O.

1.4.1 Recovery methods

Absorption technologies are a commonly used method to recover high value VOCs by scrubbing contaminated air streams with a liquid solvent [60]. This process results in soluble VOCs absorbing into a suitable solvent which can then be recovered by further processing. It is stated that this method benefits from a removal efficiency of 90-98%, in addition to being simple to operate with the use of either traditional or rotating pack beds [61,62]. However, absorption technologies suffer from requiring post treatment of the absorbent to recycle VOCs, which leads to high operation costs [63]. Another disadvantage of this method is that it is inefficient when dealing with dilute concentrations of VOCs in waste streams, as it requires larger quantities of absorbent to acquire an effective contact time between the solvent and VOC [64].

To overcome the disadvantages of absorption technologies, such as ineffectiveness for dilute VOC concentrations, adsorption technologies can be used. Adsorption methods use porous materials to adsorb VOCs from dilute waste streams, which can then be recovered or destroyed by further processing [63]. Materials including activated carbon, zeolites, silica gels and synthetic polymers have been used as suitable adsorbent materials, due to their high surface areas and developed pore structures [65]. Similarly to absorption methods, the choice of material is very important to effectively remove selected VOCs from waste streams. The main advantages of adsorption technologies are the low operating cost, reusability of materials and high removal efficiency, which can be over 90% [66]. Despite this, adsorption methods offer similar issues to the ones noted for absorption methods. Post processing of materials to recover trapped VOCs can lead to increased operation costs. Furthermore, species present in waste streams, like water vapour, have been shown to deactivate adsorbents as a result of competition for the binding sites as well as blocking pores [63,66].

Another new technology has emerged in recent years for the removal of VOCs. Membrane separation techniques have been researched as viable alternatives to absorption and adsorption methods. This technology involves the use of semi-permeable materials that allow diffusion of VOCs from waste streams into solvents [67]. Silicone rubber, polymers and zeolites are all types of membranes that have been identified as applicable materials for this process [68,69]. Though in early development, these materials show good VOC removal efficiency for a range of compounds. However, membrane materials are expensive to produce and there is limited use with low VOC concentration waste streams [60,67].

1.4.2 Destructive methods

The simplest destructive method used in industry is thermal oxidation or incineration of VOCs from waste streams. This method uses temperatures around 900-1000°C to convert VOCs to CO_2 and H_2O [64]. A key benefit of this process is that it works for a wide range of VOCs, able to remove broad ranging mixtures at medium to high concentration [70]. Conversely, the use of such high temperatures can lead to high operation costs and the production of secondary pollutants like NO_x, dioxins and dibenzofurans which then result in more environmental and health problems, as mentioned previously [60,71]. To combat these issues, other technologies have been developed which involve the oxidation of VOCs but avoid harsh operating conditions.

Catalytic oxidation is a process similar to thermal oxidation but incorporates the use of a catalytic material to improve operational conditions. As mentioned in Section 1.1, catalysts lower the activation energy for the reaction, resulting in the requirement of much lower temperatures for VOC oxidation [64]. This leads to lower operating costs from lower temperatures and less harmful by-products like NO_x being produced. Catalytic oxidation also provides the benefit of flexibility as a broad range of materials with different advantages are available to suit most conditions [63,72]. Furthermore, this method is suitable for low concentrations of VOCs, with a high removal efficiency, and does not require further complex post processing, compared with recovery methods [60]. With a broad range of catalysts available, research into the most applicable materials for VOC oxidation is extensive and explored in Section 1.5.

1.5 Catalytic VOC total oxidation

As mentioned in Section 1.4.2, catalytic oxidation is a desirable option for VOC abatement. With a wide variety of catalysts to suit many applications, this area has been extensively researched to improve understanding and develop new materials. Catalysts for VOC oxidation can be separated into two distinct categories; these being supported metal catalysts and metal oxide catalysts.

1.5.1 Supported metal catalysts

Supported metal catalysts mainly consist of precious metals deposited onto a metal oxide support. Precious metals such as Au, Pt, Pd, Rh and Ru are widely used for VOC oxidation due to their impressive catalytic activity and durability [73]. Of the precious metals used, Pt and Pd have been identified as highly active metals for VOC total oxidation [74,75]. Supported Pd catalysts have been used for the oxidation of aromatic VOCs such as toluene and benzene [76,77], as well as the oxidation of methane [78]. Features such as particle size and Pd oxidation state have been established as important factors to understand catalytic activity for these catalysts. Pt catalysts have shown significant low temperature activity compared with other noble metals for VOC oxidation [79]. Research carried out by Ordonez *et al*. showed that Pt/γ-Al_2O_3 catalysts were able to fully oxidise toluene, benzene and hexane under 200°C [80]. Furthermore, Pt dispersion on Al_2O_3 was identified as an important factor for the oxidation of propene and CO by Haneda *et al.* [81]. Au is another precious metal that has been extensively investigated for VOC oxidation. Initially thought to be an inactive compound, when deposited on a metal oxide support, Au catalysts show good activity for the oxidation of various VOCs [82]. A key factor affecting the catalytic activity of supported Au catalysts are the interaction of Au nanoparticles with the support [18,83,84].

Catalyst supports play an important role in determining the catalytic activity for supported metal catalysts, usually being divided into two types: active and inert supports [73]. Active supports consist of metal oxides that have certain catalytic activity towards the oxidation reaction. Examples of some active supports are CeO_2, ZrO_2, Fe_2O_3, TiO_2, Co_3O_4 and CuO [85,86]. In contrast, materials such as SiO_2, Al_2O_3 and Carbon can be used as inert supports for VOC oxidation [81,87]. Both types of supports have different advantages and can impact catalytic activity, with factors such as support surface area, metal nanoparticle dispersion and metal-support interactions being important for VOC total oxidation. For inert supports, the activity is highly correlated to the active component of the metal nanoparticle. Whereas with active supports, the activity can be governed by the metal nanoparticle, the reaction of the VOC on the support and how the support interacts with the metal nanoparticle [88]. Development of mixed supports, where an active metal oxide is deposited onto an inert support or mixed with it, which are then loaded with precious metal nanoparticles, have shown increased catalytic activity, as well as nanoparticle stability, for VOC oxidation reactions [89–91]. The improved activity can occur from a synergetic effect between the active sites on the metal oxide and dispersed precious metal nanoparticles.

The use of multiple precious metals on supported catalysts have been researched more recently. Bimetallic catalysts, using precious metal combinations such as AuPd, AuPt, and PtPd have been found to be more active than their monometallic counterparts for VOC oxidation [92,93]. The alloying of Pt and Pd nanoparticles can result in changes to the co-ordination environment, by affecting the electronic and geometric structure of the nanoparticles, in addition to manipulating adsorption sites, which then impacts fundamental catalytic processes [94]. Hosseini *et al*. synthesised AuPd bimetallic catalysts with varied core-shell structures for the oxidation of toluene and propene VOCs [95]. It was found that the order of deposition greatly affected the catalytic activity for both VOCs, with a Au core and Pd shell resulting in the most active catalyst. AuPt supported catalysts have been less commonly reported compared to the widely researched AuPd bimetallic system. However, supported AuPt catalysts have shown good activity for the total oxidation of soot and CO [96,97]. It has been proposed that surface enrichment can occur on this catalyst system under different conditions, which can impact the alloying of the two metals [97,98].

1.5.2 Metal oxide catalysts

Metal oxide catalysts have been well researched recently as an alternative material to supported precious metal catalysts. This is due to the cheap and abundant nature of metal oxides when compared to elements such as Pt or Pd [82,99]. The limited cost of production as well as versatility provided by the wide range of metals used are enticing factors to consider for catalyst uses [100]. In addition, metal oxide catalysts have shown increased resistance to poisons in waste streams [101], making them beneficial for industrial uses. However, metal oxide catalysts generally exhibit lower catalytic activity when compared to supported metal catalysts [101]. Research has therefore focused on the optimisation of metal oxide catalysts to produce materials that are equivalent or superior to supported precious metal catalysts in activity, selectivity and stability.

Of the many metal oxides available, cerium(IV) oxide (CeO_2) is commonly known as an effective oxidation catalyst. Cerium is the most abundant rare earth metal [82], making it a suitable candidate for use in catalysis. CeO_2 exhibits a cubic structure, represented by the *Fm3m* space group, with a face centred cubic (FCC) unit cell [102]. Defect formation can occur in crystalline CeO_2 materials, these being either intrinsic or extrinsic. Intrinsic defects can occur in both stoichiometric and non-stoichiometric CeO_2 and are defined as either Schottky or Frenkel type defects. Schottky defects are formed when oppositely charged ions leave the cubic lattice, producing vacancies [103]. Whereas Frenkel type defects occur when a lattice ion is displaced into an interstitial site creating a vacancy in the original lattice position [103,104]. Extrinsic defects are promoted in the CeO_2 structure by the addition of dopants such as aliovalent ions [105,106]. Oxygen defect formation is associated with CeO_2 materials, where oxygen ions are removed from the lattice and the charge neutrality is maintained by the reduction of the Ce^{4+} ion to Ce^{3+}. Previous literature

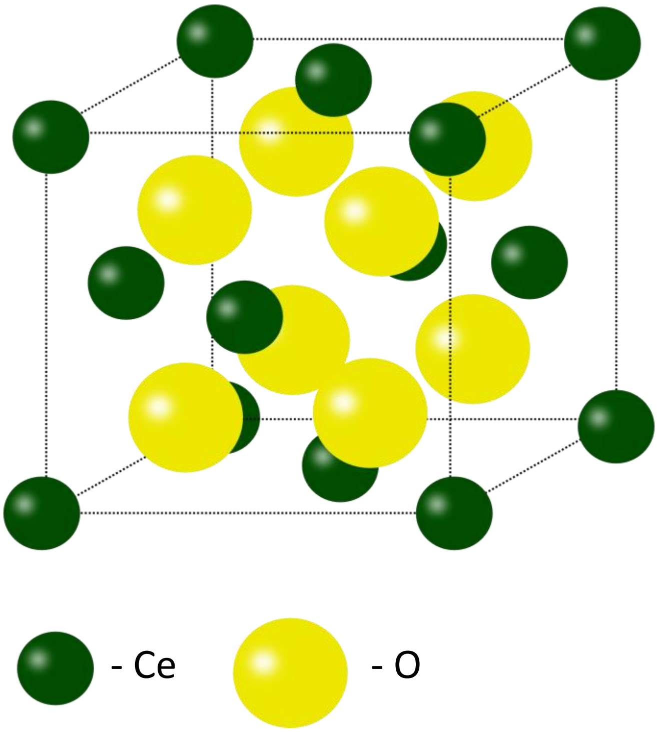

Figure 3: Representation of the CeO_2 unit cell.

has discussed the importance of this mechanism for improving oxygen mobility through the CeO_2 lattice [107], which can then facilitate oxidation reactions. In addition to defect formation, CeO_2 boasts impressive redox properties from the facile cycle between $Ce^{4+} \leftrightarrow Ce^{3+}$. The facile reducibility of CeO_2 enables it to act as an oxygen reservoir, relating to the high oxygen storage capacity (OSC) linked with these materials.

These characteristics have been utilised for the improvement of catalysts for oxidation reactions. Most prominently, CeO_2 was used as a promoter in the commercial three-way catalyst [108], where its OSC was exploited to ensure better control of the oxygen:fuel ratio, allowing for improved conversion of CO and hydrocarbons. CeO_2 has been shown as an efficient oxidation catalyst for aromatic VOCs, such as toluene, benzene and naphthalene [109]. In particular, naphthalene total oxidation has been shown to be the most effective over CeO_2 catalysts compared with other metal oxide catalysts [110]. García *et al.* also found that by varying the preparation method, the CeO_2 catalyst exhibited better activity compared to a supported 0.5% Pt/γ-Al_2O_3 catalyst [48]. Furthermore, research by Ndifor *et al.* has expanded upon this work and shown that high surface area CeO_2, with a large quantity of oxygen defects, was responsible for the activity measured for naphthalene total oxidation [46].

Transition metals have also been utilised as functional catalysts for VOC abatement. The different properties of the transition metals provides a wide variety of options to help specifically tailor catalyst design towards a certain VOC. Therefore, many different transition metal oxide catalysts are recorded in the literature for a range of VOC oxidation reactions. Metal oxide catalysts, such as cobalt oxide (Co_3O_4), copper oxide (CuO), iron oxide (Fe_2O_3), nickel oxide (NiO) and manganese oxide (Mn_2O_3), have all been widely regarded as good alternative catalysts for VOC total oxidation. Co_3O_4 has shown remarkable activity for the total oxidation of propane [111]. Research by Marin *et al.* showed that a Co_3O_4 catalyst prepared by supercritical antisolvent preparation presented higher activity for propane total oxidation when compared with a commercial 5% Pt/Al_2O_3 catalyst [112].

The use of Fe_2O_3 as an alternative oxidation catalyst has been discussed in the literature. Research carried out by Solsona *et al.* has shown that Fe_2O_3 presented good catalytic activity for propane and toluene total oxidation [113], when prepared by different methods. Whilst it was suggested that the activity for propane total oxidation using Fe_2O_3

was lower compared to other metal oxide catalysts like Co_3O_4, the Fe_2O_3 catalyst provides many advantages as it is an extremely cheap and abundant material whilst having non-toxic properties [113]. Another advantage of Fe_2O_3 is the high thermal stability of the material [114], resulting in limited deactivation from thermal sintering when reactions occur at elevated temperatures. Fe_2O_3 has also shown good activity for other VOCs, including the total oxidation of acetone, methanol and toluene [115,116]. Metal oxides such as Fe_2O_3, Co_3O_4 and Mn_2O_3 also present structure dependent activity as they can form spinel structures, having mixed valence ions in the crystalline lattice, which has been shown to improve catalytic activity for the total oxidation of VOCs [117]. Kim *et al.* tested a set of manganese oxide catalysts with different valence states for the total oxidation of toluene and found that the Mn_3O_4 catalyst was the most active, correlating to the improved oxygen mobility from the structure [118].

Whilst initial research on the application of metal oxides as catalysts for VOC oxidation showed promise, the materials are limited by process conditions. As metal oxide catalysts generally present lower activity compared with precious metal catalysts [101], harsher reaction conditions are required to promote activity. This results in slightly higher reaction temperatures, which can then lead to deactivation of metal oxides by sintering. Many approaches have been taken to overcome these issues, with examples of using metal oxides, like iron oxide, with higher thermal stability [113,114]. However, the most promising method of improving catalyst stability in addition to activity at low temperatures is the preparation of mixed metal oxide catalysts.

1.5.3 Mixed metal oxide catalysts

Mixed metal oxide catalysts have been the focus of recent research due to the limitations of both supported precious metal catalysts and single metal oxide catalysts. Benefits of improved stability, activity and use of cost effective materials have been reported throughout the literature for these catalysts [99,101]. Mixed metal catalysts encompass a wide variety of different mixing methods, with direct mixing of two or more metal oxides the most common. However, other methods such as doping small quantities of metals into bulk metal oxide catalysts and mixtures of metals deposited onto supports are also employed, creating a diverse range of catalytic possibilities.

Mixing of CeO_2 based catalysts is widely reported in the literature with many metals utilised. The well-known combination of CeO_2 and zirconia (ZrO_2) is well researched for use as an effective oxidation catalyst. Although monometallic ZrO_2 has been used as a catalyst or catalyst support previously, incorporation into the cubic CeO_2 structure has been employed to produce highly active mixed catalysts with enhanced resistance to thermal sintering [119]. It has been reported that Zr can be inserted into the CeO_2 structure in high quantities, creating a defective structure which promotes oxygen mobility [120]. This has resulted in improved catalytic activity for the total oxidation of naphthalene and chlorinated VOCs, compared to the standard CeO_2 catalyst [121–123]. The most well-known examples of $CeZrO_x$ materials are in the development of the three-way catalyst for hydrocarbon and CO oxidation. The promotional effect of CeO_2 was beneficial for the three-way catalyst, but it suffered from thermal instability, with sintering occurring at elevated temperatures [108]. When Zr was introduced into the CeO_2 structure, the thermal stability was increased as well as the OSC of the system, leading to enhanced performance [119].

Transition metal oxides have also been mixed with CeO_2 to produce active oxidation catalysts. The incorporation of aliovalent ions into the cubic lattice can create extrinsic defect structures that promote oxygen mobility [106]. Due to the charge and size differences of the transition metal ions, incorporation into the cubic CeO_2 structure can occur by different mechanisms. In the case of doping with trivalent cations like Fe^{3+}, incorporation can occur by an interstitial method, where three Ce^{4+} ions are substituted with four M^{3+} ions to maintain charge neutrality, with the extra trivalent cation occupying an interstitial site [124]. Whereas another method follows the direct substitution of Ce^{4+} for M^{3+}, with charge neutrality maintained by the formation of oxygen defects [124]. A selection of $CeFeO_x$ catalysts have been developed by multiple synthesis methods , showing promise for improved catalytic activity and stability. In particular, $CeFeO_x$ mixed catalysts have shown good activity for the oxidation of soot, with the formation of Fe-O-Ce solid solutions facilitating oxygen defect formation, which was suggested to be crucial for the enhanced activity measured [125,126]. In addition to this, $CeFeO_x$ mixed catalysts have presented appreciable activity for the total oxidation of aliphatic VOCs, such as propane and methane [127,128]. $CeFeO_x$ catalysts prepared by Laguna *et al.* exhibited reduced Ce crystallite size, which was suggested to be linked with the ability of Fe species to limit sintering of Ce species [129], supporting the improved stability of the mixed oxide catalysts.

The substitution of CeO_2 in the cubic structure has also been carried out using other abundant transition metals, such as Mn, Co and Cu. For $CeCuO_x$ mixed catalysts, the incorporation of Cu into the system can create a complementary redox cycle between Cu^+

$\leftrightarrow Cu^{2+}$ and $Ce^{4+} \leftrightarrow Ce^{3+}$ species which promotes the catalyst reducibility [130]. These types of catalysts have shown good catalytic activity for toluene, benzene and CO total oxidation [130–132]. As Co_3O_4 is regarded as the most effective metal oxide catalyst for propane total oxidation, many variations of $CeCoO_x$ catalysts have been developed to try and further improve upon the catalytic activity. $CeCoO_x$ catalysts prepared by a sol-gel and citric acid method exhibited impressive catalytic activity for propane total oxidation, which was related to the increased oxygen mobility, reducibility and higher proportion of Co^{3+} on the surface of the mixed catalysts [133,134].

In addition to mixing metal oxides in large ratios, doping small quantities of metal oxides into CeO_2 based materials have also been tested in order to enhance catalytic activity. Doping small quantities of metals allows for increased activity with insignificant additional cost when compared to using large quantities of materials. Furthermore, with low loadings used, limited phase segregation can be observed, leading to better catalyst performance where bulk inactive species are not present [135]. Work by Aranda *et al.* shows a good example of this, where small quantities of Cu were doped into CeO_2 for the total oxidation of naphthalene [136]. The activity was significantly increased at low loadings of 3.6 at.%, where an increased amount of surface defects were formed, but at higher loadings inactive CuO species were present which negatively impacted catalytic activity.

1.6 Oxidation mechanisms

Three main mechanisms are reported for oxidation reactions in the literature, these being the Mars-van Krevelen, Langmuir-Hinshelwood and Eley-Rideal. The Mars-van Krevelen mechanism is mainly associated with oxidation reactions occurring over metal oxide catalysts [101]. The reaction pathway follows an initial adsorption stage of the VOC on the catalyst surface. This is then oxidised on the catalyst surface by lattice oxygen from the metal oxide catalyst, forming the reaction products. Finally, product desorption occurs from the catalyst surface and the lattice oxygen is replenished by gaseous or bulk oxygen species [82]. As this mechanism involves a reduction of the catalyst surface, followed by re-oxidation, it is commonly referred to as a redox mechanism and has been suggested for the total oxidation of both propane and naphthalene VOCs over metal oxide catalysts [110,121,137].

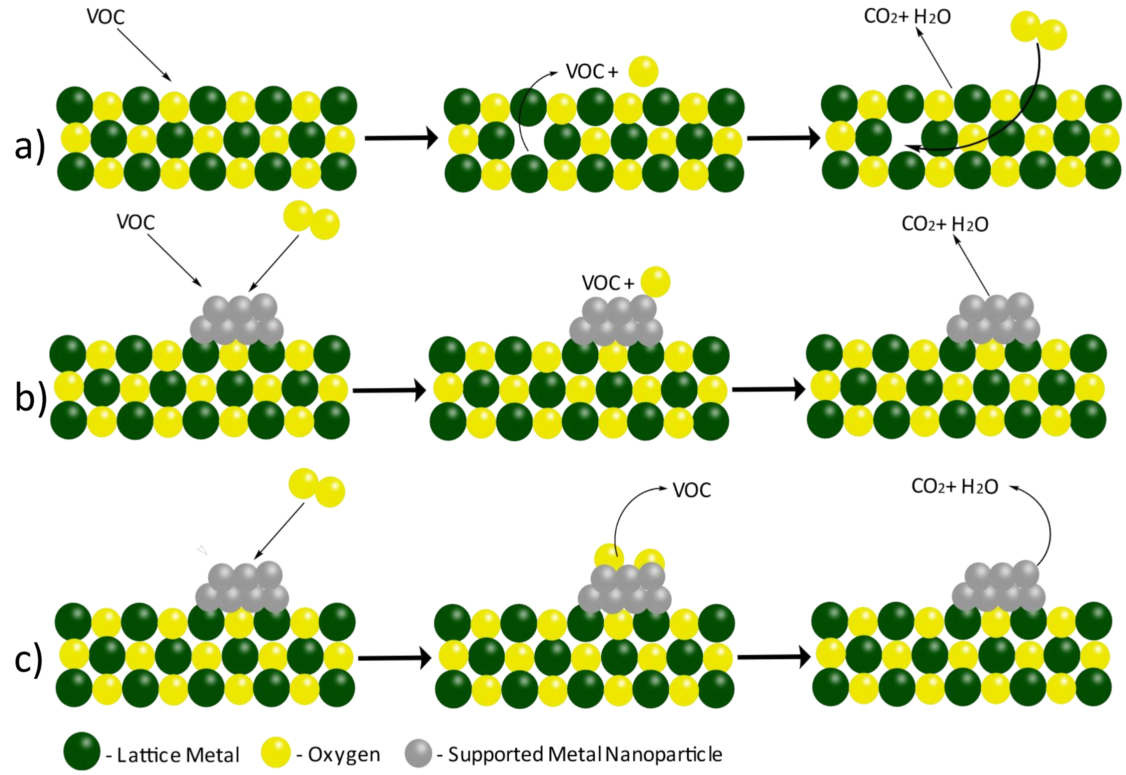

Figure 4: a) Mars-van Krevelen, b) Langmuir-Hinshelwood and c) Eley-Rideal oxidation mechanisms for VOC total oxidation.

The Langmuir-Hinshelwood mechanism occurs by a different pathway. In this mechanism, both reactants are firstly adsorbed to the catalyst surface on adjacent active sites. In the case of VOC total oxidation, these reactants being the VOC and oxygen molecules. Following this, the oxidation reaction occurs on the surface of the catalyst, with product desorption as the final step [138]. It has been suggested that this mechanism occurs for VOC total oxidation over supported precious metal catalysts, with research proposing this mechanism for propene and toluene oxidation over supported Pd or Pd/Au catalysts [95,139]. The Langmuir-Hinshelwood model involves competitive adsorption of both VOC and oxygen on the catalyst surface, where the controlling step is suggested to rely on the surface reaction of the two compounds [86].

Finally, a slightly different mechanism to the Langmuir-Hinshelwood was proposed, called the Eley-Rideal. In this model, the reaction occurs by adsorbed oxygen on the catalyst surface reacting directly with an organic molecule in the gas phase, with no adsorption of the VOC occurring [140]. The controlling step in this model is suggested to be the reaction between the adsorbed oxygen and gaseous molecule [86]. This mechanism is less commonly applied but has been suggested for the total oxidation of CO over a Pd oxide surface [141].

1.7 Project outline

The main objective of this thesis is the preparation of active, selective and stable heterogeneous catalysts for the total oxidation of a variety of volatile organic compounds. The main focus of this project will be on the use of cheap and abundant metal oxides for catalyst synthesis, with a further outlook on the preparation of novel supported catalysts for industrial application. The systems to be investigated throughout this thesis will relate to the use of CeO_2 based metal oxide catalysts for the total oxidation of propane and naphthalene VOCs. In addition, precious metal catalysts deposited onto a novel silica support will be studied for the total oxidation of a VOC mixture consisting of propene, toluene and CO.

The preparation of catalysts by simple and reproducible methods is advantageous for catalyst design, with the ability to alter minor variables to improve catalytic activity. The use of different catalyst precursors for a widely studied metal oxide catalyst will be investigated in Chapter 3, looking at how this small change can impact on the physiochemical properties of the resulting catalyst and how this relates to catalytic activity for VOC total oxidation. Following this, Chapter 4 will expand upon the work carried out in Chapter 3 and apply it to a mixed metal oxide system, using cheap and abundant materials. The influence of precursor and mixture of metals will be assessed on their contribution towards catalytic activity in this system.

The impact of minor changes to the catalyst synthesis method will again be investigated in Chapter 5, but with the use of small dopant quantities into a well-studied mixed metal system as the focus. Different metal dopants will be studied and the effect on the catalyst properties correlated to catalytic activity for propane and naphthalene total oxidation. Finally, Chapter 6 will aim to investigate precious metal catalysts supported on UVM-7, a novel silica support, for the simultaneous total oxidation of propene, toluene and CO. This work can be used to model VOC oxidation over these catalysts for industrial processes such as cold start in engines.

1.8 References

[1] J.A. Moulijn, P.W.N.M. van Leeuwen, R.A. van Santen, eds., History of catalysis: Chapter 1, in: Stud. Surf. Sci. Catal., Elsevier, 1993: pp. 3–21. https://doi.org/10.1016/S0167-2991(08)63805-7.

[2] J. Wisniak, The History of Catalysis. From the Beginning to Nobel Prizes, Educ. Quím. 21 (2010) 60–69. https://doi.org/10.1016/S0187-893X(18)30074-0.

[3] M. Barbato, C. Bruno, Heterogeneous Catalysis: Theory, Models and Applications, in: M. Capitelli (Ed.), Mol. Phys. Hypersonic Flows, Springer Netherlands, Dordrecht, 1996: pp. 139–160. https://doi.org/10.1007/978-94-009-0267-1_8.

[4] B. Lindström, L.J. Pettersson, A Brief History of Catalysis, CATTECH. 7 (2003) 130–138. https://doi.org/10.1023/A:1025001809516.

[5] J.N. Armor, A history of industrial catalysis, Catal. Today. 163 (2011) 3–9. https://doi.org/10.1016/j.cattod.2009.11.019.

[6] K.P. de Jong, General Aspects, in: Synth. Solid Catal., John Wiley & Sons, Ltd, 2009: pp. 1–11. https://doi.org/10.1002/9783527626854.ch1.

[7] M. Boudart, B.H. Davis, H. Heinemann, Introduction, in: Handb. Heterog. Catal., John Wiley & Sons, Ltd, 2008: pp. 1–48. https://doi.org/10.1002/9783527619474.ch1.

[8] M. Misono, Chapter 1 - Basis of Heterogeneous Catalysis, in: M. Misono (Ed.), Stud. Surf. Sci. Catal., Elsevier, 2013: pp. 1–23. https://doi.org/10.1016/B978-0-444-53833-8.00001-6.

[9] Directive 2004/42/CE of the European Parliament and of the Council of 21 April 2004 on the limitation of emissions of volatile organic compounds due to the use of organic solvents in certain paints and varnishes and vehicle refinishing products and amending Directive 1999/13/EC, 2004. http://data.europa.eu/eli/dir/2004/42/oj/eng.

[10] Electronic Code of Federal Regulations (eCFR), Electron. Code Fed. Regul. ECFR. (n.d.). https://www.ecfr.gov/ (accessed October 14, 2020).

[11] J. Williams, R. Koppmann, Volatile Organic Compounds in the Atmosphere: An Overview, in: Volatile Org. Compd. Atmosphere, John Wiley & Sons, Ltd, 2007: pp. 1–32. https://doi.org/10.1002/9780470988657.ch1.

[12] A.H. Steiner, A.L. Goldstein, Biogenic VOCs, in: Volatile Org. Compd. Atmosphere, John Wiley & Sons, Ltd, 2007: pp. 82–128. https://doi.org/10.1002/9780470988657.ch3.

[13] X. Lun, Y. Lin, F. Chai, C. Fan, H. Li, J. Liu, Reviews of emission of biogenic volatile organic compounds (BVOCs) in Asia, J. Environ. Sci. 95 (2020) 266–277. https://doi.org/10.1016/j.jes.2020.04.043.

[14] R. Rinnan, Å. Rinnan, T. Holopainen, J.K. Holopainen, P. Pasanen, Emission of non-methane volatile organic compounds (VOCs) from boreal peatland microcosms—effects of ozone exposure, Atmos. Environ. 39 (2005) 921–930. https://doi.org/10.1016/j.atmosenv.2004.09.076.

[15] V. Ferracci, C.G. Bolas, R.A. Freshwater, Z. Staniaszek, T. King, K. Jaars, F. Otu-Larbi, J. Beale, Y. Malhi, T.W. Waine, R.L. Jones, K. Ashworth, N.R.P. Harris, Continuous Isoprene Measurements in a UK Temperate Forest for a Whole Growing Season: Effects of Drought Stress During the 2018 Heatwave, Geophys. Res. Lett. 47 (2020) e2020GL088885. https://doi.org/10.1029/2020GL088885.

[16] Y.M. Kim, S. Harrad, R.M. Harrison, Concentrations and Sources of VOCs in Urban Domestic and Public Microenvironments, Environ. Sci. Technol. 35 (2001) 997–1004. https://doi.org/10.1021/es000192y.

[17] S. Reimann, A.C. Lewis, Anthropogenic VOCs, in: Volatile Org. Compd. Atmosphere, John Wiley & Sons, Ltd, 2007: pp. 33–81. https://doi.org/10.1002/9780470988657.ch2.

[18] M.S. Kamal, S.A. Razzak, M.M. Hossain, Catalytic oxidation of volatile organic compounds (VOCs) – A review, Atmos. Environ. 140 (2016) 117–134. https://doi.org/10.1016/j.atmosenv.2016.05.031.

[19] A.A. Almetwally, M. Bin-Jumah, A.A. Allam, Ambient air pollution and its influence on human health and welfare: an overview, Environ. Sci. Pollut. Res. 27 (2020) 24815–24830. https://doi.org/10.1007/s11356-020-09042-2.

[20] S.G. Al-Kindi, R.D. Brook, S. Biswal, S. Rajagopalan, Environmental determinants of cardiovascular disease: lessons learned from air pollution, Nat. Rev. Cardiol. 17 (2020) 656–672. https://doi.org/10.1038/s41569-020-0371-2.

[21] A.A. Singh, S.B. Agrawal, Tropospheric ozone pollution in India: effects on crop yield and product quality, Environ. Sci. Pollut. Res. 24 (2017) 4367–4382. https://doi.org/10.1007/s11356-016-8178-8.

[22] D.J. Wuebbles, S. Sanyal, Air Quality in a Cleaner Energy World, Curr. Pollut. Rep. 1 (2015) 117–129. https://doi.org/10.1007/s40726-015-0009-x.

[23] K.R. Solomon, X. Tang, S.R. Wilson, P. Zanis, A.F. Bais, Changes in tropospheric composition and air quality due to stratospheric ozone depletion, Photochem. Photobiol. Sci. 2 (2003) 62–67. https://doi.org/10.1039/B211086E.

[24] X. Tang, S. R. Wilson, K. R. Solomon, M. Shao, S. Madronich, Changes in air quality and tropospheric composition due to depletion of stratospheric ozone and interactions with climate, Photochem. Photobiol. Sci. 10 (2011) 280–291. https://doi.org/10.1039/C0PP90039G.

[25] S. Cakmak, R.E. Dales, L. Liu, L.M. Kauri, C.L. Lemieux, C. Hebbern, J. Zhu, Residential exposure to volatile organic compounds and lung function: Results from a population-based cross-sectional survey, Environ. Pollut. 194 (2014) 145–151. https://doi.org/10.1016/j.envpol.2014.07.020.

[26] L. Massolo, M. Rehwagen, A. Porta, A. Ronco, O. Herbarth, A. Mueller, Indoor–outdoor distribution and risk assessment of volatile organic compounds in the atmosphere of industrial and urban areas, Environ. Toxicol. 25 (2010) 339–349. https://doi.org/10.1002/tox.20504.

[27] N. Borduas, N.M. Donahue, Chapter 3.1 - The Natural Atmosphere, in: B. Török, T. Dransfield (Eds.), Green Chem., Elsevier, 2018: pp. 131–150. https://doi.org/10.1016/B978-0-12-809270-5.00006-6.

[28] A. Rossati, Global Warming and Its Health Impact, Int. J. Occup. Environ. Med. 8 (2016) 7–20. https://doi.org/10.15171/ijoem.2017.963.

[29] A. Nourian, M.K. Abba, G. G. Nasr, Measurements and analysis of non-methane VOC (NMVOC) emissions from major domestic aerosol sprays at “source,” Environ. Int. 146 (2021) 106152. https://doi.org/10.1016/j.envint.2020.106152.

[30] Ø. Hodnebrog, S.B. Dalsøren, G. Myhre, Lifetimes, direct and indirect radiative forcing, and global warming potentials of ethane (C2H6), propane (C3H8), and butane (C4H10), Atmospheric Sci. Lett. 19 (2018) e804. https://doi.org/10.1002/asl.804.

[31] W.J. Collins, R.G. Derwent, C.E. Johnson, D.S. Stevenson, The Oxidation of Organic Compounds in the Troposphere and their Global Warming Potentials, Clim. Change. 52 (2002) 453–479. https://doi.org/10.1023/A:1014221225434.

[32] U. Baltensperger, M. Kalberer, J. Dommen, D. Paulsen, M.R. Alfarra, H. Coe, R. Fisseha, A. Gascho, M. Gysel, S. Nyeki, M. Sax, M. Steinbacher, A.S.H. Prevot, S. Sjögren, E. Weingartner, R. Zenobi, Secondary organic aerosols from anthropogenic and biogenic precursors, Faraday Discuss. 130 (2005) 265–278. https://doi.org/10.1039/B417367H.

[33] J.R. Odum, T.P.W. Jungkamp, R.J. Griffin, R.C. Flagan, J.H. Seinfeld, The Atmospheric Aerosol-Forming Potential of Whole Gasoline Vapor, Science. 276 (1997) 96–99. https://doi.org/10.1126/science.276.5309.96.

[34] D. Han, S. Gao, Q. Fu, J. Cheng, X. Chen, H. Xu, S. Liang, Y. Zhou, Y. Ma, Do volatile organic compounds (VOCs) emitted from petrochemical industries affect regional PM2.5?, Atmospheric Res. 209 (2018) 123–130. https://doi.org/10.1016/j.atmosres.2018.04.002.

[35] I.M. Al-Naiema, E.A. Stone, Evaluation of anthropogenic secondary organic aerosol tracers from aromatic hydrocarbons, Atmospheric Chem. Phys. 17 (2017) 2053–2065. https://doi.org/10.5194/acp-17-2053-2017.

[36] E. Ahlberg, J. Falk, A. Eriksson, T. Holst, W.H. Brune, A. Kristensson, P. Roldin, B. Svenningsson, Secondary organic aerosol from VOC mixtures in an oxidation flow reactor, Atmos. Environ. 161 (2017) 210–220. https://doi.org/10.1016/j.atmosenv.2017.05.005.

[37] Y.-F. Xing, Y.-H. Xu, M.-H. Shi, Y.-X. Lian, The impact of PM2.5 on the human respiratory system, J. Thorac. Dis. 8 (2016) E69–E74. https://doi.org/10.3978/j.issn.2072-1439.2016.01.19.

[38] M.A. Leiva G, D.A. Santibañez, S. Ibarra E, P. Matus C, R. Seguel, A five-year study of particulate matter (PM2.5) and cerebrovascular diseases, Environ. Pollut. 181 (2013) 1–6. https://doi.org/10.1016/j.envpol.2013.05.057.

[39] F. Huang, B. Pan, J. Wu, E. Chen, L. Chen, Relationship between exposure to PM2.5 and lung cancer incidence and mortality: A meta-analysis, Oncotarget. 8 (2017) 43322–43331. https://doi.org/10.18632/oncotarget.17313.

[40] T. Garcia, B. Solsona, S.H. Taylor, The catalytic oxidation of hydrocarbon volatile organic compounds, in: D. Duprez, F. Cavani (Eds.), Handb. Adv. Methods Process. Oxid. Catal., Imperial College Press, London, 2014: pp. 51–90. https://doi.org/Garcia, Tomas, Solsona, Benjamin and Taylor, Stuart Hamilton <http://orca.cf.ac.uk/view/cardiffauthors/A0358999.html> 2014. The catalytic oxidation of hydrocarbon volatile organic compounds. In: Duprez, Daniel and Cavani, Fabrizio eds. Handbook of Advanced Methods and Processes in Oxidation Catalysis, London: Imperial College Press, pp. 51-90. (10.1142/9781848167513_0003 <http://dx.doi.org/10.1142/9781848167513_0003>).

[41] A. Ragothaman, W.A. Anderson, Air Quality Impacts of Petroleum Refining and Petrochemical Industries, Environments. 4 (2017) 66. https://doi.org/10.3390/environments4030066.

[42] J.T. Shaw, A.R. Rickard, M.J. Newland, T.J. Dillon, Rate coefficients for reactions of OH with aromatic and aliphatic volatile organic compounds determined by the multivariate relative rate technique, Atmospheric Chem. Phys. 20 (2020) 9725–9736. https://doi.org/10.5194/acp-20-9725-2020.

[43] V. R. Choudhary, G. M. Deshmukh, D. P. Mishra, Kinetics of the Complete Combustion of Dilute Propane and Toluene over Iron-Doped ZrO2 Catalyst, Energy Fuels. 19 (2005) 54–63. https://doi.org/10.1021/ef0498871.

[44] A.S. Ramadhas, Alternative Fuels for Transportation, CRC Press, 2016.

[45] Z. Hu, Z. Wang, Y. Guo, L. Wang, Y. Guo, J. Zhang, W. Zhan, Total Oxidation of Propane over a Ru/CeO2 Catalyst at Low Temperature, Environ. Sci. Technol. 52 (2018) 9531–9541. https://doi.org/10.1021/acs.est.8b03448.

[46] E.N. Ndifor, T. Garcia, B. Solsona, S.H. Taylor, Influence of preparation conditions of nano-crystalline ceria catalysts on the total oxidation of naphthalene, a model polycyclic aromatic hydrocarbon, Appl. Catal. B Environ. 76 (2007) 248–256. https://doi.org/10.1016/j.apcatb.2007.05.027.

[47] C. Jia, S. Batterman, A Critical Review of Naphthalene Sources and Exposures Relevant to Indoor and Outdoor Air, Int. J. Environ. Res. Public. Health. 7 (2010) 2903–2939. https://doi.org/10.3390/ijerph7072903.

[48] T. Garcia, B. Solsona, S.H. Taylor, Nano-crystalline Ceria Catalysts for the Abatement of Polycyclic Aromatic Hydrocarbons, Catal. Lett. 105 (2005) 183–189. https://doi.org/10.1007/s10562-005-8689-2.

[49] R. Lu, J. Wu, R.P. Turco, A.M. Winer, R. Atkinson, J. Arey, S.E. Paulson, F.W. Lurmann, A.H. Miguel, A. Eiguren-Fernandez, Naphthalene distributions and human exposure in Southern California, Atmos. Environ. 39 (2005) 489–507. https://doi.org/10.1016/j.atmosenv.2004.09.045.

[50] P. Granger, Challenges and breakthroughs in post-combustion catalysis: how to match future stringent regulations, Catal. Sci. Technol. 7 (2017) 5195–5211. https://doi.org/10.1039/C7CY00983F.

[51] A. Aboukaïs, S. Aouad, H. El-Ayadi, M. Skaf, M. Labaki, R. Cousin, E. Abi-Aad, Catalytic Oxidation of Propylene, Toluene, Carbon Monoxide, and Carbon Black over Au/CeO2 Solids: Comparing the Impregnation and the Deposition-Precipitation Methods, Sci. World J. 2013 (2013) 6. https://doi.org/10.1155/2013/824979.

[52] M. Navlani-García, F.J. Varela-Gandía, A. Bueno-López, D. Cazorla-Amorós, B. Puértolas, J.M. López, T. García, D. Lozano-Castelló, BETA Zeolite Thin Films Supported on Honeycomb Monoliths with Tunable Properties as Hydrocarbon Traps under Cold-Start Conditions, ChemSusChem. 6 (2013) 1467–1477. https://doi.org/10.1002/cssc.201300215.

[53] R.F. Sawyer, Vehicle emissions: progress and challenges, J. Expo. Sci. Environ. Epidemiol. 20 (2010) 487–488. https://doi.org/10.1038/jes.2010.44.

[54] J.J. Rose, L. Wang, Q. Xu, C.F. McTiernan, S. Shiva, J. Tejero, M.T. Gladwin, Carbon Monoxide Poisoning: Pathogenesis, Management, and Future Directions of Therapy, Am. J. Respir. Crit. Care Med. 195 (2016) 596–606. https://doi.org/10.1164/rccm.201606-1275CI.

[55] A.L. Chiew, N.A. Buckley, Carbon monoxide poisoning in the 21st century, Crit. Care. 18 (2014) 221. https://doi.org/10.1186/cc13846.

[56] R.J. Levy, Carbon monoxide pollution and neurodevelopment: A public health concern, Neurotoxicol. Teratol. 49 (2015) 31–40. https://doi.org/10.1016/j.ntt.2015.03.001.

[57] M. Ousmane, L.F. Liotta, G.D. Carlo, G. Pantaleo, A.M. Venezia, G. Deganello, L. Retailleau, A. Boreave, A. Giroir-Fendler, Supported Au catalysts for low-temperature abatement of propene and toluene, as model VOCs: Support effect, Appl. Catal. B Environ. 101 (2011) 629–637. https://doi.org/10.1016/j.apcatb.2010.11.004.

[58] R.G. Derwent, M.E. Jenkin, M.J. Pilling, W.P.L. Carter, A. Kaduwela, Reactivity Scales as Comparative Tools for Chemical Mechanisms, J. Air Waste Manag. Assoc. 60 (2010) 914–924. https://doi.org/10.3155/1047-3289.60.8.914.

[59] T.-T. Win-Shwe, H. Fujimaki, Neurotoxicity of toluene, Toxicol. Lett. 198 (2010) 93–99. https://doi.org/10.1016/j.toxlet.2010.06.022.

[60] F.I. Khan, A. Kr. Ghoshal, Removal of Volatile Organic Compounds from polluted air, J. Loss Prev. Process Ind. 13 (2000) 527–545. https://doi.org/10.1016/S0950-4230(00)00007-3.

[61] Y.-S. Son, Decomposition of VOCs and odorous compounds by radiolysis: A critical review, Chem. Eng. J. 316 (2017) 609–622. https://doi.org/10.1016/j.cej.2017.01.063.

[62] L.-J. Hsu, C.-C. Lin, Removal of methanol and 1-butanol from binary mixtures by absorption in rotating packed beds with blade packings, Chem. Eng. J. 168 (2011) 190–200. https://doi.org/10.1016/j.cej.2010.12.062.

[63] C. Yang, G. Miao, Y. Pi, Q. Xia, J. Wu, Z. Li, J. Xiao, Abatement of various types of VOCs by adsorption/catalytic oxidation: A review, Chem. Eng. J. 370 (2019) 1128–1153. https://doi.org/10.1016/j.cej.2019.03.232.

[64] A. Krishnamurthy, B. Adebayo, T. Gelles, A. Rownaghi, F. Rezaei, Abatement of gaseous volatile organic compounds: A process perspective, Catal. Today. 350 (2020) 100–119. https://doi.org/10.1016/j.cattod.2019.05.069.

[65] T. Dobre, O.C. Pârvulescu, G. Iavorschi, M. Stroescu, A. Stoica, Volatile Organic Compounds Removal from Gas Streams by Adsorption onto Activated Carbon, Ind. Eng. Chem. Res. 53 (2014) 3622–3628. https://doi.org/10.1021/ie402504u.

[66] X. Zhang, B. Gao, A.E. Creamer, C. Cao, Y. Li, Adsorption of VOCs onto engineered carbon materials: A review, J. Hazard. Mater. 338 (2017) 102–123. https://doi.org/10.1016/j.jhazmat.2017.05.013.

[67] A. Luengas, A. Barona, C. Hort, G. Gallastegui, V. Platel, A. Elias, A review of indoor air treatment technologies, Rev. Environ. Sci. Biotechnol. 14 (2015) 499–522. https://doi.org/10.1007/s11157-015-9363-9.

[68] Y. Liu, X. Feng, D. Lawless, Separation of gasoline vapor from nitrogen by hollow fiber composite membranes for VOC emission control, J. Membr. Sci. 271 (2006) 114–124. https://doi.org/10.1016/j.memsci.2005.07.012.

[69] S. Aguado, A.C. Polo, M.P. Bernal, J. Coronas, J. Santamaría, Removal of pollutants from indoor air using zeolite membranes, J. Membr. Sci. 240 (2004) 159–166. https://doi.org/10.1016/j.memsci.2004.05.004.

[70] D.R. van der Vaart, W.M. Vatvuk, A.H. Wehe, Thermal and Catalytic Incinerators for the Control of VOCs, J. Air Waste Manag. Assoc. 41 (1991) 92–98. https://doi.org/10.1080/10473289.1991.10466828.

[71] M.R.B. Abas, S. Mohamad, Hazardous (Organic) Air Pollutants, in: J. Nriagu (Ed.), Encycl. Environ. Health Second Ed., Elsevier, Oxford, 2011: pp. 405–416. https://doi.org/10.1016/B978-0-444-63951-6.00070-X.

[72] S. Ojala, S. Pitkäaho, T. Laitinen, N. Niskala Koivikko, R. Brahmi, J. Gaálová, L. Matejova, A. Kucherov, S. Päivärinta, C. Hirschmann, T. Nevanperä, M. Riihimäki, M. Pirilä, R.L. Keiski, Catalysis in VOC Abatement, Top. Catal. 54 (2011) 1224. https://doi.org/10.1007/s11244-011-9747-1.

[73] Y. Guo, M. Wen, G. Li, T. An, Recent advances in VOC elimination by catalytic oxidation technology onto various nanoparticles catalysts: a critical review, Appl. Catal. B Environ. 281 (2021) 119447. https://doi.org/10.1016/j.apcatb.2020.119447.

[74] S. Song, S. Zhang, X. Zhang, P. Verma, M. Wen, Advances in Catalytic Oxidation of Volatile Organic Compounds over Pd-Supported Catalysts: Recent Trends and Challenges, Front. Mater. 0 (2020). https://doi.org/10.3389/fmats.2020.595667.

[75] T.V. Choudhary, S. Banerjee, V.R. Choudhary, Catalysts for combustion of methane and lower alkanes, Appl. Catal. Gen. 234 (2002) 1–23. https://doi.org/10.1016/S0926-860X(02)00231-4.

[76] X. Zhao, R. Zhang, Y. Liu, J. Deng, P. Xu, S. Lv, S. Li, W. Pei, K. Zhang, H. Dai, Pd/meso-CoO derived from in situ reduction of the one-step synthesized Pd/meso-Co3O4: high-performance catalysts for benzene combustion, New J. Chem. 43 (2019) 12358–12368. https://doi.org/10.1039/C9NJ03039E.

[77] X. Weng, B. Shi, A. Liu, J. Sun, Y. Xiong, H. Wan, S. Zheng, L. Dong, Y. Chen, Highly dispersed Pd/modified-Al2O3 catalyst on complete oxidation of toluene: Role of basic sites and mechanism insight, Appl. Surf. Sci. 497 (2019) 143747. https://doi.org/10.1016/j.apsusc.2019.143747.

[78] K. Fujimoto, F.H. Ribeiro, M. Avalos-Borja, E. Iglesia, Structure and Reactivity of PdOx/ZrO2Catalysts for Methane Oxidation at Low Temperatures, J. Catal. 179 (1998) 431–442. https://doi.org/10.1006/jcat.1998.2178.

[79] Z. Zhang, Z. Jiang, W. Shangguan, Low-temperature catalysis for VOCs removal in technology and application: A state-of-the-art review, Catal. Today. 264 (2016) 270–278. https://doi.org/10.1016/j.cattod.2015.10.040.

[80] S. Ordóñez, L. Bello, H. Sastre, R. Rosal, F.V. Díez, Kinetics of the deep oxidation of benzene, toluene, n-hexane and their binary mixtures over a platinum on γ-alumina catalyst, Appl. Catal. B Environ. 38 (2002) 139–149. https://doi.org/10.1016/S0926-3373(02)00036-X.

[81] M. Haneda, T. Watanabe, N. Kamiuchi, M. Ozawa, Effect of platinum dispersion on the catalytic activity of Pt/Al2O3 for the oxidation of carbon monoxide and propene, Appl. Catal. B Environ. 142–143 (2013) 8–14. https://doi.org/10.1016/j.apcatb.2013.04.055.

[82] H. Huang, Y. Xu, Q. Feng, D.Y.C. Leung, Low temperature catalytic oxidation of volatile organic compounds: a review, Catal. Sci. Technol. 5 (2015) 2649–2669. https://doi.org/10.1039/C4CY01733A.

[83] S. Minicò, S. Scirè, C. Crisafulli, R. Maggiore, S. Galvagno, Catalytic combustion of volatile organic compounds on gold/iron oxide catalysts, Appl. Catal. B Environ. 28 (2000) 245–251. https://doi.org/10.1016/S0926-3373(00)00181-8.

[84] Y. Liu, H. Dai, J. Deng, S. Xie, H. Yang, W. Tan, W. Han, Y. Jiang, G. Guo, Mesoporous Co3O4-supported gold nanocatalysts: Highly active for the oxidation of carbon monoxide, benzene, toluene, and o-xylene, J. Catal. 309 (2014) 408–418. https://doi.org/10.1016/j.jcat.2013.10.019.

[85] S.A.C. Carabineiro, X. Chen, O. Martynyuk, N. Bogdanchikova, M. Avalos-Borja, A. Pestryakov, P.B. Tavares, J.J.M. Órfão, M.F.R. Pereira, J.L. Figueiredo, Gold supported on metal oxides for volatile organic compounds total oxidation, Catal. Today. 244 (2015) 103–114. https://doi.org/10.1016/j.cattod.2014.06.034.

[86] Liotta, L.F, Catalytic oxidation of volatile organic compounds on supported noble metals, Appl. Catal. B Environ. 100 (2010) 403–412. https://doi.org/10.1016/j.apcatb.2010.08.023.

[87] H. Wu, G. Pantaleo, A.M. Venezia, L.F. Liotta, Mesoporous Silica Based Gold Catalysts: Novel Synthesis and Application in Catalytic Oxidation of CO and Volatile Organic Compounds (VOCs), Catalysts. 3 (2013) 774–793. https://doi.org/10.3390/catal3040774.

[88] S. Gil, J.M. Garcia-Vargas, L.F. Liotta, G. Pantaleo, M. Ousmane, L. Retailleau, A. Giroir-Fendler, Catalytic Oxidation of Propene over Pd Catalysts Supported on CeO2, TiO2, Al2O3 and M/Al2O3 Oxides (M = Ce, Ti, Fe, Mn), Catalysts. 5 (2015) 671–689. https://doi.org/10.3390/catal5020671.

[89] Z. Abdelouahab-Reddam, R.E. Mail, F. Coloma, A. Sepúlveda-Escribano, Platinum supported on highly-dispersed ceria on activated carbon for the total oxidation of VOCs, Appl. Catal. Gen. 494 (2015) 87–94. https://doi.org/10.1016/j.apcata.2015.01.026.

[90] T. Garcia, B. Solsona, D. Cazorla-Amorós, Á. Linares-Solano, S.H. Taylor, Total oxidation of volatile organic compounds by vanadium promoted palladium-titania catalysts: Comparison of aromatic and polyaromatic compounds, Appl. Catal. B Environ. 62 (2006) 66–76. https://doi.org/10.1016/j.apcatb.2005.06.016.

[91] H.-J. Sedjame, C. Fontaine, G. Lafaye, J. Barbier Jr, On the promoting effect of the addition of ceria to platinum based alumina catalysts for VOCs oxidation, Appl. Catal. B Environ. 144 (2014) 233–242. https://doi.org/10.1016/j.apcatb.2013.07.022.

[92] X. Fu, Y. Liu, W. Yao, Z. Wu, One-step synthesis of bimetallic Pt-Pd/MCM-41 mesoporous materials with superior catalytic performance for toluene oxidation, Catal. Commun. 83 (2016) 22–26. https://doi.org/10.1016/j.catcom.2016.05.001.

[93] L. Ilieva, A.M. Venezia, P. Petrova, G. Pantaleo, L.F. Liotta, R. Zanella, Z. Kaszkur, T. Tabakova, Effect of Y Modified Ceria Support in Mono and Bimetallic Pd–Au Catalysts for Complete Benzene Oxidation, Catalysts. 8 (2018) 283. https://doi.org/10.3390/catal8070283.

[94] F. Liao, T.W.B. Lo, S.C.E. Tsang, Recent Developments in Palladium-Based Bimetallic Catalysts, ChemCatChem. 7 (2015) 1998–2014. https://doi.org/10.1002/cctc.201500245.

[95] M. Hosseini, T. Barakat, R. Cousin, A. Aboukaïs, B.-L. Su, G. De Weireld, S. Siffert, Catalytic performance of core–shell and alloy Pd–Au nanoparticles for total oxidation of VOC: The effect of metal deposition, Appl. Catal. B Environ. 111–112 (2012) 218–224. https://doi.org/10.1016/j.apcatb.2011.10.002.

[96] Y. Wei, Z. Zhao, J. Liu, S. Liu, C. Xu, A. Duan, G. Jiang, Multifunctional catalysts of three-dimensionally ordered macroporous oxide-supported Au@Pt core–shell nanoparticles with high catalytic activity and stability for soot oxidation, J. Catal. 317 (2014) 62–74. https://doi.org/10.1016/j.jcat.2014.05.014.

[97] P.E. Plyusnin, E.M. Slavinskaya, R.M. Kenzhin, A.K. Kirilovich, E.V. Makotchenko, O.A. Stonkus, Y.V. Shubin, A.A. Vedyagin, Synthesis of bimetallic AuPt/CeO2 catalysts and their comparative study in CO oxidation under different reaction conditions, React. Kinet. Mech. Catal. 127 (2019) 69–83. https://doi.org/10.1007/s11144-019-01545-5.

[98] L. Lu, Y. Nie, Y. Wang, G. Wu, L. Li, J. Li, X. Qi, Z. Wei, Preparation of highly dispersed carbon supported AuPt nanoparticles via a capping agent-free route for efficient methanol oxidation, J. Mater. Chem. A. 6 (2018) 104–109. https://doi.org/10.1039/C7TA08343B.

[99] W.B. Li, J.X. Wang, H. Gong, Catalytic combustion of VOCs on non-noble metal catalysts, Catal. Today. 148 (2009) 81–87. https://doi.org/10.1016/j.cattod.2009.03.007.

[100] P.M. Heynderickx, J.W. Thybaut, H. Poelman, D. Poelman, G.B. Marin, The total oxidation of propane over supported Cu and Ce oxides: A comparison of single and binary metal oxides, J. Catal. 272 (2010) 109–120. https://doi.org/10.1016/j.jcat.2010.03.006.

[101] C. He, J. Cheng, X. Zhang, M. Douthwaite, S. Pattisson, Z. Hao, Recent Advances in the Catalytic Oxidation of Volatile Organic Compounds: A Review Based on Pollutant Sorts and Sources, Chem. Rev. 119 (2019) 4471–4568. https://doi.org/10.1021/acs.chemrev.8b00408.

[102] T. Montini, M. Melchionna, M. Monai, P. Fornasiero, Fundamentals and Catalytic Applications of CeO2-Based Materials, Chem. Rev. 116 (2016) 5987–6041. https://doi.org/10.1021/acs.chemrev.5b00603.

[103] S. Agarwal, X. Zhu, E.J.M. Hensen, L. Lefferts, B.L. Mojet, Defect Chemistry of Ceria Nanorods, J. Phys. Chem. C. 118 (2014) 4131–4142. https://doi.org/10.1021/jp409989y.

[104] E. Mamontov, T. Egami, Structural defects in a nano-scale powder of CeO2 studied by pulsed neutron diffraction, J. Phys. Chem. Solids. 61 (2000) 1345–1356. https://doi.org/10.1016/S0022-3697(00)00003-2.

[105] M. Dosa, M. Piumetti, S. Bensaid, T. Andana, C. Novara, F. Giorgis, D. Fino, N. Russo, Novel Mn–Cu-Containing CeO2 Nanopolyhedra for the Oxidation of CO and Diesel

Soot: Effect of Dopants on the Nanostructure and Catalytic Activity, Catal. Lett. 148 (2018) 298–311. https://doi.org/10.1007/s10562-017-2226-y.

[106] K. Polychronopoulou, A.A. AlKhoori, A.M. Efstathiou, M.A. Jaoude, C.M. Damaskinos, M.A. Baker, A. Almutawa, D.H. Anjum, M.A. Vasiliades, A. Belabbes, L.F. Vega, A.F. Zedan, S.J. Hinder, Design Aspects of Doped CeO2 for Low-Temperature Catalytic CO Oxidation: Transient Kinetics and DFT Approach, ACS Appl. Mater. Interfaces. 13 (2021) 22391–22415. https://doi.org/10.1021/acsami.1c02934.

[107] J.M. López, A.L. Gilbank, T. García, B. Solsona, S. Agouram, L. Torrente-Murciano, The prevalence of surface oxygen vacancies over the mobility of bulk oxygen in nanostructured ceria for the total toluene oxidation, Appl. Catal. B Environ. 174–175 (2015) 403–412. https://doi.org/10.1016/j.apcatb.2015.03.017.

[108] S. Rood, S. Eslava, A. Manigrasso, C. Bannister, Recent advances in gasoline three-way catalyst formulation: A review, Proc. Inst. Mech. Eng. Part J. Automob. Eng. 234 (2020) 936–949. https://doi.org/10.1177/0954407019859822.

[109] Q. Wang, K.L. Yeung, M.A. Bañares, Ceria and its related materials for VOC catalytic combustion: A review, Catal. Today. 356 (2020) 141–154. https://doi.org/10.1016/j.cattod.2019.05.016.

[110] T. García, B. Solsona, S.H. Taylor, Naphthalene total oxidation over metal oxide catalysts, Appl. Catal. B Environ. 66 (2006) 92–99. https://doi.org/10.1016/j.apcatb.2006.03.003.

[111] B. Solsona, T.E. Davies, T. Garcia, I. Vázquez, A. Dejoz, S.H. Taylor, Total oxidation of propane using nanocrystalline cobalt oxide and supported cobalt oxide catalysts, Appl. Catal. B Environ. 84 (2008) 176–184. https://doi.org/10.1016/j.apcatb.2008.03.021.

[112] R.P. Marin, S.A. Kondrat, R.K. Pinnell, T.E. Davies, S. Golunski, J.K. Bartley, G.J. Hutchings, S.H. Taylor, Green preparation of transition metal oxide catalysts using supercritical CO2 anti-solvent precipitation for the total oxidation of propane, Appl. Catal. B Environ. 140–141 (2013) 671–679. https://doi.org/10.1016/j.apcatb.2013.04.076.

[113] B. Solsona, T. García, R. Sanchis, M.D. Soriano, M. Moreno, E. Rodríguez-Castellón, S. Agouram, A. Dejoz, J.M. López Nieto, Total oxidation of VOCs on mesoporous iron oxide catalysts: Soft chemistry route versus hard template method, Chem. Eng. J. 290 (2016) 273–281. https://doi.org/10.1016/j.cej.2015.12.109.

[114] J.G. McCarty, M. Gusman, D.M. Lowe, D.L. Hildenbrand, K.N. Lau, Stability of supported metal and supported metal oxide combustion catalysts, Catal. Today. 47 (1999) 5–17. https://doi.org/10.1016/S0920-5861(98)00279-X.

[115] R. Sanchis, D. Alonso-Domínguez, A. Dejoz, M.P. Pico, I. Álvarez-Serrano, T. García, M.L. López, B. Solsona, Eco-Friendly Cavity-Containing Iron Oxides Prepared by Mild Routes as Very Efficient Catalysts for the Total Oxidation of VOCs, Materials. 11 (2018). https://doi.org/10.3390/ma11081387.

[116] Y. Xia, H. Dai, H. Jiang, L. Zhang, J. Deng, Y. Liu, Three-dimensionally ordered and wormhole-like mesoporous iron oxide catalysts highly active for the oxidation of acetone and methanol, J. Hazard. Mater. 186 (2011) 84–91. https://doi.org/10.1016/j.jhazmat.2010.10.073.

[117] Y. Gao, S. Wang, L. Lv, D. Li, X. Yue, S. Wang, Insights into the Behaviors of the Catalytic Combustion of Propane over Spinel Catalysts, Catal. Lett. 150 (2020) 3617–3625. https://doi.org/10.1007/s10562-020-03239-3.

[118] S.C. Kim, W.G. Shim, Catalytic combustion of VOCs over a series of manganese oxide catalysts, Appl. Catal. B Environ. 98 (2010) 180–185. https://doi.org/10.1016/j.apcatb.2010.05.027.

[119] D. Devaiah, L.H. Reddy, S.-E. Park, B.M. Reddy, Ceria–zirconia mixed oxides: Synthetic methods and applications, Catal. Rev. 60 (2018) 177–277. https://doi.org/10.1080/01614940.2017.1415058.

[120] M. Piumetti, S. Bensaid, D. Fino, N. Russo, Nanostructured ceria-zirconia catalysts for CO oxidation: Study on surface properties and reactivity, Appl. Catal. B Environ. 197 (2016) 35–46. https://doi.org/10.1016/j.apcatb.2016.02.023.

[121] D.R. Sellick, A. Aranda, T. García, J.M. López, B. Solsona, A.M. Mastral, D.J. Morgan, A.F. Carley, S.H. Taylor, Influence of the preparation method on the activity of ceria zirconia mixed oxides for naphthalene total oxidation, Appl. Catal. B Environ. 132–133 (2013) 98–106. https://doi.org/10.1016/j.apcatb.2012.11.036.

[122] J.I. Gutiérrez-Ortiz, B. de Rivas, R. López-Fonseca, J.R. González-Velasco, Catalytic purification of waste gases containing VOC mixtures with Ce/Zr solid solutions, Appl. Catal. B Environ. 65 (2006) 191–200. https://doi.org/10.1016/j.apcatb.2006.02.001.

[123] B. de Rivas, J.I. Gutiérrez-Ortiz, R. López-Fonseca, J.R. González-Velasco, Analysis of the simultaneous catalytic combustion of chlorinated aliphatic pollutants and toluene over ceria-zirconia mixed oxides, Appl. Catal. Gen. 314 (2006) 54–63. https://doi.org/10.1016/j.apcata.2006.08.005.

[124] H. Bao, K. Qian, J. Fang, W. Huang, Fe-doped CeO2 solid solutions: Substituting-site doping versus interstitial-site doping, bulk doping versus surface doping, Appl. Surf. Sci. 414 (2017) 131–139. https://doi.org/10.1016/j.apsusc.2017.04.018.

[125] H. Li, K. Li, H. Wang, X. Zhu, Y. Wei, D. Yan, X. Cheng, K. Zhai, Soot combustion over Ce1-xFexO2-δ and CeO2/Fe2O3 catalysts: Roles of solid solution and interfacial interactions in the mixed oxides, Appl. Surf. Sci. 390 (2016) 513–525. https://doi.org/10.1016/j.apsusc.2016.08.122.

[126] B. Li, A. Raj, E. Croiset, J.Z. Wen, Reactive Fe-O-Ce Sites in Ceria Catalysts for Soot Oxidation, Catalysts. 9 (2019) 815. https://doi.org/10.3390/catal9100815.

[127] Q. Song, R. Ran, J. Ding, X. Wu, Z. Si, D. Weng, The controlled preparation and performance of Fe, Co-modified porous ceria nanorods for the total oxidation of propane, Mol. Catal. 480 (2020) 110663. https://doi.org/10.1016/j.mcat.2019.110663.

[128] R. Suarez Anzorena, M.O. Mazan, A. Soldati, S.A. Larrondo, The effect of incorporation of iron in cerium oxide structure on reducibility and catalytic performance for methane oxidation in diluted streams, Ceram. Int. 45 (2019) 19757–19765. https://doi.org/10.1016/j.ceramint.2019.06.229.

[129] O.H. Laguna, M.A. Centeno, M. Boutonnet, J.A. Odriozola, Fe-doped ceria solids synthesized by the microemulsion method for CO oxidation reactions, Appl. Catal. B Environ. 106 (2011) 621–629. https://doi.org/10.1016/j.apcatb.2011.06.025.

[130] C. He, Y. Yu, L. Yue, N. Qiao, J. Li, Q. Shen, W. Yu, J. Chen, Z. Hao, Low-temperature removal of toluene and propanal over highly active mesoporous CuCeOx catalysts synthesized via a simple self-precipitation protocol, Appl. Catal. B Environ. 147 (2014) 156–166. https://doi.org/10.1016/j.apcatb.2013.08.039.

[131] C. Hu, Q. Zhu, Z. Jiang, Y. Zhang, Y. Wang, Preparation and formation mechanism of mesoporous CuO–CeO2 mixed oxides with excellent catalytic performance for removal of VOCs, Microporous Mesoporous Mater. 113 (2008) 427–434. https://doi.org/10.1016/j.micromeso.2007.11.043.

[132] F. Yang, J. Wei, W. Liu, J. Guo, Y. Yang, Copper doped ceria nanospheres: surface defects promoted catalytic activity and a versatile approach, J. Mater. Chem. A. 2 (2014) 5662–5667. https://doi.org/10.1039/C3TA15253G.

[133] X. Li, X. Li, X. Zeng, T. Zhu, Correlation between the physicochemical properties and catalytic performances of micro/mesoporous CoCeOx mixed oxides for propane

combustion, Appl. Catal. Gen. 572 (2019) 61–70. https://doi.org/10.1016/j.apcata.2018.12.026.

[134] S. Zhang, S. Liu, X. Zhu, Y. Yang, W. Hu, H. Zhao, R. Qu, C. Zheng, X. Gao, Low temperature catalytic oxidation of propane over cobalt-cerium spinel oxides catalysts, Appl. Surf. Sci. 479 (2019) 1132–1140. https://doi.org/10.1016/j.apsusc.2019.02.118.

[135] P.M. Shah, J.W.H. Burnett, D.J. Morgan, T.E. Davies, S.H. Taylor, Ceria–Zirconia Mixed Metal Oxides Prepared via Mechanochemical Grinding of Carbonates for the Total Oxidation of Propane and Naphthalene, Catalysts. 9 (2019) 475. https://doi.org/10.3390/catal9050475.

[136] A. Aranda, S. Agouram, J.M. López, A.M. Mastral, D.R. Sellick, B. Solsona, S.H. Taylor, T. García, Oxygen defects: The key parameter controlling the activity and selectivity of mesoporous copper-doped ceria for the total oxidation of naphthalene, Appl. Catal. B Environ. 127 (2012) 77–88. https://doi.org/10.1016/j.apcatb.2012.07.033.

[137] T. Garcia, D. Sellick, F. Varela, I. Vázquez, A. Dejoz, S. Agouram, S.H. Taylor, B. Solsona, Total oxidation of naphthalene using bulk manganese oxide catalysts, Appl. Catal. Gen. 450 (2013) 169–177. https://doi.org/10.1016/j.apcata.2012.10.029.

[138] C. Becker, From Langmuir to Ertl: The “Nobel” History of the Surface Science Approach to Heterogeneous Catalysis, in: K. Wandelt (Ed.), Encycl. Interfacial Chem., Elsevier, Oxford, 2018: pp. 99–106. https://doi.org/10.1016/B978-0-12-409547-2.13527-9.

[139] J. Bedia, J.M. Rosas, J. Rodríguez-Mirasol, T. Cordero, Pd supported on mesoporous activated carbons with high oxidation resistance as catalysts for toluene oxidation, Appl. Catal. B Environ. 94 (2010) 8–18. https://doi.org/10.1016/j.apcatb.2009.10.015.

[140] J.E. Lee, Y.S. Ok, D.C.W. Tsang, J. Song, S.-C. Jung, Y.-K. Park, Recent advances in volatile organic compounds abatement by catalysis and catalytic hybrid processes: A critical review, Sci. Total Environ. 719 (2020) 137405. https://doi.org/10.1016/j.scitotenv.2020.137405.

[141] Z. Duan, G. Henkelman, CO Oxidation on the Pd(111) Surface, ACS Catal. 4 (2014) 3435–3443. https://doi.org/10.1021/cs5006025.

2. Experimental

2.1 List of chemicals

Substance	**Supplier**	**Purity**
Helium	BOC	99.99%
Nitrogen	BOC	>99.99%
Oxygen	BOC	>99.99%
5000 ppm Propane in synthetic air	BOC	95%
1000 ppm Propene, 1000 ppm CO and 100 ppm Toluene in 6% O_2/N_2	BOC	99%
Naphthalene	Merck	99%
$(NH_4)_2Ce(NO_3)_6$	Acros Organics	99%
$Ce(NO_3)_6.6H_2O$	Merck	99%
$Fe(NO_3)_3.9H_2O$	Merck	>98%
Na_2CO_3 Anhydrous	Fisher Scientific	>99.8%
$Co(NO_3)_2.6H_2O$	Merck	>98%
$Cu(NO_3)_2.2.5H_2O$	Merck	98%
$ZrO(NO_3)_2.xH_2O$	Merck	99%
NaOH Anhydrous	Merck	>98%

2.2 Catalyst preparation

2.2.1 Wet impregnation

The wet impregnation method was utilised to synthesise supported metal catalysts. In a standard synthesis, $Fe(NO_3)_3.9H_2O$ was dissolved in deionised water (50 mL). To this solution, an appropriate amount of CeO_2 powder, prepared by co-precipitation (Section 2.2.2.2), was added to obtain the required loading. This mixture was heated to 80°C and stirred until a slurry was formed. The slurry was then dried at 110°C for 16 h, followed by calcination in static air at 500°C for 3 h, with a ramp rate of 5°C min^{-1}.

2.2.2 Co-precipitation

2.2.2.1 Co-precipitation using an auto-titrator

The co-precipitation method was carried out using a Metrohm Titrando auto-titrator, fitted with two Dosino dosing units that were connected to a thermostatically water heated, jacketed vessel (Figure 1). The Dosino dosing units were used to control the addition of metal nitrate solution and precipitating agent used for each synthesis. These units were computer controlled and allowed careful adjustments over the flow rate of solutions being added to the heated vessel, to regulate pH. An electrochemical probe was used to monitor pH and temperature. This set-up afforded complete control over factors such as: pH, aging time, addition of precursor solutions and temperature.

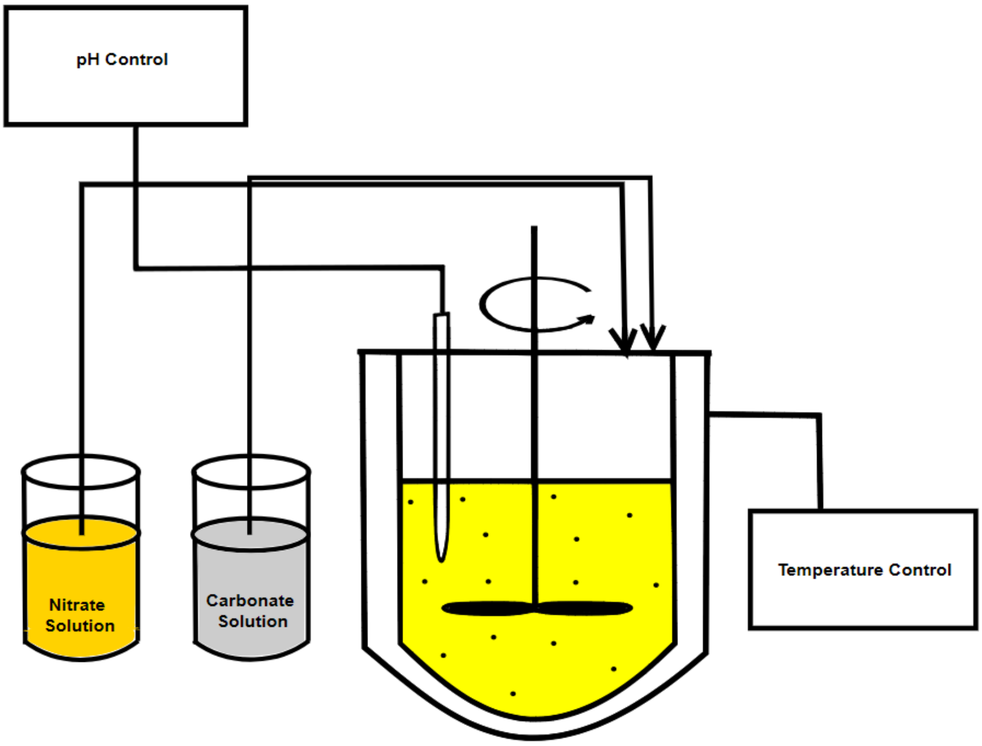

Figure 1: Schematic of Metrohm Titrando auto-titrator apparatus.

2.2.2.2 Precipitation of CeO_2 catalysts

$(NH_4)_2Ce(NO_3)_6$ and $Ce(NO_3)_3.6H_2O$ were used as Ce^{IV} and Ce^{III} sources respectively with Na_2CO_3 or NaOH as the precipitating agent. In a typical synthesis, 100 mL of nitrate solution (0.25 M) was added to a solution of Na_2CO_3 or NaOH (1 M) in a thermostatically water heated, jacketed vessel. Addition rate of the Ce^{IV} or Ce^{III} nitrate solution was maintained constant, whilst addition of precipitating agent was automatically varied to maintain a constant pH of 9. The precipitate formed was then held at 80°C for 1 h before being collected by filtration, and washed with 2 L of hot deionised water.

The precipitates were dried at 110°C for 16 h. Dried catalyst precursors, prior to calcination, were denoted as d-CeO_2 (IV) and d-CeO_2 (III). Samples denoted as CeO_2 (IV) and CeO_2 (III) were final catalysts, prepared by calcination of the precursors in static air at 500°C for 3 h, with a ramp rate of 5°C min^{-1}.

2.2.2.3 Co-precipitation of $CeFeO_x$ catalysts

$(NH_4)_2Ce(NO_3)_6$ and $Ce(NO_3)_3.6H_2O$ were used as Ce^{IV} and Ce^{III} sources respectively, with $Fe(NO_3)_3.9H_2O$ used as the Fe source and Na_2CO_3 as the precipitating agent. The Ce:Fe ratios investigated were 25:75, 50:50, 75:25, with single metal oxides of CeO_2 and Fe_2O_3 produced as standards. In a typical synthesis, 100 mL of pre-mixed Ce:Fe nitrate solution (0.25 M) was added to a solution of Na_2CO_3 (1 M) in a thermostatically water heated jacketed vessel. Addition rate of the mixed nitrate solution was maintained constant, whilst addition of Na_2CO_3 solution was automatically varied to maintain a constant pH of 9. The precipitate formed was then held at 80°C for 1 h, before being collected by filtration and washed with 2 L of hot deionised water. The precipitates were dried at 110°C for 16 h, with the final catalysts prepared by calcination in static air at 500°C for 3 h, with a ramp rate of 5°C min^{-1}. Samples prepared using the Ce^{IV} precursor were denoted $CeFeO_x$ (IV), whereas the catalysts prepared using the Ce^{III} precursor were denoted $CeFeO_x$ (III).

2.2.2.4 Co-precipitation of $CeZrMO_x$ catalysts

In a typical synthesis, metal nitrate solutions (0.25M) were prepared with $(NH_4)_2Ce(NO_3)_6$ used as the Ce source, $ZrO(NO_3)_2.xH_2O$ as the Zr source and $Fe(NO_3)_3.9H_2O$, $Co(NO_3)_2.6H_2O$, $Cu(NO_3)_2.2.5H_2O$ used as the Fe, Co and Cu sources respectively. 100 mL solutions were prepared with a Ce:Zr:M ratio (M = Fe, Co, Cu) of 90:10:1 and were added to a solution of Na_2CO_3 (1 M) in a thermostatically water heated jacketed vessel. Addition rate of the nitrate solution was maintained constant, whilst addition of Na_2CO_3 solution was automatically varied to maintain a constant pH of 9. The precipitate formed was then held at 80°C for 1 h before being collected by filtration and washed with 2 L of hot deionised water. The precipitates were dried at 110°C for 16 h, with the final catalysts prepared by calcination in static air at 500°C for 3 h, with a ramp rate of 5°C min^{-1}.

2.2.3 Preparation of Pt-Au/40%ZrO_2/UVM-7-C catalysts

Catalysts were supplied by the Instituto de Carboquímica and used as provided, without any further treatment.

For the preparation of the UVM-7-C support, the synthesis was based on the atrane route [1] with a molar ratio composition of 2 $Si(OC_2H_5)_4$: 7 $(HOCH_2CH_2)_3N.HCl$: 0.52

$CH_3(CH_2)_{15}N(Br)(CH_3)_3$: 180 H_2O. In a typical synthesis, corresponding amounts of $Si(OC_2H_5)_4$ and $(HOCH_2CH_2)_3N.HCl$ were mixed under continuous stirring at 140°C until a homogeneous dispersion was achieved. The temperature was then decreased to 120°C and the $CH_3(CH_2)_{15}N(Br)(CH_3)_3$ added. The resulting gel was cooled to 80°C and deionised water was added. The mixture was aged at room temperature for 16 h under continuous stirring. The resulting mesostructured powder was separated by filtration and washed extensively with deionised water and ethanol. The filtered powder was dried for 16 h at 60°C. To prepare the final porous material, the template was removed by calcination at 550°C for 6 h under static air, with a ramp rate of 5°C min^{-1}.

The 40% ZrO_2/UVM-7-C support was prepared by a standard wet impregnation synthesis method. 1.48 g of $ZrO(NO_3)_2.xH_2O$ was dissolved in 30 mL of deionized water under vigorous stirring. Impregnation of the calcined UVM-7-C support (0.6 g) was carried out by stirring the sample for 13 h in the nitrate solution. The mixture was dried overnight at 110°C and the resulting material was calcined in air at 550°C for 4 h, with a ramp rate of 1°C min^{-1}.

The single and bimetallic Pt/Au supported catalysts were prepared by a colloidal deposition method. For the synthesis of Au/Pt colloids, fresh aqueous solutions of $(HOCH_2)_4PCl$ (0.0675 M) and NaOH (0.2 M) were prepared by adding 1.5 mL of NaOH and 1 mL of $(HOCH_2)_4PCl$ to 45.5 mL of deionized water. Whilst stirring, an appropriate amount of aqueous $KAuCl_4$/$PtCl_4$ solution was then added under vigorous stirring at 60°C. After the reduction step, the hydrosols were stirred for 30 min and the desired amount of support was added (acidified to pH 2 by H_2SO_4) to obtain the required metal loading. After 2 h the slurry was filtered, with the catalyst washed thoroughly with deionised water and dried at 120°C overnight in static air. The material was then calcined in air at 400°C for 2 h, with a ramp rate of 5°C min^{-1}. For the bimetallic catalysts, the required amount of aqueous $KAuCl_4$/$PtCl_4$ solutions were added simultaneously. Whereas, for the catalysts prepared by different loading order, the aqueous $KAuCl_4$/$PtCl_4$ solutions were added consecutively with the drying and calcination process occurring between each metal loading.

2.3 Characterisation techniques

2.3.1 Thermogravimetric Analysis (TGA)

TGA is a technique which measures change in mass as a function of time or temperature, in a controlled environment [2]. This is done by incrementally increasing the temperature of a sample under a desired atmosphere, whilst the changes in mass are determined by an analytical balance. Mass loss corresponds to the decomposition of the sample by methods such as loss of volatile compounds or water. Mass loss can be plotted against temperature to illustrate thermal transition periods, which provide quantitative information on sample composition. This can be used to determine appropriate calcination conditions to form the required catalyst sample and identify decomposition products to deduce the decomposition pathway.

Analysis was carried out using a Perkin Elmer TGA 4000. Approximately 30 mg of sample was placed into ceramic crucibles and loaded into the instrument. Samples were then heated to 700°C at a rate of 5°C min^{-1}, under a flow of synthetic air (50 mL min^{-1}). Mass losses were recorded as changes in mg and converted into a percentage loss of the total mass of sample.

2.3.1.1 Thermogravimetric – Differential Thermal Analysis (TG-DTA)

TG-DTA is a simultaneous technique which combines TG analysis (see Section 2.3.1) with differential thermal analysis (DTA). DTA measures the temperature difference between the sample and a reference material, detecting changes of enthalpy or heat capacity [3,4]. The combination of these techniques allows for more detailed analysis of decomposition pathways which can then provide more information on the possible decomposition products.

Thermogravimetric - differential thermal analysis (TG-DTA) were performed using a Setaram Labsys 1600 instrument. Approximately 30 mg of sample was loaded into an alumina crucible and heated to 700°C at a rate of 5°C min^{-1}, in a flow of synthetic air (50 mL min^{-1}). For all TGA runs, blank runs were subtracted from the relevant data to account for buoyancy effects.

2.3.2 Powder X-ray Diffraction (XRD)

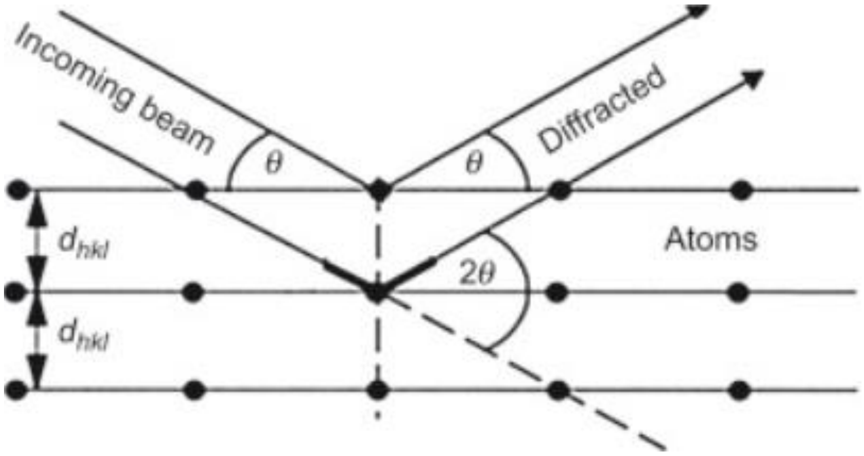

Figure 2: X-ray diffraction in a crystalline sample. Reproduced with permission from [5].

XRD is a technique used for the analysis of crystalline samples. It can provide information on structural parameters, such as: phases present in the sample, crystallite size, lattice strain and crystal defects [6]. The analysis of constructive interference, arising from diffracted X-ray radiation, is used to produce a diffraction pattern. Crystalline compounds produce a characteristic fingerprint from XRD, which can be compared to the International Centre for Diffraction Data (ICDD) database, to identify the crystalline phases. In addition, information such as the d-spacing can be acquired from the diffraction pattern. This method requires the sample to have long range order, such as a repeating unit cell, to form constructive interference. Therefore, it is not possible to produce a defined diffraction pattern for amorphous samples.

A monochromatic X-ray source is used to produce X-ray radiation which interacts with a crystalline sample, creating either constructive or destructive interference. Destructive interference arises from out of phase radiation which cancels out diffracted radiation. Constructive interference is a result of satisfying Bragg's law (Equation 1), causing the incident X-ray radiation to be in phase [5]. When X-ray radiation interacts with the sample, a cone of diffracted x-rays is produced for each angle. Each cone varies in intensity depending on the occurrence of the phase in the sample and the nature of the phase. A detector, moving in an arc over the sample, is used to determine the data and extract a pattern which can then be compared to the ICDD database.

Equation 1: Bragg's law

$$n\lambda = 2dsin\theta$$

Where:

d = Lattice spacing

ϴ = Diffraction angle

n = Integer

λ = Wavelength of the X-ray

Calculation of the crystallite size for a given phase can be done using the Scherrer equation (Equation 2). This equation relates the crystallite size to the line broadening [7]. The equation has certain limitations, such as not taking into account particle size distribution and structural disorder which can lead to errors in the calculation [8].

Equation 2: Scherrer equation

$$\tau = \frac{K\lambda}{\beta cos\theta}$$

Where:

τ = Mean crystallite size

λ = Wavelength of X-ray

K = Shape factor constant

β = Peak broadening measured from the FWHM

ϴ = Bragg angle

Powder X-ray diffraction (XRD) analysis was performed using a Panalytical X'Pert diffractometer, equipped with a Cu X-ray source operating at 40 kV and 40 mA. Patterns were attained over the 2θ range 5 - 80°, resulting in a total run time of 40 min. Entries from the International Centre for Diffraction Data (ICDD) database were used to acquire phase identification by comparison with experimental patterns. Application of the Scherrer equation was used to calculate crystallite size, with an average calculated from the four most intense peaks for CeO_2 based samples.

2.3.3 Laser Raman Spectroscopy

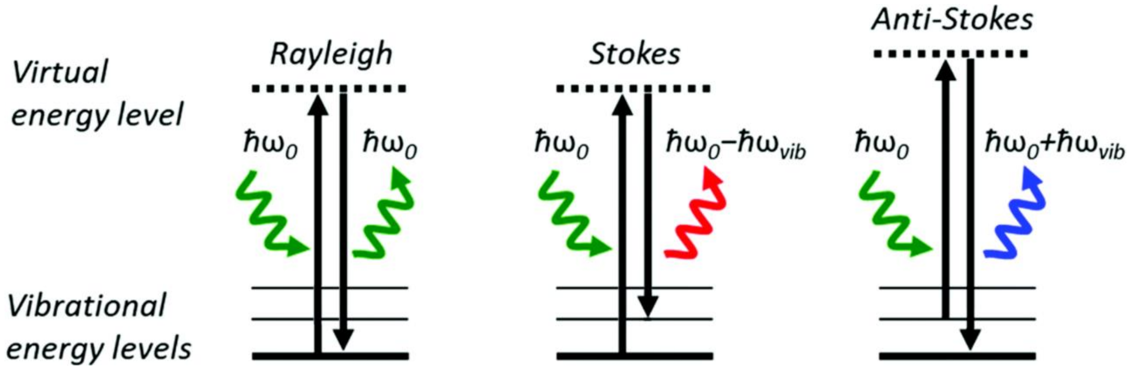

Figure 3: Different forms of elastic and inelastic scattering from excitement by electromagnetic radiation. Image reproduced from [9]*, with permission from the Royal Society of Chemistry.*

In laser Raman spectroscopy a sample is irradiated by electromagnetic radiation, resulting in the scattering of radiation. This radiation can be scattered elastically or inelastically, with the former being known as Rayleigh scattering, and the latter known as the Raman effect [10]. In elastic scattering energy is conserved, with excitation to a virtual energy level and relaxation to the same ground vibrational energy level. Whereas during inelastic scattering, a change in vibrational energy level is observed upon relaxation. If the frequency of the incident radiation is higher than the scattered radiation then stokes scattering occurs; however, if the frequency of the incident radiation is lower than the scattered radiation then anti-stokes scattering is observed [11]. As stokes scattering involves a transition from lower to higher vibrational energy levels, they are more intense and are measured in Raman spectroscopy. For a molecule to be Raman active, there must be a change in polarizability during vibration [12]. Irradiating a sample with a laser can result in the Raman effect. The measurement of the change in frequency of scattered light allows for the calculation of the vibrational energy levels, which can then provide information on the molecular structure that are characteristic to each sample.

Raman spectroscopy was carried out using a Renishaw inVia confocal Raman microscope equipped with an Ar^+ visible green laser, with an emission wavelength of 514 nm. Catalyst samples were placed onto a steel plate and spectra were collected in a reflective mode by a highly sensitive charge couple device (CCD) detector. Typically, 10 accumulations were used in each scan, with a laser exposure of 10 s and power of 10%.

2.3.4 Brunauer-Emmett-Teller Surface Area Analysis (BET)

Brunauer-Emmett-Teller (BET) analysis is a commonly used technique to determine the surface area of catalysts. The BET method is an extension of the Langmuir kinetic theory, incorporating the idea of multilayer adsorption [13]. It utilises data acquired from a sorption isotherm, of the volume of molecules adsorbed relative to pressure, and converts this to a BET plot. Information from this plot can then be used in the BET equation (Equation 3) to determine the surface area [14].

Equation 3: BET equation

$$\frac{P}{V(P_0 - P)} = \left(\frac{P}{P_0}\right)\frac{C-1}{V_m C} + \frac{1}{V_m C}$$

Where:

P = Equilibrium pressure

P_0 = Saturation pressure

V = Adsorbed volume

V_m = Monolayer volume

C = BET Constant

The BET equation is used in the linear form so a value of the BET monolayer capacity (V_m) can be derived. This can then be used to calculate the surface area using Equation 4.

Equation 4: Surface area calculation

$$S_{BET} = \frac{V_m N_A \sigma}{mv}$$

Where:

S_{BET} = BET Surface area

V_m = Monolayer Volume

σ = Cross-sectional area of N_2 molecule (0.162 nm^2)

N_A = Avogadro’s Constant

m = Sample mass

ν = Molar volume of gas

The shape of sorption isotherms can be defined by the pore structure and surface-adsorbate interactions of the material investigated. These have been classified into six sorption isotherms (Figure 4) with varying characteristics. Type I, II and IV isotherms are commonly assessed by BET theory due to the inflection point (B, Figure 4) usually referred to as the point at which a monolayer is formed [15]. The C constant associated with BET analysis is generally accepted as a useful indicator of how valid the BET method is for certain isotherms. A low C constant can be linked to isotherms III and V resulting in the BET method being insufficient [14].

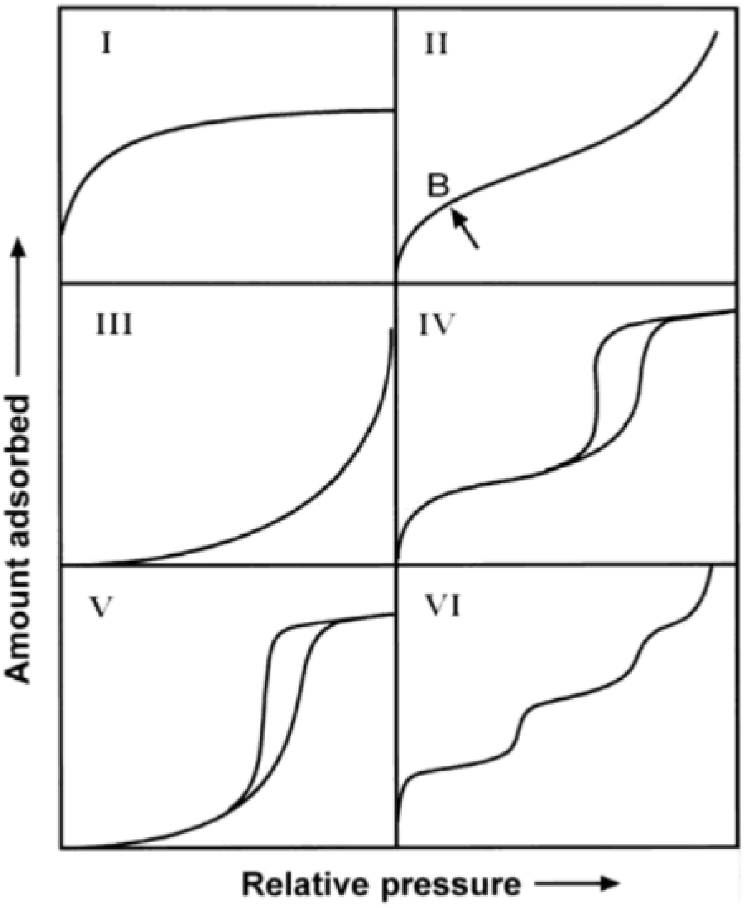

Figure 4: Classification of sorption isotherms. Reproduced with permission from [15].

BET surface area analysis was obtained using a Quantachrome Quadrasorb Evo Analyser. Catalyst samples (0.150 g) were degassed under vacuum for 16 h at 120°C prior to analysis. Surface areas of the samples were determined from 20-point adsorption-desorption isotherms using N_2 as the adsorbate gas, measured at −196°C. The data were treated using the Brunauer–Emmett–Teller (BET) method.

2.3.5 Temperature Programmed Reduction (TPR)

Temperature programmed reduction (TPR) is a technique which investigates the reducibility of a sample and the types of reducible species present. To achieve this, a reducible atmosphere, such as dilute H_2, is employed whilst linear heating of the sample is applied. H_2 in the feed is consumed by reacting with oxygen species in the sample, resulting in the sample being reduced. In this way, reducibility can also be somewhat linked to the oxygen mobility in the sample. The change in H_2 concentration is analysed by a thermal conductivity detector (TCD), which is presented as a peak in the TPR profile. Each peak can then be associated with a certain reduction process of the material which can be used to assess oxidation state [16]. H_2 consumption can also be quantified by the peak area following a calibration using a known sample, such as CuO [17].

TPR was performed using a Quantachrome ChemBET TPD/R/O, fitted with a thermal conductivity detector (TCD) to monitor H_2 uptake. Samples were pre-treated under a flow of He for 1 h at 120°C. Reduction profiles were attained by analysing approximately 50 mg of catalyst under a flow of 10% H_2/Ar (50 mL min^{-1}), over the temperature range 50 to 700°C, with a heating rate of 10°C min^{-1}. H_2 consumption was calculated by calibration against a CuO standard.

2.3.5.1 Temperature Programmed Reduction - Temperature Programmed Oxidation Cycles (TPR-TPO)

TPR-TPO cycles incorporate the TPR method (see Section 2.3.5), with the addition of a temperature programmed oxidation (TPO) experiment run in succession. During the TPO experiment, the sample is in the reduced state and is introduced to a dilute oxidising atmosphere whilst being heated by a pre-determined temperature programme. Peaks in the TPO profile, arising from changes in O_2 concentration detected by a TCD, can be associated with the re-oxidation of the sample. This type of experiment can be used to assess redox properties of samples, such as: the ease and degree of reduction/oxidation, the dynamic oxygen storage capacity and the ability to complete the redox cycle [18].

TPR-TPO cycles were performed using a Quantachrome ChemBET TPD/R/O, fitted with a TCD. Samples were pre-treated under a flow of He for 1 h at 120°C. Reduction profiles were attained by analysing approximately 50 mg of catalyst under a flow of 10% H_2/Ar (50 mL min^{-1}), over the temperature range 50 to 700°C, with a heating rate of 10°C min^{-1}. Once the TPR cycle was complete, the catalyst sample was left to cool under flowing He. Oxidation profiles were then attained by analysing the sample under a flow of 10% O_2/He at 50 mL min^{-1}, over the temperature range 50 to 700°C, with a heating rate of 10°C min^{-1}.

2.3.6 X-ray Photoelectron Spectroscopy (XPS)

X-ray photoelectron spectroscopy (XPS) is a surface sensitive technique used for the analysis of elemental composition and determination of surface oxidation state. This technique is underpinned by the photoelectric effect; a process in which, when a sample is irradiated with X-ray radiation, an electron is emitted from the sample with a certain kinetic energy [19]. The kinetic energy of the emitted electron can be measured and related to the binding energy using Equation 5.

Equation 5: The Photoelectric effect

$$E_k = hv - E_b - \varphi$$

Where:

E_k = Kinetic energy

h = The Planck constant

v = Frequency of exciting electrons

E_b = Binding energy

φ = Work function of the spectrometer

The binding energy is characteristic of each element and can change depending on the chemical environment of the ejected electron, or the orbital from which it was ejected. This then allows for the identification and quantification of surface species present on the sample. It is also possible to assess the oxidation state of the elements. As a result of an electron in an oxidised element having a greater coulombic interaction with the core, this will lead to an increased binding energy which can be used to calculate the oxidation state. XPS is commonly referred to as a surface sensitive technique due to the short mean free path of electrons through solid materials, resulting in analysis depths of a few nanometres [20].

X-ray photoelectron spectroscopy (XPS) was carried out using a Kratos Axis Ultra DLD system, spectra were collected using a monochromatic Al Kα X-ray source operating at 140 W (10 mA and 14 kV). Data were collected with pass energies of 160 eV for survey spectra and 20 eV for the high-resolution scans, with step sizes of 1 eV and 0.1 eV respectively. The system was operated in the Hybrid mode, using a combination of magnetic immersion and electrostatic lenses and acquired over an area approximately 300 x 700 μm^2. A magnetically confined charge compensation system was used to minimize charging of the sample surface, with all spectra taken at a 90° angle. A base pressure of *ca*. $1x10^{-9}$ Torr was maintained during collection of the spectra. Data were analysed using CasaXPS v2.3.24 [21] after subtraction of a Shirley background and using modified Wagner sensitivity factors as supplied by the manufacturer .

2.3.7 Scanning Electron Microscopy – Energy Dispersive X-ray Spectroscopy (SEM-EDX)

Electron microscopy techniques such as SEM or TEM are useful methods to determine topology, morphology and elemental composition of a sample. SEM uses an incident electron beam that interacts with the sample, resulting in the emission of electrons from the sample that can be analysed to form an image. Two main types of electrons can be detected, these being secondary electrons (SE) or backscattered electrons (BSE) [22]. Secondary electrons are emitted by inelastic processes and tend to be of low energy, only escaping from <10 nm below the surface. These can be used to determine topology of a sample. Backscattered electrons are detected as a result of incident electrons being elastically scattered by the sample. There is a strong relationship between atomic number and the intensity of the scattering that occurs, which allows elemental composition to be analysed. The scattering interactions and depth of analysis can depend of many factors, one of which being the application of varying accelerating voltage of the incident electrons, usually being between 1-40 kV [23].

EDX is a technique that can be used in collaboration with SEM. This technique analyses the emission of X-rays from the sample, when bombarded with high energy incident electrons. X-rays are emitted from the sample by relaxation of an outer electron to fill a hole left by the removal of a core electron. EDX can be used to quantitively and qualitatively analyse the elements present in the sample to gain information on the elemental composition [24].

Scanning electron microscopy (SEM) was performed using a Tescan MAIA3 field emission gun scanning electron microscope (FEG-SEM) fitted with secondary and backscattered electron detectors. Energy-dispersive X-ray (EDX) analysis was performed using an Oxford Instruments X-ray Max^N 80 detector. EDX analysis was performed using the Point and ID function on the Oxford Aztec software. A minimum of 3 areas were analysed across multiple particles and averaged to produce atomic % (at.%). Catalysts loaded onto carbon tape were sputter coated with 15 nm Au/Pd to prevent charging.

2.3.8 Transmission Electron Microscopy (TEM)

Transmission electron microscopy (TEM) is another electron microscopy technique used to analyse samples at the nanometre scale, providing information such as morphological, compositional and crystallographic properties of catalytic materials [7]. The acquisition of TEM images occurs from high energy monochromatic electrons passing through an ultra-thin sample. Depending on the density of the sample, electrons pass through the sample to a detector, whilst others are scattered. The detected electrons are converted to an image where the different contrast represents the differences in charge density present in the sample.

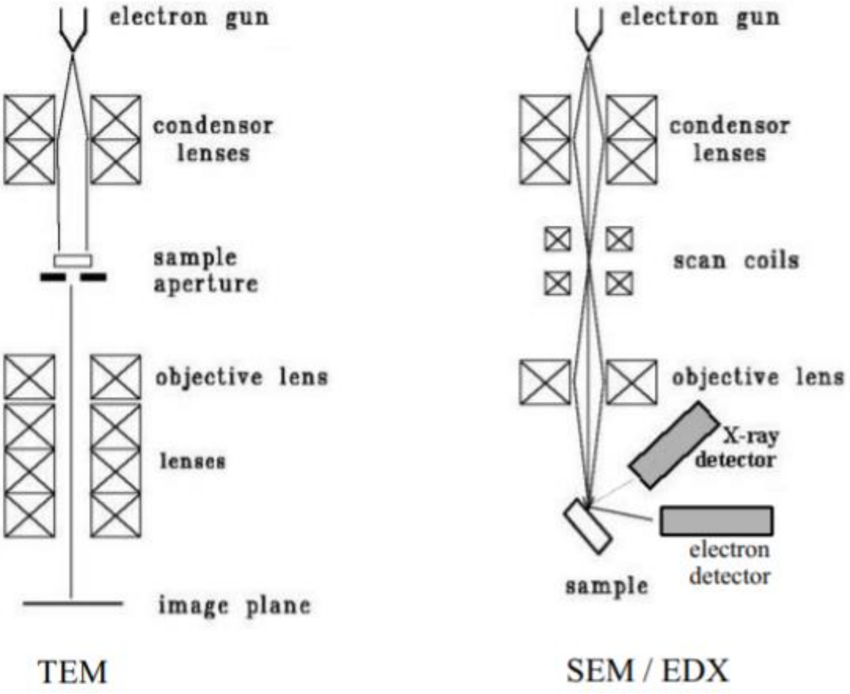

Figure 5: Schematic of electron microscope used for TEM and SEM-EDX analysis. Reproduced with permission from [7].

Crystallographic properties of the sample can be deduced by TEM analysis, usually in the form of selected area electron diffraction (SAED). Emitted electrons can be diffracted by the sample, producing diffraction patterns of either spots or rings depending on the crystallinity of the sample. These diffraction patterns can then be analysed to determine lattice spacing and planes present [7].

Transmission electron microscopy (TEM) was performed using a JEOL JEM 2100 operating at 200 kV. Samples were prepared by dry dispersion over a 300 mesh copper grid coated with holey carbon film.

2.3.9 CO-Diffuse Reflectance Infrared Fourier Transform Spectroscopy (DRIFTS)

Diffuse reflectance infrared Fourier Transform spectroscopy (DRIFTS) is an infrared (IR) technique that can be used to identify surface adsorption sites of catalytic materials. IR spectroscopy works on the basis that molecules possess discrete vibrational and rotational energy levels, which are related to their structure. Photons are absorbed by a molecule with the same energy as the incident photons, causing the adsorption of IR radiation to reveal structural information about the sample. Similarly to Raman spectroscopy, molecules must be IR active to observe the vibrations. For a sample to be IR active, the vibration of the molecule must result in a change in the dipole moment. Therefore, highly symmetrical diatomic molecules, such as N_2 or H_2, exhibit no change in the dipole moment so are IR inactive.

A Fourier transform is a mathematical operation that has greatly increased the power of IR spectroscopy. Standard IR spectrometers use one wavelength of light sequentially and measure the absorbance/reflectance at a given wavelength, whereas Fourier Transform spectrometers allow the measurement of multiple wavelengths simultaneously. The use of a Michelson interferometer, in which a configuration of mirrors enables each wavelength to be transmitted and blocked, obtains IR spectra over a wide spectral range [25]. This occurs due to wave interference which is modulated by a moving mirror. The use of Fourier Transform provides a better signal-to-noise ratio due to low interference occurring over multiple scans. CO is used as an effective probe molecule in DRIFTS analysis due to the sensitive interaction with metal nanoparticles, allowing for information on adsorption sites and metal species to be gathered [26].

CO-DRIFTS measurements were obtained on a Bruker Tensor 27 spectrometer, fitted with a mercury cadmium telluride detector and ZnSe windows. Samples were loaded into the Praying Mantis high temperature (HVC-DRP-4) in situ cell before pre-treatment with N_2. A background was obtained using KBr and measurements were recorded every minute at room temperature. 1% CO/N_2 was then flowed over the sample at 50 mL min^{-1} until CO adsorption bands were maintained constant. Once this occurred, the gas feed was changed to purge with N_2 and measurements were made until no change in subsequent spectra were observed.

2.4 Catalyst testing

2.4.1 Propane total oxidation

2.4.1.1 Reactor set-up

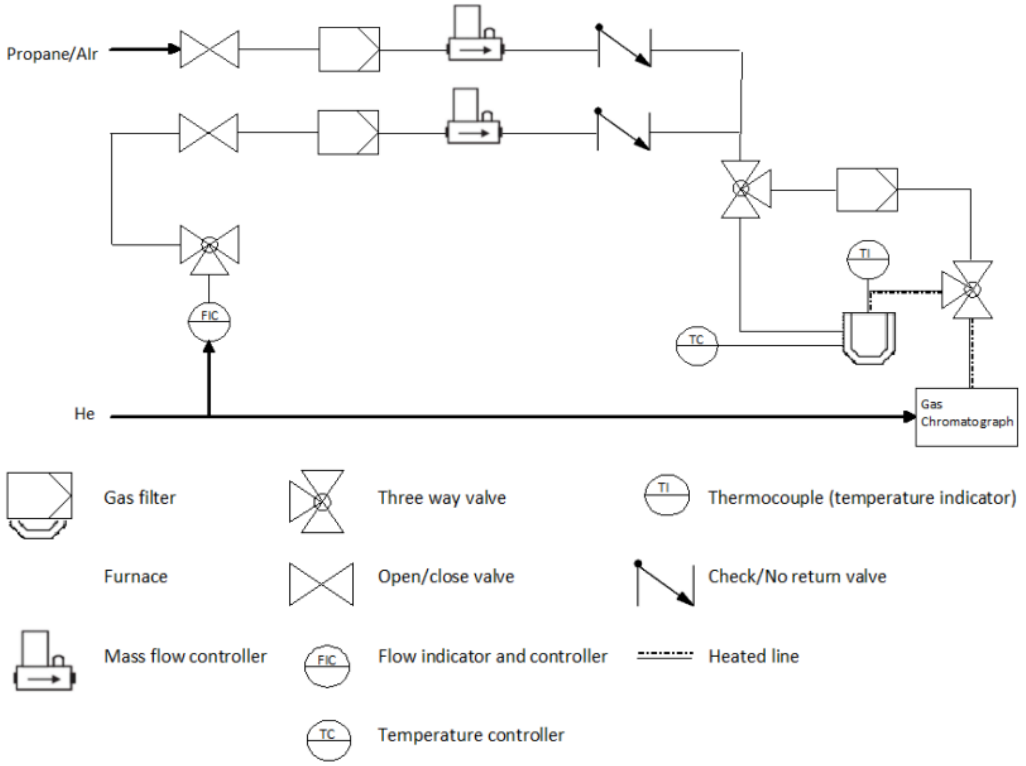

Figure 6: Reactor schematic for equipment used in propane total oxidation reactions.

Catalyst performance for the total oxidation of propane was assessed using a continuous-flow fixed bed microreactor. Catalysts samples were secured in a ¼ inch stainless steel tube between two plugs of quartz wool. A premixed cylinder of 5000 ppm propane in synthetic air was used, with the gas flow regulated at 50 mL min^{-1} by electronic mass flow controllers (MFCs). The powders were packed un-pelleted to a constant volume of 0.0667 mL, to achieve a gas hourly space velocity (GHSV) of 45000 h^{-1}. The catalyst activity was measured over the temperature range 200–600°C, with the temperature maintained and controlled by a K-type thermocouple placed into the catalyst bed. The reactor temperature was increased incrementally and allowed to stabilise before analysing the reactor effluent.

The reaction effluent was analysed by an online gas chromatograph (Agilent 7890B) with two detectors in series. A thermal conductivity detector (TCD) was used to analyse O_2 and N_2. In addition, a flame ionisation detector (FID) equipped with a methaniser was used to analyse CO, CO_2 and hydrocarbons. Separation was achieved using Haysep Q (80–100 mesh, 1.8 m x 3.2 mm) and MolSieve 13 X (80–100 mesh, 2 m x 3.2 mm) packed columns, with a series/by-pass valve configuration. Analyses were performed at each temperature until *steady-state* was attained and three consistent sets of analytical data were obtained. For catalyst testing involving water vapour in the feed, a water saturator was attached downstream of the MFC port and held at a constant temperature to produce a water saturation of 5%.

2.4.1.2 Product analysis

Products analysed using the online gas chromatography (GC) system were separated using different columns and a series of valve operations. Three six-port valves were used, with valve operations occurring at set times to control gas flow through the columns to the detectors. A schematic of the valve operation system is shown below:

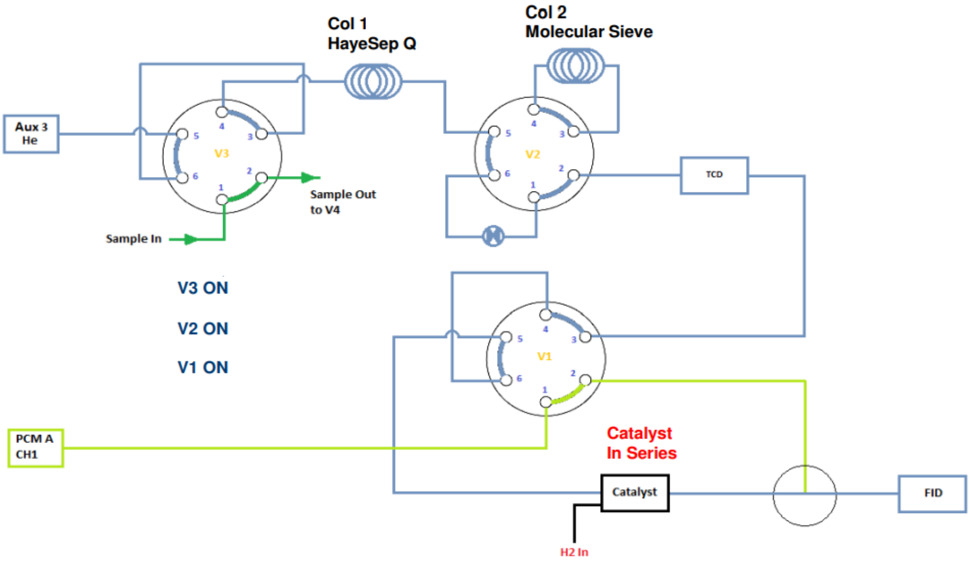

Figure 7: GC schematic for an example of valve operations used in propane total oxidation reactions.

The analysis of CO, CO_2 and hydrocarbons by the FID was achieved by initial combustion through the methaniser, which converted the products to methane using a Ni catalyst under a H_2 stream. This was done to obtain a signal for the CO and CO_2 products, which couldn't be analysed by the FID alone. Propane conversion was calculated from comparing the concentration obtained at each temperature against the concentration measured in the initial blank run, where the reaction gas was passed through a bypass.

Equation 6: Calculation of propane conversion.

$$Propane\ Conversion = \frac{Propane\ concentration\ at\ x\ temperature}{Propane\ concentration\ in\ blank\ run} \times 100$$

Selectivity to CO_2 was calculated by comparing the concentration of CO_2 at each temperature to the sum of all the products obtained at each temperature:

Equation 7: Calculation of selectivity to CO_2 for propane total oxidation.

$$CO_2\ Selectivity = \frac{Concentration\ of\ CO_2\ at\ x\ temperature}{Concentration\ of\ all\ products\ obtained\ at\ x\ temperature} \times 100$$

Carbon balance was measured by comparing the total amount of carbon in the initial blank run to the total amount of carbon measured at each temperature:

Equation 8: Calculation of carbon balance for propane total oxidation.

$$Carbon\ Balance = \frac{Concentration\ of\ all\ carbon\ containing\ compounds\ at\ x\ temperature}{Concentration\ of\ all\ carbon\ containing\ compounds\ in\ the\ blank\ run} \times 100$$

2.4.2 Naphthalene total oxidation

2.4.2.1 Reactor set-up

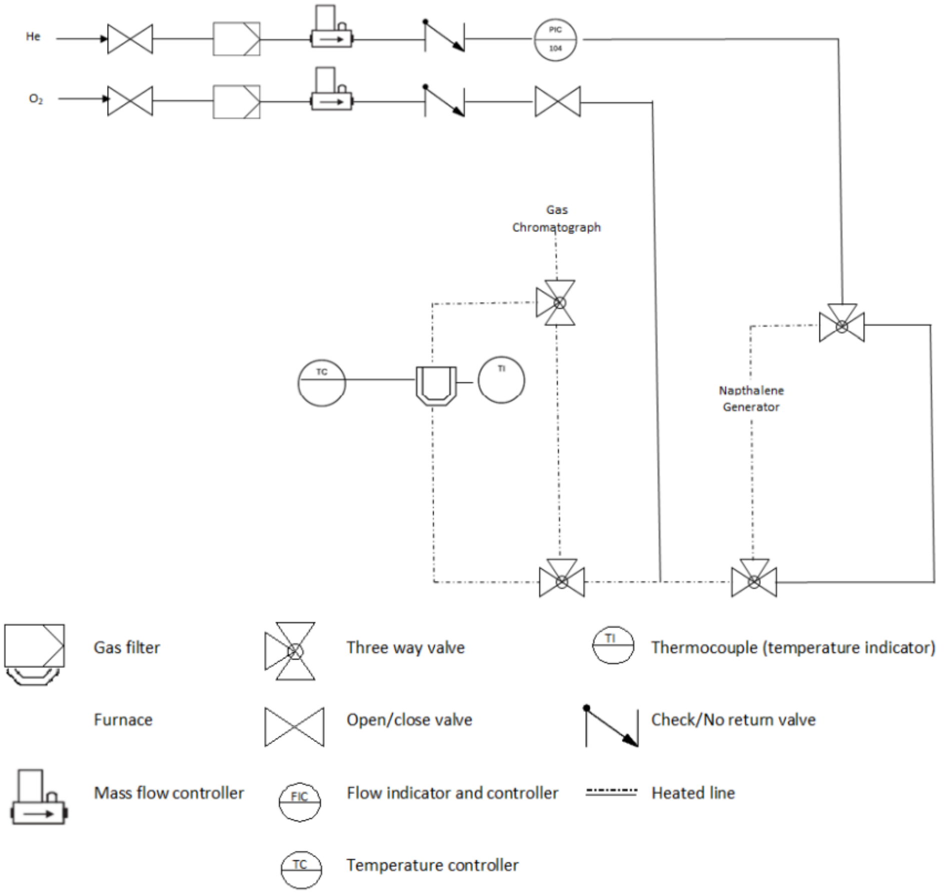

Figure 8: Reactor schematic for equipment used in naphthalene total oxidation reactions.

Naphthalene total oxidation was evaluated using a second continuous flow fixed bed reactor. A fixed volume (0.0667 mL) of un-pelleted catalyst powders were packed between plugs of quartz wool in a ¼ inch stainless steel tube. A GHSV of 45000 h^{-1} was achieved by using a total gas flow of 50 mL min^{-1}. 200 ppm of naphthalene was generated by subliming naphthalene in a thermostatically controlled heater at 35°C under a He flow (40 mL min^{-1}). O_2 (10 mL min^{-1}) was then added before reaching the reactor to provide the total flow. The gas flow was passed through the reactor tube containing the catalyst, which was heated in a clam-shell furnace. The activity was measured over a temperature range of 100–350°C, at 25°C intervals, with the temperature monitored using a K-type thermocouple placed in the catalyst bed.

The reaction effluent was analysed using an Agilent 7890B GC (columns: HP-5, 30 m x 0.32 mm x 0.25 µm and Haysep Q, 80–100 mesh, 3 m x 3.2 mm), fitted with 2 FIDs, one of which was fitted with a methaniser. Four analyses were undertaken at each temperature after a period of stabilisation. The reaction temperature was then increased incrementally and after appropriate stabilisation time to attain *steady-state*, the analysis procedure was repeated.

2.4.2.2 Product analysis

Products analysed using the online gas chromatography (GC) system were separated using different columns and a series of valve operations. One ten-port valve and one six-port valve were used, with valve operations occurring at set times to control gas flow through the columns to the different detectors.

In the GC system, gaseous products were split using valve operations, with one FID used to analyse hydrocarbon products, and the other, fitted with a methaniser, used to analyse CO and CO_2. Naphthalene conversion was calculated by comparing concentration at each temperature to those measured in the initial blank run, where the reaction mixture was flowed through a bypass.

Equation 9: Calculation of naphthalene conversion.

$$Naphthalene\ Conversion = \frac{Naphthalene\ concentration\ at\ x\ temperature}{Naphthalene\ concentration\ in\ blank\ run} \times 100$$

However, naphthalene conversion has been shown to fluctuate due to the strong adsorption to the catalyst surface, resulting in misleading conclusions for catalytic activity

[27]. Therefore, CO_2 yield was used as a more appropriate method to assess catalytic total oxidation activity. This was calculated by comparing the concentration of CO_2 at a given temperature to the expected concentration of CO_2 determined from the full conversion of naphthalene present in the initial blank run [28]:

Equation 10: Calculation of CO_2 yield for naphthalene total oxidation.

$$CO_2\ Yield = \frac{Concentration\ of\ CO_2\ at\ x\ temperature}{Concentration\ of\ expected\ CO_2\ from\ full\ conversion\ of\ naphthalene} \times 100$$

2.4.3 Toluene, propene and CO simultaneous total oxidation

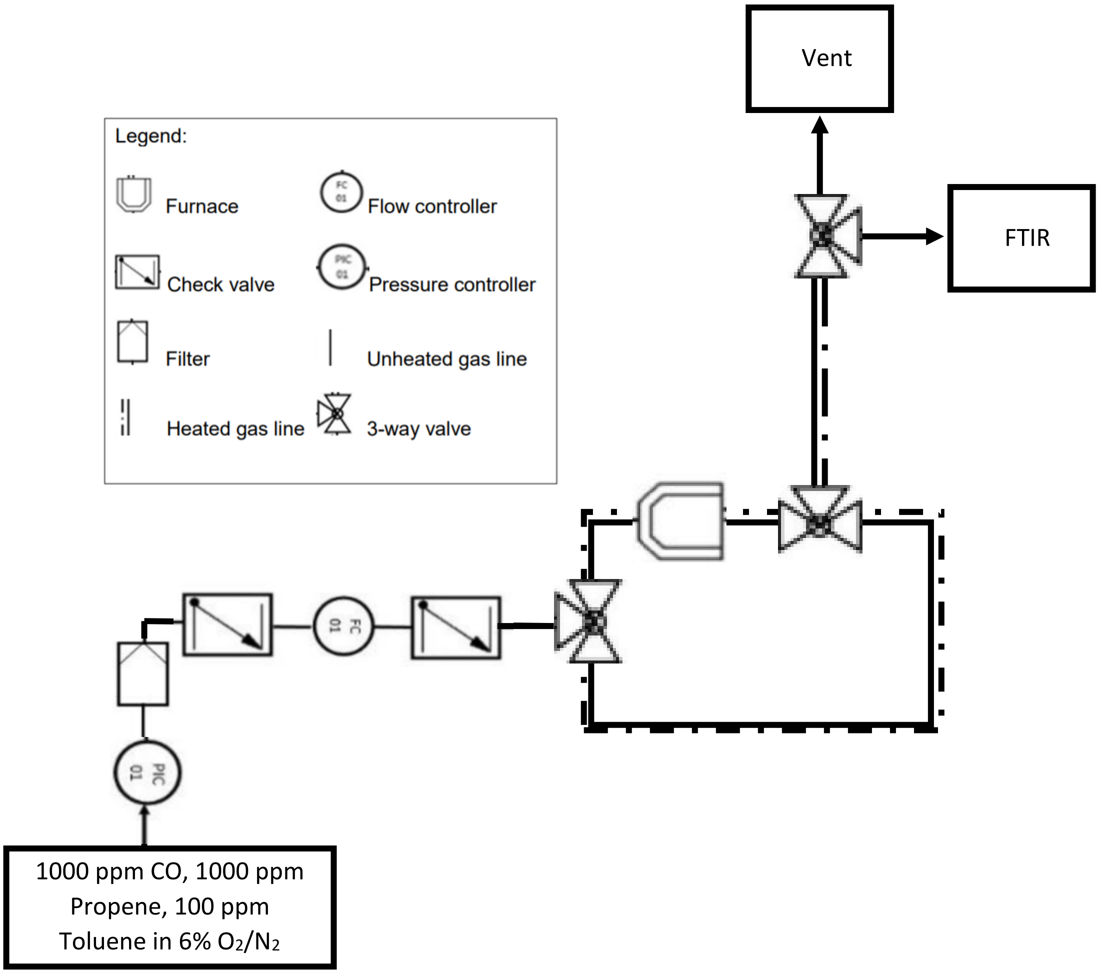

Figure 9: Reactor schematic for equipment used in simultaneous CO, propene and toluene total oxidation reactions.

The simultaneous total oxidation of propene, toluene and CO was performed using a fixed bed flow reactor. Un-pelleted powder catalysts were packed between plugs of quartz wool into a ½ inch quartz tube. Catalysts were pre-treated for 1 h at 100°C, under flowing N_2 at 50 mL min^{-1}. Once pre-treated, the reaction mixture of 1000 ppm propene, 1000 ppm CO and 100 ppm toluene in 6% O_2/N_2 was passed through the bypass loop until stabilised, to acquire a background measurement. The reaction mixture was then passed through the catalyst bed at 50 mL min^{-1} to achieve a GHSV of 45000 h^{-1}. Catalyst activity was measured over the temperature range 100-500°C at 50°C intervals, with a K-type thermocouple used to monitor the temperature in the catalyst bed. The effluent analysis was recorded by a Gasmet DX-4000 FT-IR spectrometer, with measurements taken every second and the software package Calcmet was used to convert FT-IR data into concentration values.

The conversion of propene, toluene and CO to CO_2 was determined by comparing the recorded ppm values of CO_2 to the sum of the ppm values for all compounds using carbon equivalents:

Equation 11: Calculation of CO_2 yield for the simultaneous total oxidation of CO, propene and toluene.

$$CO_2 Yield = \frac{ppm\ values\ of\ CO_2\ at\ x\ tempertaure}{ppm\ values\ of\ all\ carbon\ equilvalent\ compounds\ at\ x\ temperature} \times 100$$

2.5 References

[1] S. Cabrera, J. El Haskouri, C. Guillem, J. Latorre, A. Beltrán-Porter, D. Beltrán-Porter, M.D. Marcos, P. Amorós *, Generalised syntheses of ordered mesoporous oxides: the atrane route, Solid State Sci. 2 (2000) 405–420. https://doi.org/10.1016/S1293-2558(00)00152-7.

[2] G.R. Heal, Thermogravimetry and Derivative Thermogravimetry, in: Princ. Therm. Anal. Calorim., 2002: pp. 10–54. https://doi.org/10.1039/9781847551764-00010.

[3] A. Riga, R. Collins, Differential Scanning Calorimetry and Differential Thermal Analysis, in: Encycl. Anal. Chem., American Cancer Society, 2006. https://doi.org/10.1002/9780470027318.a6602.

[4] S.B. Warrington, Simulataneous thermal analysis techniques, in: Princ. Therm. Anal. Calorim., 2002: pp. 166–189. https://doi.org/10.1039/9781847551764-00166.

[5] J. Epp, X-ray diffraction (XRD) techniques for materials characterization, in: G. Hübschen, I. Altpeter, R. Tschuncky, H.-G. Herrmann (Eds.), Mater. Charact. Using Nondestruct. Eval. NDE Methods, Woodhead Publishing, 2016: pp. 81–124. https://doi.org/10.1016/B978-0-08-100040-3.00004-3.

[6] A.A. Bunaciu, E. gabriela Udriştioiu, H.Y. Aboul-Enein, X-Ray Diffraction: Instrumentation and Applications, Crit. Rev. Anal. Chem. 45 (2015) 289–299. https://doi.org/10.1080/10408347.2014.949616.

[7] I. Chorkendorff, J. W. Niemantsverdriet, Catalyst Characterization, in: Concepts Mod. Catal. Kinet., John Wiley & Sons, Ltd, 2005: pp. 129–166. https://doi.org/10.1002/3527602658.ch4.

[8] C. Weidenthaler, Pitfalls in the characterization of nanoporous and nanosized materials, Nanoscale. 3 (2011) 792–810. https://doi.org/10.1039/C0NR00561D.

[9] R. Schmitt, A. Nenning, O. Kraynis, R. Korobko, A.I. Frenkel, I. Lubomirsky, S.M. Haile, J.L.M. Rupp, A review of defect structure and chemistry in ceria and its solid

solutions, Chem. Soc. Rev. 49 (2020) 554–592. https://doi.org/10.1039/C9CS00588A.

[10] R.R. Jones, D.C. Hooper, L. Zhang, D. Wolverson, V.K. Valev, Raman Techniques: Fundamentals and Frontiers, Nanoscale Res. Lett. 14 (2019) 231. https://doi.org/10.1186/s11671-019-3039-2.

[11] G.S. Bumbrah, R.M. Sharma, Raman spectroscopy – Basic principle, instrumentation and selected applications for the characterization of drugs of abuse, Egypt. J. Forensic Sci. 6 (2016) 209–215. https://doi.org/10.1016/j.ejfs.2015.06.001.

[12] P. Colomban, G. Gouadec, Raman Scattering Theory and Elements of Raman Instrumentation, in: Raman Spectrosc. Soft Matter Appl., John Wiley & Sons, Ltd, 2008: pp. 11–29. https://doi.org/10.1002/9780470475997.ch2.

[13] S. Lowell, J.E. Shields, Powder Surface Area and Porosity, Springer Science & Business Media, 2013.

[14] M. Thommes, K. Kaneko, A.V. Neimark, J.P. Olivier, F. Rodriguez-Reinoso, J. Rouquerol, K.S.W. Sing, Physisorption of gases, with special reference to the evaluation of surface area and pore size distribution (IUPAC Technical Report), Pure Appl. Chem. 87 (2015) 1051–1069. https://doi.org/10.1515/pac-2014-1117.

[15] S. Lowell, J.E. Shields, M.A. Thomas, M. Thommes, Characterization of Porous Solids and Powders: Surface Area, Pore Size and Density, Springer Science & Business Media, 2012.

[16] A. Jones, Temperature-Programmed Reduction for Solid Materials Characterization, CRC Press, 1986.

[17] H. Knözinger, Temperature-Programmed Reduction and Oxidation, in: Handb. Heterog. Catal., American Cancer Society, 2008: pp. 1080–1096. https://doi.org/10.1002/9783527610044.hetcat0056.

[18] A. Gervasini, Temperature Programmed Reduction/Oxidation (TPR/TPO) Methods, in: A. Auroux (Ed.), Calorim. Therm. Methods Catal., Springer Berlin Heidelberg, Berlin, Heidelberg, 2013: pp. 175–195. https://doi.org/10.1007/978-3-642-11954-5_5.

[19] T.L. Alford, L.C. Feldman, J.W. Mayer, eds., X-ray Photoelectron Spectroscopy, in: Fundam. Nanoscale Film Anal., Springer US, Boston, MA, 2007: pp. 199–213. https://doi.org/10.1007/978-0-387-29261-8_10.

[20] A. Jablonski, C.J. Powell, Relationships between electron inelastic mean free paths, effective attenuation lengths, and mean escape depths, J. Electron Spectrosc. Relat. Phenom. 100 (1999) 137–160. https://doi.org/10.1016/S0368-2048(99)00044-4.

[21] N. Fairley, V. Fernandez, M. Richard-Plouet, C. Guillot-Deudon, J. Walton, E. Smith, D. Flahaut, M. Greiner, M. Biesinger, S. Tougaard, D. Morgan, J. Baltrusaitis, Systematic and collaborative approach to problem solving using X-ray photoelectron spectroscopy, Appl. Surf. Sci. Adv. 5 (2021) 100112. https://doi.org/10.1016/j.apsadv.2021.100112.

[22] D.C. Joy, Scanning Electron Microscopy: Theory, History and Development of the Field Emission Scanning Electron Microscope, in: Biol. Field Emiss. Scanning Electron Microsc., John Wiley & Sons, Ltd, 2019: pp. 1–6. https://doi.org/10.1002/9781118663233.ch1.

[23] K. Akhtar, S.A. Khan, S.B. Khan, A.M. Asiri, Scanning Electron Microscopy: Principle and Applications in Nanomaterials Characterization, in: S.K. Sharma (Ed.), Handb. Mater. Charact., Springer International Publishing, Cham, 2018: pp. 113–145. https://doi.org/10.1007/978-3-319-92955-2_4.

[24] J. Hamuyuni, M.O. Daramola, O.O. Oluwasina, Energy-Dispersive X-Ray Spectroscopy: Theory and Application in Engineering and Science, in: Encycl. Phys. Org. Chem., American Cancer Society, 2017: pp. 1–23. https://doi.org/10.1002/9781118468586.epoc4030.

[25] P. Larkin, Chapter 3 - Instrumentation and Sampling Methods, in: P. Larkin (Ed.), Infrared Raman Spectrosc., Elsevier, Oxford, 2011: pp. 27–54. https://doi.org/10.1016/B978-0-12-386984-5.10003-5.

[26] C. Lentz, S.P. Jand, J. Melke, C. Roth, P. Kaghazchi, DRIFTS study of CO adsorption on Pt nanoparticles supported by DFT calculations, J. Mol. Catal. Chem. 426 (2017) 1–9. https://doi.org/10.1016/j.molcata.2016.10.002.

[27] T. García, B. Solsona, S.H. Taylor, Naphthalene total oxidation over metal oxide catalysts, Appl. Catal. B Environ. 66 (2006) 92–99. https://doi.org/10.1016/j.apcatb.2006.03.003.

[28] X.-W. Zhang, S.-C. Shen, L.E. Yu, S. Kawi, K. Hidajat, K.Y. Simon Ng, Oxidative decomposition of naphthalene by supported metal catalysts, Appl. Catal. Gen. 250 (2003) 341–352. https://doi.org/10.1016/S0926-860X(03)00412-5.

3. Comparison of cerium (III) & (IV) precursors for the synthesis of CeO_2 catalysts for propane and naphthalene total oxidation

3.1 Introduction

Volatile organic compounds (VOCs) have been associated with various issues affecting the environment and human health [1]. As mentioned in Chapter 1.3, VOCs emitted into the atmosphere can react with NO_x species to form ground level ozone, which has been linked with respiratory and cardiovascular issues in humans [2–4]. Furthermore, some VOCs are known to be toxic, further threatening human health [5]. VOCs have also been shown to affect the environment by contributing to ozone depletion and climate change effects, caused by the emission of greenhouse gases [6–8]. By definition, VOCs are wide ranging in chemical nature and can be categorised into many types of compounds. Short chain alkane VOCs, such as propane, are known to be difficult to remove from the atmosphere as a result of difficult C-H bond activation [9], hence propane is an excellent model compound to study. Propane as a VOC has been continuously studied throughout the literature because of its use in industry, where the increasing use of liquid petroleum gas (LPG) as a transport fuel has been linked to rising propane emissions [10]. Polyaromatic hydrocarbons (PAHs) are another type of VOC, where emissions have been linked with health issues due to their toxic or carcinogenic nature [11]. Naphthalene, the simplest PAH, is present in many combustion processes, and can be used as another appropriate and contrasting model compound to study the removal of VOCs from waste streams [12].

VOC abatement techniques can be achieved in many ways, such as destructive techniques like thermal and catalytic oxidation or by recovery methods such as adsorption and absorption processes [13,14]. Of the methods mentioned, catalytic oxidation has been identified as a more efficient way to remove VOCs from the atmosphere. This process is less complex when compared with adsorption and absorption techniques, where recovery of VOCs and replacement of material used can become expensive [13]. In addition, compared to thermal oxidation, catalytic oxidation is less energy intensive, whilst also having the benefit of producing more environmentally benign products compared with toxic by-products often created by thermal oxidation [15]. However, a slight drawback for catalytic oxidation is the dependence on the conditions used. Previous literature has shown that catalyst deactivation can occur when poison compounds, such as water vapour or sulphur, are present in waste streams [16,17]. This issue further highlights the importance of research in this area.

Supported noble metal catalysts containing Pd and Pt have been widely reported as active catalysts for VOC oxidation [5,18]. More recently, there has been a driving force to move towards the use of metal oxide catalysts. Metal oxide catalysts have the advantage of being less expensive, more abundant and less susceptible to poisons when compared to precious metal catalysts [19,20]. Moreover, some metal oxide catalysts have shown similar, or even improved activity when compared with precious metal catalysts for VOC oxidation [21,22].

Of the metal oxide catalysts reported in the literature, cerium(IV) oxide (CeO_2) is widely regarded as an effective oxidation catalyst. CeO_2 catalysts have shown remarkable redox properties from the facile shift between $Ce^{4+} \leftrightarrow Ce^{3+}$ in the redox cycle [23]. In addition, CeO_2 exhibits a high oxygen storage capacity (OSC) and can form oxygen defects, which enable enhanced oxygen mobility through the lattice [24–26]. Intrinsic defects present in CeO_2 catalysts occur by two predominant pathways, either from the displacement of ions in the lattice to an interstitial site, or by oppositely charged ions leaving the lattice sites. These are referred to as Frenkel and Schottky defects respectively [27]. Extrinsic defects can also be promoted in CeO_2 catalysts by the addition of impurities, such as the addition of aliovalent ions to the lattice [28]. These characteristics have made CeO_2 catalysts the preferred choice for various oxidation reactions [26,29–31]. Studies on the morphology of CeO_2 catalysts have also been carried out to selectively control the exposed facets, which has led to improved surface interactions and catalytic activity for various oxidation reactions [25,32,33]. The structure and transformation of cerium precursors to form CeO_2 have been studied in the literature, but few consider the catalytic uses for these materials and only focus on the different characteristics of the final CeO_2 materials [34]. Recent research on the influence of the cerium precursor when producing CeO_2 catalysts have mainly been studied in the context of mixed metal oxides [35–37], but single oxide CeO_2 has rarely been investigated.

The use of different synthesis routes for catalyst preparation can drastically influence the activity trends for various reactions [38]. Altering factors, such as preparation method and calcination conditions, have resulted in varied catalyst characteristics, which can improve activity [29]. Using precipitation as a synthesis method allows for the careful control of synthesis parameters like pH, aging time, solution concentrations, addition rate and precipitating agent. However, the influence of the metal precursor can sometimes be overlooked. To this effect, precipitation methods can be utilised as a reproducible procedure to compare slight changes to the preparation method, and how these impact the final catalyst characteristics.

In this work, CeO_2 catalysts were prepared by a co-precipitation method, using either $(NH_4)_2Ce(NO_3)_6$ or $Ce(NO_3)_3$ as the precursor cerium source. The precipitate formation and resulting catalyst characteristics were compared for each precursor. Catalysts were characterised by Thermal gravimetric – Differential thermal analysis (TG-DTA), Powder X-ray diffraction (XRD), Laser Raman spectroscopy, X-ray photoelectron spectroscopy (XPS), Temperature programmed reduction (TPR), Electron microscopy (TEM/SEM-EDX), and Brunauer-Emmett-Teller (BET) surface area analysis. Catalysts were evaluated for the oxidation of model VOCs, focusing on the impact the cerium precursor had on catalytic activity and how this was related to the structure, redox properties, and surface state of the CeO_2 catalysts. Testing conditions for VOC total oxidation were also evaluated, by including water vapour, a known catalyst poison, to the feed.

3.2 Effect of cerium precursor

3.2.1 Precursor characterisation

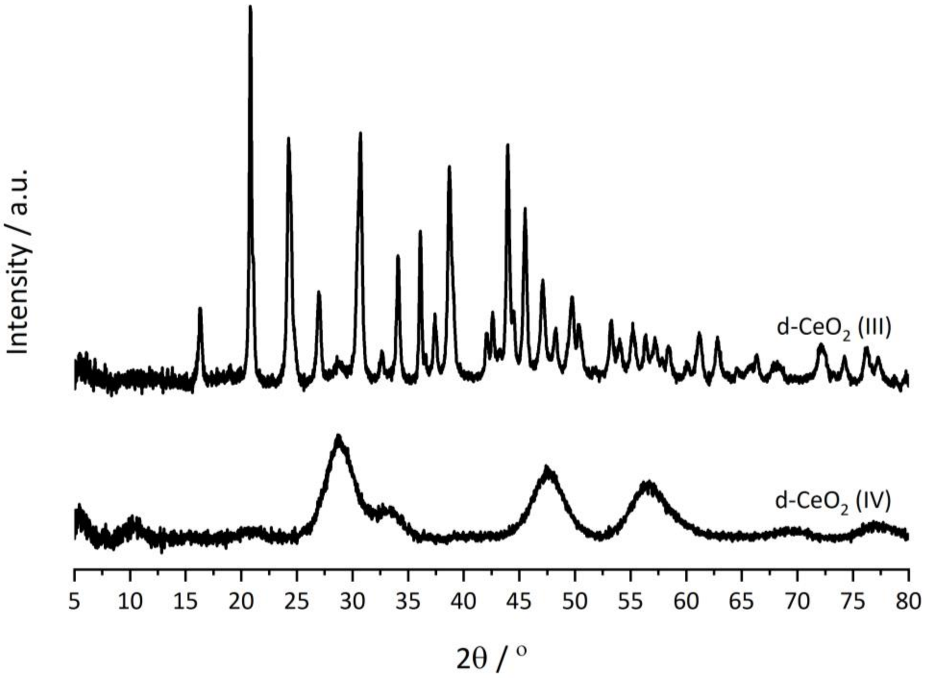

Figure 1: XRD patterns for the Ce^{IV} and Ce ^{III} precipitate precursors prior to calcination

Dried catalyst precipitate precursors, denoted as d-CeO$_2$ (IV) or (III), were analysed using powder XRD (Figure 1), with significant differences shown between the two precipitates. The d-CeO$_2$ (IV) sample showed a structure representative of a cubic fluorite CeO$_2$ phase with low crystallinity, exhibiting broad reflections around 29°, 33°, 47° and 57°, corresponding to (111), (200), (220) and (311) lattice planes, respectively [39]. Whereas the d-CeO$_2$ (III) sample predominantly exhibited reflections representative of an orthorhombic Ce$_2$(OH)$_2$(CO$_3$)$_2$.H$_2$O structure [40], with other additional reflections identified as hexagonal Ce(OH)(CO$_3$) [39]. Hence, under these synthesis conditions, the Ce^{IV} and Ce^{III} precursors followed two different chemical precipitation mechanisms.

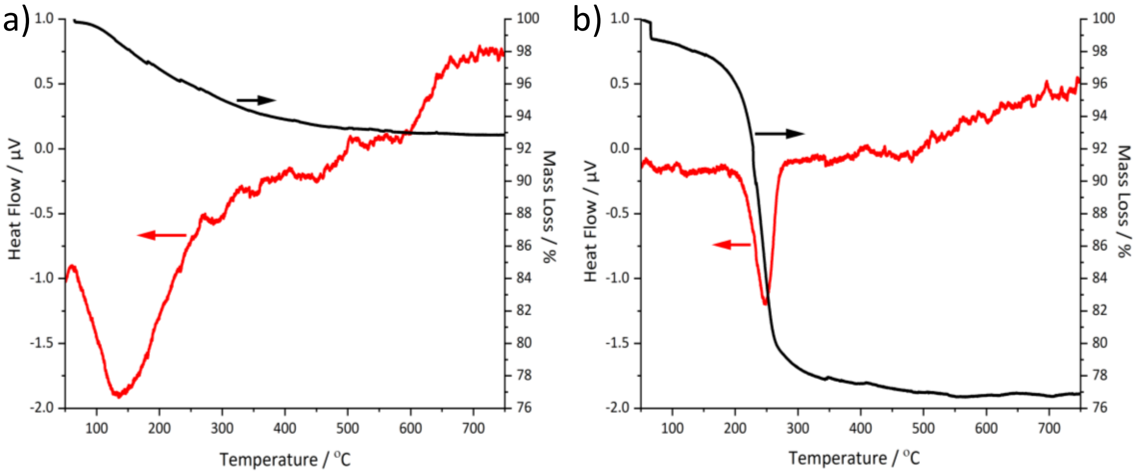

Figure 2: TG-DTA of the precipitated catalyst precursors: a) d-CeO_2 (IV) and b) d-CeO_2 (III). Samples heated under flowing air from 50 to 750 °C at 5 °C min^{-1}.

Thermal decomposition of the precipitates was analysed using TG-DTA (Figures 2a and 2b). Around 7% mass loss was observed from the d-CeO_2 (IV) sample (Figure 2a) over the temperature range of 100-700°C. In comparison, the d-CeO_2 (III) sample showed a mass loss of 23% over the same temperature range, with a small decrease around 70°C, followed by a sharp decrease between 250-300°C. These mass loss stages were associated with the evolution of H_2O species and decomposition of carbonate species from the dried sample respectively; confirming conclusions drawn from XRD analysis (Figure 1), that the precipitate formed from the Ce^{III} precursor was a $Ce(CO_3)_x(OH)_y$ type species [41]. Moreover, the endothermic peak around 250°C (Figure 2b), characterised by DTA, was attributed to the liberation of CO_2 from the decomposition of carbonate species [42]. The broad endothermic peak observed between 50-250°C, in the d-CeO_2 (IV) sample, can be attributed to the evolution of H_2O.

Previous work carried out by Hirano *et al.* looked at the precipitation mechanism of different Ce^{IV} and Ce^{III} precursors using urea, prepared by a hydrothermal synthesis [43,44]. They discovered that when using the Ce^{IV} precursor, hydrated $[Ce(OH)(H_2O)_n]^{4+}$ ions were formed as a result of the ability to undergo strong hydration from the lower basicity and higher charge of the Ce^{4+} ion. This caused hydrated CeO_2 nanoparticles ($CeO_2.nH_2O$) to precipitate before the carbonate could react to form the $Ce(CO_3)_x(OH)_y$ type species. Further evidence of hydrated CeO_2 nanoparticle formation, from the hydrolysis of ammonium cerium nitrate in aqueous solution without the addition of a base, has also been documented by Pettinger *et al.* [45]. Data acquired by TG-DTA and XRD analysis for the d-CeO_2 (IV) sample is in good agreement with these conclusions drawn from the literature.

Furthermore, this effect was not observed when using different Ce^{III} precursors, and the products formed were the carbonates, either $Ce_2O(CO_3)_2.H_2O$ or $Ce(OH)CO_3$ [43].

Based on the assumption that stoichiometric CeO_2 was the final product, the theoretical mass losses were calculated for each thermal decomposition, using bulk precipitate phases identified from XRD.

$$Ce_2(OH)_2(CO_3)_2.H_2O \longrightarrow 2CeO_2$$

$$CeO_2.nH_2O \longrightarrow CeO_2$$

For the Ce^{III} precursor, the theoretical mass loss was calculated to be 24% which is in good agreement with the 23% experimental loss identified by TG-DTA analysis. From the XRD data, when using the Ce^{IV} precursor, the formation of hydrated CeO_2 particles in solution was the only product formed. Therefore, a mass loss of 7% equated to 0.67 H_2O.

3.2.2 Catalyst characterisation

Table 1: Physiochemical properties of the calcined CeO_2 (IV) and CeO_2 (III) catalysts.

Catalyst	Surface Area / $m^2 g^{-1}$	Position of Ce (111) reflection / °	Average Crystallite Size / nm	Lattice Parameter / nm	A_{590}/A_{463}	FWHM
CeO_2 (IV)	81	28.56	8.7	0.5409	0.018	17.8
CeO_2 (III)	19	28.57	9.3	0.5408	0.019	17.6

A summary of the physiochemical properties of the two calcined CeO_2 catalysts is presented in Table 1. The catalyst surface areas, analysed by the BET method, were significantly different for the two catalysts. The CeO_2 (IV) catalyst displayed a surface area roughly four times larger than CeO_2 (III) (81 m^2g^{-1} vs 19 m^2g^{-1}, Table 1). The adsorption-desorption isotherms for the two catalysts (Figures 3a and 3b), indicated diverse pore structures. Both plots represented a type IV isotherm, indicative of a mesoporous type structure, with the CeO_2 (IV) catalyst having a H2 hysteresis loop [46]. This type of hysteresis is indicative of capillary condensation in disordered and ill-defined pore structures, suggesting a higher porosity, which would be consistent with the higher surface area shown for this catalyst. In contrast, the CeO_2 (III) catalyst showed a H3 hysteresis loop which is related to the formation of non-rigid, plate-like particles that form a disordered pore structure with slit-shaped pores [46]. In addition, hysteresis of this kind is linked with the incomplete filling of macropores, suggesting a higher concentration of macropores in this catalyst [47]. It could be postulated that the liberation of CO_2 from the d-CeO_2 (III) precipitate, upon calcination, resulted in these larger pore structures identified by the adsorption-desorption isotherm. Furthermore, the low surface area of the CeO_2 (III) catalyst could be linked to the inaccessibility of these pores created by the calcination of the $Ce(OH)_x(CO_3)_y$ precipitate. Previous studies have also shown a relationship between the different hysteresis loops obtained and varying surface area for CeO_2 catalysts [48].

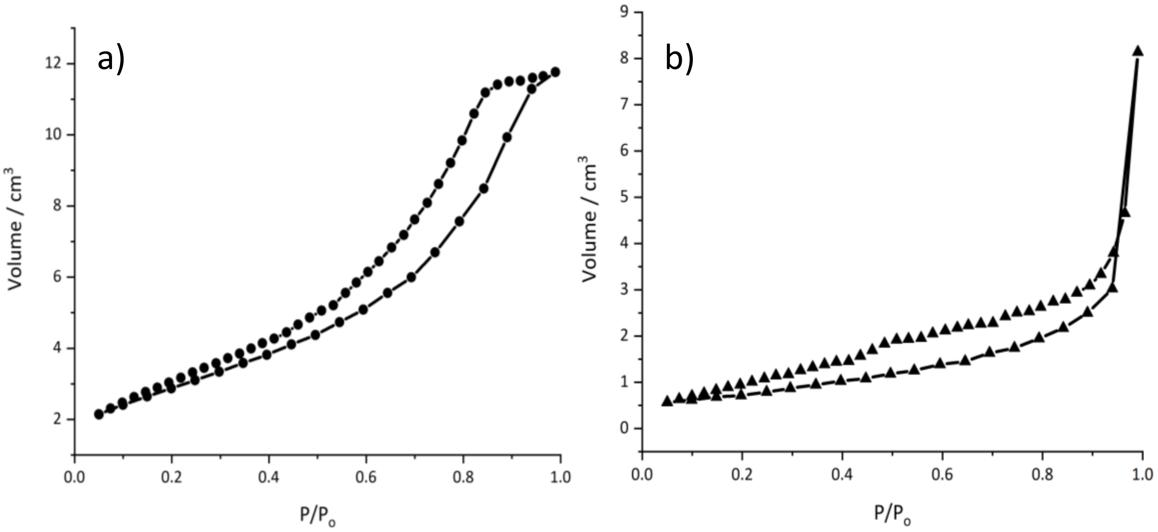

Figure 3: N_2 Adsorption–desorption isotherms of a) CeO_2 (IV) and b) CeO_2 (III) catalysts.

SEM images (Figures 4a and 4b) indicated different morphologies of the catalysts. Information obtained by this technique helps to rationalise the surface area and adsorption-desorption isotherm data previously discussed. The CeO_2 (III) catalyst displayed clumped aggregates with platelet or needle-like structures, which is representative of the H3 hysteresis loop; whereas, the CeO_2 (IV) catalyst formed large, well-defined particles. From the XRD and TG-DTA characterisation of the precipitates formed during the synthesis, it can be suggested that the formation of the $Ce_2(OH)_2(CO_3)_2.H_2O$ type species ensures the transformation to these type of non-rigid aggregates identified for CeO_2 (III). In contrast, forming the $CeO_2.nH_2O$ precipitate leads to the formation of well-defined structures shown for CeO_2 (IV).

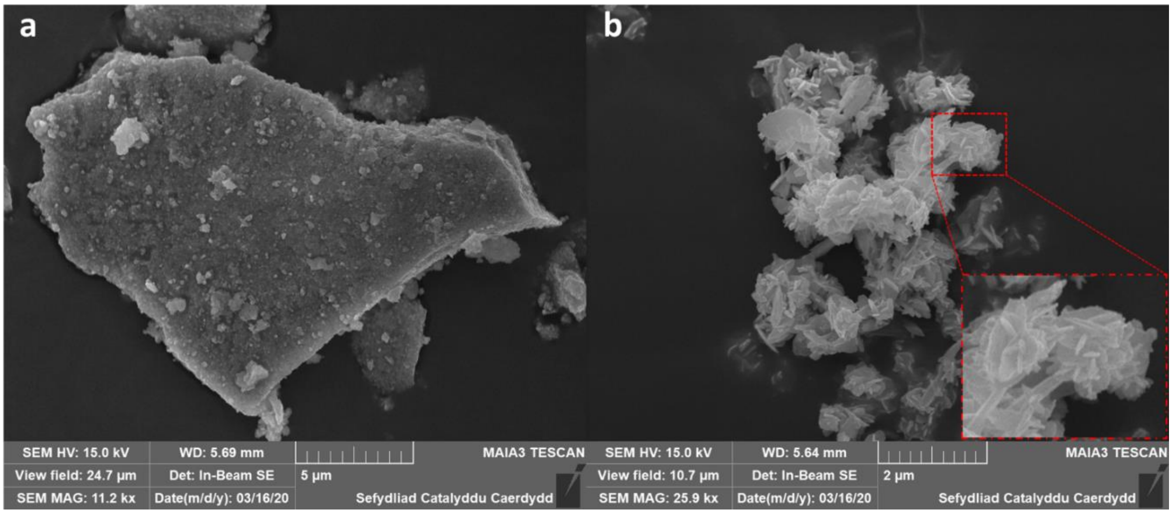

Figure 4: SEM images of the a) CeO_2 (IV) and b) CeO_2 (III) catalysts. Inset shows magnification of platelet morphology.

TEM images (Figure 5a-f) expand upon conclusions drawn from the SEM data. Differences in large scale microstructure morphology were apparent between the CeO_2 (IV) and CeO_2 (III) catalysts (Figures 5a and 5d), which was identified by SEM analysis. However, the small scale nanostructure morphology appeared similar (Figures 5b and 5e). Both CeO_2 (IV) and CeO_2 (III) samples showed agglomerated, small facetted CeO_2 nanoparticles of 8-10 nm, consistent with the crystallite size determined by XRD (Table 1). The interplanar distances measured on the CeO_2 (IV) and CeO_2 (III) catalysts (Figures 5c and 5f) were 0.31 nm which is representative of the (111) lattice planes, indicating their preferential exposure.

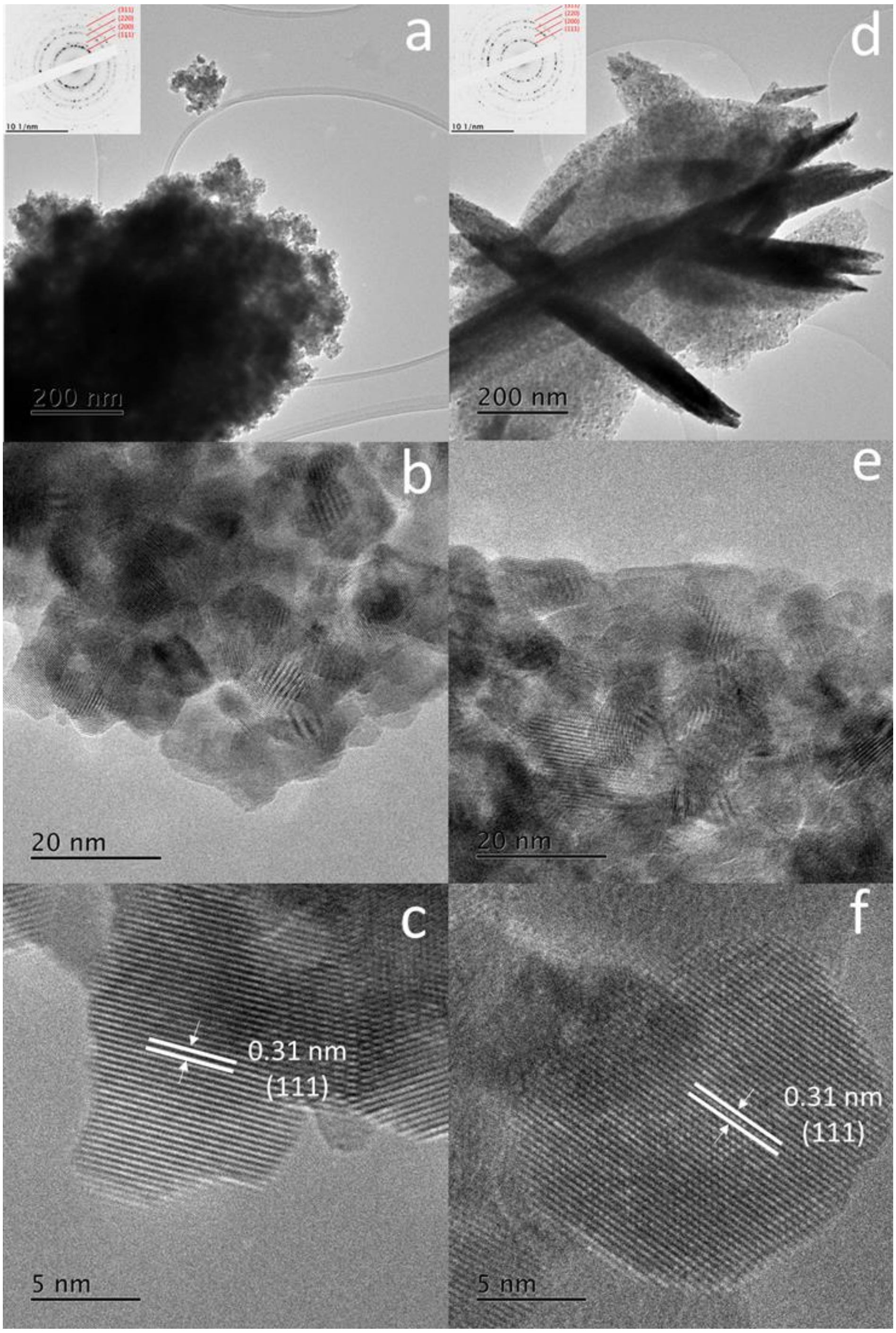

Figure 5: TEM images of a-c) CeO₂ (IV) and d-f) CeO₂ (III) catalysts. Inset shows selected area electron diffraction patterns of a) CeO₂ (IV) and d) CeO₂ (III)

Data acquired from XRD analysis of the calcined catalysts (Figure 6) indicated a similar bulk structure for both catalysts. XRD patterns of the catalysts only showed the cubic fluorite structure of CeO_2, with lattice parameters of both catalysts within experimental error (Table 1). The similar lattice parameters illustrate that both CeO_2 (IV) and CeO_2 (III) had little distortions to the cubic lattice. This cubic fluorite structure is also consistent with the structure identified by selected area electron diffraction (SAED) analysis (Figures 5a and 5d). The crystallite sizes were calculated using the Scherrer equation by taking an average of the values obtained by analysing the peak widths of the 4 dominant (111), (200), (220), and (311) reflections. The sizes calculated were similar for both catalysts, with the CeO_2 (IV) catalyst having a slightly smaller crystallite size on average (8.7 nm verses 9.3 nm, Table 1). However, the average crystallite sizes calculated were within the experimental error (±1.2 nm), hence little significant difference was identified. Crystallite sizes determined by this method are also in agreement with TEM data. Previous literature has shown an inverse relationship between particle size and catalyst surface area [49]. This relationship usually relates decreasing particle size to increasing surface area, but this was not reciprocated by the data presented in Table 1. Both catalysts had a similar particle size but largely varying surface areas, which complements ideas drawn from the adsorption-desorption isotherms suggesting that the diverse pore structures caused the different surface areas observed.

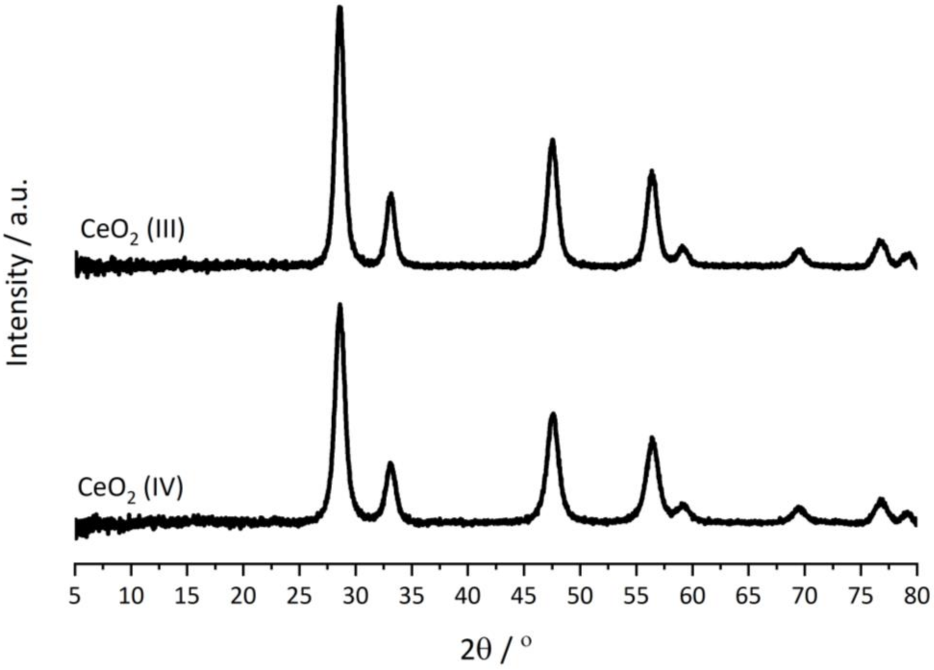

Figure 6: XRD patterns of the calcined CeO_2 (IV) and CeO_2 (III) catalysts.

It is well established in the literature that CeO_2 catalysts exhibit an intense Raman band around 460 cm^{-1}, relating to the F_{2g} vibrational mode, which corresponds to the symmetrical stretching of the $Ce-O_8$ local structure [50]. Other weaker bands are also active for these materials, such as a band around 600 cm^{-1}, which is commonly associated with the presence of intrinsic defect sites [51]. These types of defects are thought to be either Frenkel or Schottky defects, which can allow for more facile oxygen mobility throughout the lattice [24]. It has been previously established that the ratio of the defect band and F_{2g} vibrational band can be used to estimate the concentration of defect sites in the material, which can then be used to understand the redox properties and oxygen mobility through the lattice of CeO_2 catalysts [52]. This factor is especially important for propane and naphthalene total oxidation as it is proposed these reactions take place *via* a Mars-van Krevelen mechanism over metal oxide catalysts [19]. The Raman spectra shown in Figure 7 matches that of the cubic fluorite CeO_2 structure, consistent with that determined by XRD. The intense band at 463 cm^{-1} showed the F_{2g} vibrational mode, and a small band around 590 cm^{-1} indicated the presence of defect species. The ratio of bands at 590 cm^{-1} and 463 cm^{-1} (A_{590}/A_{463}, Table 1) were very similar for both catalysts, implying the bulk defect concentrations of both catalysts, detectable by Laser Raman spectroscopy, were similar. Furthermore, the full width half maximum (FWHM) of the F_{2g} vibrational band has also been related to the concentration of defects within the material [52,53]. However, this measurement can also be influenced by the crystallinity and crystallite size of CeO_2, usually identified by XRD analysis [54]. Table 1 shows the FWHM of both catalysts being very similar, further endorsing the similarities in bulk defect concentration and crystallite size identified.

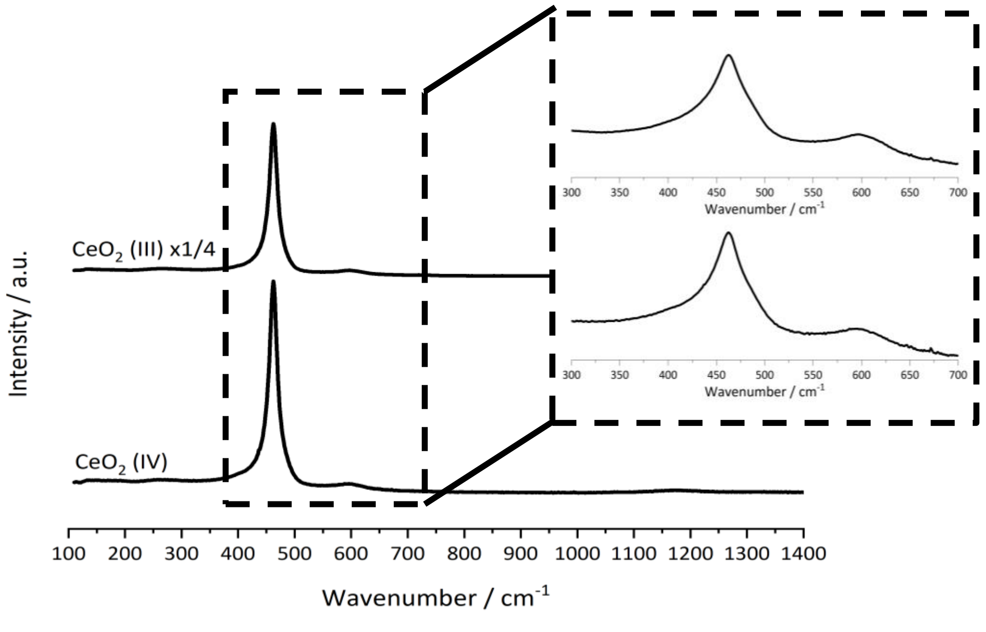

Figure 7: Laser Raman spectra of the CeO_2 (IV) and CeO_2 (III) catalysts. Inset shows magnification of the defect band around 590 cm^{-1}.

TPR profiles of the catalysts (Figure 8) only showed one main reduction peak over the temperature range analysed. This peak occurred at 478°C for CeO_2 (III) and 498°C for CeO_2 (IV). From previous literature, it is known that CeO_2 has two main types of reduction features, these being the reduction of surface species and the reduction of bulk species [55]. Bulk reduction has been shown to occur at temperatures above 700°C, whilst surface reduction occurs around 500°C [56], therefore, the reduction peak present in the TPR profiles were related to the surface reduction of these materials. H_2 consumption normalised for surface area and mass are shown in Table 2 for both catalysts. The CeO_2 (III) catalyst displayed a higher H_2 consumption normalised for surface area compared with CeO_2 (IV). Whilst both catalysts exhibited good redox ability, the combination of the lower reduction temperature and higher H_2 consumption per surface area suggests the CeO_2 (III) catalyst had a more facile surface reduction, with reduction occurring to a greater extent. These differences in redox properties, could possibly arise as a result of different structures produced by the varying precipitation mechanisms and subsequent transformation into the CeO_2 catalysts.

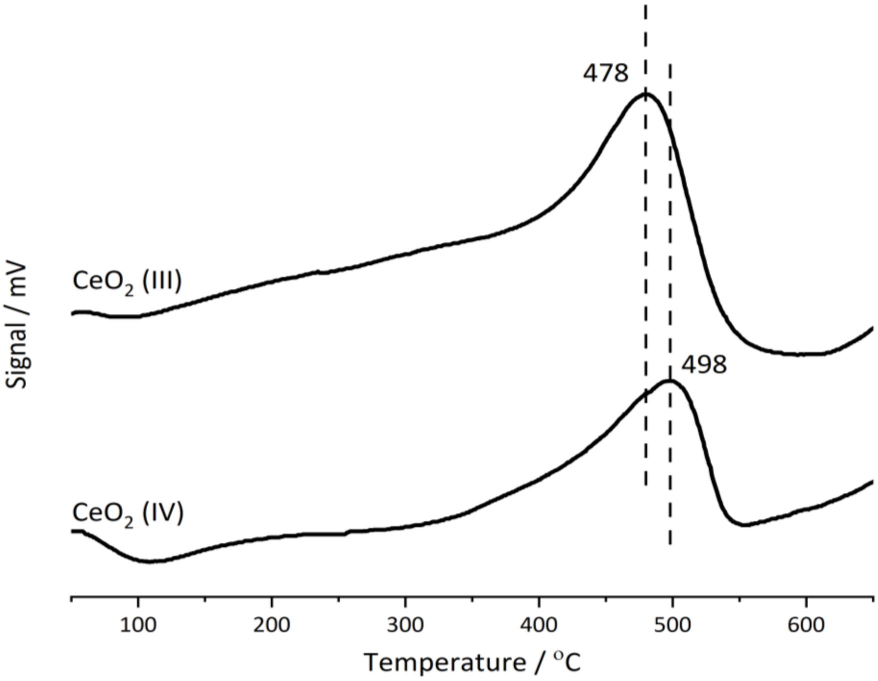

Figure 8: TPR profiles of the CeO_2 (IV) and CeO_2 (III) catalysts. Conditions: 10% H_2/Ar, 30 mL min^{-1}, 50–700 °C at 10 °C min^{-1}.

Table 2: Mass and surface area normalised H_2 consumption for the CeO_2 (IV) and CeO_2 (III) catalysts, determined from TPR-TPO cycles.

Catalyst	TPR Cycle	H_2 Consumption per surface area /µmol m^{-2}	H_2 Consumption per mass /µmol g^{-1}
CeO_2 (IV)	1	0.435	35.20
	2	0.145	11.73
CeO_2 (III)	1	4.575	86.93
	2	0.464	8.81

The dynamic oxygen storage capacity (OSC) of the catalysts were assessed by performing TPR-TPO cycles. Data in Table 2 shows that upon re-oxidising and then reducing the catalysts, the H_2 consumption for the CeO_2 (III) catalyst decreased significantly. The H_2 consumption per surface area showed a decrease by a factor of 10 for the CeO_2 (III) catalyst, whilst the decrease was only 3-fold for the CeO_2 (IV) catalyst. As the oxidation of propane and naphthalene is proposed to occur *via* a Mars-van Krevelen mechanism [19], which is influenced by the redox ability of the catalyst, it can be suggested that the re-oxidation of the catalyst is also an important factor [55]. As the re-oxidation step is not taken into account under the 1st TPR conditions, it may not be entirely representative of the redox properties of the catalyst under reaction conditions. However, previous research has also shown a correlation between decreased surface area and low surface reducibility of CeO_2 catalysts, which could have occurred to a greater extent for CeO_2 (III), as a result of sintering at higher treatment temperatures [56,57]. Therefore, only tentative conclusions can be drawn from these data.

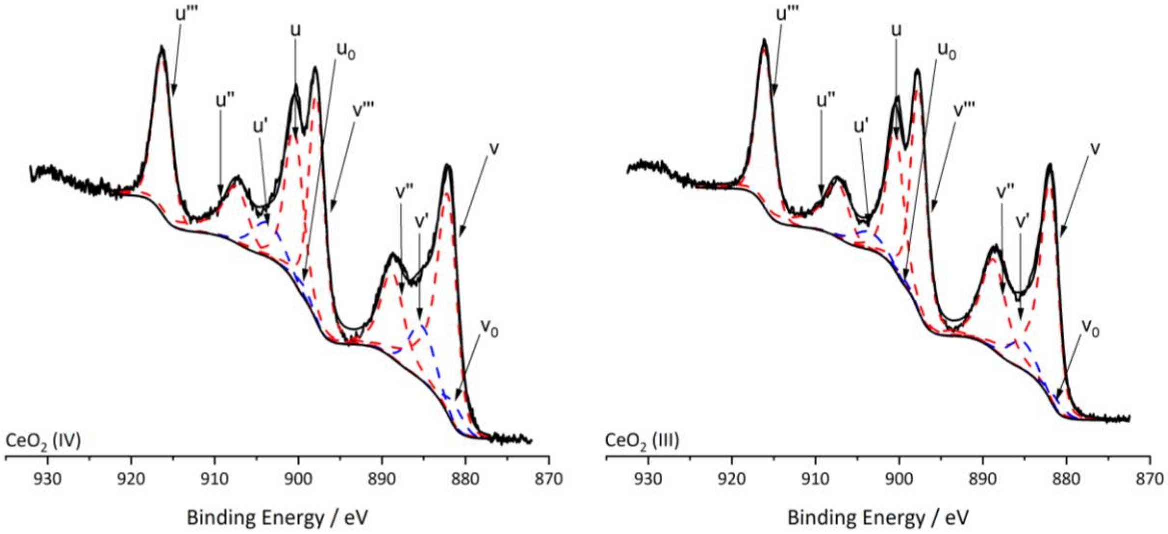

Figure 9: XPS spectra of Ce 3d region for the CeO_2 (IV) and CeO_2 (III) catalysts. Fitted peaks refer to Ce^{3+} (blue) and Ce^{4+} (red) states

Figure 9 details the core-level Ce 3d photoelectron spectra for both CeO_2 (III) and CeO_2 (IV) catalysts. It is understood in the literature that a large number of final states arise from photoemission of CeO_2, causing the Ce 3d XPS spectra to be difficult to analyse. However, it is generally accepted a total of 10 peaks are present for CeO_2, relating to the Ce $3d_{5/2}$ and Ce $3d_{3/2}$ splitting of mixed III/IV states [58]. These peaks are divided into Ce^{3+} oxidation states denoted as v_0, v', u_0, u' and Ce^{4+} oxidation states denoted as v, v'', v''', u, u'', u''' [59]. It is proposed in the literature that the higher concentration of Ce^{3+} surface species directly relates to an increased amount of surface defect sites, which have been shown to affect catalytic activity [33,52,55,60]. The ratio of surface Ce^{3+} to Ce^{4+} was calculated using the sum of the integrated peak areas of each relative fitting for the two oxidation states (Table 3). The CeO_2 (IV) catalyst showed a higher concentration of reduced Ce^{3+} species, which is initially counterintuitive when using the $(NH_4)_2Ce(NO_3)_6$ precursor with cerium in the 4+ oxidation state. The higher concentration of Ce^{3+} species identified suggests an initially more reduced surface for the CeO_2 (IV) catalyst which could explain the lower H_2 consumption measured by TPR analysis.

Table 3: XPS and EDX analysis derived surface elemental composition for the CeO_2 catalysts.

Catalyst	XPS Ce:O:Na Ratio	O^{β}/O^{α} Ratio	Ce^{3+}/Ce^{4+} Ratio	EDX Ce:O:Na Ratio
CeO_2 (IV)	29:68:3	0.438	0.155	30:68:2
CeO_2 (III)	22:67:11	0.289	0.086	34:59:7

From the O 1s core-level XPS spectra (Figure 10), two distinct oxygen species can be extracted, which were ascribed as O^{β} (531 eV) and O^{α} (529 eV) states, reported to be characteristic of defect oxygen and lattice oxygen species respectively [52,61]. Labelling of the O^{β} region has little consensus in the literature as it has been proposed that this region could also relate to the presence of hydroxyl or carbonate oxygen species [52]. Furthermore, other researchers have linked this region to the appearance of low co-ordination oxide ions [61,62]. As a result, the species represented by the O^{β} region have been referred to as surface oxygen defect sites, with the fitting around 532-533 eV (orange curve, Figure 10) tentatively attributed to the presence of OH species [63,64]. The ratio of O^{β}/O^{α} (Table 3) indicated the CeO_2 (IV) catalyst had an increased concentration of surface oxygen defect sites compared to the CeO_2 (III) catalyst. These data are consistent with the higher quantity of Ce^{3+} determined by XPS analysis of the Ce 3d region for this catalyst. The surface oxygen defect concentration trend differs to that of the bulk defect concentration, analysed by Laser Raman spectroscopy, suggesting the different defect concentrations were highly localised on the catalyst surface, due to the surface sensitivity of XPS. It is noted in the literature that the presence of surface oxygen defect sites are important for VOC oxidation reactions as they produce active oxygen species that can participate in the reaction [55,60,65]. Previous studies have shown that these active oxygen species can facilitate the facile breaking of C-H bonds which then correlates to improved catalytic activity [66,67].

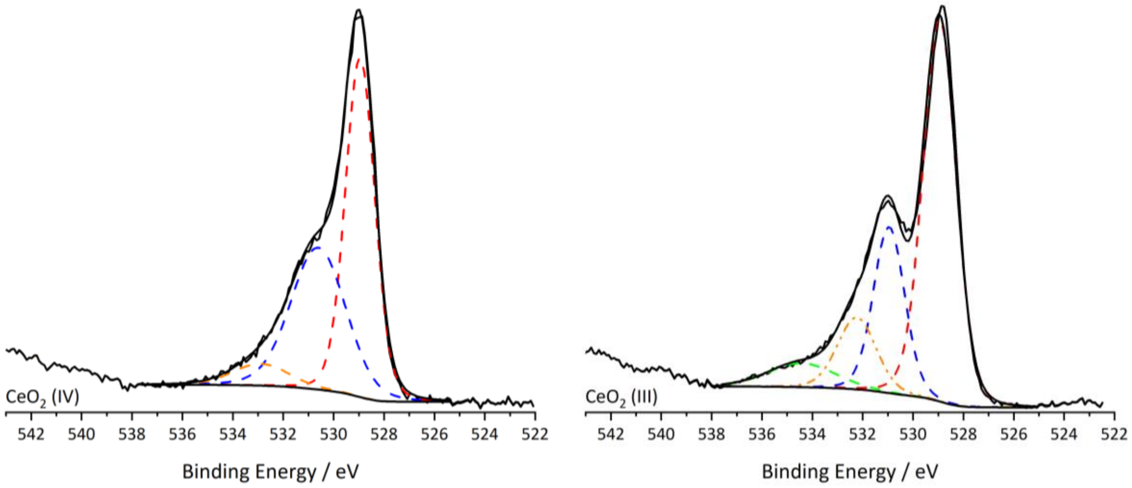

Figure 10: XPS spectra of O 1s region for the CeO$_2$ (IV) and CeO$_2$ (III) catalysts. Fitting shows the O$^{\alpha}$ (red), O$^{\beta}$ (blue) oxygen species as described in the main text, with orange and green fittings referring to the overlapping hydroxyl and Na Auger peaks.

In addition to using XPS analysis to identify cerium and surface oxygen species, it was also used to identify other surface species that could be present. Alkali metals, such as Na, present from the synthesis process utilising Na_2CO_3, have been proposed to deactivate metal oxide catalysts for certain oxidation reactions [68]. From the XPS data (Table 3), the surface content of Na was increased on CeO$_2$ (III) compared with CeO$_2$ (IV). This is also evidenced by the appearance of the Na Auger signal (green curve, Figure 10) in the O 1s spectra for CeO$_2$ (III). Moreover, EDX images (Figure 11a and 11b) showed that both catalysts exhibited Na homogeneously distributed throughout the catalyst. Quantification by both XPS and EDX analysis were consistent (Table 3), with the CeO$_2$ (III) catalyst showing increased Na content.

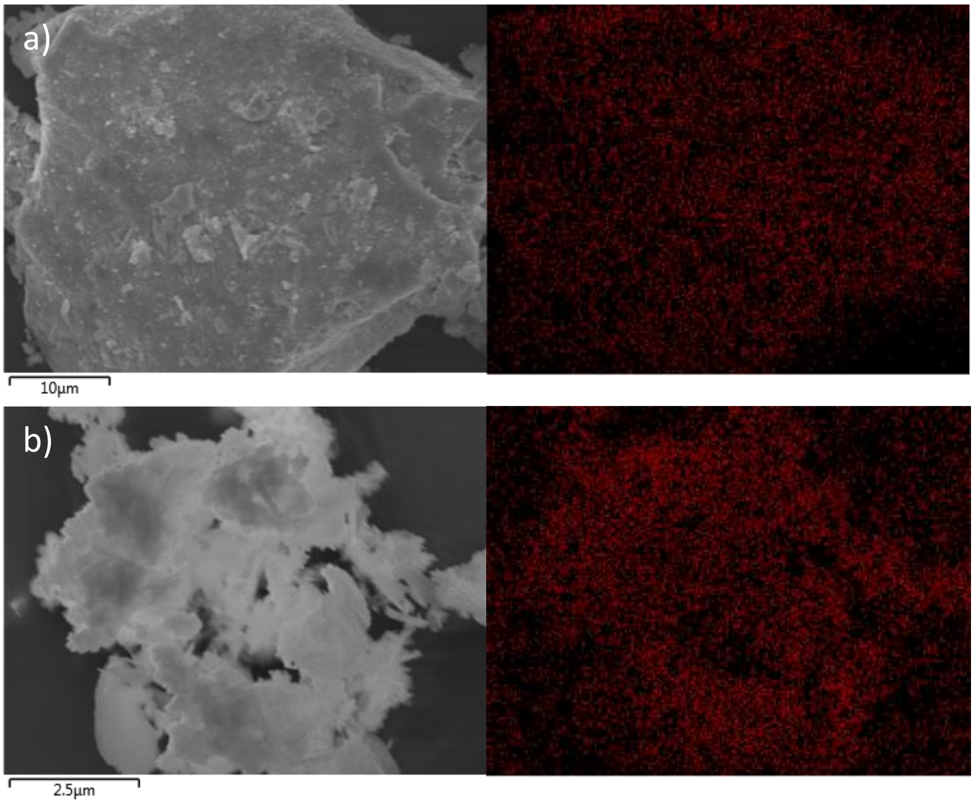

Figure 11: SEM images and corresponding Na Kα EDX mapping of the a) CeO_2 (IV) and b) CeO_2 (III) catalysts

3.2.3 Catalyst testing

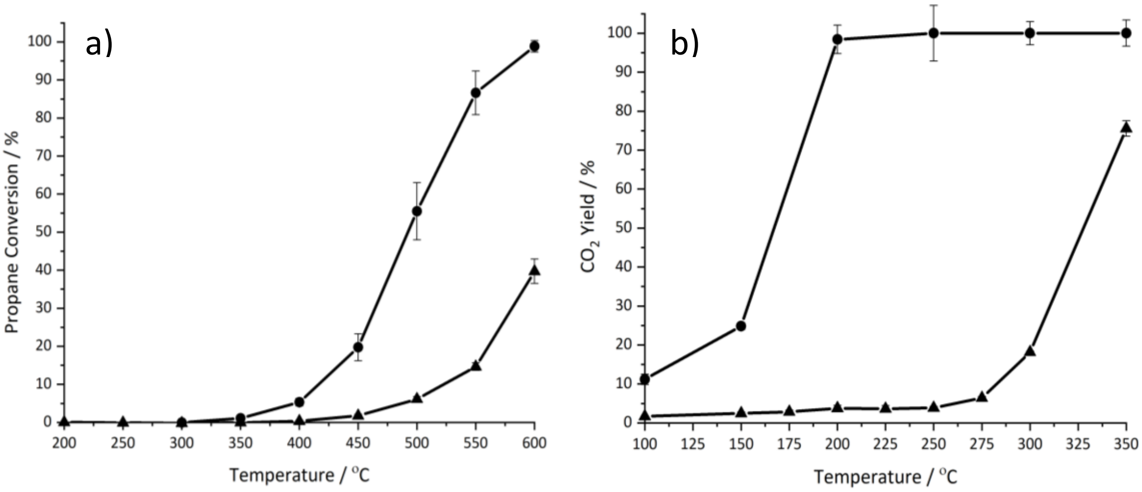

Figure 12: Catalyst activity for a) propane and b) naphthalene total oxidation: (Circle) CeO_2 (IV) and (Triangle) CeO_2 (III). Conditions: 5000 ppm propane in air, GHSV = 45000 h^{-1}. 200 ppm naphthalene in 20% O_2/He, GHSV = 45000 h^{-1}.

The catalyst performance for the total oxidation of propane and naphthalene are shown in Figures 12a and 12b respectively, for the CeO_2 (IV) and CeO_2 (III) catalysts. The main reaction product detected for both reactions was CO_2. For propane oxidation, the carbon balance of both catalysts was >98%. Selectivity to CO_2 was >99% across the temperature range for CeO_2 (IV), whilst at 550°C it was 96% for CeO_2 (III) due to the formation of propene. It is clear in both reactions that the CeO_2 (IV) catalyst was more active for propane and naphthalene total oxidation. Contrary to the reaction data in Figure 12a, data shown in Table 4 indicates that, when normalised for surface area, CeO_2 (III) was more active for propane total oxidation. No significant difference was evident for surface normalised activity with regard to naphthalene total oxidation (Table 5). Whilst the surface normalised activity is discussed when understanding the characteristics responsible for the catalytic activity noted in both reactions throughout this section; it should be recognised that, as a result of the very different conversions obtained by the different catalysts, these data should be used tentatively.

Table 4: Mass and surface area normalised catalytic activity of the CeO_2 (IV) and CeO_2 (III) catalysts for propane total oxidation.

Catalyst	**Propane Conversion / %**	**Surface Area Normalised Propane Oxidation[a] /mol s^{-1} m^{-2}**	**Mass Normalised Propane Oxidation[a] /mol s^{-1} g^{-1}**
CeO_2 (IV)	45	$3.78x10^{-3}$	$3.06x10^{-1}$
CeO_2 (III)	6	$7.10x10^{-3}$	$1.35x10^{-1}$

a – Measured at 500°C

From the bulk characterisation techniques, such as XRD and Laser Raman spectroscopy, both catalysts exhibited the common cubic fluorite CeO_2 structure. In addition, the lattice parameter, average crystallite size and bulk defect concentration calculated using these characterisation methods showed little significant difference. Whilst changes in large-scale morphology were identified by TEM (Figure 5c and 5f) and SEM, the small-scale nanomorphology for both catalysts were similar, with the (111) lattice plane preferentially exposed for both catalysts. Therefore, it can be concluded that no significant differences in bulk structure could be distinguished for both CeO_2 (IV) and CeO_2 (III).

Table 5: Mass and surface area normalised catalytic activity of the CeO_2 (IV) and CeO_2 (III) catalysts for naphthalene total oxidation.

Catalyst	**Naphthalene Conversion / %**	**Surface Area Normalised Naphthalene Oxidation[a] /mol s^{-1} m^{-2}**	**Mass Normalised Naphthalene Oxidation[a] /mol s^{-1} g^{-1}**
CeO_2 (IV)	25	$7.54x10^{-5}$	$6.11x10^{-3}$

CeO_2 (III)	2	$7.19\text{x}10^{-5}$	$1.37\text{x}10^{-3}$

a – Measured at 150°C

The resulting surface areas, from the calcination of the different precipitate precursors, were very influential when understanding the catalytic activity for both propane and naphthalene total oxidation. It has been well documented by various researchers that the high surface area of CeO_2 is a key factor for improved catalytic activity for naphthalene total oxidation [29,69,70]. The data obtained for naphthalene total oxidation was concurrent with conclusions presented by other researchers, with the high surface area CeO_2 (IV) catalyst being more active compared with CeO_2 (III). Furthermore, when normalised for surface area, the activity was similar for both catalysts, suggesting the most significant parameter affecting naphthalene total oxidation was the catalyst surface area. The CeO_2 (IV) catalyst, with higher surface area, was also more active for propane total oxidation as shown in Figure 12a. Previous literature has suggested the increased surface area of CeO_2 catalysts results in a higher quantity of accessible active sites for propane oxidation, which then results in improved catalytic activity [71,72]. When assessing the surface normalised activity for propane total oxidation, the CeO_2 (III) catalyst showed significantly higher activity than CeO_2 (IV). This suggests the decreased surface area significantly limited the overall activity of the CeO_2 (III) catalyst under the reaction conditions but it was not the only factor that influenced catalytic activity. In fact, the mass normalised activity shows that CeO_2 (IV) was roughly 2 times more active but has a surface area 4 times higher than CeO_2 (III), further contributing to the idea that the relationship between catalytic activity and surface area was not direct for propane total oxidation.

Redox properties of CeO_2 catalysts are known to be important for oxidation reactions that occur *via* a Mars-van Krevelen mechanism [11,73,74]. It has been stated in the literature that there is a relationship between more facile reducibility of metal oxide catalysts and improved catalytic activity for propane total oxidation [11]. As discussed, the ability to easily remove active oxygen from the catalyst surface facilitates C-H bond activation, which is known to be the rate determining step for propane oxidation [75]. The CeO_2 (IV) catalyst performed much better for propane total oxidation, initially suggesting that the redox properties were not a significant factor for these catalysts. However, CeO_2 (III) had an increased surface normalised activity which corresponds with the improved redox properties of this catalyst. This may suggest the enhanced redox behaviour of the CeO_2 (III) catalyst became insignificant as a consequence of the low total surface area when compared with the CeO_2 (IV) catalyst. The low surface area of the catalyst could also inhibit the re-oxidation step of the reaction which would help rationalise results from the TPR-TPO data. Similarly to the lower surface area correlating with less surface reduction [56], this could also be the case as less accessible surface sites would be available for re-oxidation. In contrast, the naphthalene total oxidation data showed the surface normalised activity data as comparable, with the CeO_2 (IV) catalyst performing much better in Figure 12b. This implies characteristics other than redox properties were of greater importance for this reaction, which is in good agreement with conclusions drawn by Garcia *et al.* on the correlation between redox properties and the oxidation of propane and naphthalene using various metal oxides [11].

XPS analysis showed that the CeO_2 (IV) catalyst contained a higher proportion of surface oxygen defect sites compared to the CeO_2 (III) catalyst (O_β/O_α, Table 3). A correlation between the amount of surface oxygen defects and improved catalytic activity for propane total oxidation has been shown in previous research [19], and is consistent with the CeO_2 catalysts prepared from the different precursors in the present work. As discussed previously, it is suggested that these surface defect sites promote active oxygen species that facilitate more facile C-H bond cleavage, which improves catalytic activity [67]. For naphthalene oxidation, the CeO_2 (IV) catalyst with a higher quantity of surface oxygen defect sites was also more active, in agreement with other studies that have shown a correlation between activity and surface defect concentration [33]. However, from the surface normalised activity data, this factor seemed to have a much less significant contribution than the catalyst surface areas.

Alkali metals, such as Na, have been shown to poison metal oxide catalysts when used for propane total oxidation, as demonstrated by Tang *et al.* [76]. This occurs by the Na inhibiting the oxygen mobility of the catalyst, which then supresses oxygen desorption at lower temperatures, in addition to accumulating high amounts of surface carbonate species at higher temperatures. The relationship between Na poisoning and the impact of poor oxygen mobility is confirmed in further research for propane total oxidation [77]. The CeO_2 (III) catalyst displayed a higher concentration of bulk and surface Na, as identified by EDX and XPS analysis, whilst performing much worse for propane total oxidation which is consistent with trends discussed in the literature.

Whilst factors such as redox properties and surface oxygen defect concentration of the final catalyst were identified to have some impact on the overall catalytic activity of the CeO_2 catalysts for the total oxidation of propane and naphthalene, it is clear that the most significant influence was the catalyst surface area. Nevertheless, it is important to highlight how these characteristics were determined by the difference in catalyst precursor used, as the relatively subtle change of cerium precursor contributed to the significant differences shown in catalyst performance.

Different precipitation products were formed when using either the Ce^{IV} or Ce^{III} precursors, as shown from the TG-DTA and XRD analysis, but on calcination they formed similar bulk cubic fluorite CeO_2 structures. Forming the $CeO_2.nH_2O$ precipitate resulted in a greatly increased surface area of the resulting CeO_2 (IV) catalyst. This effect has been shown in previous research when synthesising Sm-doped CeO_2 mixed oxide catalysts [78]. Moreover, previous research has drawn similar conclusions, with the Ce^{IV} precursor or the $CeO_2.H_2O$ precipitate resulting in the largest surface area [35,79]. Decomposition of the $CeO_2.H_2O$ precipitate to CeO_2 is likely to be topotactic, with very little alteration to the crystal structure from the removal of H_2O or ^{-}OH species. In contrast, the structure of the orthorhombic $Ce_2(OH)_2(CO_3)_2.H_2O$ precipitate, identified by XRD analysis, differed significantly to the cubic fluorite structure of CeO_2, and decomposition occurs *via* an intermediate oxycarbonate species [42,80]. This phase transformation mechanism will likely be disruptive and result in the decreased surface area shown by the CeO_2 (III) catalyst. Furthermore, transformation of the $Ce_2(OH)_2(CO_3)_2.H_2O$ precipitate to the cubic CeO_2 structure must contain an oxidation step as cerium is in the Ce^{3+} oxidation state. Research conducted by Spiridigliozzi *et al.* suggested that under prolonged hydrothermal conditions, the initially formed metastable $Ce(OH)(CO_3)$ precipitate can oxidise in solution, as well as undergo structural changes [81]. However, XRD data (Figure 1) provided evidence for the formation of the $Ce_2(OH)_2(CO_3)_2.H_2O$ precipitate, suggesting that decomposition of the precipitate by thermal treatment induced the oxidation from Ce^{3+} to Ce^{4+}. Previous studies have confirmed this theory as it has been stated the thermal decomposition of the $Ce(OH)(CO_3).H_2O$ species results in a combination of endothermic decomposition from dehydration and decarbonation, in addition to an exothermic reaction from the oxidation of Ce^{3+} to Ce^{4+} [42]. This exothermic oxidation step could enhance the driving force to form the thermodynamically stable CeO_2 structure with the increased Ce^{4+} surface concentration observed for the low activity CeO_2 (III) catalyst.

3.2.4 Catalyst stability

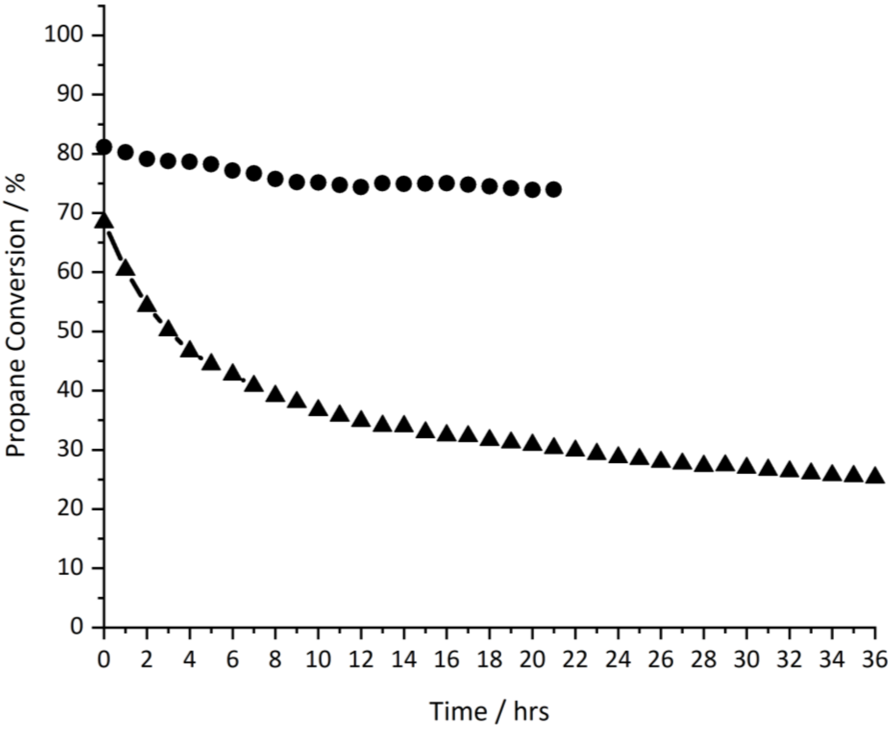

Figure 13: Time on line stability analysis of CeO_2 (IV) (Circle) and CeO_2 (III) (Triangle) for propane total oxidation. Conditions: 5000 ppm propane in air, GHSV = 45000 h^{-1}, 550 °C, 36 hrs.

In addition to catalytic activity, catalyst stability is also another important factor to assess the application of the catalyst. Catalyst stability of CeO_2 (IV) and CeO_2 (III) were assessed by time on line reactions for the total oxidation of propane (Figure 13). The CeO_2 (III) catalyst rapidly deactivated over a 12 h period. This deactivation continued more slowly until the final analysis at 36 h, where the propane conversion decreased to 25 %. In contrast, CeO_2 (IV) showed a much less significant deactivation over a 21 h period, with propane conversion decreasing from 81 % to 74 %. The selectivity to CO_2 was >99% for CeO_2 (IV), whereas selectivity dropped from 98% to 94% for the CeO_2 (III) catalyst, due to propene formation, over the time on line analysis. The large deactivation observed for the CeO_2 (III) catalyst could have occurred as a result of the limited re-oxidation inferred from the TPR-TPO data, which could be a direct result of the lower surface area of the catalyst. Moreover, CeO_2 catalysts have been shown to rapidly sinter at high temperatures resulting in the reduction of surface area [49], which could again factor into the deactivation of both CeO_2 catalysts. These data further supports the need to carefully consider catalyst precursors, as the subtle change of cerium oxidation state resulted in a more stable and active catalyst.

3.3 Impact of a mixture of Ce^{IV} and Ce^{III} precursors

3.3.1 Catalyst characterisation

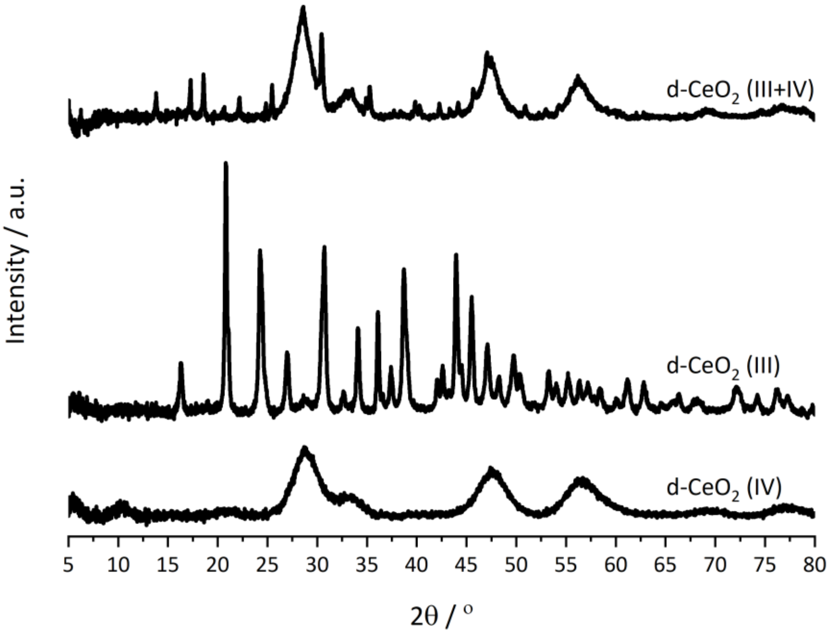

Figure 14: XRD patterns of the dried precipitates for the Ce^{IV}, Ce^{III} and mixed precursors.

In addition to comparing both Ce^{III} and Ce^{IV} precursors individually, a combination of both precursors was used in a 1:1 ratio to synthesise a CeO_2 catalyst, denoted as CeO_2 (III+IV). This catalyst was prepared to further determine the characteristics shown when using the different precursors and if these characteristics displayed a linear relationship upon changing concentration of precursor. When a mixture of both precursors was used during the synthesis procedure, a mixture of the low crystallinity $CeO_2.H_2O$ and $Ce_2(OH)_2(CO_3)_2.H_2O$ precipitates could be identified by XRD analysis (Figure 14). These data further supports the notion that the precipitation mechanism is directly controlled by the oxidation state of the precursor used during this synthesis method, as discussed previously [43,44].

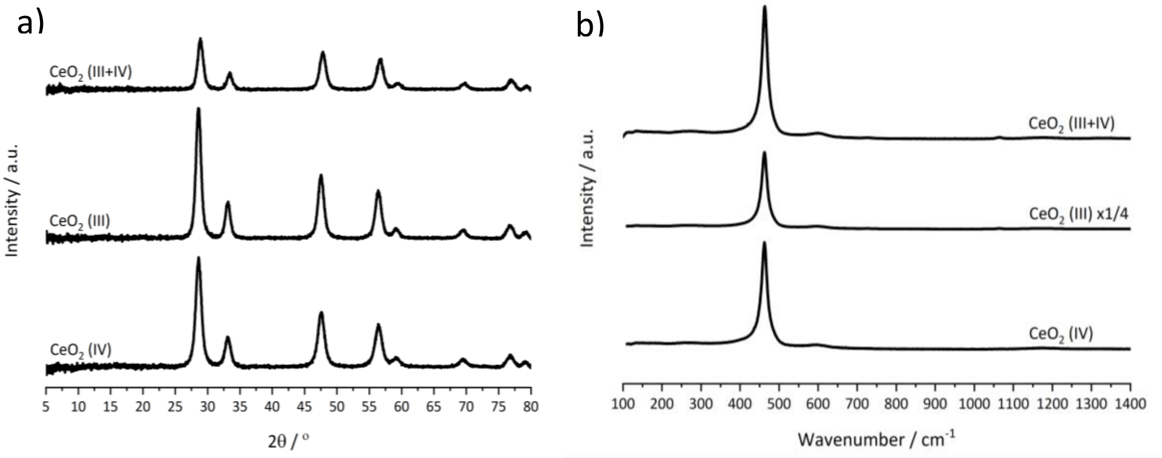

Figure 15: Bulk structures of the CeO_2 (IV), CeO_2 (III) and CeO_2 (III+IV) catalysts, determined by a) XRD patterns and b) Laser Raman spectra

The thermal decomposition of d-CeO_2 (III+IV) produced similar results as the d-CeO_2 (IV) and d-CeO_2 (III) precipitates, forming a bulk cubic fluorite CeO_2 structure, identified by XRD and Laser Raman analysis of the calcined CeO_2 (III+IV) catalyst (Figure 15a and 15b). Furthermore, the average crystallite size was also similar to the Ce^{IV} and Ce^{III} precursor CeO_2 catalysts (Table 6). However, a contraction of the cubic lattice could be identified from the lattice parameter of the mixed CeO_2 (III+IV) catalyst, when compared with CeO_2 (IV) and CeO_2 (III). Lattice contraction has been correlated with decreasing crystallite size from the increasing pressure between the crystallite and the external atmosphere [82], but this relationship was not observed in the data (Table 6). Therefore, this lattice contraction could occur from the lower crystallinity seen in the XRD pattern (Figure 15a) or it could suggest the formation of bulk defects throughout the cubic structure. However, the effect of defects on the lattice parameter is difficult to evaluate as previous studies have shown competing lattice expansion, from the increased concentration and size of Ce^{3+} ions, and lattice contraction occurs simultaneously [83]. The bulk defect concentration (A_{590}/A_{463}, Table 6), determined by Laser Raman spectroscopy, supports the presence of bulk defects in the CeO_2 (III+IV) catalyst as a larger concentration was observed when compared with CeO_2 (III) and CeO_2 (IV). Furthermore, as the FWHM of the F_{2g} band and crystallites size showed no significant difference compared to CeO_2 (IV) and CeO_2 (III), this supports the differences noted in the A_{590}/A_{463} ratio as a direct result of defects in the bulk structure.

Table 6: Physiochemical properties of the calcined CeO_2 (IV), CeO_2 (III) and CeO_2 (III+IV) catalysts.

Catalyst	**Surface Area / m^2g^{-1}**	**Position of Ce (111) reflection / °**	**Average Crystallite Size / nm**	**Lattice Parameter / nm**	**A_{590}/A_{463}**	**FWHM**
CeO_2 (IV)	81	28.56	8.7	0.5409	0.018	17.8
CeO_2 (III)	19	28.57	9.3	0.5408	0.019	17.6
CeO_2 (III + IV)	42	28.87	8.4	0.5352	0.051	17.6

It can be shown in Table 6 that the CeO_2 (III+IV) catalysts displayed an increased surface area compared with the CeO_2 (III) catalyst but was lower compared to the CeO_2 (IV) catalyst. A linear relationship between surface area and precursor used was deduced from this data (Figure 16), concurring with conclusions made previously for the CeO_2 (IV) and CeO_2 (III) catalysts (Section 3.2.3).

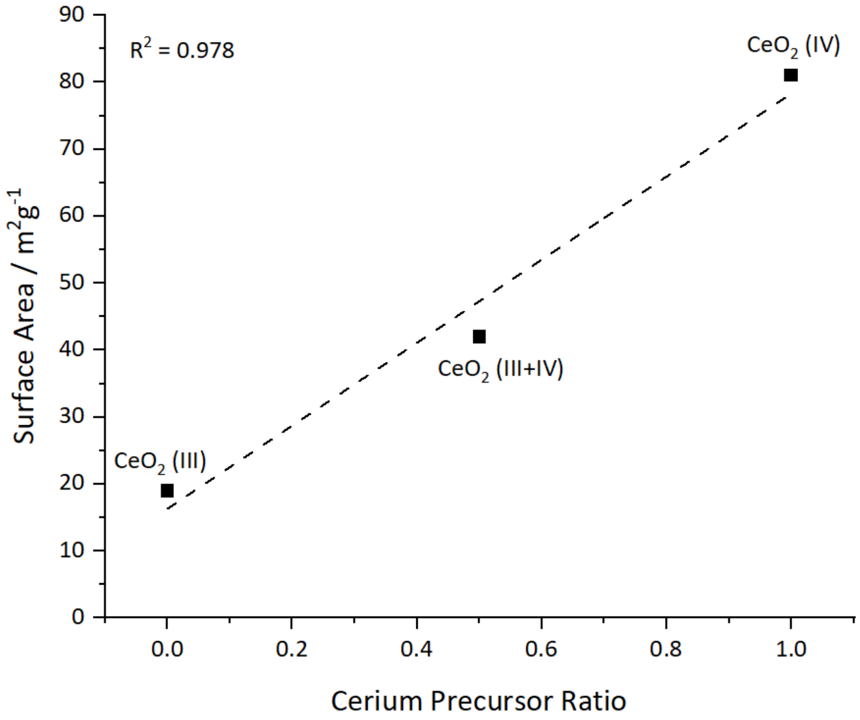

Figure 16: Relationship between catalyst precursor and surface area, measured by BET analysis.

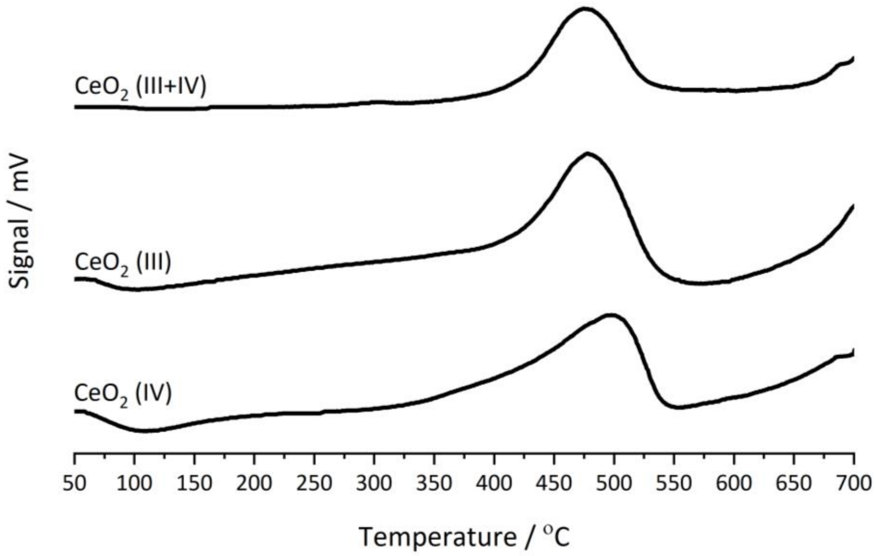

Figure 17: TPR profiles of the calcined CeO$_2$ (IV), CeO$_2$ (III) and CeO$_2$ (III+IV) catalysts. Conditions: 10% H$_2$/Ar, 30 mL min^{-1}, 50–700 °C at 10 °C min^{-1}.

A comparison of TPR profiles for the mixed and singular cerium precursors are shown in Figure 17. Similarly to CeO$_2$ (IV) and CeO$_2$ (III), the CeO$_2$ (III+IV) catalyst exhibited good redox properties with only one reduction peak noted at 475°C, relating to the reduction of CeO$_2$ surface species [56]. This peak occurred at a similar temperature to the CeO$_2$ (III) reduction peak, suggesting a more facile reduction of the catalyst surface. When taking into account the surface normalised H$_2$ consumption (Table 7), the CeO$_2$ (III+IV) displayed a value closer to the CeO$_2$ (IV) catalyst which then implies the reduction of the surface was more facile but occurred to a lesser extent. As mentioned previously, the initial TPR analysis does not factor in the re-oxidation step of the catalyst under reaction conditions and was inferred to be limited by the lower surface area for CeO$_2$ (III), hence this measurement may not be entirely representative of the catalyst under operating conditions.

Table 7: Mass and surface area normalised H$_2$ consumption for the CeO$_2$ (IV), CeO$_2$ (III) and CeO$_2$ (III+IV) catalysts. Determined by TPR analysis.

Catalyst	**H$_2$ Consumption per surface area /µmol m^{-2}**	**H$_2$ Consumption per mass /µmol g^{-1}**
CeO$_2$ (IV)	0.435	35.20
CeO$_2$ (III)	4.575	86.93
CeO$_2$ (III+IV)	0.442	18.57

Comparisons from XPS analysis of the Ce 3d and O 1s regions, shown in Table 8, indicated the CeO_2 (III+IV) catalyst had a larger quantity of surface oxygen defect sites compared with both CeO_2 (IV) and CeO_2 (III). However, a lower concentration of Ce^{3+} surface species was also highlighted, which was not consistent with trends noted for CeO_2 (IV), where the surface defects were thought to be induced by the loss of oxygen resulting in the creation of Ce^{3+} species, to maintain charge neutrality [33,52]. Therefore, other oxide surface species, such as hydroxyl or low co-ordination oxygen species, could also contribute to the O^{β} region as discussed in the literature [62–64]. Surface Na concentration was also determined by XPS analysis (Table 8) and showed a high quantity of residual Na. This was also noted for the CeO_2 (III) catalyst and could suggest the formation of the $Ce(CO_3)_x(OH)_y$ type precipitate results in higher Na retention.

Table 8: Surface composition of the CeO_2 (IV), CeO_2 (III) and CeO_2 (III+IV) catalysts, determined by XPS analysis.

Catalyst	XPS Ce:O:Na Ratio	O^{β}/O^{α} Ratio	Ce^{3+}/Ce^{4+} Ratio
CeO_2 (IV)	29:68:3	0.438	0.155
CeO_2 (III)	22:67:11	0.289	0.086
CeO_2 (III+IV)	25:62:13	0.567	0.114

3.3.2 Catalyst testing

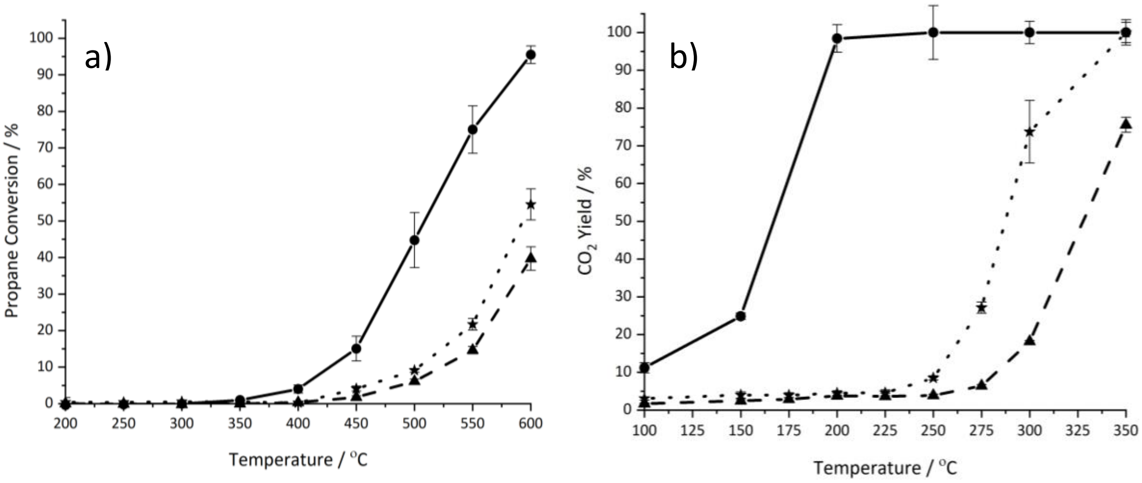

Figure 18: Catalyst activity for a) propane and b) naphthalene total oxidation: (Circle) CeO_2 (IV), (Triangle) CeO_2 (III), (Star) CeO_2 (III+IV). Conditions: 5000 ppm propane in air, GHSV = 45000 h^{-1}. 200 ppm naphthalene in 20% O_2/He, GHSV = 45000 h^{-1}.

A comparison between CeO_2 (IV), CeO_2 (III) and the CeO_2 (III+IV) mixed catalyst for the total oxidation of propane and naphthalene is shown in Figures 18a and 18b. For both reactions the main product detected was CO_2, with the CeO_2 (III+IV) catalyst presenting a carbon balance >99% across the temperature range for propane total oxidation. Moreover, selectivity to CO_2 was 100% but decreased to 98% from 450°C due to the formation of propene. For both propane and naphthalene total oxidation, the CeO_2 (III+IV) catalyst was more active than CeO_2 (III) but less active than CeO_2 (IV). Calculations of the surface normalised activity (Tables 9 and 10) showed a different trend to the reaction data presented in Figures 18a and 18b, indicating the CeO_2 (III+IV) catalyst to be less active for both reactions.

Table 9: Mass and surface area normalised catalytic activity of the CeO_2 (IV), CeO_2 (III) and CeO_2 (III+IV) catalysts for propane total oxidation.

Catalyst	**Propane Conversion / %**	**Surface Area Normalised Propane Oxidation[a] /mol s^{-1} m^{-2}**	**Mass Normalised Propane Oxidation[a] /mol s^{-1} g^{-1}**
CeO_2 (IV)	45	3.78×10^{-3}	3.06×10^{-1}
CeO_2 (III)	6	7.10×10^{-3}	1.35×10^{-1}
CeO_2 (III+IV)	9	1.63×10^{-3}	6.83×10^{-2}

a – Measured at 500°C

As discussed in Section 3.2.3, the surface area of the calcined CeO_2 (IV) and CeO_2 (III) catalysts was found to be a very influential characteristic; responsible for the reaction data highlighted in Figure 12a and 12b for both naphthalene and propane total oxidation, which was in good agreement with previous studies [29,71,72]. This was also apparent for CeO_2 (III+IV) as the catalyst had a higher surface area and performed better than CeO_2 (III), but performed worse than CeO_2 (IV) for both reactions. However, this factor was not linear for both reactions, suggesting other factors also contributed to the activity trends.

Table 10: Mass and surface area normalised catalytic activity of the CeO_2 (IV), CeO_2 (III) and CeO_2 (III+IV) catalysts for naphthalene total oxidation

Catalyst	**Naphthalene Conversion / %**	**Surface Area Normalised Naphthalene Oxidation[b] /mol s^{-1} m^{-2}**	**Mass Normalised Naphthalene Oxidation[b] /mol s^{-1} g^{-1}**
CeO_2 (IV)	25	7.54×10^{-5}	6.11×10^{-3}
CeO_2 (III)	2	7.19×10^{-5}	1.37×10^{-3}
CeO_2 (III+IV)	4	3.62×10^{-5}	1.52×10^{-3}

a – Measured at 150°C

It is interesting to note that the surface normalised activity trends differ for the CeO_2 (III+IV) catalyst, especially regarding naphthalene total oxidation. Previous research has discussed a direct correlation between surface area and catalytic activity for naphthalene total oxidation [11,70], as well as the importance of oxygen mobility through the catalyst [84]. It has been proposed that the rate determining step of naphthalene total oxidation over $CeZrO_x$ type catalysts was the re-oxidation of the catalyst [85], which further highlights the importance of improved oxygen mobility improving activity. Laser Raman analysis indicated the CeO_2 (III+IV) catalyst as having more bulk defects, which have been observed to promote oxygen mobility [24,52]. However, the surface normalised activity was lower for this catalyst which contradicts previous discussions showing this factor to directly influence catalytic activity. A potential reason for this reduced catalytic activity could relate to the increased surface Na concentration, analysed by XPS. As mentioned, increased Na can poison metal oxide catalysts by inhibiting oxygen mobility [77], therefore resulting in the poor surface normalised activity shown for naphthalene total oxidation.

Whilst XPS analysis showed the CeO_2 (III+IV) catalyst to have an increased number of surface oxygen defect sites, this did not directly correlate to improved catalytic activity for both propane and naphthalene total oxidation. Further supporting claims made earlier about the smaller contribution of this factor compared with the catalyst surface areas. Another rationale behind the inconsistent contribution of this factor could again relate to the suppression of oxygen mobility by the increased amount of surface Na species. Similarly to the surface defect site factor, inconsistent trends were shown for the redox properties of CeO_2 (III+IV) compared with CeO_2 (III) and CeO_2 (IV), therefore making it difficult to draw any significant conclusions. The more facile surface reduction of CeO_2 (III+IV) would support easier cleavage of the C-H bond, known to be the rate determining step for propane total oxidation. However, this factor had little correlation when comparing surface normalised activity.

As discussed in Section 3.2.3, the importance of the cerium precursor on final catalyst characteristics, affecting catalytic activity, have been further expanded upon. Data from the CeO_2 (III+IV) catalyst reinforces conclusions made regarding the creation of a higher surface area catalyst when forming the $CeO_2.H_2O$ precipitate. This factor was again shown to be very influential for controlling catalytic activity for propane and naphthalene total oxidation, but was found to not have linear behaviour. Furthermore, the impact of Na as a catalyst poison was also suggested to be a limiting factor for this catalyst, which is in good agreement with the literature.

3.4 Formation of a $CeO_2.H_2O$ precipitate using a Ce^{III} precursor

3.4.1 Catalyst characterisation

The synthesis of a CeO_2 catalyst using the Ce^{III} precursor and a NaOH precipitating agent was carried out to assess the impact of the resulting precipitate formed, and how that then influenced catalyst characteristics and the catalytic activity for propane and naphthalene total oxidation. It was postulated that the removal of carbonate species from the precipitation mechanism would favour the creation of the hydrated $CeO_2.H_2O$ nanoparticles, allowing for a more direct comparison of the precipitate formation for the final catalyst characteristics. As can be seen in Figure 19, the dried d-CeO_2 (III) NaOH precipitate formed the cubic fluorite CeO_2 structure similar to d-CeO_2 (IV), with a much greater crystallinity.

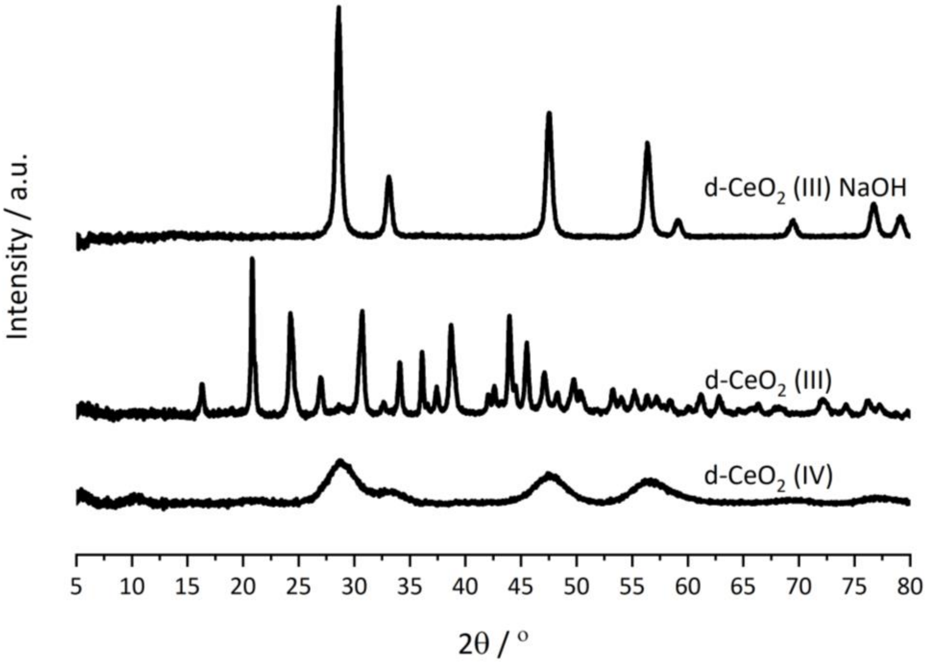

Figure 19: Comparison of XRD patterns for the dried precipitates resulting from the synthesis using the Ce^{IV} and Ce^{III} precursors and either Na_2CO_3 or NaOH as precipitating agent.

Upon calcination of the precipitate, the final CeO_2 (III) NaOH catalyst displayed an increased surface area compared with CeO_2 (III) (Table 11), further confirming previous conclusions drawn regarding the formation of the $CeO_2.H_2O$ precipitate (Section 3.2.3 and Section 3.3.1). Furthermore, as with the calcination of the other precursors, only the cubic fluorite CeO_2 structure was produced, as shown by Laser Raman spectroscopy and XRD analysis

(Figures 20a and 20b). The crystallite size, determined by XRD analysis, differed from the CeO_2 (IV) and CeO_2 (III) catalysts as CeO_2 (III) NaOH demonstrated a much higher crystallite size of 18.9 nm. This factor could also contribute to the lower surface area of CeO_2 (III) NaOH compared with CeO_2 (IV) as previous literature has shown an inverse relationship between particle size and surface area [49]. The increased crystallite size may have occurred from sintering of the already highly crystalline $CeO_2.H_2O$ precipitate formed (Figure 19).

Table 11: Physiochemical properties of the calcined CeO_2 (IV), CeO_2 (III) and CeO_2 (III) NaOH catalysts.

Catalyst	Surface Area / m^2g^{-1}	Position of Ce (111) reflection / °	Average Crystallite Size / nm	Lattice Parameter / nm	A_{590}/A_{463}	FWHM
CeO_2 (IV)	81	28.56	8.7	0.5409	0.018	17.8
CeO_2 (III)	19	28.57	9.3	0.5408	0.019	17.6
CeO_2 (III) NaOH	55	28.90	18.9	0.5347	0.028	13.6

A decrease in the lattice parameter for the CeO_2 (III) NaOH catalyst is seen in Table 11, which suggests the contraction of the cubic lattice. As mentioned for the CeO_2 (III+IV) catalyst (Section 3.3.1), this contraction could be induced by defect formation in the bulk structure, which may facilitate oxygen mobility, but was difficult to establish as a result of competing factors, such as varying crystallite size [83]. The bulk defect concentration determined by Laser Raman analysis (Table 11, A_{590}/A_{463}) for CeO_2 (III) NaOH was larger compared with CeO_2 (IV) and CeO_2 (III), which does support the formation of bulk defects. However, as discussed previously, the FWHM of the F_{2g} band also differs which has been linked to changes in defect concentration and inversely related to crystallite size [53,54,86]. Therefore, it was difficult to accurately quantify the presence of these defects due to the competing factors.

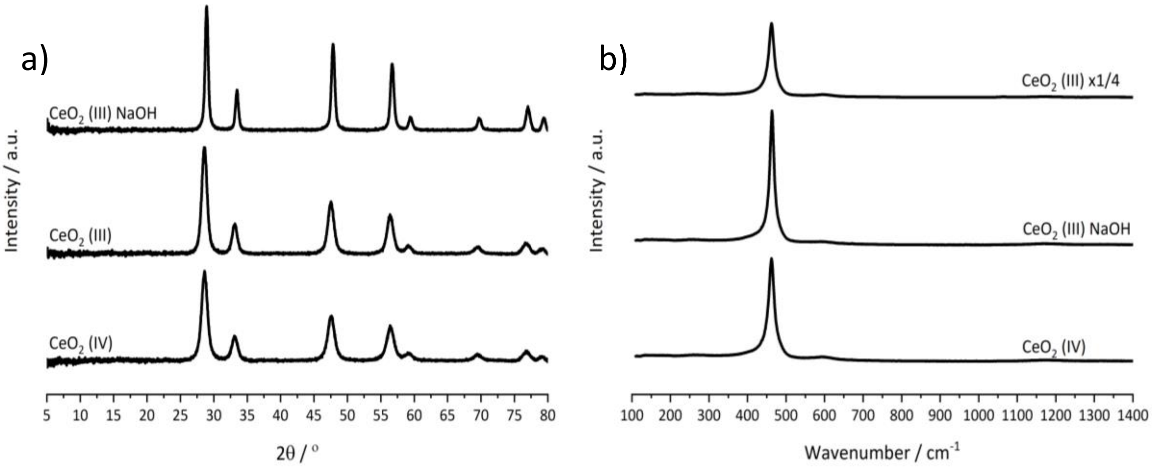

Figure 20: Bulk structures of the CeO_2 (IV), CeO_2 (III) and CeO_2 (III) NaOH catalysts, determined by a) XRD patterns and b) Laser Raman Spectra.

The surface species of the CeO_2 (III) NaOH catalyst, identified by XPS analysis, were similar to the surface species of CeO_2 (IV). As shown in Table 12, the surface oxygen defect site concentration was slightly increased compared with the same measurement for the CeO_2 (IV) catalyst. Furthermore, this was complimented by a minor increase in the Ce^{3+} surface concentration, implying these defects were a direct result of maintaining charge neutrality on the CeO_2 (III) NaOH catalyst surface. Finally, a comparison of the surface Na content of the CeO_2 catalysts (Table 12) indicated CeO_2 (III) NaOH had no quantifiable Na present on the surface. This result provides evidence to suggest that the formation of the $Ce_2(OH)_2(CO_3)_2.H_2O$ precipitate favoured the retention of Na during catalyst synthesis as shown for CeO_2 (III) and CeO_2 (III+IV) in previous discussions (Section 3.3.1).

Table 12: Surface composition of the CeO_2 (IV), CeO_2 (III) and CeO_2 (III) NaOH catalysts, determined by XPS analysis.

Catalyst	XPS Ce:O:Na Ratio	O^{β}/O^{α} Ratio	Ce^{3+}/Ce^{4+} Ratio
CeO_2 (IV)	29:68:3	0.438	0.155
CeO_2 (III)	22:67:11	0.289	0.086
CeO_2 (III) NaOH	30:70:0	0.490	0.169

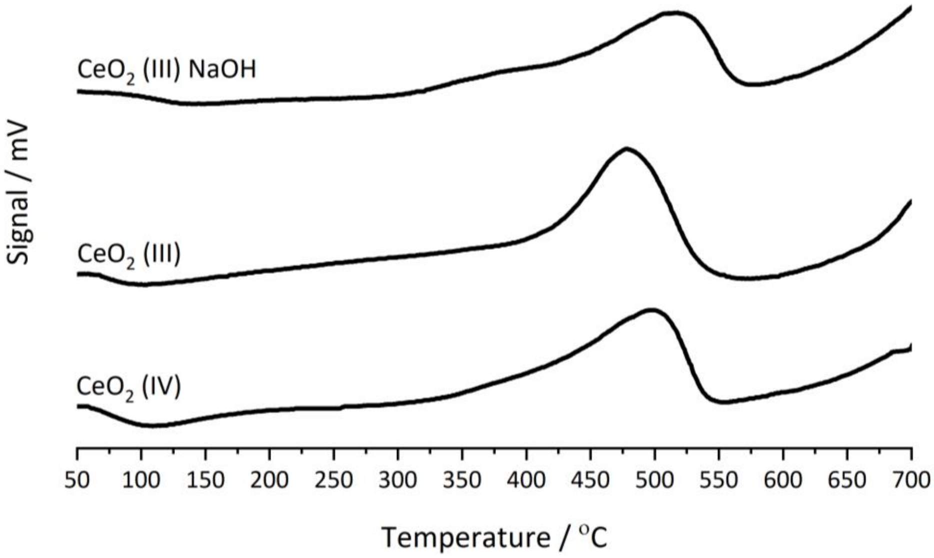

Figure 21: TPR profiles of the CeO$_2$ (IV), CeO$_2$ (III) and CeO$_2$ (III) NaOH catalysts.

The TPR profile of the CeO$_2$ (III) NaOH catalyst (Figure 21) indicated slightly worse redox properties compared with CeO$_2$ (IV) and CeO$_2$ (III). The reduction of the cerium surface species occurred at 517°C for CeO$_2$ (III) NaOH, suggesting less facile reduction, as a result of the increased reduction temperature. Moreover, the surface normalised H_2 consumption for CeO$_2$ (III) NaOH was comparable to CeO$_2$ (IV), which was shown to be much lower than CeO$_2$ (III) (Table 13). As stated previously, this could correlate to the more reduced surface of the catalyst as demonstrated by the increased Ce^{3+} species in the XPS analysis. It can also be concluded that, although the Ce^{III} precursor was used, the formation of the $CeO_2.H_2O$ precipitate from synthesis using NaOH resulted in inferior redox properties compared with the formation of the $Ce_2(OH)_2(CO_3)_2.H_2O$ precipitate. This may indicate that the redox properties of these catalysts are inherently linked to the structure formed by the decomposition of the $Ce_2(OH)_2(CO_3)_2.H_2O$ precipitate and not by the precursor oxidation state.

Table 13: Mass and surface area normalised H_2 consumption of the CeO$_2$ (IV), CeO$_2$ (III) and CeO$_2$ (III) NaOH catalysts, determined from TPR analysis.

Catalyst	H_2 Consumption per surface area /µmol m^{-2}	H_2 Consumption per mass /µmol g^{-1}
CeO$_2$ (IV)	0.435	35.20
CeO$_2$ (III)	4.575	86.93
CeO$_2$ (III) NaOH	0.451	24.80

3.4.2 Catalyst testing

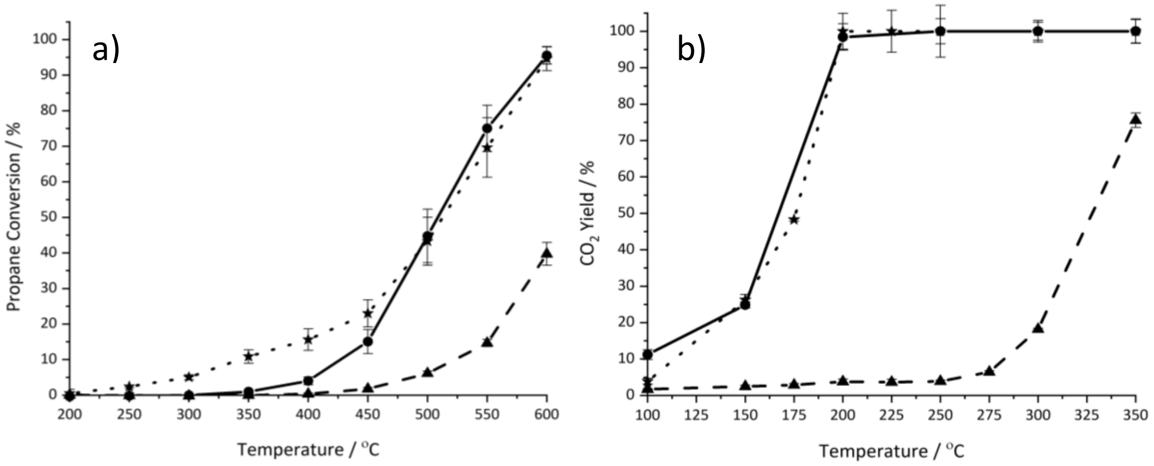

Figure 22: Catalyst activity for a) propane and b) naphthalene total oxidation: (Circle) CeO_2 (IV), (Triangle) CeO_2 (III), (Star) CeO_2 (III) NaOH. Conditions: 5000 ppm propane in air, GHSV = 45000 h^{-1}. 200 ppm naphthalene in 20% O_2/He, GHSV = 45000 h^{-1}.

Figures 22a and 22b show the catalyst performance for propane and naphthalene total oxidation using the CeO_2 (III) NaOH, CeO_2 (IV) and CeO_2 (III) catalysts. CO_2 was the main product identified during both reactions, with CeO_2 (III) NaOH achieving a carbon balance of >96% for propane total oxidation. Selectivity of the CeO_2 (III) NaOH catalyst was >98% across the temperature range due to forming small quantities of propene. For propane total oxidation, CeO_2 (III) NaOH was more active at lower temperatures compared to CeO_2 (IV) and CeO_2 (III), but showed similar activity to the CeO_2 (IV) catalyst upon increasing temperature. Whereas for naphthalene total oxidation, the activity of CeO_2 (III) NaOH was similar to CeO_2 (IV) across the whole temperature range. When normalised for surface area, the catalytic activity of CeO_2 (III) NaOH for propane total oxidation was calculated to be less than CeO_2 (III), but greater than CeO_2 (IV) (Table 14). Whereas, regarding naphthalene total oxidation, the surface normalised activity was greater for CeO_2 (III) NaOH (Table 15).

Table 14: Mass and surface area normalised catalytic activity of the CeO_2 (IV), CeO_2 (III) and CeO_2 (III) NaOH catalysts for propane total oxidation.

Catalyst	Propane Conversion / %	Surface Area Normalised Propane Oxidation[a] /mol s^{-1} m^{-2}	Mass Normalised Propane Oxidation[a] /mol s^{-1} g^{-1}
CeO_2 (IV)	45	3.78×10^{-3}	3.06×10^{-1}
CeO_2 (III)	6	7.10×10^{-3}	1.35×10^{-1}
CeO_2 (III) NaOH	43	5.32×10^{-3}	2.93×10^{-1}

a – Measured at 500°C

As previously discussed (Sections 3.2.2 and 3.3.2), catalyst surface area was shown to affect catalytic activity for both reactions. However, from data presented for the CeO_2 (III) NaOH catalyst, the contribution of this factor was not linear for either propane or naphthalene total oxidation. CeO_2 (III) NaOH performed better than the higher surface area CeO_2 (IV) catalyst for propane total oxidation and equivalently for naphthalene total oxidation, further contributing to the idea that multiple factors affected the activity trends discussed throughout this chapter.

Table 15: Mass and surface area normalised catalytic activity of the CeO_2 (IV), CeO_2 (III) and CeO_2 (III) NaOH catalysts for naphthalene total oxidation.

Catalyst	Naphthalene Conversion / %	Surface Area Normalised Naphthalene Oxidation^b /mol s^{-1} m^{-2}	Mass Normalised Naphthalene Oxidation^b /mol s^{-1} g^{-1}
CeO_2 (IV)	25	$7.54x10^{-5}$	$6.11x10^{-3}$
CeO_2 (III)	2	$7.19x10^{-5}$	$1.37x10^{-3}$
CeO_2 (III) NaOH	26	$1.44x10^{-4}$	$7.90x10^{-3}$

a – Measured at 150°C

Redox properties of the catalyst, as well as increased surface oxygen defects, have been linked to improved propane oxidation [11,15,73], with both factors relating to the more facile cleavage of the C-H bond, known to be the rate determining step for propane total oxidation. It can be argued that these were limiting factors for the CeO_2 catalysts as shown by a direct comparison between the CeO_2 (IV) and CeO_2 (III) NaOH catalysts. Both catalysts displayed similar redox and surface defect parameters (Tables 12 and 13) and demonstrated equivalent propane conversions at higher temperatures. The slightly improved performance of CeO_2 (III) NaOH at lower temperatures could correspond to the improved oxygen mobility inferred by increased bulk defects and the reduced surface concentration of Na species [52,77]. These factors may also contribute to differences in the surface normalised activity for the catalysts (Table 14). The improved surface normalised activity of CeO_2 (III) was previously thought to relate to the improved redox properties of the catalyst; however, this does not directly correlate with CeO_2 (III) NaOH suggesting an influence of other factors.

In contrast to propane total oxidation, little correlation between redox properties and catalytic activity for naphthalene total oxidation has been shown in the literature [11], which compliments data in Figure 22b. Catalyst surface areas have been continuously mentioned throughout this chapter, and in the literature, as a significant factor influencing naphthalene oxidation [33,69,70]. However, this parameter was not found to have a directly linear effect. The CeO_2 (III) NaOH catalyst performed equivalently to the CeO_2 (IV) catalyst, whilst displaying a lower surface area, and demonstrated improved surface normalised activity compared to both catalysts. This improved activity can be associated with the enhanced oxygen mobility of CeO_2 (III) NaOH. As stated, Laser Raman analysis indicated increased bulk defects which are known to promote oxygen mobility through the lattice [24,52]. Furthermore, the low levels of surface Na, identified by XPS analysis, also supports improved oxygen mobility as this factor has been related to the suppression of oxygen mobility in previous research [76,77]. These conclusions are in good agreement with previous studies on the relationship between improved naphthalene oxidation and enhanced oxygen mobility [84].

The data presented in this section compliments earlier conclusions on the significance of the $CeO_2.H_2O$ precipitate for forming higher surface area catalysts. Despite previous sections suggesting the catalyst surface area to be the most influential factor when determining catalytic activity for propane and naphthalene total oxidation, this was not so apparent for these data. Whilst this factor was still significant, evidence of other factors impacting catalytic activity were also illustrated. Moreover, characteristics such as redox properties and Na content could be linked to precipitate formation from the differing cerium precursors, which further demonstrates the importance of the precursors used and the precipitate formation mechanism.

3.5 Influence of reaction conditions for CeO_2 (IV) and CeO_2 (III) catalysts

As mentioned, the importance of the reaction conditions used for oxidation catalysts has become important due to the application of these materials for industrial use. Other compounds present in waste streams have been shown to compete with VOCs on the catalyst surface, with certain compounds deactivating the catalysts used [5,16]. Water vapour (H_2O) is a prominent compound found in waste streams where VOC removal is required [87,88]. Hence, it is necessary to determine the affect water vapour had on the catalytic activity when using the CeO_2 catalysts prepared using different cerium precursors.

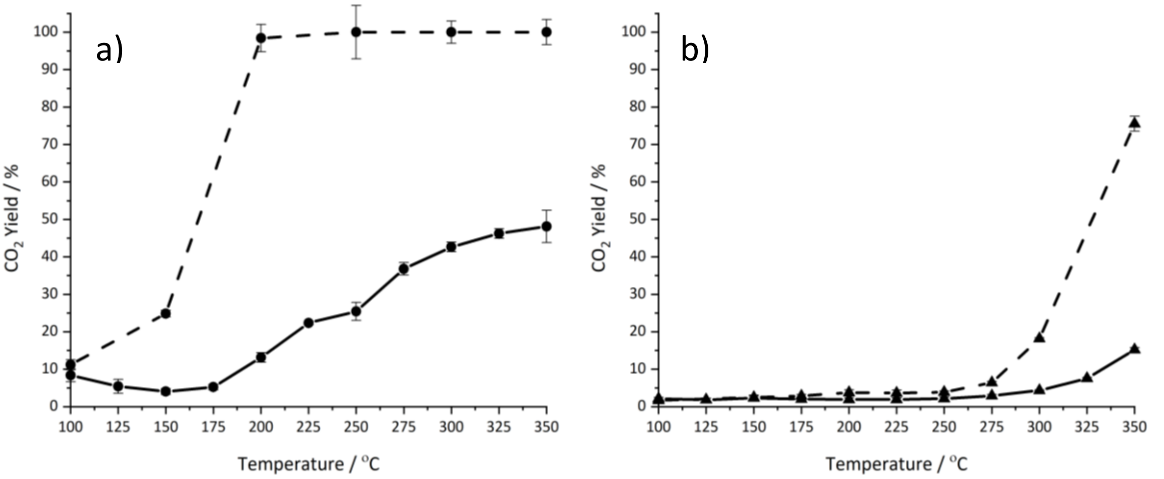

Figure 23: Catalyst activity of a) CeO_2 (IV) (Circle) and b) CeO_2 (III) (Triangle) for naphthalene total oxidation under dry and wet conditions. Dry conditions (dotted line), wet conditions (solid line). Dry conditions: 200 ppm naphthalene in 20% O_2/He, GHSV = 45000 h^{-1}. Wet conditions: 200 ppm naphthalene in 20% O_2/He, 5% water vapour saturation, GHSV = 45000 h^{-1}.

A comparison between dry and wet conditions, where the addition of 5% water was included in the gas feed, was assessed for both naphthalene (Figures 23a and 23b) and propane (Figures 24a and 24b) total oxidation using the CeO_2 (IV) and CeO_2 (III) catalysts. For naphthalene total oxidation, saturation of the gas feed with 5% water resulted in both CeO_2 catalysts being much less active compared to the dry conditions. Despite the decreased activity, the original trend was maintained with the CeO_2 (IV) catalyst demonstrating better activity overall, compared to CeO_2 (III). This data is in good agreement with previous research, where the addition of water vapour was found to hinder the oxidation of other aromatic VOCs such as toluene [5]. It was proposed that the addition of water vapour created competition for adsorption sites with the VOC, leading to surface active sites being blocked by water species [89,90]. Under the wet conditions stated, the CeO_2 (IV) catalyst seemed to show deactivation at higher temperatures. Whilst the CO_2

yield was shown to stagnate (Figure 23a), naphthalene conversion continued to increase over the temperature range, suggesting the deactivation occurred due to a change in the oxidation mechanism by the addition of water vapour. As stated in previous studies, naphthalene conversion can provide inconsistent results due to naphthalene adsorption on the catalyst surface [11] but it is still a useful indicator of reaction progress. It is possible that, due to the competitive adsorption of water vapour, naphthalene adsorption to the catalyst surface was weakened leading to a partial oxidation mechanism [11,91].

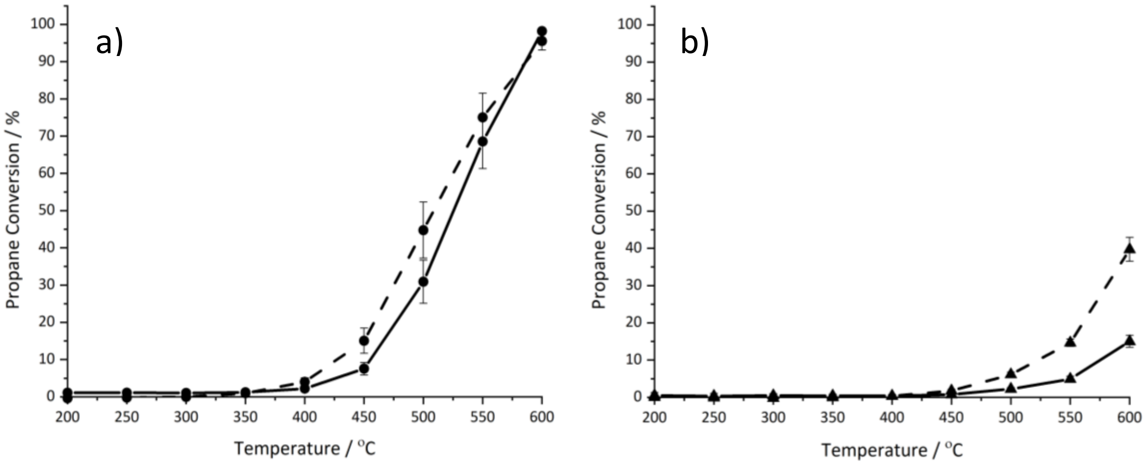

Figure 24: Catalyst activity of a) CeO_2 (IV) (Circle) and b) CeO_2 (III) (Triangle) for propane total oxidation under dry and wet conditions. Dry conditions (dotted line), wet conditions (solid line). Dry conditions: 5000 ppm propane in air, GHSV = 45000 h^{-1}. Wet conditions: 5000 ppm propane in air, 5% water vapour saturation, GHSV = 45000 h^{-1}.

Activity trends shown for propane total oxidation mirrored that of naphthalene total oxidation, with both catalysts exhibiting a lower activity under the wet conditions (Figure 24a and 24b). In contrast, this effect occurred to a lesser extent compared with naphthalene total oxidation. Research conducted by Marécot *et al*. reported the inhibition of propane and propene oxidation over Pt and Pd catalysts by the addition of water vapour [92]. The suppression of catalytic activity for these catalysts was thought to occur as a result of decreased active surface sites available. Furthermore, the supression of catalytic activity for propane total oxidation over metal oxide catalysts has also been identified in previous research [67]. Inhibiton of propane oxidation was proposed to occur from competitive adsorption between water and propane on the catalyst surface, which led to fewer active sites available.

3.6 Conclusions

A Ce^{IV} or Ce^{III} precursor was used to synthesise CeO_2 catalysts, which were then assessed for the total oxidation of propane and naphthalene VOCs. The influence of the cerium precursor on the resulting catalyst characteristics was assessed and how those characteristics then determined catalytic activity for the oxidation reactions. The CeO_2 catalyst prepared using the Ce^{IV} precursor displayed enhanced performance for both propane and naphthalene total oxidation.

The catalytic activity for both propane and naphthalene total oxidation was related to factors such as bulk and surface defect concentrations, redox properties, presence of Na species, but the most significant factor was determined to be the final catalyst surface areas. Catalyst characteristics responsible for the activity trends were linked to the different precipitates formed when using the different precursors in the synthesis procedure. The formation of a $CeO_2.H_2O$ precipitate resulted in higher surface area catalysts; whereas, the formation of a $Ce_2(OH)_2(CO_3)_2.H_2O$ precipitate led to increased residual Na retention and improved redox properties, possibly as a result of the different structure of the final calcined catalyst.

When water vapour was introduced into the VOC feed, catalysts prepared using either the Ce^{IV} or Ce^{III} precursor exhibited poorer catalytic performance compared to the dry conditions used. The observed decrease in catalytic activity was proposed to occur from less active sites being available during both reactions, from competitive adsorption of water and VOC species.

3.7 References

[1] D.J. Wuebbles, S. Sanyal, Air Quality in a Cleaner Energy World, Curr. Pollut. Rep. 1 (2015) 117–129. https://doi.org/10.1007/s40726-015-0009-x.

[2] K.R. Smith, M. Jerrett, H.R. Anderson, R.T. Burnett, V. Stone, R. Derwent, R.W. Atkinson, A. Cohen, S.B. Shonkoff, D. Krewski, C.A. Pope, M.J. Thun, G. Thurston, Public health benefits of strategies to reduce greenhouse-gas emissions: health implications of short-lived greenhouse pollutants, Lancet. 374 (2009) 2091–2103. https://doi.org/10.1016/S0140-6736(09)61716-5.

[3] M. Jerrett, R.T. Burnett, C.A. Pope, K. Ito, G. Thurston, D. Krewski, Y. Shi, E. Calle, M. Thun, Long-Term Ozone Exposure and Mortality, N. Engl. J. Med. 360 (2009) 1085–1095. https://doi.org/10.1056/NEJMoa0803894.

[4] A.A. Almetwally, M. Bin-Jumah, A.A. Allam, Ambient air pollution and its influence on human health and welfare: an overview, Environ. Sci. Pollut. Res. 27 (2020) 24815–24830. https://doi.org/10.1007/s11356-020-09042-2.

[5] C. He, J. Cheng, X. Zhang, M. Douthwaite, S. Pattisson, Z. Hao, Recent Advances in the Catalytic Oxidation of Volatile Organic Compounds: A Review Based on Pollutant Sorts and Sources, Chem. Rev. 119 (2019) 4471–4568. https://doi.org/10.1021/acs.chemrev.8b00408.

[6] N. Mohd Hanif, N.S.S. Limi Hawari, M. Othman, H.H. Abd Hamid, F. Ahamad, R. Uning, M.C.G. Ooi, M.I.A. Wahab, M. Sahani, M.T. Latif, Ambient volatile organic compounds in tropical environments: Potential sources, composition and impacts – A review, Chemosphere. 285 (2021) 131355. https://doi.org/10.1016/j.chemosphere.2021.131355.

[7] R. Rinnan, L.L. Iversen, J. Tang, I. Vedel-Petersen, M. Schollert, G. Schurgers, Separating direct and indirect effects of rising temperatures on biogenic volatile emissions in the Arctic, Proc. Natl. Acad. Sci. 117 (2020) 32476–32483. https://doi.org/10.1073/pnas.2008901117.

[8] W. Wu, B. Zhao, S. Wang, J. Hao, Ozone and secondary organic aerosol formation potential from anthropogenic volatile organic compounds emissions in China, J. Environ. Sci. 53 (2017) 224–237. https://doi.org/10.1016/j.jes.2016.03.025.

[9] P. Wang, Chenrui Cui, Kai Li, Jing Yi, Lili Lei, The Effect of Mn Content on Catalytic Activity of the Co–Mn–Ce Catalysts for Propane Oxidation: Importance of Lattice Defect and Surface Active Species, Catal. Lett. 150 (2020) 1505/1514. https://doi.org/10.1007/s10562-019-03061-6.

[10] V. R. Choudhary, G. M. Deshmukh, D. P. Mishra, Kinetics of the Complete Combustion of Dilute Propane and Toluene over Iron-Doped ZrO2 Catalyst, Energy Fuels. 19 (2005) 54–63. https://doi.org/10.1021/ef0498871.

[11] T. García, B. Solsona, S.H. Taylor, Naphthalene total oxidation over metal oxide catalysts, Appl. Catal. B Environ. 66 (2006) 92–99. https://doi.org/10.1016/j.apcatb.2006.03.003.

[12] F.J. Varela-Gandía, Á. Berenguer-Murcia, D. Lozano-Castelló, D. Cazorla-Amorós, D.R. Sellick, S.H. Taylor, Total oxidation of naphthalene at low temperatures using palladium nanoparticles supported on inorganic oxide-coated cordierite honeycomb monoliths, Catal. Sci. Technol. 3 (2013) 2708–2716. https://doi.org/10.1039/C3CY00323J.

[13] C. Yang, G. Miao, Y. Pi, Q. Xia, J. Wu, Z. Li, J. Xiao, Abatement of various types of VOCs by adsorption/catalytic oxidation: A review, Chem. Eng. J. 370 (2019) 1128–1153. https://doi.org/10.1016/j.cej.2019.03.232.

[14] A. Krishnamurthy, B. Adebayo, T. Gelles, A. Rownaghi, F. Rezaei, Abatement of gaseous volatile organic compounds: A process perspective, Catal. Today. 350 (2020) 100–119. https://doi.org/10.1016/j.cattod.2019.05.069.

[15] P.M. Shah, J.W.H. Burnett, D.J. Morgan, T.E. Davies, S.H. Taylor, Ceria–Zirconia Mixed Metal Oxides Prepared via Mechanochemical Grinding of Carbonates for the Total Oxidation of Propane and Naphthalene, Catalysts. 9 (2019) 475. https://doi.org/10.3390/catal9050475.

[16] H. Pan, M. Xu, Z. Li, S. Huang, C. He, Catalytic combustion of styrene over copper based catalyst: Inhibitory effect of water vapor, Chemosphere. 76 (2009) 721–726. https://doi.org/10.1016/j.chemosphere.2009.04.019.

[17] T.-C. Yu, H. Shaw, The effect of sulfur poisoning on methane oxidation over palladium supported on γ-alumina catalysts, Appl. Catal. B Environ. 18 (1998) 105–114. https://doi.org/10.1016/S0926-3373(98)00031-9.

[18] S. Song, S. Zhang, X. Zhang, P. Verma, M. Wen, Advances in Catalytic Oxidation of Volatile Organic Compounds over Pd-Supported Catalysts: Recent Trends and Challenges, Front. Mater. 0 (2020). https://doi.org/10.3389/fmats.2020.595667.

[19] P.M. Shah, A.N. Day, T.E. Davies, D.J. Morgan, S.H. Taylor, Mechanochemical preparation of ceria-zirconia catalysts for the total oxidation of propane and

naphthalene Volatile Organic Compounds, Appl. Catal. B Environ. 253 (2019) 331–340. https://doi.org/10.1016/j.apcatb.2019.04.061.

[20] W.B. Li, J.X. Wang, H. Gong, Catalytic combustion of VOCs on non-noble metal catalysts, Catal. Today. 148 (2009) 81–87. https://doi.org/10.1016/j.cattod.2009.03.007.

[21] C. Lahousse, A. Bernier, P. Grange, B. Delmon, P. Papaefthimiou, T. Ioannides, X. Verykios, Evaluation of γ-MnO2as a VOC Removal Catalyst: Comparison with a Noble Metal Catalyst, J. Catal. 178 (1998) 214–225. https://doi.org/10.1006/jcat.1998.2148.

[22] C.-H. Wang, S.-S. Lin, Preparing an active cerium oxide catalyst for the catalytic incineration of aromatic hydrocarbons, Appl. Catal. Gen. 268 (2004) 227–233. https://doi.org/10.1016/j.apcata.2004.03.040.

[23] A. Trovarelli, M. Boaro, E. Rocchini, C. de Leitenburg, G. Dolcetti, Some recent developments in the characterization of ceria-based catalysts, J. Alloys Compd. 323–324 (2001) 584–591. https://doi.org/10.1016/S0925-8388(01)01181-1.

[24] K. Polychronopoulou, A.A. AlKhoori, A.M. Efstathiou, M.A. Jaoude, C.M. Damaskinos, M.A. Baker, A. Almutawa, D.H. Anjum, M.A. Vasiliades, A. Belabbes, L.F. Vega, A.F. Zedan, S.J. Hinder, Design Aspects of Doped CeO2 for Low-Temperature Catalytic CO Oxidation: Transient Kinetics and DFT Approach, ACS Appl. Mater. Interfaces. 13 (2021) 22391–22415. https://doi.org/10.1021/acsami.1c02934.

[25] M. Lykaki, E. Pachatouridou, S.A.C. Carabineiro, E. Iliopoulou, C. Andriopoulou, N. Kallithrakas-Kontos, S. Boghosian, M. Konsolakis, Ceria nanoparticles shape effects on the structural defects and surface chemistry: Implications in CO oxidation by Cu/CeO2 catalysts, Appl. Catal. B Environ. 230 (2018) 18–28. https://doi.org/10.1016/j.apcatb.2018.02.035.

[26] T. Montini, M. Melchionna, M. Monai, P. Fornasiero, Fundamentals and Catalytic Applications of CeO2-Based Materials, Chem. Rev. 116 (2016) 5987–6041. https://doi.org/10.1021/acs.chemrev.5b00603.

[27] S. Agarwal, X. Zhu, E.J.M. Hensen, L. Lefferts, B.L. Mojet, Defect Chemistry of Ceria Nanorods, J. Phys. Chem. C. 118 (2014) 4131–4142. https://doi.org/10.1021/jp409989y.

[28] M. Dosa, M. Piumetti, S. Bensaid, T. Andana, C. Novara, F. Giorgis, D. Fino, N. Russo, Novel Mn–Cu-Containing CeO2 Nanopolyhedra for the Oxidation of CO and Diesel Soot: Effect of Dopants on the Nanostructure and Catalytic Activity, Catal. Lett. 148 (2018) 298–311. https://doi.org/10.1007/s10562-017-2226-y.

[29] T. Garcia, B. Solsona, S.H. Taylor, Nano-crystalline Ceria Catalysts for the Abatement of Polycyclic Aromatic Hydrocarbons, Catal. Lett. 105 (2005) 183–189. https://doi.org/10.1007/s10562-005-8689-2.

[30] A. Setiabudi, J. Chen, G. Mul, M. Makkee, J.A. Moulijn, CeO2 catalysed soot oxidation: The role of active oxygen to accelerate the oxidation conversion, Appl. Catal. B Environ. 51 (2004) 9–19. https://doi.org/10.1016/j.apcatb.2004.01.005.

[31] X. Zheng, Y. Li, L. Zhang, L. Shen, Y. Xiao, Y. Zhang, C. Au, L. Jiang, Insight into the effect of morphology on catalytic performance of porous CeO2 nanocrystals for H2S selective oxidation, Appl. Catal. B Environ. 252 (2019) 98–110. https://doi.org/10.1016/j.apcatb.2019.04.014.

[32] S. Datta, L. Torrente-Murciano, Nanostructured faceted ceria as oxidation catalyst, Curr. Opin. Chem. Eng. 20 (2018) 99–106. https://doi.org/10.1016/j.coche.2018.03.009.

[33] L. Torrente-Murciano, A. Gilbank, B. Puertolas, T. Garcia, B. Solsona, D. Chadwick, Shape-dependency activity of nanostructured CeO2 in the total oxidation of polycyclic aromatic hydrocarbons, Appl. Catal. B Environ. 132–133 (2013) 116–122. https://doi.org/10.1016/j.apcatb.2012.10.030.

[34] M. Kurian, C. Kunjachan, Investigation of size dependency on lattice strain of nanoceria particles synthesised by wet chemical methods, Int. Nano Lett. 4 (2014) 73–80. https://doi.org/10.1007/s40089-014-0122-7.

[35] L. Qi, Q. Yu, Y. Dai, C. Tang, L. Liu, H. Zhang, F. Gao, L. Dong, Y. Chen, Influence of cerium precursors on the structure and reducibility of mesoporous CuO-CeO2 catalysts for CO oxidation, Appl. Catal. B Environ. 119–120 (2012) 308–320. https://doi.org/10.1016/j.apcatb.2012.02.029.

[36] C. Zhang, W. Chu, F. Chen, L. Li, R. Jiang, J. Yan, Effects of cerium precursors on surface properties of mesoporous CeMnOx catalysts for toluene combustion, J. Rare Earths. 38 (2020) 70–75. https://doi.org/10.1016/j.jre.2019.04.013.

[37] N. Guillén-Hurtado, I. Atribak, A. Bueno-López, A. García-García, Influence of the cerium precursor on the physico-chemical features and NO to NO2 oxidation activity of ceria and ceria–zirconia catalysts, J. Mol. Catal. Chem. 323 (2010) 52–58. https://doi.org/10.1016/j.molcata.2010.03.010.

[38] D.R. Sellick, A. Aranda, T. García, J.M. López, B. Solsona, A.M. Mastral, D.J. Morgan, A.F. Carley, S.H. Taylor, Influence of the preparation method on the activity of ceria zirconia mixed oxides for naphthalene total oxidation, Appl. Catal. B Environ. 132–133 (2013) 98–106. https://doi.org/10.1016/j.apcatb.2012.11.036.

[39] Z. Guo, F. Du, G. Li, Z. Cui, Synthesis and Characterization of Single-Crystal Ce(OH)CO3 and CeO2 Triangular Microplates, Inorg. Chem. 45 (2006) 4167–4169. https://doi.org/10.1021/ic052189r.

[40] L.M. D’Assunção, I. Giolito, M. Ionashiro, Thermal decomposition of the hydrated basic carbonates of lanthanides and yttrium, Thermochim. Acta. 137 (1989) 319–330. https://doi.org/10.1016/0040-6031(89)87224-7.

[41] C. Padeste, N.W. Cant, D.L. Trimm, Thermal decomposition of pure and rhodium impregnated cerium(III) carbonate hydrate in different atmospheres, Catal. Lett. 24 (1994) 95–105. https://doi.org/10.1007/BF00807379.

[42] H. Wakita, S. Kinoshita, A Synthetic Study of the Solid Solutions in the Systems and La2(CH3)3·8H2O-Ce2(CO3)3·8H2O and La(OH)CO3–Ce(OH)CO3, Bull. Chem. Soc. Jpn. 52 (1979) 428–432. https://doi.org/10.1246/bcsj.52.428.

[43] M. Hirano, E. Kato, Hydrothermal Synthesis of Two Types of Cerium Carbonate Particles, J. Mater. Sci. Lett. 18 (1999) 403–405. https://doi.org/10.1023/A:1006653305821.

[44] M. Hirano, E. Kato, Hydrothermal Synthesis of Nanocrystalline Cerium(IV) Oxide Powders, J. Am. Ceram. Soc. 82 (1999) 786–788. https://doi.org/10.1111/j.1151-2916.1999.tb01838.x.

[45] N.W. Pettinger, R.E.A. Williams, J. Chen, B. Kohler, Crystallization kinetics of cerium oxide nanoparticles formed by spontaneous, room-temperature hydrolysis of cerium(IV) ammonium nitrate in light and heavy water, Phys. Chem. Chem. Phys. 19 (2017) 3523–3531. https://doi.org/10.1039/C6CP08227K.

[46] S. Lowell, J.E. Shields, M.A. Thomas, M. Thommes, Characterization of Porous Solids and Powders: Surface Area, Pore Size and Density, Springer Science & Business Media, 2012.

[47] M. Thommes, K. Kaneko, A.V. Neimark, J.P. Olivier, F. Rodriguez-Reinoso, J. Rouquerol, K.S.W. Sing, Physisorption of gases, with special reference to the

evaluation of surface area and pore size distribution (IUPAC Technical Report), Pure Appl. Chem. 87 (2015) 1051–1069. https://doi.org/10.1515/pac-2014-1117.

[48] L. Gong, W. Jie, Y. Liu, X. Lin, W. Deng, M. Qiu, X. Hu, Q. Liu, Enhanced Activity for CO Preferential Oxidation over CuO Catalysts Supported on Nanosized CeO2 with High Surface Area and Defects, Catalysts. 11 (2021) 884. https://doi.org/10.3390/catal11080884.

[49] C. Bueno-Ferrer, S. Parres-Esclapez, D. Lozano-Castelló, A. Bueno-López, Relationship between surface area and crystal size of pure and doped cerium oxides, J. Rare Earths. 28 (2010) 647–653. https://doi.org/10.1016/S1002-0721(09)60172-1.

[50] L.R. Smith, M.A. Sainna, M. Douthwaite, T.E. Davies, N.F. Dummer, D.J. Willock, D.W. Knight, C.R.A. Catlow, S.H. Taylor, G.J. Hutchings, Gas Phase Glycerol Valorization over Ceria Nanostructures with Well-Defined Morphologies, ACS Catal. 11 (2021) 4893–4907. https://doi.org/10.1021/acscatal.0c05606.

[51] Z. Wu, M. Li, J. Howe, H.M. Meyer, S.H. Overbury, Probing Defect Sites on CeO2 Nanocrystals with Well-Defined Surface Planes by Raman Spectroscopy and O2 Adsorption, Langmuir. 26 (2010) 16595–16606. https://doi.org/10.1021/la101723w.

[52] J.M. López, A.L. Gilbank, T. García, B. Solsona, S. Agouram, L. Torrente-Murciano, The prevalence of surface oxygen vacancies over the mobility of bulk oxygen in nanostructured ceria for the total toluene oxidation, Appl. Catal. B Environ. 174–175 (2015) 403–412. https://doi.org/10.1016/j.apcatb.2015.03.017.

[53] K. Kappis, C. Papadopoulos, J. Papavasiliou, J. Vakros, Y. Georgiou, Y. Deligiannakis, G. Avgouropoulos, Tuning the Catalytic Properties of Copper-Promoted Nanoceria via a Hydrothermal Method, Catalysts. 9 (2019) 138. https://doi.org/10.3390/catal9020138.

[54] I. Kosacki, T. Suzuki, H.U. Anderson, P. Colomban, Raman scattering and lattice defects in nanocrystalline CeO2 thin films, Solid State Ion. 149 (2002) 99–105. https://doi.org/10.1016/S0167-2738(02)00104-2.

[55] Q. Wang, K.L. Yeung, M.A. Bañares, Ceria and its related materials for VOC catalytic combustion: A review, Catal. Today. 356 (2020) 141–154. https://doi.org/10.1016/j.cattod.2019.05.016.

[56] G.R. Rao, Influence of metal particles on the reduction properties of ceria-based materials studied by TPR, Bull. Mater. Sci. 22 (1999) 89–94. https://doi.org/10.1007/BF02745559.

[57] F. Giordano, A. Trovarelli, C. de Leitenburg, M. Giona, A Model for the Temperature-Programmed Reduction of Low and High Surface Area Ceria, J. Catal. 193 (2000) 273–282. https://doi.org/10.1006/jcat.2000.2900.

[58] E. Paparazzo, Use and mis-use of x-ray photoemission spectroscopy Ce3d spectra of Ce2O3 and CeO2, J. Phys. Condens. Matter. 30 (2018) 343003. https://doi.org/10.1088/1361-648X/aad248.

[59] F. Zhang, P. Wang, J. Koberstein, S. Khalid, S.-W. Chan, Cerium oxidation state in ceria nanoparticles studied with X-ray photoelectron spectroscopy and absorption near edge spectroscopy, Surf. Sci. 563 (2004) 74–82. https://doi.org/10.1016/j.susc.2004.05.138.

[60] A. Trovarelli, J. Llorca, Ceria Catalysts at Nanoscale: How Do Crystal Shapes Shape Catalysis?, ACS Catal. 7 (2017) 4716–4735. https://doi.org/10.1021/acscatal.7b01246.

[61] K. Wang, Y. Chang, L. Lv, Y. Long, Effect of annealing temperature on oxygen vacancy concentrations of nanocrystalline CeO2 film, Appl. Surf. Sci. 351 (2015) 164–168. https://doi.org/10.1016/j.apsusc.2015.05.122.

[62] J.P. Holgado, G. Munuera, J.P. Espinós, A.R. González-Elipe, XPS study of oxidation processes of CeOx defective layers, Appl. Surf. Sci. 158 (2000) 164–171. https://doi.org/10.1016/S0169-4332(99)00597-8.

[63] D.R. Mullins, S.H. Overbury, D.R. Huntley, Electron spectroscopy of single crystal and polycrystalline cerium oxide surfaces, Surf. Sci. 409 (1998) 307–319. https://doi.org/10.1016/S0039-6028(98)00257-X.

[64] J. Yao, H. Lu, B. Hou, Y. Xiao, L. Jia, D. Li, J. Wang, The Promotional Effect of La Dopant on Co3O4 Catalytic Performance Towards C3H8 Combustion, Catal. Lett. 151 (2021) 1745–1754. https://doi.org/10.1007/s10562-020-03429-z.

[65] M. Yang, G. Shen, Q. Wang, K. Deng, M. Liu, Y. Chen, Y. Gong, Z. Wang, Roles of Oxygen Vacancies of CeO2 and Mn-Doped CeO2 with the Same Morphology in Benzene Catalytic Oxidation, Molecules. 26 (2021) 6363. https://doi.org/10.3390/molecules26216363.

[66] M.D. Krcha, A.D. Mayernick, M.J. Janik, Periodic trends of oxygen vacancy formation and C–H bond activation over transition metal-doped CeO2 (111) surfaces, J. Catal. 293 (2012) 103–115. https://doi.org/10.1016/j.jcat.2012.06.010.

[67] W. Zhu, X. Chen, J. Jin, X. Di, C. Liang, Z. Liu, Insight into catalytic properties of Co3O4-CeO2 binary oxides for propane total oxidation, Chin. J. Catal. 41 (2020) 679–690. https://doi.org/10.1016/S1872-2067(19)63523-0.

[68] A.A. Mirzaei, H.R. Shaterian, R.W. Joyner, M. Stockenhuber, S.H. Taylor, G.J. Hutchings, Ambient temperature carbon monoxide oxidation using copper manganese oxide catalysts: Effect of residual Na+ acting as catalyst poison, Catal. Commun. 4 (2003) 17–20. https://doi.org/10.1016/S1566-7367(02)00231-5.

[69] A. Aranda, B. Puértolas, B. Solsona, S. Agouram, R. Murillo, A.M. Mastral, S.H. Taylor, T. Garcia, Total Oxidation of Naphthalene Using Mesoporous CeO2 Catalysts Synthesized by Nanocasting from Two Dimensional SBA-15 and Three Dimensional KIT-6 and MCM-48 Silica Templates, Catal. Lett. 134 (2010) 110–117. https://doi.org/10.1007/s10562-009-0203-9.

[70] E.N. Ndifor, T. Garcia, B. Solsona, S.H. Taylor, Influence of preparation conditions of nano-crystalline ceria catalysts on the total oxidation of naphthalene, a model polycyclic aromatic hydrocarbon, Appl. Catal. B Environ. 76 (2007) 248–256. https://doi.org/10.1016/j.apcatb.2007.05.027.

[71] B. Solsona, T. Garcia, E. Aylón, A.M. Dejoz, I. Vázquez, S. Agouram, T.E. Davies, S.H. Taylor, Promoting the activity and selectivity of high surface area Ni–Ce–O mixed oxides by gold deposition for VOC catalytic combustion, Chem. Eng. J. 175 (2011) 271–278. https://doi.org/10.1016/j.cej.2011.09.104.

[72] T. Garcia, S. Agouram, J.F. Sánchez-Royo, R. Murillo, A.M. Mastral, A. Aranda, I. Vázquez, A. Dejoz, B. Solsona, Deep oxidation of volatile organic compounds using ordered cobalt oxides prepared by a nanocasting route, Appl. Catal. Gen. 386 (2010) 16–27. https://doi.org/10.1016/j.apcata.2010.07.018.

[73] B. Solsona, T. García, R. Sanchis, M.D. Soriano, M. Moreno, E. Rodríguez-Castellón, S. Agouram, A. Dejoz, J.M. López Nieto, Total oxidation of VOCs on mesoporous iron oxide catalysts: Soft chemistry route versus hard template method, Chem. Eng. J. 290 (2016) 273–281. https://doi.org/10.1016/j.cej.2015.12.109.

[74] M.S. Leguizamón Aparicio, M.A. Ocsachoque, D. Gazzoli, I.L. Botto, I.D. Lick, Total Oxidation of Naphthalene with Zirconia-Supported Cobalt, Copper and Nickel Catalysts, Catalysts. 7 (2017) 293. https://doi.org/10.3390/catal7100293.

[75] J.-Y. Luo, M. Meng, J.-S. Yao, X.-G. Li, Y.-Q. Zha, X. Wang, T.-Y. Zhang, One-step synthesis of nanostructured Pd-doped mixed oxides MOx-CeO2 (M=Mn, Fe, Co, Ni,

Cu) for efficient CO and C3H8 total oxidation, Appl. Catal. B Environ. 87 (2009) 92–103. https://doi.org/10.1016/j.apcatb.2008.08.017.

[76] W. Tang, J. Weng, X. Lu, L. Wen, A. Suburamanian, C.-Y. Nam, P.-X. Gao, Alkali-metal poisoning effect of total CO and propane oxidation over Co3O4 nanocatalysts, Appl. Catal. B Environ. 256 (2019) 117859. https://doi.org/10.1016/j.apcatb.2019.117859.

[77] G. Chai, W. Zhang, Y. Guo, J.L. Valverde, A. Giroir-Fendler, The Influence of Residual Sodium on the Catalytic Oxidation of Propane and Toluene over Co3O4 Catalysts, Catalysts. 10 (2020) 867. https://doi.org/10.3390/catal10080867.

[78] L. Spiridigliozzi, G. Dell'Agli, M. Biesuz, V.M. Sglavo, M. Pansini, Effect of the Precipitating Agent on the Synthesis and Sintering Behavior of 20 mol Sm-Doped Ceria, Adv. Mater. Sci. Eng. (2016). https://doi.org/10.1155/2016/6096123.

[79] L. Wang, H. Liu, Y. Liu, Y. Chen, S. Yang, Effect of precipitants on Ni-CeO2 catalysts prepared by a co-precipitation method for the reverse water-gas shift reaction, J. Rare Earths. 31 (2013) 969–974. https://doi.org/10.1016/S1002-0721(13)60014-9.

[80] J.-G. Li, T. Ikegami, Y. Wang, T. Mori, Reactive Ceria Nanopowders via Carbonate Precipitation, J. Am. Ceram. Soc. 85 (2002) 2376–2378. https://doi.org/10.1111/j.1151-2916.2002.tb00465.x.

[81] L. Spiridigliozzi, G. Accardo, D. Frattini, A. Marocco, S. Esposito, F.S. Freyria, M. Pansini, G. Dell'Agli, Effect of RE3+ on Structural Evolution of Rare-Earth Carbonates Synthesized by Facile Hydrothermal Treatment, Adv. Mater. Sci. Eng. 2019 (2019) e1241056. https://doi.org/10.1155/2019/1241056.

[82] Q. Jiang, L.H. Liang, D.S. Zhao, Lattice Contraction and Surface Stress of fcc Nanocrystals, J. Phys. Chem. B. 105 (2001) 6275–6277. https://doi.org/10.1021/jp010995n.

[83] L. Chen, P. Fleming, V. Morris, J.D. Holmes, M.A. Morris, Size-Related Lattice Parameter Changes and Surface Defects in Ceria Nanocrystals, J. Phys. Chem. C. 114 (2010) 12909–12919. https://doi.org/10.1021/jp1031465.

[84] T. Garcia, D. Sellick, F. Varela, I. Vázquez, A. Dejoz, S. Agouram, S.H. Taylor, B. Solsona, Total oxidation of naphthalene using bulk manganese oxide catalysts, Appl. Catal. Gen. 450 (2013) 169–177. https://doi.org/10.1016/j.apcata.2012.10.029.

[85] A. Bampenrat, V. Meeyoo, B. Kitiyanan, P. Rangsunvigit, T. Rirksomboon, Catalytic oxidation of naphthalene over CeO2–ZrO2 mixed oxide catalysts, Catal. Commun. 9 (2008) 2349–2352. https://doi.org/10.1016/j.catcom.2008.05.029.

[86] T. Hattori, K. Kobayashi, M. Ozawa, Size effect of Raman scattering on CeO2 nanocrystal by hydrothermal method, Jpn. J. Appl. Phys. 56 (2016) 01AE06. https://doi.org/10.7567/JJAP.56.01AE06.

[87] Y. Wang, X. Zhang, B. Shen, R.L. Smith, H. Guo, Role of impurity components and pollutant removal processes in catalytic oxidation of o-xylene from simulated coal-fired flue gas, Sci. Total Environ. 764 (2021) 142805. https://doi.org/10.1016/j.scitotenv.2020.142805.

[88] F. Hu, J. Chen, Y. Peng, H. Song, K. Li, J. Li, Novel nanowire self-assembled hierarchical CeO2 microspheres for low temperature toluene catalytic combustion, Chem. Eng. J. 331 (2018) 425–434. https://doi.org/10.1016/j.cej.2017.08.110.

[89] Y. Xia, L. Xia, Y. Liu, T. Yang, J. Deng, H. Dai, Concurrent catalytic removal of typical volatile organic compound mixtures over Au-Pd/α-MnO2 nanotubes, J. Environ. Sci. 64 (2018) 276–288. https://doi.org/10.1016/j.jes.2017.06.025.

[90] J. Fang, X. Chen, Q. Xia, H. Xi, Z. Li, Effect of Relative Humidity on Catalytic Combustion of Toluene over Copper Based Catalysts with Different Supports, Chin. J. Chem. Eng. 17 (2009) 767–772. https://doi.org/10.1016/S1004-9541(08)60275-X.

[91] X.-W. Zhang, S.-C. Shen, L.E. Yu, S. Kawi, K. Hidajat, K.Y. Simon Ng, Oxidative decomposition of naphthalene by supported metal catalysts, Appl. Catal. Gen. 250 (2003) 341–352. https://doi.org/10.1016/S0926-860X(03)00412-5.

[92] P. Marécot, A. Fakche, B. Kellali, G. Mabilon, P. Prigent, J. Barbier, Propane and propene oxidation over platinum and palladium on alumina: Effects of chloride and water, Appl. Catal. B Environ. 3 (1994) 283–294. https://doi.org/10.1016/0926-3373(94)00003-4.

4. Ceria-Iron mixed oxides for the total oxidation of propane and naphthalene VOCs: Effect of molar ratios and cerium precursor

4.1 Introduction

As previously mentioned (Chapter 3), CeO_2 can be used as an effective catalyst for the oxidation of VOCs. Nevertheless, metal oxide catalysts such as CeO_2 can suffer from poor activity and stability, when compared to supported metal catalysts [1]. Mixed metal oxide catalysts have been identified as a possible alternative to improve catalytic activity whilst maintaining the benefits of low cost and deactivation resistance. The combination of different metal oxides has been established at improving catalytic activity for a range of oxidation reactions when compared with the single oxide counterparts [2–4].

The use of metal oxides that are cheap and abundant, such as iron oxide (Fe_2O_3), provide further benefit for catalytic systems. Hence, iron oxide has been studied and found to be a suitable alternative oxidation catalyst [5,6]. The mixture of metals such as Co, Cu and Zr with CeO_2 have shown synergetic effects which enhance catalytic activity [7–10]. For $CeZrO_x$ catalysts, the synergetic effect is thought to increase catalytic activity by promoting lattice defects, enabling more facile oxygen mobility [11]. Whilst for materials like $CeCuO_x$, the mixture of the two metals promotes the reducibility of the catalyst by forming complementary redox cycles, as well as promoting oxygen vacancies [12]. Cerium-Iron oxide ($CeFeO_x$) catalysts have demonstrated impressive activity for a range of catalytic reactions, including N_2O decomposition and CO, methane, and soot oxidation [13–16] but are rarely studied for VOC oxidation.

In the previous chapter it was shown that the use of different cerium precursors can affect the physiochemical properties of the resultant catalyst, which then leads to different catalytic activity. This idea can be brought into consideration when preparing mixed metal oxides involving CeO_2. Previous research by Guillen-Hurtado *et al.* showed that using either a Ce^{III} or Ce^{IV} precursor could influence the physio-chemical features of $CeZrO_x$ catalysts, which resulted in the improved oxidation of NO to NO_2 [17]. Additionally, work carried out by Qi *et al.* on mixed $CeCuO_x$ catalysts indicated the importance of the cerium precursor for facilitating the creation of more active Cu^+ species, which enhanced CO oxidation activity [18].

In this work a range of $CeFeO_x$ mixed oxide catalysts were prepared using either a Ce^{IV} or Ce^{III} precursor as the cerium source. Catalysts were characterised by Thermal gravimetric analysis (TGA), Powder X-ray diffraction (XRD), X-ray photoelectron spectroscopy (XPS), Temperature programmed reduction (TPR), Electron microscopy (SEM-EDX), and Brunauer-Emmett-Teller (BET) surface area analysis. Catalysts were evaluated for the total oxidation of propane and naphthalene VOCs, focusing on the influence of the cerium precursor and Ce:Fe ratio on the catalytic activity.

4.2 Effect of molar ratios and cerium precursor

4.2.1 Precursor characterisation

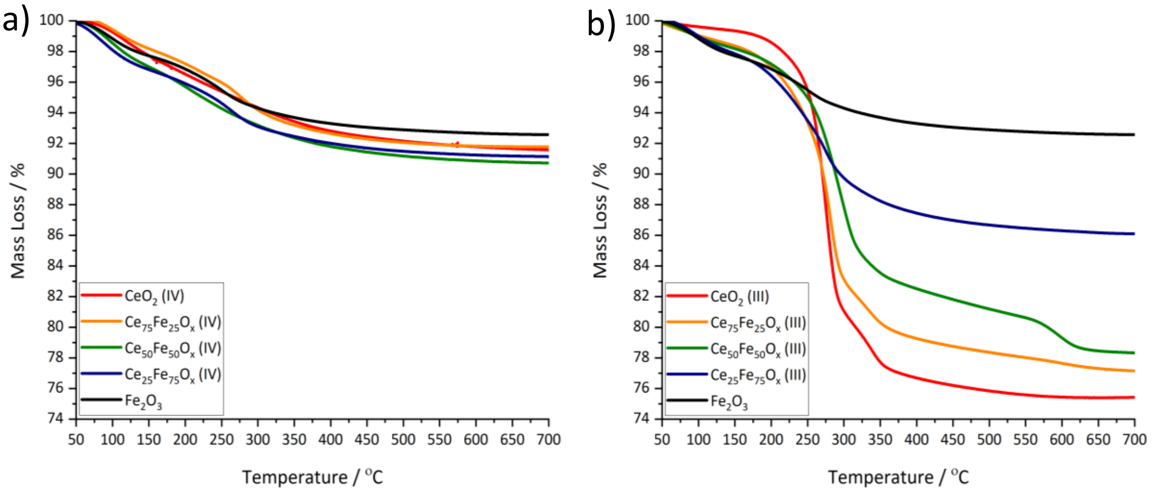

Figure 1: TGA Profiles for a) $CeFeO_x$ (IV) and b) $CeFeO_x$ (III) set of catalysts. Legend refers to catalysts analysed. Samples heated in flowing air from 50-700 °C with a heating rate of 5 °C min^{-1}.

The TGA profiles (Figures 1a and 1b) show different mass loss trends for the Ce^{IV} and Ce^{III} precursors with increasing amount of Fe incorporation. As mentioned previously in Chapter 3, the Ce^{IV} precursor formed a $CeO_2.H_2O$ precipitate when synthesised using Na_2CO_3. The $CeFeO_x$ (IV) range of catalysts, prepared using the Ce^{IV} precursor, displayed one mass loss event from 50-350°C, with a total mass loss between 6-9%, implying the formation of hydrated or hydroxylated $CeFeO_x$ particles in solution, which is in good agreement with work in Chapter 3 on the formation of CeO_2 (IV) [19]. The $CeFeO_x$ (III) range of catalysts showed decreasing mass loss when Fe content was increased. It was previously confirmed in Chapter 3 that catalyst synthesis using the Ce^{III} precursor resulted in a

$Ce_2(OH)_2(CO_3)_2.H_2O$ precipitate, which was identified by the sharp mass loss event around 300°C, relating to the decomposition of carbonate species [20,21]. It is understood that the precipitation of Fe^{3+} ions in solution is very complex and depends on many factors such as pH, counter ions present, and temperature of the synthesis. Hydroxylation of Fe^{3+} ions occurs upon addition of a base above pH 3, resulting in the formation of thermodynamically unstable ferrihydrite, which then transforms to either α-Fe_2O_3 or α-FeOOH depending on pH [22]. Furthermore, research carried out by Blanco-Andujar *et al*. on the precipitation of a mixture of Fe^{2+} and Fe^{3+} species by Na_2CO_3 found that α-FeOOH and Fe_3O_4 particles were preferentially formed under the conditions used, with no carbonate containing iron species identified at pH 9 [23]. From the TGA data, it can be suggested that the precipitation of Fe^{3+} species with Na_2CO_3 formed hydrated α-Fe_2O_3 or α-FeOOH particles. Hence, upon increasing Fe content of the $CeFeO_x$ (III) catalysts, the mass loss decreased due to less carbonate content in the precipitates.

4.2.2 Catalyst characterisation

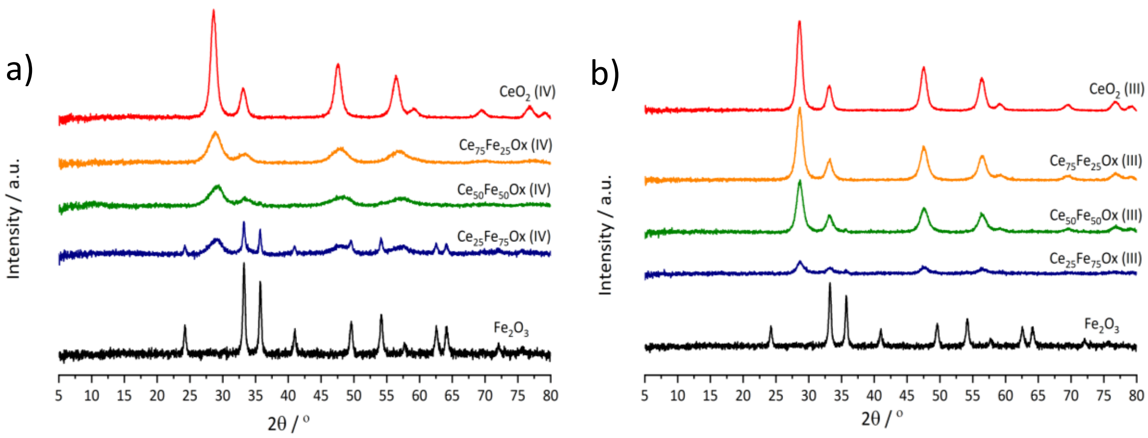

Figure 2: XRD patterns of the calcined a) $CeFeO_x$ (IV) and b) $CeFeO_x$ (III) catalysts.

XRD patterns, shown in Figures 2a and 2b, indicated slight differences between the catalysts prepared by the varying cerium precursors. For the $CeFeO_x$ (IV) range of catalysts (Figure 2a) all mixed catalysts presented the cubic fluorite bulk structure that was also identified for CeO_2 (IV), with predominant reflections around 28°, 33°, 47° and 57° representing the (111), (200), (220) and (311) planes respectively [24]. As Fe content increased, the crystallinity of the mixed catalysts decreased, as identified by the broadening of the reflections relating to the cubic fluorite structure. In addition to line broadening, a slight shift to higher 2ϴ values was identified, which has previously been related to the incorporation of Fe into the cubic lattice by substitution of Ce^{4+} cations [25]. The structure of the Fe_2O_3 catalyst was identified to be pure hematite α-Fe_2O_3, with the predominant reflections around 24°, 33°, 35°, 41°, 49°, 54°, 57°, 62° and 64° representing the (012), (104), (110), (113), (024), (116), (018), (214) and (300) planes [26]. Some of these reflections were also observed in the $Ce_{25}Fe_{75}O_x$ (IV) catalyst, suggesting bulk phase segregation of the CeO_2 and α-Fe_2O_3 structures occurred, in addition to incorporation of Fe ions into the cubic structure. A similar trend was established for the $CeFeO_x$ (III) range of catalysts, where line broadening of the reflections relating to the cubic CeO_2 structure occurred as Fe content increased. However, reflections relating to the α-Fe_2O_3 structure could not be clearly distinguished in the mixed catalysts, suggesting the formation of $CeFeO_x$ solid solutions as opposed to phase segregation seen in the $Ce_{25}Fe_{75}O_x$ (IV) catalyst. A very small reflection at 35.69° could be observed in the XRD patterns for the $Ce_{25}Fe_{75}O_x$ (III) and $Ce_{50}Fe_{50}O_x$ (III) catalysts which may relate to the α-Fe_2O_3 structure, but the low resolution of the data made this difficult to confirm.

The average crystallite sizes of CeO_2 species are shown in Table 1. For both Ce^{IV} and Ce^{III} precursors, the mixed $CeFeO_x$ catalysts displayed decreased crystallite sizes, compared with the CeO_2 catalysts, which was in good agreement with previous literature, suggesting the addition of Fe to the CeO_2 structure inhibited crystal growth [15,27]. The mixed $CeFeO_x$ (IV) catalysts prepared using the Ce^{IV} precursor showed slightly smaller crystallite sizes compared to the catalysts prepared by the Ce^{III} precursor. Nonetheless, there was no linear relationship between decreasing crystallite size and increasing Fe content for any of the mixed catalysts. Due to the absence of reflections relating to Fe_2O_3 nanoparticles in the mixed catalysts, the average crystallite size could only be analysed for the $Ce_{25}Fe_{75}O_x$ (IV) catalyst and was similar to that measured for the Fe_2O_3 catalyst (Error = ±3.8 nm).

Table 1: Physiochemical properties of the $CeFeO_x$ (IV) and (III) catalysts, determined by XRD and BET surface area analysis.

Catalyst	Surface Area / $m^2\,g^{-1}$	Position of Ce (111) reflection / °	Average CeO_2 Crystallite Size / nm	Average Fe_2O_3 Crystallite Size / nm	Lattice Parameter from CeO_2 (111) / nm
CeO_2 (IV)	81	28.56	8.7	-	0.5409
$Ce_{25}Fe_{75}O_x$ (IV)	68	28.92	3.7	28.0	0.5343

$Ce_{50}Fe_{50}O_x$ (IV)	113	29.05	2.9	-	0.5320
$Ce_{75}Fe_{25}O_x$ (IV)	88	28.82	3.2	-	0.5374
Fe_2O_3	37	-	-	27.3	-
CeO_2 (III)	19	28.57	9.3	-	0.5408
$Ce_{25}Fe_{75}O_x$ (III)	92	28.71	5.7	-	0.5381
$Ce_{50}Fe_{50}O_x$ (III)	45	28.64	7.2	-	0.5395
$Ce_{75}Fe_{25}O_x$ (III)	49	28.60	7.4	-	0.5402

In addition to crystallite size, the lattice parameter of the $CeFeO_x$ catalysts are also displayed in Table 1. This parameter was calculated using the (111) CeO_2 plane so correlated to the cubic CeO_2 structure identified for all mixed catalysts. As discussed in Chapter 3, a comparison of the CeO_2 (IV) and CeO_2 (III) catalysts showed little difference in the lattice parameter, corresponding to no significant defects or disruption to the cubic structure, when prepared from the different precursors. For the $CeFeO_x$ (IV) range of mixed catalysts, a contraction in the lattice was identified. This contraction reached a maximum for the $Ce_{50}Fe_{50}O_x$ (IV) catalyst but upon increasing Fe content the lattice contraction effect was not as extensive. Previous studies have shown that when aliovalent metals are incorporated into CeO_2 materials, a contraction of the lattice occurs due to the smaller cation size [28]. This effect has been demonstrated for $CeFeO_x$ materials by the substitution of larger Ce^{4+} ions with smaller Fe^{3+} cations [29]. It has also been suggested that the substitution of aliovalent ions, and subsequent lattice contraction, can form bulk defects in the structure, which then facilitate improved oxygen mobility [12,30]. As shown by the $Ce_{25}Fe_{75}O_x$ (IV) catalyst, the lattice contraction was not linear for increasing Fe content, which can be rationalised by the phase segregation shown in the XRD pattern. This has also been suggested in previous research, where the segregation of Fe_2O_3 from the cubic structure results in lattice expansion [31,32].

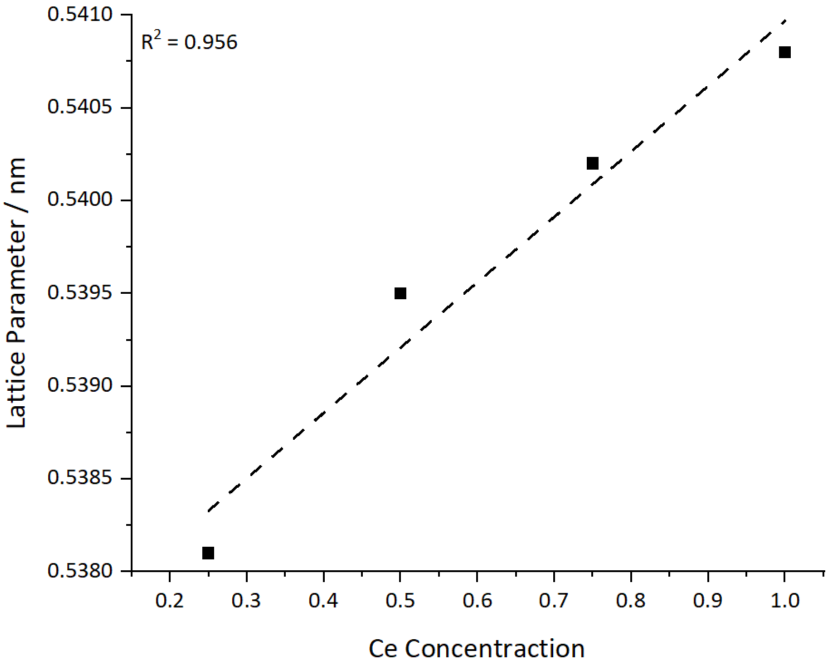

Figure 3: Relationship between Ce content and lattice parameter, determined from XRD analysis, for the $CeFeO_x$ (III) catalysts.

A similar trend was established for the $CeFeO_x$ (III) range of mixed catalysts, but with lattice contraction linearly increasing with Fe content (Figure 3). This linear change suggested that the use of a Ce^{III} precursor facilitated the formation of Ce-Fe solid solutions more easily. It can also be noted that the variation of lattice parameter was less significant compared to the $CeFeO_x$ (IV) catalysts, with maximum difference of 0.0027 nm. There is limited consensus in the literature on the solubility limit of Fe in the CeO_2 cubic structure, with maximum Fe content of 10-30 at.% reported [33]. However, the XRD data in Table 1 suggested the solubility limit was over 50 at.% for catalysts prepared by this method, due to the absence of reflections representing Fe_2O_3 as well as a linear decrease in the lattice parameter. It was difficult to extensively evaluate the differences in the lattice parameter for each set of $CeFeO_x$ catalysts as previous research has shown a direct dependence of lattice parameter with changing crystallite size [34]. Furthermore, competing expansion effects have also been identified as a result of defect formation, followed by the creation of more Ce^{3+} species, known to be larger than Ce^{4+} ions [35]. For $CeFeO_x$ materials, it has been suggested in the literature that the substitution mechanism could occur *via* two ways; the first being vacancy compensation where trivalent Fe ions replace Ce^{4+} and the formation of oxygen defects maintains charge neutrality or the second, where the charge is maintained by a Fe^{3+} ion occupying an interstitial site [27]. These different mechanisms would again invoke conflicting effects on the cubic lattice structure. Therefore, as a result of the competing expansion and contraction effects, only tentative conclusions can be inferred from this data, however, it is evident that incorporation of Fe into the cubic CeO_2 structure occurred to varied extent.

Surface areas for the $CeFeO_x$ (IV) and $CeFeO_x$ (III) catalysts (Table 1) indicated a general trend of increased surface area for the mixed metal catalysts compared to the single metal CeO_2 and Fe_2O_3 catalysts. As discussed in Chapter 3, the formation of the $CeO_2.H_2O$ precipitate facilitated the creation of higher surface area catalysts [36,37], which was also shown for the $CeFeO_x$ (IV) catalysts. Furthermore, the $CeFeO_x$ (IV) mixed catalysts demonstrated a smaller crystallite size compared with the $CeFeO_x$ (III) range. This could also account for the increased surface area of these catalysts, as the inverse relationship between surface area and crystallite size is well documented in the literature [38]. The improved surface area of the mixed $CeFeO_x$ catalysts was in good agreement with previous literature on the formation of $CeFeO_x$ solid solutions [39,40]. The $Ce_{25}Fe_{75}O_x$ (IV) catalyst presented a lower surface area compared to CeO_2 (IV), which was most likely a result of the phase segregation of Fe_2O_3 in the catalyst, as identified by XRD analysis.

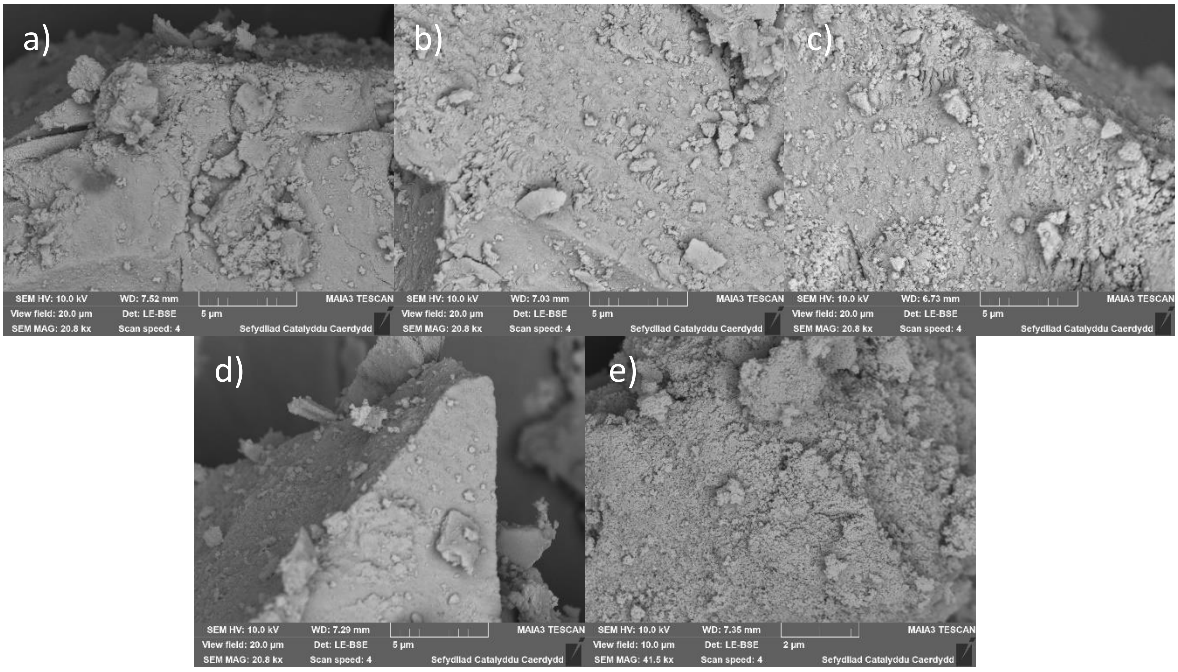

Figure 4: SEM images of a) $Ce_{25}Fe_{75}O_x$ (IV), b) $Ce_{50}Fe_{50}O_x$ (IV), c) $Ce_{75}Fe_{25}O_x$ (IV), d) CeO_2 (IV) and e) Fe_2O_3 catalysts.

SEM images of the $CeFeO_x$ (IV) catalysts (Figures 4a-e) indicated a similar morphology for the single and mixed metal oxides containing cerium. Well defined particles were formed when the Ce^{IV} precursor was used which was in good agreement with data from Chapter 3. The Fe_2O_3 catalyst displayed a more spherical morphology with a sponge-like texture, however this spherical texture was not observed for the mixed $CeFeO_x$ (IV) catalysts. Some contrast could be identified in the backscattered SEM images of the mixed $CeFeO_x$ (IV) catalysts, suggesting segregation of the CeO_2 and Fe_2O_3 components. This occurred to a greater extent as the concentration of Fe was increased. These data contradicted conclusions drawn from the XRD analysis, which suggested only the $Ce_{25}Fe_{75}O_x$ (IV) catalyst displayed evidence of phase segregation. This has previously been discussed in the literature, where encapsulated Fe_2O_3 species were observed by high resolution TEM but were undetectable during XRD analysis [41]. Further evidence of phase segregation was identified by EDX analysis (Figures 5a-c). Both $Ce_{25}Fe_{75}O_x$ (IV) and $Ce_{50}Fe_{50}O_x$ (IV) displayed areas of high Fe concentration, whilst a more homogeneous distribution of the Ce and Fe species was identified for the $Ce_{75}Fe_{25}O_x$ (IV) catalyst.

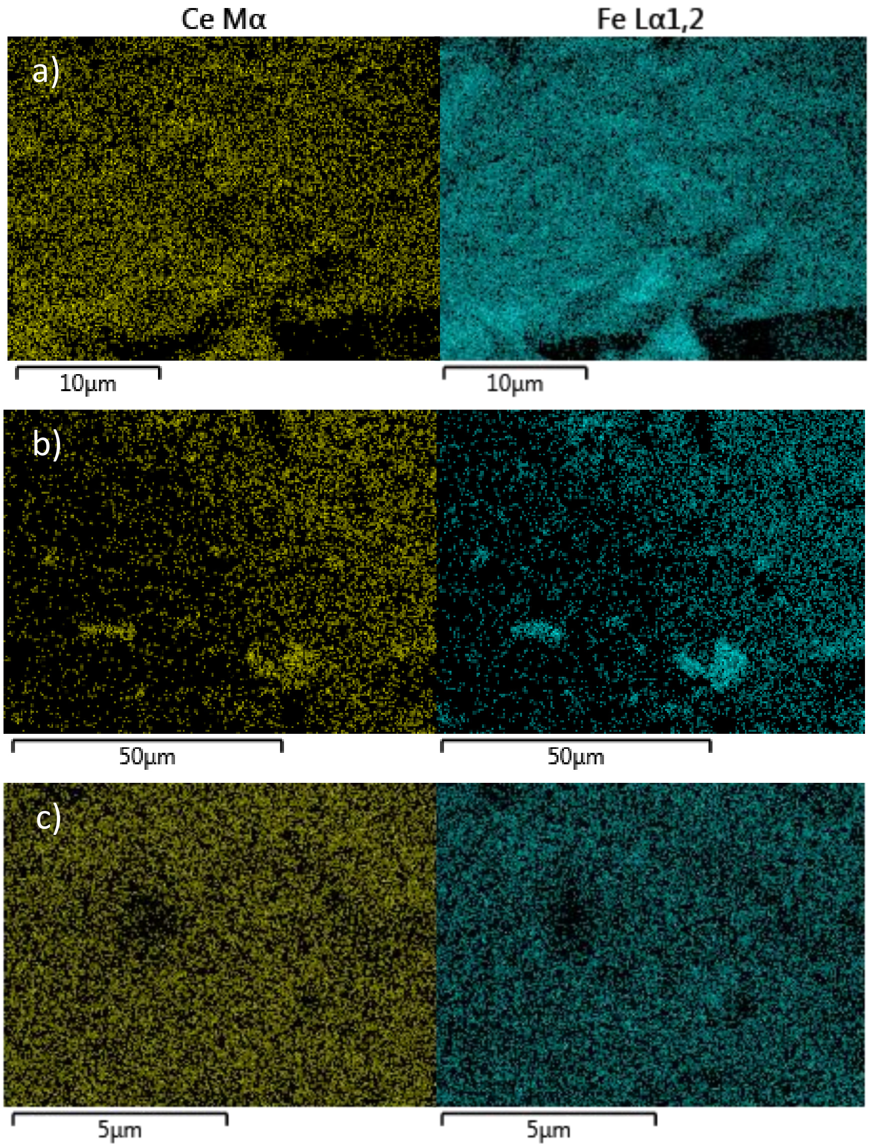

Figure 5: Ce Mα and Fe Lα EDX mapping of a) $Ce_{25}Fe_{75}O_x$ (IV), b) $Ce_{50}Fe_{50}O_x$ (IV) and c) $Ce_{75}Fe_{25}O_x$ (IV) catalysts.

SEM images of the $CeFeO_x$ (III) catalysts (Figure 6a-e) displayed a different morphology compared with the catalysts synthesised using the Ce^{IV} precursor. This was also shown for the CeO_2 (III) catalyst in Chapter 3, where a platelet type morphology was identified and was thought to occur as a result of the different precipitates formed. For the mixed $CeFeO_x$ (III) catalysts two types of morphology were observed. The $Ce_{25}Fe_{75}O_x$ (III) catalyst presented more well defined particles, similar to the structures observed when using the Ce^{IV} precursor. However, the $Ce_{50}Fe_{50}O_x$ (III) and $Ce_{75}Fe_{25}O_x$ (III) catalysts displayed more platelet-like morphology, similar to CeO_2 (III). These data support previous conclusions in Chapter 3, where it was proposed that formation of either the $CeO_2.H_2O$ or $Ce_2(OH)_2(CO_3)_2.H_2O$ precipitate resulted in the different morphologies identified. Furthermore, as suggested by the TGA data, the Fe species likely formed hydroxylated precipitates, rather than carbonated precipitates, which further suggests the presence of carbonate containing precipitates led to the synthesis of the platelet morphology observed.

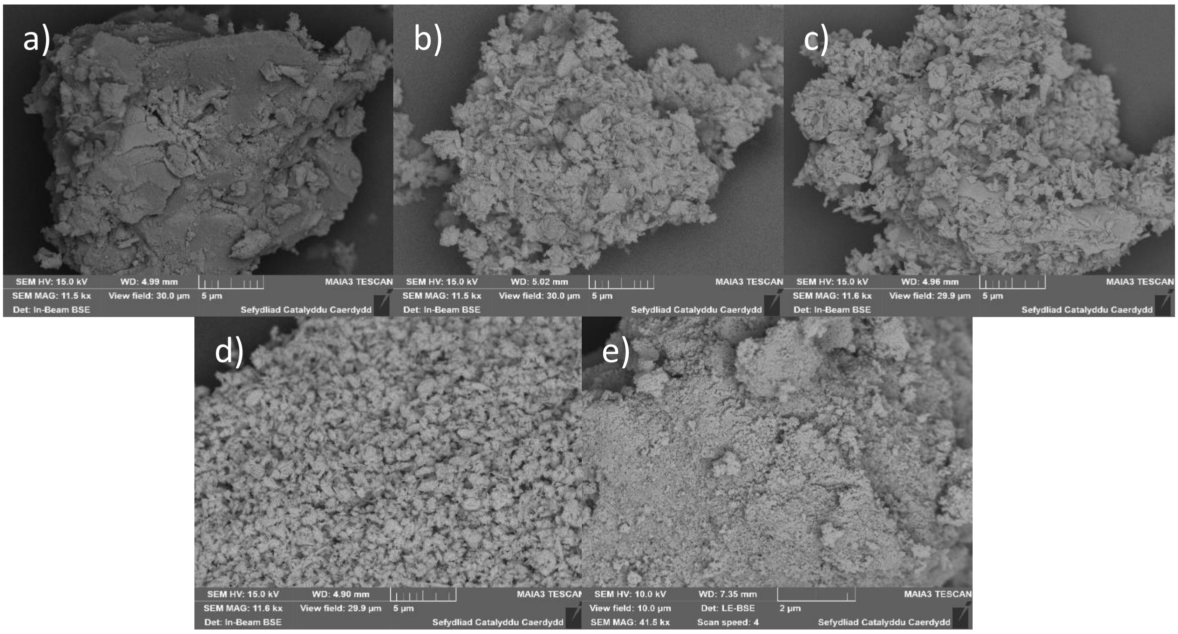

Figure 6: SEM images of a) $Ce_{25}Fe_{75}O_x$ (III), b) $Ce_{50}Fe_{50}O_x$ (III), c) $Ce_{75}Fe_{25}O_x$ (III), d) CeO_2 (III) and e) Fe_2O_3 catalysts.

Similarly to the $CeFeO_x$ (IV) range of mixed metal oxides, the mixed $CeFeO_x$ (III) catalysts showed some contrast differences in the backscattered SEM images (Figures 6a and 6b). Both $Ce_{25}Fe_{75}O_x$ (III) and $Ce_{50}Fe_{50}O_x$ (III) displayed areas of contrast which suggested segregation of the Fe_2O_3 and CeO_2 species. This was also established by EDX analysis, with $Ce_{25}Fe_{75}O_x$ (III) and $Ce_{50}Fe_{50}O_x$ (III) showing segregation of Fe and Ce species, whereas the $Ce_{75}Fe_{25}O_x$ (III) catalyst displayed a more homogeneous distribution (Figures 7a-c). As with the $CeFeO_x$ (IV) mixed catalysts, these data were also in contrast to XRD analysis suggesting better incorporation of Fe into the cubic CeO_2 structure for the $CeFeO_x$ (III) catalysts. As mentioned previously, the solubility limit for Fe into the CeO_2 structure has been suggested to be limited to 10-30% in the literature. SEM-EDX analysis of the mixed $CeFeO_x$ catalysts dismisses earlier suggestions of an increased solubility limit for these catalysts, when only assessed by XRD analysis.

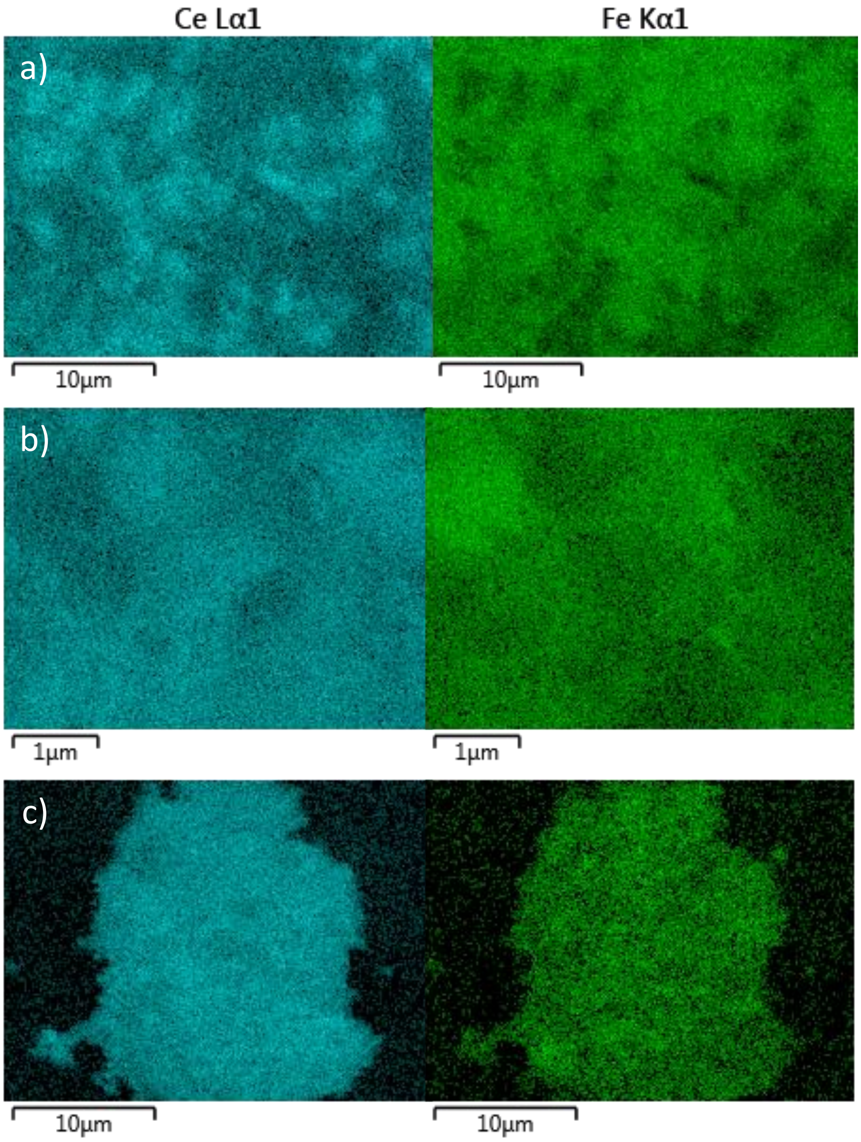

Figure 7: Ce Lα and Fe Kα EDX mapping of a) $Ce_{25}Fe_{75}O_x$ (III), b) $Ce_{50}Fe_{50}O_x$ (III) and c) $Ce_{75}Fe_{25}O_x$ (III) catalysts.

EDX analysis was also used to quantify the Ce:Fe ratio of the mixed catalysts (Table 2). The $CeFeO_x$ (IV) range of mixed catalysts showed similar ratios to those expected from the preparation method. Alternatively, the $CeFeO_x$ (III) mixed catalysts showed slight deviation from the expected ratios. Due to the slight limitation of the SEM-EDX analysis, where only a snapshot of the material was used to obtain results, these minor variations could be a result of poor mixing in the overall catalysts.

Table 2: Elemental composition of the $CeFeO_x$ (IV) and (III) catalysts, determined by EDX analysis.

Catalyst	EDX Ce:Fe Ratio	EDX Ce:Fe:Na Ratio
CeO_2 (IV)	N/A	94:0:6
$Ce_{25}Fe_{75}O_x$ (IV)	24:76	24:74:2

$Ce_{50}Fe_{50}O_x$ (IV)	51:49	51:49:0
$Ce_{75}Fe_{25}O_x$ (IV)	76:24	76:23:1
Fe_2O_3	N/A	0:100:0
CeO_2 (III)	N/A	83:0:17
$Ce_{25}Fe_{75}O_x$ (III)	30:70	28:65:7
$Ce_{50}Fe_{50}O_x$ (III)	51:49	44:39:17
$Ce_{75}Fe_{25}O_x$ (III)	81:19	67:16:16

In addition to the Ce and Fe concentration, the Na concentration was also measured. As previously discussed in Chapter 3, Na is a known catalyst poison for propane total oxidation [42]. It was proposed that residual Na inhibits oxygen mobility of the catalyst by supressing oxygen desorption at low temperatures [43]. Figures 8a-f indicated residual Na was homogeneously distributed on all the mixed catalysts for both precursors. However, when quantified in Table 2, the catalysts prepared using the Ce^{IV} precursor had much less Na present. Only trace amounts of Na were observed for $Ce_{50}Fe_{50}O_x$ (IV) and $Ce_{75}Fe_{25}O_x$ (IV), whereas; for the $Ce_{50}Fe_{50}O_x$ (III) and $Ce_{75}Fe_{25}O_x$ (III) catalysts, much higher quantities were measured. Na concentration of the CeO_2 catalysts was previously discussed in Chapter 3 and found a similar relationship for the retention of Na when using the different precursors. EDX data further supports these conclusions, where it was theorised that the formation of a carbonate containing precipitate facilitated the retention of more Na species. The $Ce_{25}Fe_{75}O_x$ (III) catalyst presented the lowest Na concentration of the mixed catalysts prepared using the Ce^{III} precursor, which could again relate to the formation of the precipitate with less carbonate species. This relationship was also noticed for Fe_2O_3 where a trace amount of Na was measured and the absence of carbonate containing precipitate was confirmed by TGA.

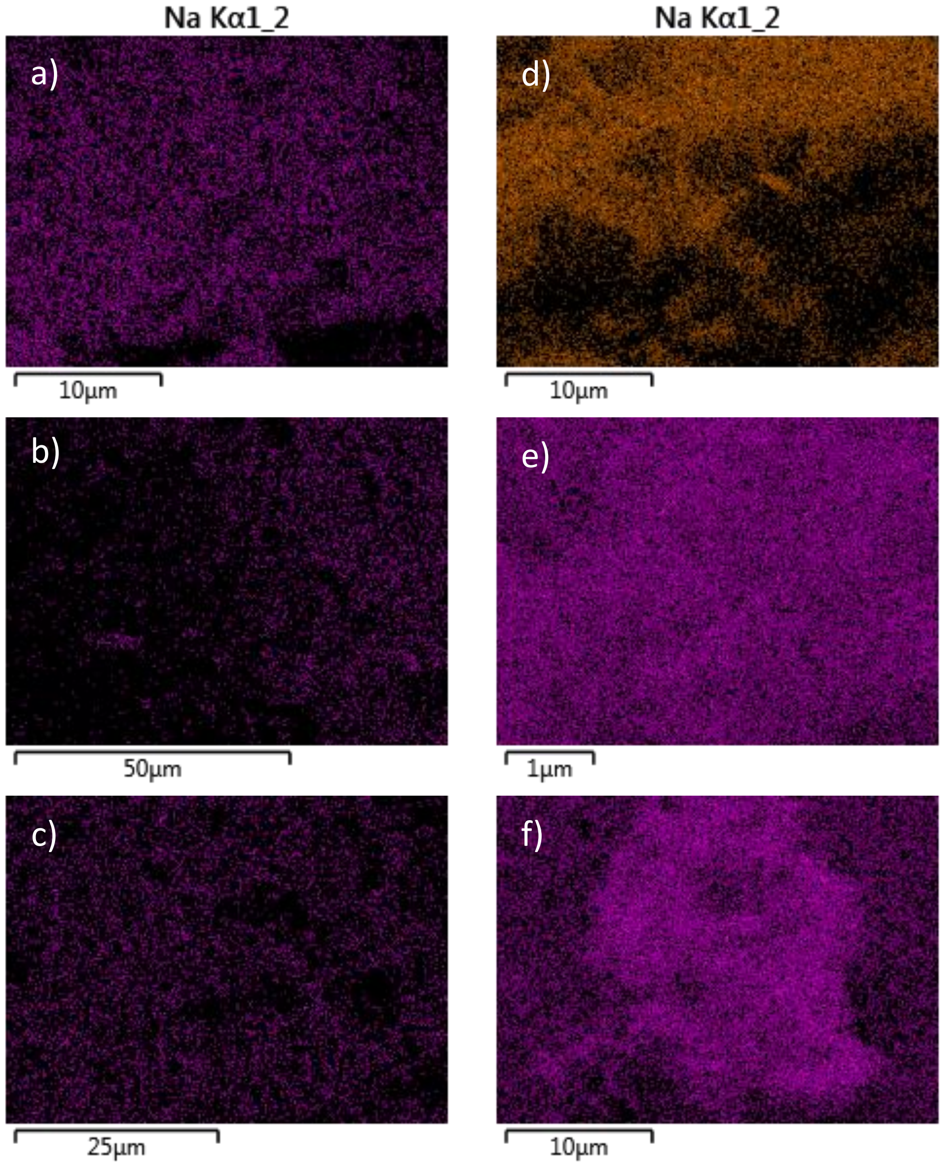

Figure 8: Na Kα EDX mapping of a) $Ce_{25}Fe_{75}O_x$ (IV), b) $Ce_{50}Fe_{50}O_x$ (IV), c) $Ce_{75}Fe_{25}O_x$ (IV), and d) $Ce_{25}Fe_{75}O_x$ (III), e) $Ce_{50}Fe_{50}O_x$ (III), f) $Ce_{75}Fe_{25}O_x$ (III) catalysts.

Determination of catalyst surface species was carried out by XPS analysis. As discussed in Chapter 3, the Ce 3d region presented ten peaks that required fitting, relating to the mixed Ce^{3+} and Ce^{4+} species [44,45]. These were all observed for both ranges of mixed $CeFeO_x$ catalysts as displayed in Figure 9a-f and fitted as shown in Chapter 3. The Ce^{3+}/Ce^{4+} ratio was also assessed from the Ce 3d spectra and is shown in Table 3. For the $CeFeO_x$ (IV) catalysts, the incorporation of Fe into the catalyst increased the surface Ce^{3+} concentration, which suggested the formation of surface defect sites [46,47]. This was in good agreement with previous studies on the incorporation of aliovalent metals into the CeO_2 structure [12,48,49]. The increased concentration of surface Ce^{3+} species occurred simultaneously with decreasing Fe content, which may indicate phase separation on the catalyst surface at higher Fe loadings. This trend also aligned with the evidence of bulk segregation, determined by XRD and EDX analysis. A similar trend was established for the $CeFeO_x$ (III) range of mixed oxide catalysts. However, the increase in Ce^{3+} surface species did not occur linearly with decreasing Fe content, where $Ce_{50}Fe_{50}O_x$ (III) presented the lowest Ce^{3+} concentration.

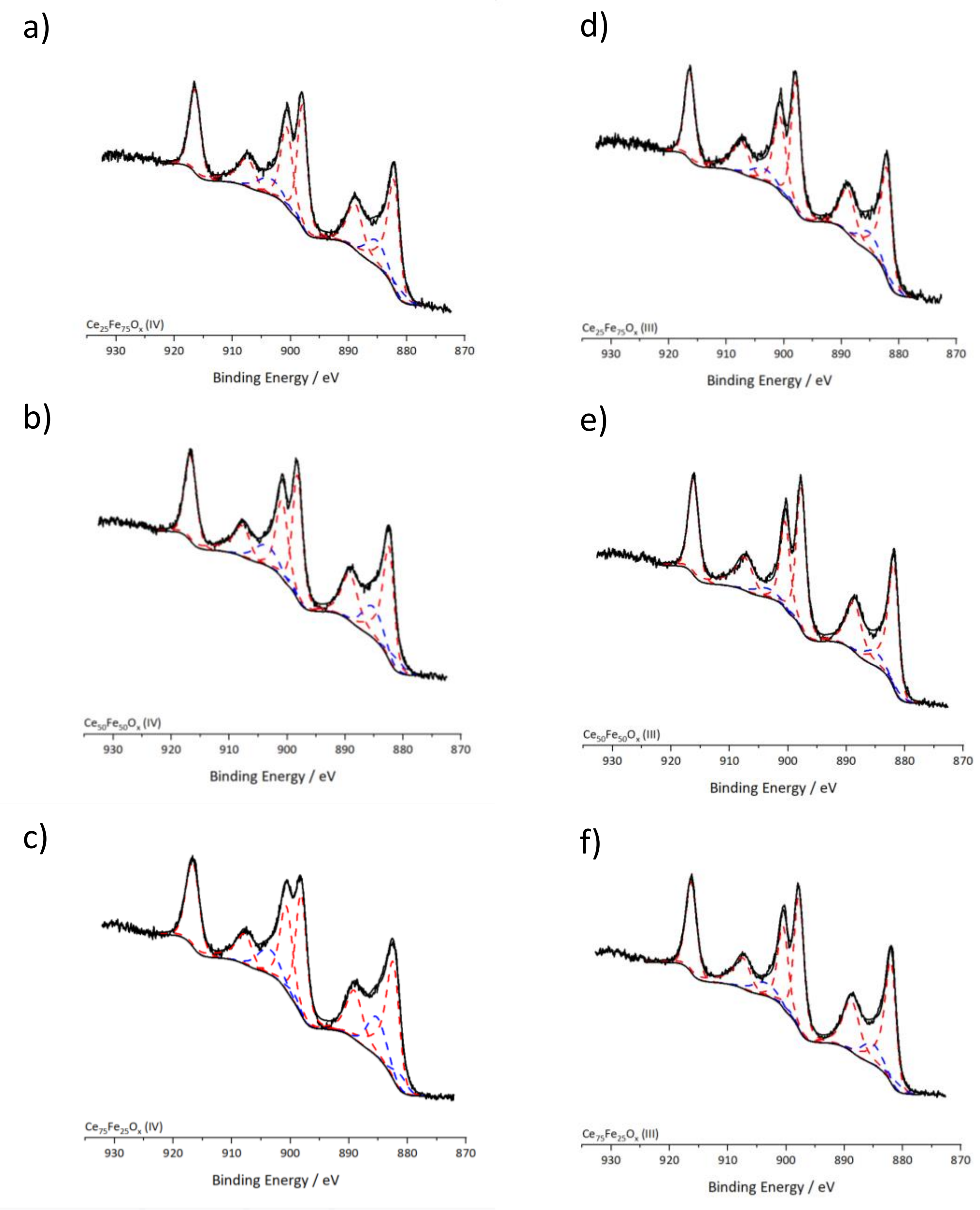

Figure 9: XPS spectra of the Ce 3d region for a) $Ce_{25}Fe_{75}O_x$ (IV), b) $Ce_{50}Fe_{50}O_x$ (IV), c) $Ce_{75}Fe_{25}O_x$ (IV), and d) $Ce_{25}Fe_{75}O_x$ (III), e) $Ce_{50}Fe_{50}O_x$ (III), f) $Ce_{75}Fe_{25}O_x$ (III) catalysts. Fitted peaks refer to Ce^{3+} (blue) and Ce^{4+} (red) oxidation states.

Table 3: Surface elemental composition of the $CeFeO_x$ (IV) and (III) catalysts, determined by XPS analysis.

Catalyst	O^β/O^α Ratio	Ce^{3+}/Ce^{4+} Ratio	XPS Ce:Fe:Na Ratio	XPS Ce :Fe Ratio
CeO_2 (IV)	0.438	0.155	93:0:7	N/A
$Ce_{25}Fe_{75}O_x$ (IV)	0.436	0.175	43:47:10	48:52
$Ce_{50}Fe_{50}O_x$ (IV)	0.455	0.211	59:41:0	59:41
$Ce_{75}Fe_{25}O_x$ (IV)	0.615	0.221	80:20:0	80:20
Fe_2O_3	0.375	N/A	100:0	N/A
CeO_2 (III)	0.289	0.089	70:0:30	N/A
$Ce_{25}Fe_{75}O_x$ (III)	0.421	0.134	29:52:19	36:64
$Ce_{50}Fe_{50}O_x$ (III)	0.469	0.095	33:33:34	50:50
$Ce_{75}Fe_{25}O_x$ (III)	0.440	0.134	53:18:29	75:25

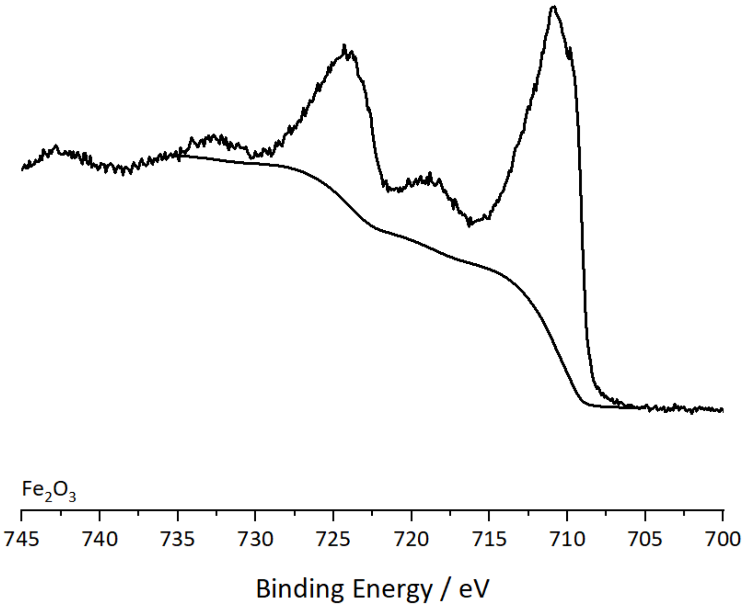

Figure 10: XPS spectrum of the Fe 2p region for the Fe_2O_3 catalyst.

Figure 10 shows the Fe 2p region of the Fe_2O_3 catalyst, analysed by XPS. The doublet peaks at 710.8 eV and 724.3 eV are due to the Fe $2p_{3/2}$ and $2p_{1/2}$ splitting respectively, commonly associated with the Fe_2O_3 material [40]. The smaller peaks identified at 718.8 eV and 732.6 eV are due to shake up satellite features, relating to the presence of Fe^{3+} species [13]. XPS analysis of the Fe 2p region (Figure 11a-f) for the mixed $CeFeO_x$ catalysts was more complex.

Doublet peaks were identified around 710.8 eV and 724.4 eV for all the mixed catalysts, which were again representative of the Fe $2p_{3/2}$ (Red fittings) and $2p_{1/2}$ (Blue fittings) splitting respectively [40]. Furthermore, satellite peaks relating to Fe^{3+} species were also present around 718.6 eV and 732.8 eV for all mixed catalysts. The doublet peaks at binding energies of 710.8 eV and 724.4 eV, relating to Fe species in the Fe^{3+} oxidation state, were in good agreement with the bulk structure of Fe_2O_3 identified by XRD analysis. In addition to the Fe $2p_{3/2}$ and $2p_{1/2}$ fittings, all catalysts showed overlapping CeO_2 Auger peaks (green fitting) [48]. The overlapping CeO_2 Auger peaks made it difficult to establish the presence of other Fe species on the catalyst surface, such as Fe^{2+} species created by defect formation. Therefore, it can only be assumed the Fe species present on the surface were in the Fe^{3+} oxidation state, from peak fittings at the observed binding energies [13,48,50]. The Ce:Fe surface ratios shown in Table 3 indicated similar results to the bulk ratios identified by EDX analysis in Table 2. However, the $Ce_{25}Fe_{75}O_x$ (IV) catalyst showed a significantly higher surface concentration of Ce, compared with the bulk EDX analysis. This difference suggested CeO_2 enrichment of the catalyst surface, which also supports the proposed phase segregation identified by bulk analysis techniques.

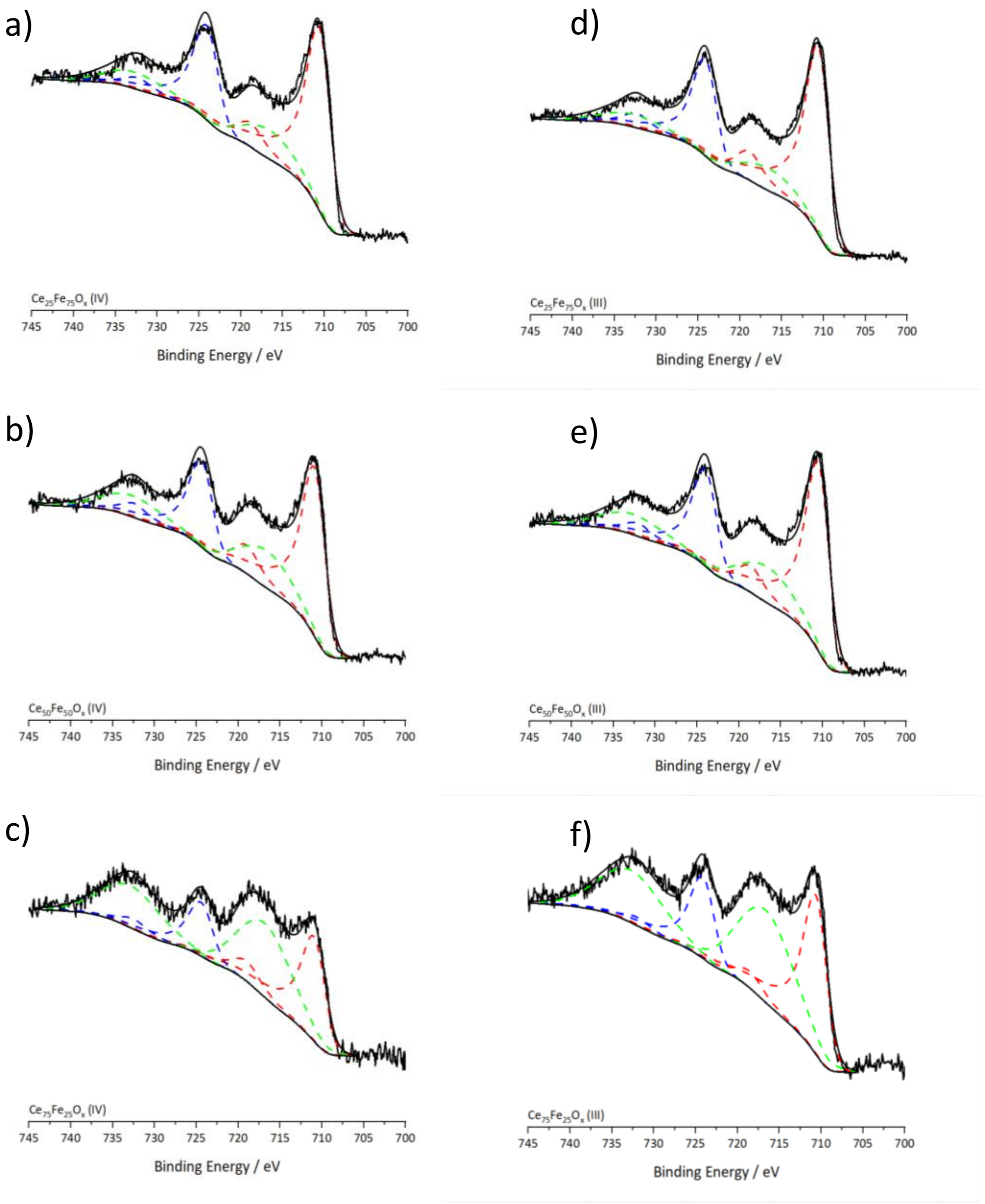

Figure 11: XPS spectra of the Fe 2p region for a) $Ce_{25}Fe_{75}O_x$ (IV), b) $Ce_{50}Fe_{50}O_x$ (IV), c) $Ce_{75}Fe_{25}O_x$ (IV), and d) $Ce_{25}Fe_{75}O_x$ (III), e) $Ce_{50}Fe_{50}O_x$ (III), f) $Ce_{75}Fe_{25}O_x$ (III) catalysts. Fitted peaks refer to Fe $2p_{3/2}$ (red), Fe $2p_{1/2}$ (blue) states and ceria Auger peak (green).

XPS analysis of the O 1s region was carried out for all the mixed $CeFeO_x$ catalysts (Figures 12a-g). As stated in Chapter 3, the fitting of the O 1s spectra is disputed in the literature [47,51]. For consistency throughout this work, the distinct peaks present around 531 eV and 529 eV for all mixed catalysts were assigned fittings, which were ascribed to defective oxygen species (O^{β}, Blue fitting) and lattice oxygen species (O^{α}, Red fitting) respectively [47,52]. Furthermore, the fitting at 532-533 eV (Orange fitting) was tentatively attributed to the presence of hydroxyl surface species, as previously discussed in Chapter 3 [53,54]. The O^{β}/ O^{α} ratio (Table 3) indicated different trends in the concentration of surface oxygen defect sites for the $CeFeO_x$ catalysts. For the $CeFeO_x$ (IV) catalysts, the surface oxygen defect site concentration was increased for $Ce_{75}Fe_{25}O_x$ (IV), whereas similar results to CeO_2 (IV) were observed for the $Ce_{25}Fe_{75}O_x$ (IV) and $Ce_{50}Fe_{50}O_x$ (IV) catalysts. This increase for $Ce_{75}Fe_{25}O_x$ (IV) was consistent with the increased Ce^{3+} surface concentration, as proposed in previous studies [46,47]. In contrast, the increased Ce^{3+} surface concentration determined for $Ce_{25}Fe_{75}O_x$ (IV) and $Ce_{50}Fe_{50}O_x$ (IV) was not directly proportional to the surface oxygen defect concentration as no significant increase was observed, suggesting the surface defect species may not have been associated with the Ce^{3+} species but rather other surface structures developed on these catalysts, possibly from segregation of Fe and Ce species [55]. The $CeFeO_x$ (III) catalysts showed an increased oxygen defect concentration compared to the CeO_2 (III) and Fe_2O_3 catalysts, however; no significant differences were observed when only comparing the mixed $CeFeO_x$ (III) catalysts. The enhanced defective surface of the $CeFeO_x$ (III) catalysts was proposed to be directly related to the increased surface Ce^{3+} species for $Ce_{25}Fe_{75}O_x$ (III) and $Ce_{75}Fe_{25}O_x$ (III). This relationship was not observed for the $Ce_{50}Fe_{50}O_x$ (III) catalyst, implying the formation of these surface defect sites were possibly related to another surface species.

As previously discussed, Na is a known catalyst poison and was shown to be present in several catalysts from EDX analysis. XPS analysis also showed good agreement with EDX analysis, indicating the presence of surface Na species for the $CeFeO_x$ catalysts (Table 3). For the $CeFeO_x$ (IV) set of catalysts, only $Ce_{25}Fe_{75}O_x$ (IV) displayed Na present from XPS analysis, which was also confirmed by the absence of the Na Auger peak in the O 1s region for $Ce_{50}Fe_{50}O_x$ (IV) and $Ce_{75}Fe_{25}O_x$ (IV) (Figures 12b and 12c). In comparison, the $CeFeO_x$ (III) range of mixed catalysts displayed significantly increased concentrations of surface Na species. The relationship between Na content and Ce precursor used, correlated with previous conclusions in Chapter 3, which found synthesis using the Ce^{III} precursor, and formation of the corresponding carbonate containing precipitate, resulted in a much higher retention of Na in the bulk and on the surface of the catalysts. However, no relationship between varying Fe content and Na retention was observed.

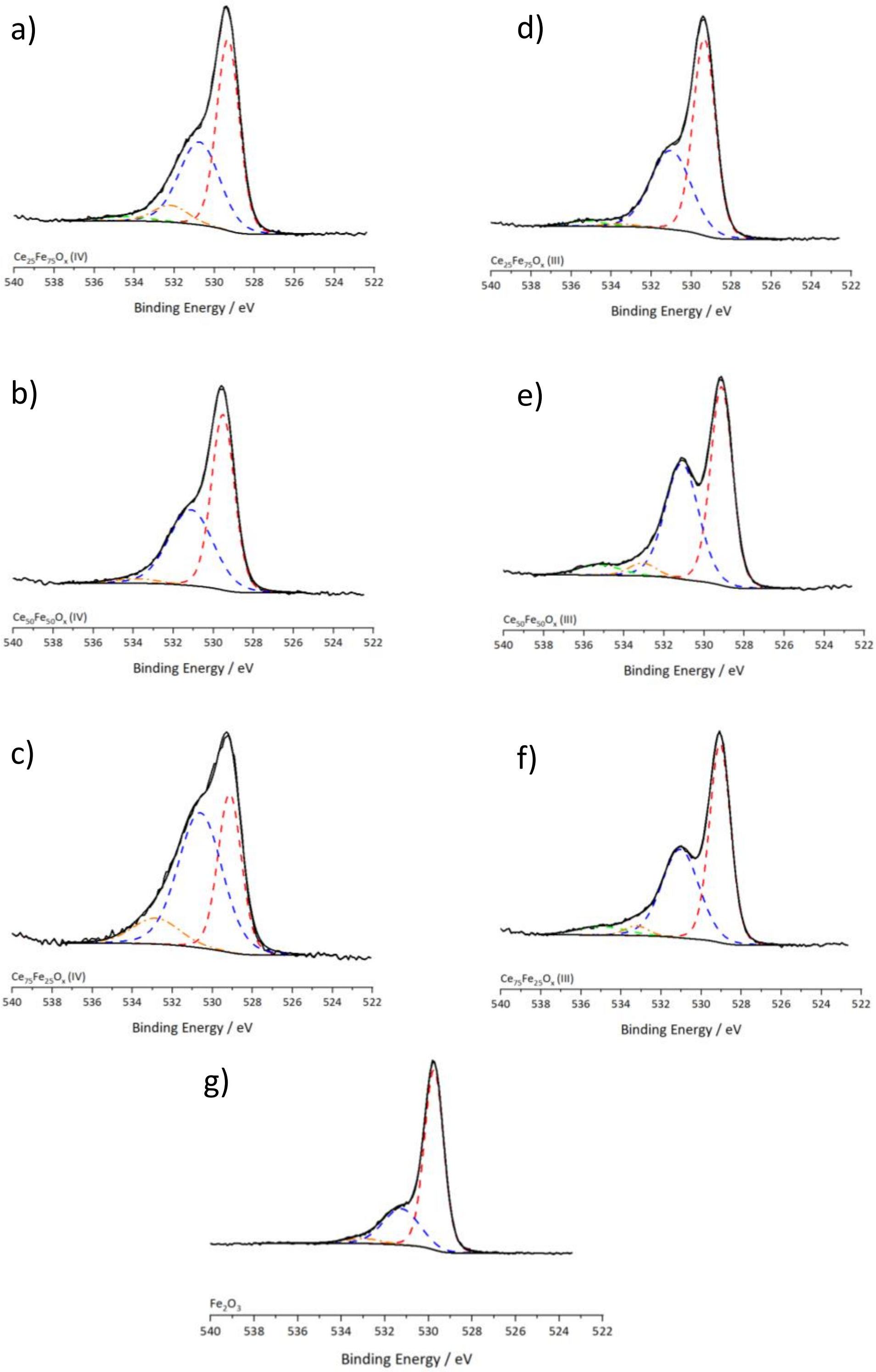

Figure 12: XPS spectra of the O 1s region for a) $Ce_{25}Fe_{75}O_x$ (IV), b) $Ce_{50}Fe_{50}O_x$ (IV), c) $Ce_{75}Fe_{25}O_x$ (IV), and d) $Ce_{25}Fe_{75}O_x$ (III), e) $Ce_{50}Fe_{50}O_x$ (III), f) $Ce_{75}Fe_{25}O_x$ (III), g) Fe_2O_3 catalysts. Fitted peaks refer to O^{α} (red), O^{β} (blue) and hydroxyl (orange) species with overlapping Na Auger peak (green) as discussed in the main text.

Redox properties of the catalysts were assessed by TPR analysis. It was previously discussed in Chapter 3 that CeO_2 based materials show two main reduction features, that of the surface and of the bulk, occurring consecutively around 500°C and 800°C [12,56]. As shown in Figures 13a and 13b, CeO_2 (III) and CeO_2 (IV) only displayed one reduction peak around

478°C and 498°C respectively, which was related to the surface reduction of CeO_2. Alternatively, the TPR profile of Fe_2O_3 was more complex with a low temperature peak, centred around 362°C, and a much broader peak ranging from 400-700°C where the analysis was stopped. The reduction profile of Fe_2O_3 has been discussed in the literature and is thought to occur stepwise, where the low temperature peak was related to the reduction of Fe_2O_3 to Fe_3O_4 [57]. Following this, the broad peak observed is thought to encompass the reduction of multiple processes, which include the reduction of Fe_3O_4 to FeO and then reduction to metallic Fe [57,58]. However, it is stated that the formation of the metastable FeO species is not always observed, as disproportionation can occur to form the Fe_3O_4 species and metallic Fe [16]. Temperatures of the predominant reduction peaks for all catalysts can be identified in Table 4.

Table 4: Reduction temperatures of the Fe and Ce species for the mixed $CeFeO_x$ (IV) and (III) catalysts, derived from TPR analysis.

Catalyst	CeO_2 Reduction Temperature / °C	Fe_2O_3 Reduction Temperature / °C	Fe_3O_4 Reduction Temperature / °C
CeO_2 (IV)	498	-	-
$Ce_{25}Fe_{75}O_x$ (IV)	-	403	560
$Ce_{50}Fe_{50}O_x$ (IV)	376	376	543
$Ce_{75}Fe_{25}O_x$ (IV)	377	377	497
Fe_2O_3	-	362	590
CeO_2 (III)	478	-	-
$Ce_{25}Fe_{75}O_x$ (III)	464	400	700
$Ce_{50}Fe_{50}O_x$ (III)	416	416	700
$Ce_{75}Fe_{25}O_x$ (III)	403	403	625

TPR profiles for the mixed $CeFeO_x$ catalysts (Figure 13a and 13b) differed when prepared using either the Ce^{IV} or Ce^{III} precursor. For the $Ce_{25}Fe_{75}O_x$ (IV) catalyst, a similar profile to the standard Fe_2O_3 profile was observed, with a low temperature peak at 403°C and broad high temperature peak centred around 560°C. It has been shown in previous studies that the intensity of the low temperature peak in mixed $CeFeO_x$ catalysts increased with increasing Fe content, suggesting this peak was related to the reduction of Fe_2O_3 species [59]. The presence of surface Fe_2O_3 species is in good agreement with XRD, EDX and XPS data confirming the segregation of the CeO_2 and Fe_2O_3 in the catalyst bulk and surface. It was difficult to assess the extent of CeO_2 reduction for this catalyst due to the predominant high temperature reduction peak, but this broad peak was shifted to lower temperatures compared with Fe_2O_3, suggesting improved reducibility of the Fe_3O_4 species from the interaction with CeO_2 species. The $Ce_{50}Fe_{50}O_x$ (IV) catalyst also exhibited a singular low temperature peak and broad high temperature peak, reminiscent of the Fe_2O_3 profile. However, it was unclear whether the peak around 376°C was solely related to Fe_2O_3 reduction, as previous studies have suggested the overlap of this peak with the improved reduction of surface Ce^{4+} species, which occurs from the interaction of Ce-O-Fe species [55]. However, the broad high temperature peak present was thought to be related to the reduction of Fe_3O_4 species, suggesting segregation of Fe and Ce species, also noted by EDX analysis. The $Ce_{75}Fe_{25}O_x$ (IV) catalyst displayed two reduction peaks at 377°C and 497°C. Similarly to the $Ce_{50}Fe_{50}O_x$ (IV) catalyst, the low temperature peak was thought to be the reduction of a combination of surface Ce^{4+} and Fe^{3+} species. Whereas, the high temperature peak was more likely related to the reduction of Fe_3O_4 species or bulk CeO_2 reduction. For all mixed $CeFeO_x$ (IV) catalysts, the low temperature reduction of Fe_2O_3 to Fe_3O_4 was supressed as this peak was shifted to slightly higher temperatures compared with the TPR profile of Fe_2O_3. This effect has been demonstrated for supported CeO_2/Fe_2O_3 catalysts, where segregated CeO_2 species increased the temperature required to reduce Fe_2O_3 [13]. In contrast, the surface Ce^{4+} reduction was shifted to lower temperatures suggesting the mixing of Ce and Fe species facilitated reduction of the CeO_2 species, which has been suggested in the literature [33,55]. In addition, the mixed $CeFeO_x$ (IV) catalysts seemed to promote the reduction of Fe_3O_4 species, as observed from the peak shift to lower temperatures.

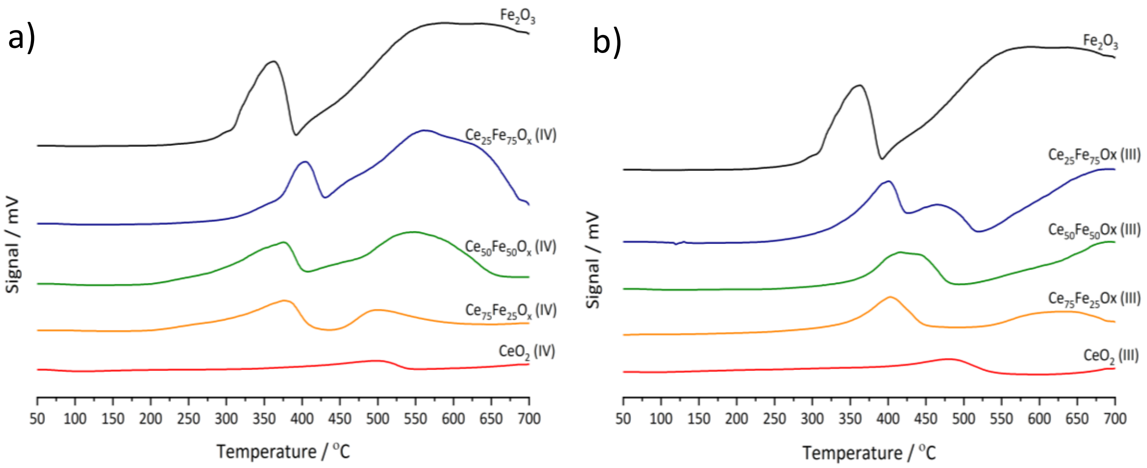

Figure 13: TPR profiles of the a) CeFeO$_x$ (IV) and b) CeFeO$_x$ (III) catalysts. Conditions: 10% H$_2$/Ar, 30 ml min^{-1}, 50-700 °C at 10 °C min^{-1}.

The TPR profiles for the CeFeO$_x$ (III) catalysts were very different to the TPR profiles for the catalysts using the Ce^{IV} precursor. The Ce$_{25}$Fe$_{75}$O$_x$ (III) catalyst displayed reduction features of both Fe$_2$O$_3$ and CeO$_2$, occurring around 400°C and 700°C for the Fe species and 464°C for the surface CeO$_2$ reduction [33]. This again suggested the phase segregation of these species on the catalyst surface, which was in good agreement with prior XPS and EDX analysis. For the Ce$_{50}$Fe$_{50}$O$_x$ (III) catalyst, a broad peak at 416°C was observed, with the beginning of another peak occurring at 700°C. The peak identified at 416°C seemed to be a combination of the reduction peaks relating to Fe$_2$O$_3$ and surface CeO$_2$ [55]. The shift of the CeO$_2$ reduction peak to lower temperatures suggested that the incorporation of Fe species improved surface CeO$_2$ reduction [13,33]. Although Fe incorporation seemed to improve CeO$_2$ reduction, the reduction of Fe$_2$O$_3$ species was slightly inhibited as identified by the peak shift to higher temperatures for Ce$_{25}$Fe$_{75}$O$_x$ (III). The Ce$_{75}$Fe$_{25}$O$_x$ (III) catalyst displayed a low temperature peak at 403°C, which was thought to resemble the combination of Fe$_2$O$_3$ and CeO$_2$ reduction, possibly from the formation of Ce-O-Fe solid solutions. In contrast to the CeFeO$_x$ (IV) catalysts, the use of the Ce^{III} precursor did not significantly improve the reducibility of the high temperature peak, thought to relate to Fe$_3$O$_4$ or bulk CeO$_2$ reduction.

4.2.3 Catalyst testing

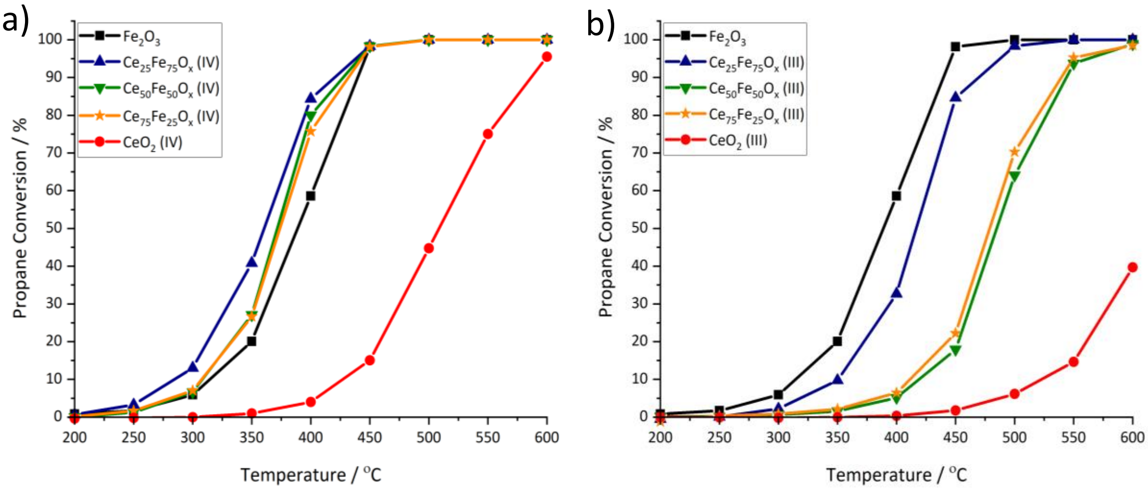

Figure 14: Catalyst activity for the total oxidation of propane using the a) $CeFeO_x$ (IV) and b) $CeFeO_x$ (III) range of catalysts. Legend refers to catalysts analysed. Conditions: 5000 ppm propane in air, 50 ml min^{-1}, GHSV = 45000 h^{-1}.

Performance of the $CeFeO_x$ (IV) and $CeFeO_x$ (III) catalysts for the total oxidation of propane are shown in Figures 14a and 14b. The main reaction product detected was CO_2 for all catalysts. The CeO_2 (IV) catalyst presented >99% selectivity to CO_2 over the temperature range, whilst at 550°C it decreased to 96% for CeO_2 (III) due to propene formation. All Fe containing catalysts showed propene formation alongside CO_2, with Fe_2O_3 having the lowest selectivity of 85% at 250°C which steadily increased to 100% at 500°C. For the $CeFeO_x$ (IV) range of mixed catalysts, propene was formed at temperatures between 200-400°C with selectivity to CO_2 increasing to 100% at 450°C. The lowest CO_2 selectivity measured for the $Ce_{25}Fe_{75}O_x$ (IV), $Ce_{50}Fe_{50}O_x$ (IV) and $Ce_{75}Fe_{25}O_x$ (IV) catalysts were 90%, 88% and 94% respectively. The $CeFeO_x$ (III) set of catalysts also showed propene formation but this occurred to a lesser extent and was observed from 300-600°C. The $Ce_{25}Fe_{75}O_x$ (III), $Ce_{50}Fe_{50}O_x$ (III) and $Ce_{75}Fe_{25}O_x$ (III) catalysts presented CO_2 selectivity of 93%, 94% and 95% respectively. From Figures 14a and 14b, the catalysts synthesised using the Ce^{IV} precursor were more active for propane total oxidation, which was in good agreement with the results obtained in Chapter 3, regarding the impact of cerium precursor. The mixed $CeFeO_x$ (IV) catalysts all presented improved conversion compared with the single oxides; however, Fe_2O_3 was shown to be more active when compared with the $CeFeO_x$ (III) mixed oxides.

Table 5: Mass and surface area normalised catalytic activity for the total oxidation of propane using the $CeFeO_x$ (IV) and $CeFeO_x$ (III) catalysts.

Catalyst	Propane Conversion / %	Surface Area Normalised Propane Oxidation[a] / mol s^{-1} m^{-2}	Mass Normalised Propane Oxidation[a] / mol s^{-1} g^{-1}
CeO_2 (IV)	3	2.52×10^{-4}	2.04×10^{-2}
$Ce_{25}Fe_{75}O_x$ (IV)	63	8.64×10^{-3}	5.88×10^{-1}
$Ce_{50}Fe_{50}O_x$ (IV)	53	4.30×10^{-3}	4.85×10^{-1}
$Ce_{75}Fe_{25}O_x$ (IV)	51	4.67×10^{-3}	4.11×10^{-1}
Fe_2O_3	39	1.45×10^{-2}	5.36×10^{-1}
CeO_2 (III)	0.2	2.37×10^{-4}	4.50×10^{-3}
$Ce_{25}Fe_{75}O_x$ (III)	21	2.97×10^{-3}	2.73×10^{-1}
$Ce_{50}Fe_{50}O_x$ (III)	3	1.18×10^{-3}	5.37×10^{-2}
$Ce_{75}Fe_{25}O_x$ (III)	4	1.59×10^{-3}	7.86×10^{-2}

a – Measured at 375°C

The surface area and mass normalised activity shown in Table 5 also indicated that the catalysts prepared using the Ce^{IV} precursor were more active for propane total oxidation. However, unlike the reaction data in Figure 14a, the surface normalised activity for Fe_2O_3 was much higher when compared with the mixed catalysts.

For the $CeFeO_x$ (IV) set of catalysts, few trends could be established relating the reaction data to the characteristics of the catalysts. As discussed in Chapter 3, catalyst surface area has been identified to affect catalytic activity for propane total oxidation, as the increased surface area creates more accessible active sites [60–62]. However, for this data set, no correlation between surface area and activity was identified, with the $Ce_{25}Fe_{75}O_x$ (IV) catalyst being the most active and having the lowest surface area of the mixed oxides. Furthermore, the surface oxygen defect concentration obtained by XPS analysis also showed little correlation to the catalyst performance, which was in contrast with previous research [63,64]. It is well documented that the redox properties of metal oxide catalysts are influential for propane total oxidation [5,9,65,66]. It is proposed that more facile reduction relates to increased active oxygen species, able to break the C-H bond of propane more easily [67], which is known to be the rate determining step of the reaction [68]. Previous research by García *et al.* has shown that CeO_2 presented the lowest activity when compared with other metal oxides, such as Fe_2O_3, for the total oxidation of propane, which was rationalised by the improved redox properties of the other metal oxide catalysts [65]. The surface normalised activity data in Table 5 is in good agreement with this conclusion, as the Fe_2O_3 catalyst was more active than all the mixed catalysts. Moreover TPR data suggested that, although the reduction of surface CeO_2 and Fe_3O_4 species were slightly improved in the mixed oxide catalysts, the reduction of Fe_2O_3 species was inhibited as the reduction peak was shifted to higher temperatures. This implies that the presence of Fe_2O_3 species was important for propane total oxidation. This conclusion is also supported by the surface normalised data, as the $Ce_{25}Fe_{75}O_x$ (IV) catalyst presented the highest surface normalised activity of the mixed oxides and showed excessive phase segregation, where Fe_2O_3 species were observed by XRD analysis. Therefore, catalytic activity of these catalysts was significantly linked to the presence of Fe_2O_3 for propane total oxidation. Although the $CeFeO_x$ (IV) mixed oxide catalysts showed worse surface normalised activity compared to the Fe_2O_3 catalyst, selectivity to CO_2 was improved upon addition of Ce. This improved selectivity could have occurred as a result of the increased active oxygen species, determined by XPS analysis, resulting in deeper oxidation.

The activity trends for the $CeFeO_x$ (III) catalysts significantly differed when compared to the $CeFeO_x$ (IV) catalysts (Figure 14b). The Fe_2O_3 catalyst was more active compared with all the $CeFeO_x$ (III) mixed oxides, which further supports the conclusions drawn from the $CeFeO_x$ (IV) data set, as the presence of extensive Fe_2O_3 segregation was not clearly identified by XRD analysis for any of the $CeFeO_x$ (III) mixed catalysts. As shown by the SEM-EDX analysis, some segregation of Fe and Ce species was identified for the $Ce_{25}Fe_{75}O_x$ (III) catalyst, which could explain the improved surface normalised activity (Table 5). Another factor to explain the poor activity of these catalysts could be the residual Na identified by EDX and XPS analysis. When compared with $Ce_{50}Fe_{50}O_x$ (III) and $Ce_{75}Fe_{25}O_x$ (III), the $Ce_{25}Fe_{75}O_x$ (III) catalyst presented much lower Na concentration whilst presenting improved activity for propane total oxidation. As previously discussed, Na is a known catalyst poison for propane total oxidation as it inhibits the oxygen mobility of the metal oxide catalysts [42,43]. It is also important to note that similar trends were observed in Chapter 3 between the different cerium precursors used, where Na retention was thought to be linked to the different precipitates formed by the Ce^{IV} and Ce^{III} precursors. For the reaction data of the mixed $CeFeO_x$ (III) catalysts in Figure 14b, a linear relationship between catalyst surface area and conversion was established (Figure 15). This is in good agreement with previous statements discussing the impact of catalyst surface area on propane total oxidation [61,62]. In contrast, no trend was observed between the surface oxygen defect site concentration and reaction data, suggesting this factor was insignificant for both sets of mixed oxide catalysts.

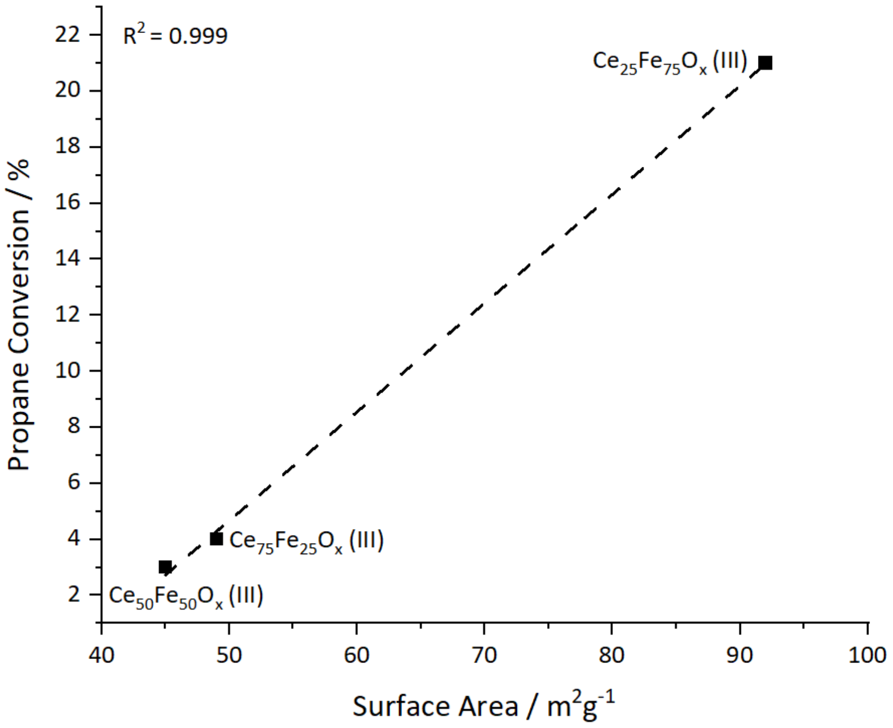

Figure 15: Relationship between surface area and propane conversion for the mixed $CeFeO_x$ (III) oxide catalysts.

Catalyst performance for the total oxidation of naphthalene using the $CeFeO_x$ (IV) and $CeFeO_x$ (III) catalysts is shown in Figures 16a and 16b. The main reaction product obtained for all catalysts was CO_2. As shown in Figure 16a, CeO_2 (IV) was the most active catalyst for naphthalene total oxidation of the $CeFeO_x$ (IV) range of catalysts. Alternatively for the $CeFeO_x$ (III) catalysts, the $Ce_{25}Fe_{75}O_x$ (III) catalyst was the most active. As identified in Chapter 3, the catalysts prepared using the Ce^{IV} precursor were more active in general for the total oxidation of naphthalene.

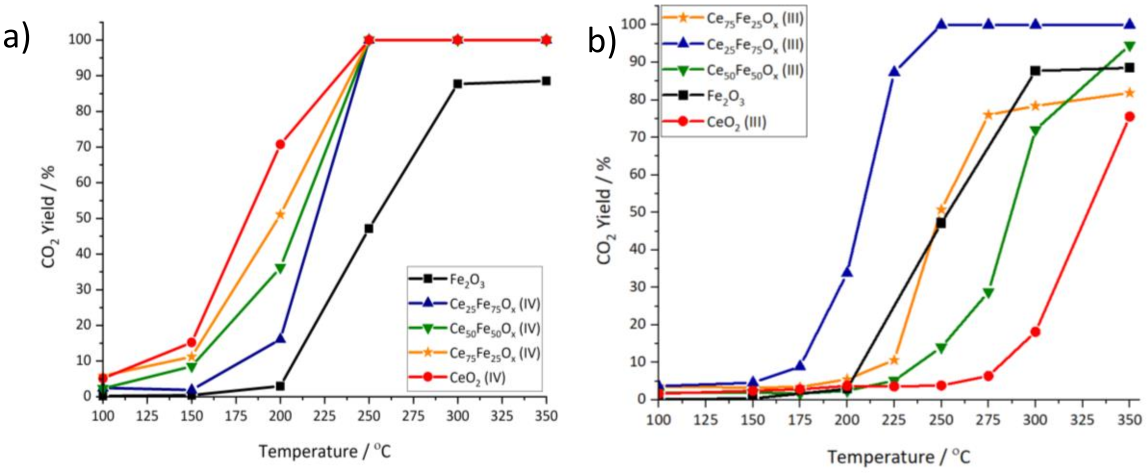

Figure 16: Catalyst activity for naphthalene total oxidation using the a) CeFeO$_x$ (IV) and b) CeFeO$_x$ (III) range of catalysts. Legend refers to catalysts analysed. Conditions: 200 ppm naphthalene in 20% O$_2$/He, 50 ml min^{-1}, GHSV = 45000 h^{-1}.

Table 6: Mass and surface area normalised catalytic activity for the total oxidation of naphthalene using the CeFeO$_x$ (IV) and CeFeO$_x$ (III) catalysts.

Catalyst	**Naphthalene Conversion / %**	**Surface Area Normalised Naphthalene Oxidation[a] / mol s^{-1} m^{-2}**	**Mass Normalised Naphthalene Oxidation[a] / mol s^{-1} g^{-1}**
CeO$_2$ (IV)	77	2.32x10^{-4}	1.88x10^{-2}
Ce$_{25}$Fe$_{75}$O$_x$ (IV)	33	1.81x10^{-4}	1.23x10^{-2}
Ce$_{50}$Fe$_{50}$O$_x$ (IV)	49	1.59x10^{-4}	1.79x10^{-2}
Ce$_{75}$Fe$_{25}$O$_x$ (IV)	61	2.23x10^{-4}	1.97x10^{-2}
Fe$_2$O$_3$	12	1.79x10^{-4}	6.59x10^{-3}
CeO$_2$ (III)	4	1.44x10^{-4}	2.73x10^{-3}
Ce$_{25}$Fe$_{75}$O$_x$ (III)	56	1.95x10^{-4}	1.79x10^{-2}
Ce$_{50}$Fe$_{50}$O$_x$ (III)	4	4.99x10^{-5}	2.27x10^{-3}
Ce$_{75}$Fe$_{25}$O$_x$ (III)	8	1.46x10^{-4}	5.85x10^{-3}

a – Measured at 210°C

For the CeFeO$_x$ (IV) set of catalysts, a linear relationship was observed between the increasing concentration of Ce present in the catalyst and improved catalytic activity (Figure 17). Research by García *et al.* has shown that, unlike propane total oxidation, CeO$_2$ was the most active metal oxide tested for naphthalene total oxidation [65]. This was thought to occur due to the weaker surface adsorption of naphthalene on CeO$_2$. The data obtained for the CeFeO$_x$ (IV) catalysts are in good agreement with these conclusions, as increased Ce content related to improved catalytic activity. It should be noted that the surface normalised activity (Table 6) also followed this trend, apart from the $Ce_{50}Fe_{50}O_x$ (IV) catalyst. This catalyst displayed a slightly decreased surface normalised activity compared with the linear relationship established for the other catalysts, which could have occurred as a result of the much higher surface area obtained for this catalyst, possibly due to the formation of a Ce-O-Fe solid solution.

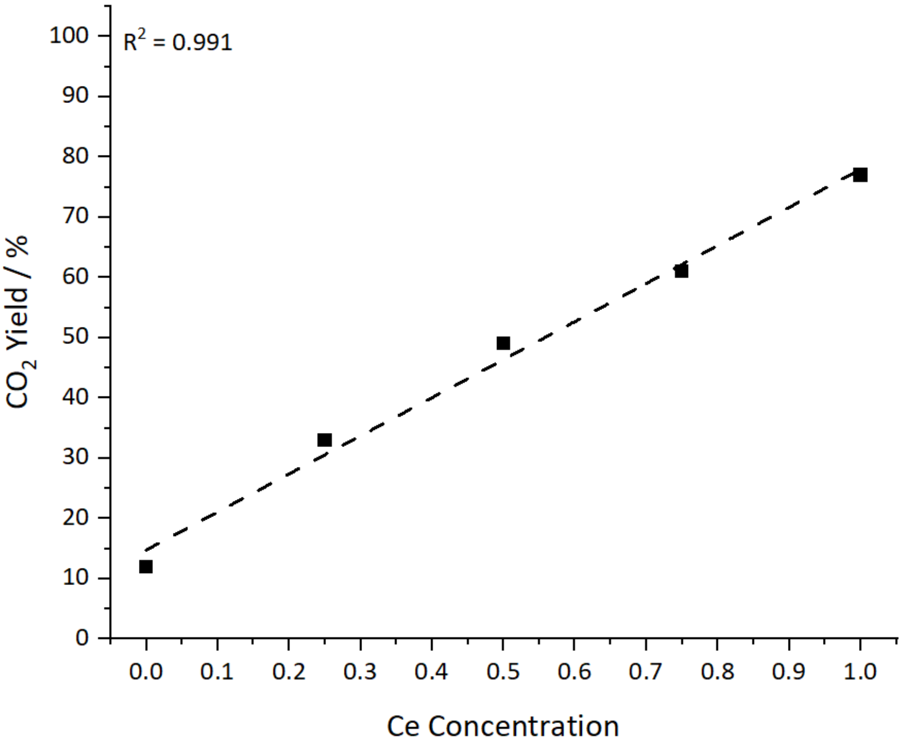

Figure 17: Relationship between Ce concentration and CO_2 yield at 210°C for the total oxidation of naphthalene using the $CeFeO_x$ (IV) range of catalysts.

The $CeFeO_x$ (III) set of catalysts displayed a contrasting trend for naphthalene total oxidation. No trend was established for the varying concentration of Ce in the mixed catalysts suggesting other factors were more important for this set of catalysts. As previously mentioned in Chapter 3, catalyst surface area has been linked to improved activity for naphthalene oxidation [69–71]. Data in Figure 16b was in good agreement with this research as the $Ce_{25}Fe_{75}O_x$ (III) exhibited the largest surface area and displayed the best activity for the mixed $CeFeO_x$ (III) catalysts. However, this factor was not linear for the data set implying other characteristics were also relevant. The residual Na present on the $CeFeO_x$ (III) catalysts could also inhibit naphthalene total oxidation. As Na has been shown to supress oxygen mobility of the catalyst [43], this factor could limit the re-oxidation of the catalyst in the redox cycle, which has been proposed as the rate determining step for naphthalene oxidation using $CeZrO_x$ catalysts [72]. This factor can help rationalise the lower activity of the $Ce_{50}Fe_{50}O_x$ (III) and $Ce_{75}Fe_{25}O_x$ (III) catalysts as they presented much higher Na concentrations, as determined by EDX and XPS analysis. The surface normalised activity data showed no significant trends related to the varying catalyst characteristics responsible for the catalytic activity, however; it should be recognised that, as a result of the very low conversions obtained by some of the catalysts, these data should be used tentatively. As for the redox properties and surface oxygen defect sites of the catalysts, no substantial trends could be identified from these characteristics for naphthalene total oxidation, which was in good agreement with previous studies [64,65].

4.3 Comparison of preparation method for $Ce_{25}Fe_{75}O_x$ (IV)

4.3.1 Catalyst characterisation

To further understand the influence of Fe_2O_3 segregation of the most active mixed catalyst ($Ce_{25}Fe_{75}O_x$ (IV)), a Fe/CeO_2 catalyst was prepared using the 25:75 Ce:Fe ratio. A wet impregnation method was utilised to deposit Fe species onto the CeO_2 support, forming segregated Fe and Ce oxide species which could then be compared against the mixed $Ce_{25}Fe_{75}O_x$ (IV) catalyst prepared by co-precipitation. This catalyst was then assessed for propane total oxidation to understand whether the incorporation of Fe into CeO_2 provided a promotional effect to Fe_2O_3 or if activity was directly influenced by the Fe species on the catalyst surface.

Table 7: Physiochemical properties of the $Ce_{25}Fe_{75}O_x$ (IV) and Fe/CeO_2 (IV) catalysts, determined by XRD and BET surface area analysis.

Catalyst	Surface Area / m^2g^{-1}	Position of Ce (111) reflection / °	Average CeO_2 Crystallite Size / nm	Average Fe_2O_3 Crystallite Size / nm	Lattice Parameter from CeO_2 (111) / nm
Fe/CeO_2 (IV)	43	28.73	8.2	22.1	0.5378
$Ce_{25}Fe_{75}O_x$ (IV)	68	28.92	3.7	28.0	0.5343

The Fe/CeO_2 (IV) catalyst presented lower surface area compared to the mixed $Ce_{25}Fe_{75}O_x$ (IV) catalyst (Table 7), which was thought to occur from surface loading of Fe species blocking pores on the CeO_2 material [73]. The bulk structure of Fe/CeO_2 (IV), assessed by

XRD analysis (Figure 18), showed features of both CeO_2 and Fe_2O_3. Peaks around 28°, 33°, 47° and 57° represented the (111), (200), (220) and (311) CeO_2 planes respectively, whilst smaller peaks at 35.78° and 54.19° were representative of the hematite Fe_2O_3 structure [24,26]. The average CeO_2 crystallite size was much smaller for the catalyst prepared by co-precipitation (Table 7). This was previously discussed to result from reduced sintering of CeO_2 from good interaction of Fe and Ce in the bulk structure, as shown in the literature [58,59]. Therefore, the larger CeO_2 crystallite size for Fe/CeO_2 (IV) suggests that limited mixing in the bulk structure occurred, which was expected from the preparation method used. However, a slight deviation from the lattice parameter of CeO_2 (IV) was observed for the Fe/CeO_2 (IV) catalyst, which was previously mentioned to occur from doping of smaller aliovalent metal ions into the bulk cubic structure [28]. This factor suggested that although Fe was deposited onto the CeO_2 (IV) surface from the preparation method used, some interaction in the bulk structure still occurred.

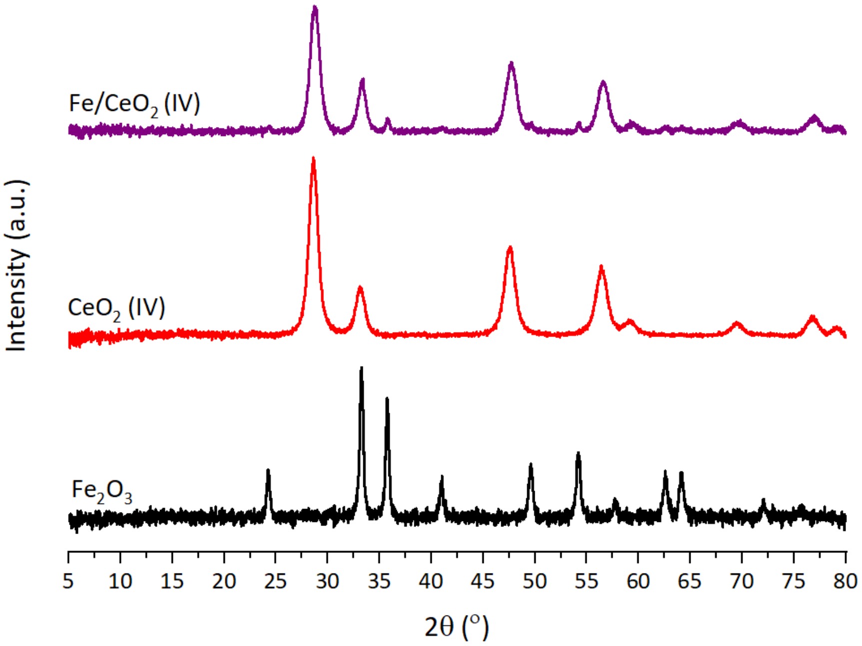

Figure 18: XRD patterns of the calcined CeO_2 (IV), Fe_2O_3 and Fe/CeO_2 (IV) catalysts.

The redox properties of the Fe/CeO_2 (IV) catalyst showed some similarities to the $CeFeO_x$ (IV) range of mixed oxides. Three distinct peaks were present in the TPR profile (Figure 19) which were thought to relate to the reduction of both Fe_2O_3 and CeO_2 surface species. The low temperature peak at 387°C was thought to relate to the reduction of Fe_2O_3 to Fe_3O_4, with the peaks at 471°C and 572°C representing CeO_2 surface reduction and Fe_3O_4 reduction respectively. As shown for the $CeFeO_x$ (IV) catalysts prepared by co-precipitation, the reduction of Fe_2O_3 was shifted to higher temperatures suggesting less facile reducibility of this species when CeO_2 was present. This was also observed for Fe/CeO_2 (IV), in addition to a shift to lower temperatures for the Fe_3O_4 reduction feature. These data suggested that no matter how Fe_2O_3 was incorporated on the CeO_2 structure, the presence of CeO_2 supressed the low temperature reduction of Fe_2O_3.

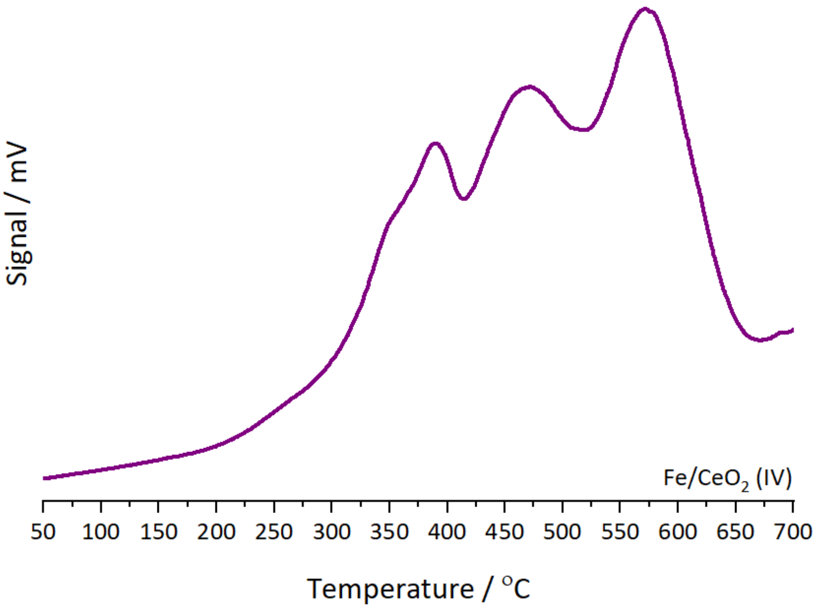

Figure 19: TPR profile of the Fe/CeO_2 (IV) catalyst. Conditions: 50-700 °C, 10% H_2/Ar, 30 ml min^{-1}.

The surface composition of the catalyst was assessed by XPS analysis. As shown in Table 8, the Ce:Fe surface ratio was much lower than expected for Fe/CeO_2, suggesting limited Fe loading on the surface by the preparation method used. However, this ratio was similar to that obtained for the $Ce_{25}Fe_{75}O_x$ (IV) catalyst, allowing for a more direct comparison of the catalyst surface. It could also be postulated from XRD data that some Fe was present in the bulk rather than the surface, causing a lower Fe concentration to be determined on the surface. When compared to $Ce_{25}Fe_{75}O_x$ (IV), an increased concentration of surface oxygen defects were observed on the Fe/CeO_2 (IV) catalyst. In contrast, a similar Ce^{3+} concentration was observed, suggesting the oxygen defect sites analysed were possibly related to different surface species such as the segregated Fe surface species [55].

Table 8: Surface elemental composition of the Fe/CeO_2 (IV) catalyst, determined by XPS analysis.

Catalyst	O^{β}/O^{α} Ratio	Ce^{3+}/Ce^{4+} Ratio	XPS Ce :Fe Ratio
Fe/CeO_2 (IV)	0.500	0.171	58:42

$Ce_{25}Fe_{75}O_x$ (IV)	0.436	0.175	48:52

4.3.2 Catalyst testing

The catalyst performance for propane total oxidation using the Fe/CeO_2 (IV), $Ce_{25}Fe_{75}O_x$ (IV) and single oxide catalysts is shown in Figure 20. For all catalysts CO_2 was the main product detected. For the Fe/CeO_2 (IV) catalyst, selectivity to CO_2 was decreased from 300 to 450°C, achieving 93% due to the formation of propene. Outside of this temperature range the selectivity to CO_2 was 100%. It was clear that the $Ce_{25}Fe_{75}O_x$ (IV) catalyst remained the most active, with Fe/CeO_2 (IV) performing worse than Fe_2O_3.

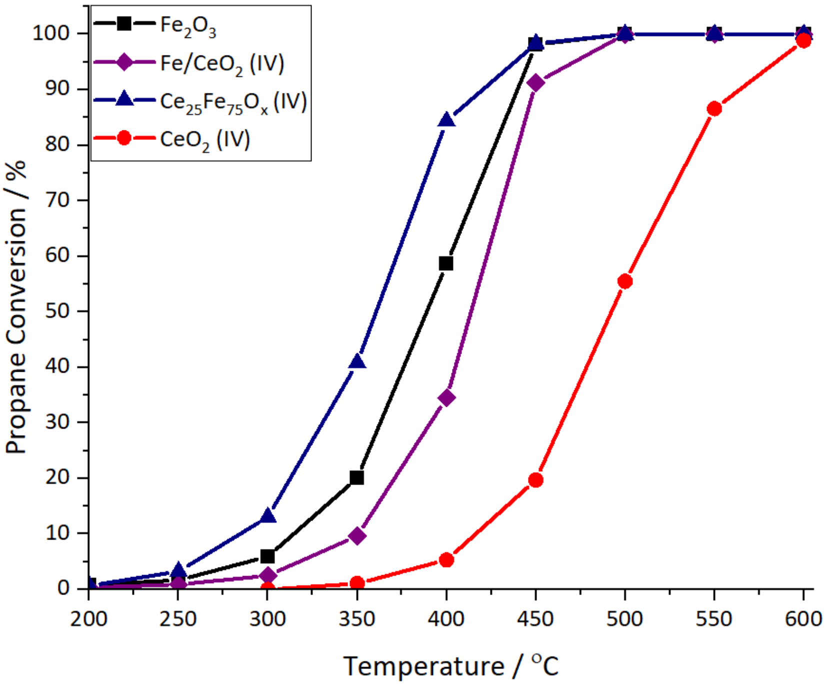

Figure 20: Catalyst activity for propane total oxidation using the mixed and supported $CeFeO_x$ (Ce:Fe Ratio = 25:75) catalysts. Legend refers to catalysts analysed. Conditions: 5000 ppm propane in air, 50 ml min^{-1}, GHSV = 45000 h^{-1}.

Surface area and mass normalised data in Table 9 showed that the Fe/CeO_2 (IV) catalyst also displayed lower surface normalised activity compared with the mixed $Ce_{25}Fe_{75}O_x$ (IV) catalyst. As discussed previously, the impressive performance of the $Ce_{25}Fe_{75}O_x$ (IV) catalyst was thought to be related to the formation of Fe_2O_3 active surface species in addition to increased surface area when compared with the single oxide Fe_2O_3 catalyst. This was supported by the increased surface normalised activity of Fe_2O_3 and previous literature demonstrating improved activity of this catalyst compared to CeO_2 [65]. The data for the Fe/CeO_2 (IV) catalyst further enhances the idea that the CeO_2 material suppressed the activity of the Fe_2O_3 species, whether it is used as a support or mixed into the bulk structure. This was proposed to happen as a result of CeO_2 mixing inhibiting the reduction of Fe_2O_3 species, as shown by TPR analysis. This was also shown in Figure 19 for the Fe/CeO_2 (IV) catalyst, suggesting that this suppression does not only occur from mixing of the materials, but also when CeO_2 is used as a support.

Table 9: Mass and surface area normalised catalytic activity of the mixed and supported $CeFeO_x$ (Ce:Fe ratio = 25:75) catalysts.

Catalyst	**Propane Conversion / %**	**Surface Area Normalised Propane Oxidation[a] / mol s^{-1} m^{-2}**	**Mass Normalised Propane Oxidation[a] / mol s^{-1} g^{-1}**
Fe/CeO_2 (IV)	22	4.10×10^{-3}	1.76×10^{-1}
$Ce_{25}Fe_{75}O_x$ (IV)	63	8.64×10^{-3}	5.88×10^{-1}
CeO_2 (IV)	3	2.52×10^{-4}	2.04×10^{-2}
Fe_2O_3	39	1.45×10^{-2}	5.36×10^{-1}

a – Measured at 375°C

4.4 Conclusions

A range of $CeFeO_x$ catalysts were prepared using either a Ce^{III} or Ce^{IV} precursor and assessed for the total oxidation of propane and naphthalene. The influence of the cerium precursor on the formation of the mixed $CeFeO_x$ catalysts was found to have a similar impact as discussed in Chapter 3, with the catalysts prepared using the Ce^{IV} precursor more active in general for propane and naphthalene total oxidation. Furthermore, the effect of cerium precursor on precipitate formation, Na retention, resulting catalyst morphology and surface area showed similar trends for the mixed $CeFeO_x$ oxides when compared to the single CeO_2 (IV) and CeO_2 (III) oxides.

The catalytic activity for propane total oxidation was linked to the formation of more active Fe_2O_3 species, increased catalyst surface area and less residual Na species, with the $Ce_{25}Fe_{75}O_x$ (IV) catalyst showing the best performance. However, when normalised for surface area, the standard Fe_2O_3 catalyst presented the highest activity. More effective propane total oxidation was proposed to occur over the active Fe_2O_3 species due to more facile reducibility of the material, with the addition of CeO_2 species supressing this reduction. It was noted that although the addition of Ce species resulted in lower catalytic activity, the selectivity to CO_2 was improved. Comparison between the preparation method used, either co-precipitation or wet impregnation, to create the best performing mixed oxide catalyst had minor influence on the catalytic activity of the Fe species, with both methods producing a less active catalyst when compared to the standard Fe_2O_3 catalyst.

An opposite effect was identified for naphthalene total oxidation, with increased Ce concentration responsible for improved catalytic activity. CeO_2 (IV) was found to be the most active catalyst for naphthalene total oxidation using the Ce^{IV} precursor. However, the $Ce_{25}Fe_{75}O_x$ (III) catalyst displayed the highest catalytic activity for the catalysts prepared using the Ce^{III} precursor. This was thought to be related to the increased surface area and decreased residual Na on the catalyst. Overall, the mixed $CeFeO_x$ catalysts prepared by either cerium precursor demonstrated insufficient catalytic activity for the total oxidation of propane or naphthalene when compared with the single metal oxides.

4.5 References

[1] C. He, J. Cheng, X. Zhang, M. Douthwaite, S. Pattisson, Z. Hao, Recent Advances in the Catalytic Oxidation of Volatile Organic Compounds: A Review Based on Pollutant Sorts and Sources, Chem. Rev. 119 (2019) 4471–4568. https://doi.org/10.1021/acs.chemrev.8b00408.

[2] P.M. Heynderickx, J.W. Thybaut, H. Poelman, D. Poelman, G.B. Marin, The total oxidation of propane over supported Cu and Ce oxides: A comparison of single and binary metal oxides, J. Catal. 272 (2010) 109–120. https://doi.org/10.1016/j.jcat.2010.03.006.

[3] X. Tang, Y. Li, X. Huang, Y. Xu, H. Zhu, J. Wang, W. Shen, MnOx–CeO2 mixed oxide catalysts for complete oxidation of formaldehyde: Effect of preparation method and calcination temperature, Appl. Catal. B Environ. 62 (2006) 265–273. https://doi.org/10.1016/j.apcatb.2005.08.004.

[4] L.F. Liotta, G. Di Carlo, G. Pantaleo, A.M. Venezia, G. Deganello, Co3O4/CeO2 composite oxides for methane emissions abatement: Relationship between Co3O4–CeO2 interaction and catalytic activity, Appl. Catal. B Environ. 66 (2006) 217–227. https://doi.org/10.1016/j.apcatb.2006.03.018.

[5] B. Solsona, T. García, R. Sanchis, M.D. Soriano, M. Moreno, E. Rodríguez-Castellón, S. Agouram, A. Dejoz, J.M. López Nieto, Total oxidation of VOCs on mesoporous iron oxide catalysts: Soft chemistry route versus hard template method, Chem. Eng. J. 290 (2016) 273–281. https://doi.org/10.1016/j.cej.2015.12.109.

[6] R. Sanchis, D. Alonso-Domínguez, A. Dejoz, M.P. Pico, I. Álvarez-Serrano, T. García, M.L. López, B. Solsona, Eco-Friendly Cavity-Containing Iron Oxides Prepared by Mild Routes as Very Efficient Catalysts for the Total Oxidation of VOCs, Materials. 11 (2018). https://doi.org/10.3390/ma11081387.

[7] J.I. Gutiérrez-Ortiz, B. de Rivas, R. López-Fonseca, J.R. González-Velasco, Catalytic purification of waste gases containing VOC mixtures with Ce/Zr solid solutions, Appl. Catal. B Environ. 65 (2006) 191–200. https://doi.org/10.1016/j.apcatb.2006.02.001.

[8] D.R. Sellick, A. Aranda, T. García, J.M. López, B. Solsona, A.M. Mastral, D.J. Morgan, A.F. Carley, S.H. Taylor, Influence of the preparation method on the activity of ceria zirconia mixed oxides for naphthalene total oxidation, Appl. Catal. B Environ. 132–133 (2013) 98–106. https://doi.org/10.1016/j.apcatb.2012.11.036.

[9] Q. Song, R. Ran, J. Ding, X. Wu, Z. Si, D. Weng, The controlled preparation and performance of Fe, Co-modified porous ceria nanorods for the total oxidation of propane, Mol. Catal. 480 (2020) 110663. https://doi.org/10.1016/j.mcat.2019.110663.

[10] F. Yang, J. Wei, W. Liu, J. Guo, Y. Yang, Copper doped ceria nanospheres: surface defects promoted catalytic activity and a versatile approach, J. Mater. Chem. A. 2 (2014) 5662–5667. https://doi.org/10.1039/C3TA15253G.

[11] D. Devaiah, L.H. Reddy, S.-E. Park, B.M. Reddy, Ceria–zirconia mixed oxides: Synthetic methods and applications, Catal. Rev. 60 (2018) 177–277. https://doi.org/10.1080/01614940.2017.1415058.

[12] Q. Wang, K.L. Yeung, M.A. Bañares, Ceria and its related materials for VOC catalytic combustion: A review, Catal. Today. 356 (2020) 141–154. https://doi.org/10.1016/j.cattod.2019.05.016.

[13] H. Li, K. Li, H. Wang, X. Zhu, Y. Wei, D. Yan, X. Cheng, K. Zhai, Soot combustion over Ce1-xFexO2-δ and CeO2/Fe2O3 catalysts: Roles of solid solution and interfacial interactions in the mixed oxides, Appl. Surf. Sci. 390 (2016) 513–525. https://doi.org/10.1016/j.apsusc.2016.08.122.

[14] M. Lykaki, S. Stefa, S.A.C. Carabineiro, P.K. Pandis, V.N. Stathopoulos, M. Konsolakis, Facet-Dependent Reactivity of Fe2O3/CeO2 Nanocomposites: Effect of Ceria Morphology on CO Oxidation, Catalysts. 9 (2019) 371. https://doi.org/10.3390/catal9040371.

[15] R. Suarez Anzorena, M.O. Mazan, A. Soldati, S.A. Larrondo, The effect of incorporation of iron in cerium oxide structure on reducibility and catalytic performance for methane oxidation in diluted streams, Ceram. Int. 45 (2019) 19757–19765. https://doi.org/10.1016/j.ceramint.2019.06.229.

[16] F.J. Perez-Alonso, I. Melián-Cabrera, M. López Granados, F. Kapteijn, J.L.G. Fierro, Synergy of FexCe1−xO2 mixed oxides for N2O decomposition, J. Catal. 239 (2006) 340–346. https://doi.org/10.1016/j.jcat.2006.02.008.

[17] N. Guillén-Hurtado, I. Atribak, A. Bueno-López, A. García-García, Influence of the cerium precursor on the physico-chemical features and NO to NO2 oxidation activity of ceria and ceria–zirconia catalysts, J. Mol. Catal. Chem. 323 (2010) 52–58. https://doi.org/10.1016/j.molcata.2010.03.010.

[18] L. Qi, Q. Yu, Y. Dai, C. Tang, L. Liu, H. Zhang, F. Gao, L. Dong, Y. Chen, Influence of cerium precursors on the structure and reducibility of mesoporous CuO-CeO2 catalysts for CO oxidation, Appl. Catal. B Environ. 119–120 (2012) 308–320. https://doi.org/10.1016/j.apcatb.2012.02.029.

[19] M. Hirano, E. Kato, Hydrothermal Synthesis of Nanocrystalline Cerium(IV) Oxide Powders, J. Am. Ceram. Soc. 82 (1999) 786–788. https://doi.org/10.1111/j.1151-2916.1999.tb01838.x.

[20] M. Hirano, E. Kato, Hydrothermal Synthesis of Two Types of Cerium Carbonate Particles, J. Mater. Sci. Lett. 18 (1999) 403–405. https://doi.org/10.1023/A:1006653305821.

[21] H. Wakita, S. Kinoshita, A Synthetic Study of the Solid Solutions in the Systems and La2(CH3)3·8H2O-Ce2(CO3)3·8H2O and La(OH)CO3–Ce(OH)CO3, Bull. Chem. Soc. Jpn. 52 (1979) 428–432. https://doi.org/10.1246/bcsj.52.428.

[22] J.-P. Jolivet, C. Chanéac, E. Tronc, Iron oxide chemistry. From molecular clusters to extended solid networks, Chem. Commun. (2004) 481–483. https://doi.org/10.1039/B304532N.

[23] C. Blanco-Andujar, D. Ortega, Q. A. Pankhurst, N.T. Kim Thanh, Elucidating the morphological and structural evolution of iron oxide nanoparticles formed by sodium carbonate in aqueous medium, J. Mater. Chem. 22 (2012) 12498–12506. https://doi.org/10.1039/C2JM31295F.

[24] A.I.Y. Tok, F.Y.C. Boey, Z. Dong, X.L. Sun, Hydrothermal synthesis of CeO2 nano-particles, J. Mater. Process. Technol. 190 (2007) 217–222. https://doi.org/10.1016/j.jmatprotec.2007.02.042.

[25] F.J. Pérez-Alonso, M. López Granados, M. Ojeda, P. Terreros, S. Rojas, T. Herranz, J.L.G. Fierro, M. Gracia, J.R. Gancedo, Chemical Structures of Coprecipitated Fe−Ce Mixed Oxides, Chem. Mater. 17 (2005) 2329–2339. https://doi.org/10.1021/cm0477669.

[26] D.E. Fouad, C. Zhang, H. El-Didamony, L. Yingnan, T.D. Mekuria, A.H. Shah, Improved size, morphology and crystallinity of hematite (α-Fe2O3) nanoparticles synthesized via the precipitation route using ferric sulfate precursor, Results Phys. 12 (2019) 1253–1261. https://doi.org/10.1016/j.rinp.2019.01.005.

[27] H. Bao, K. Qian, J. Fang, W. Huang, Fe-doped CeO2 solid solutions: Substituting-site doping versus interstitial-site doping, bulk doping versus surface doping, Appl. Surf. Sci. 414 (2017) 131–139. https://doi.org/10.1016/j.apsusc.2017.04.018.

[28] F. Lu, B. Jiang, J. Wang, Z. Huang, Z. Liao, Y. Yang, Insights into the improvement effect of Fe doping into the CeO2 catalyst for vapor phase ketonization of carboxylic acids, Mol. Catal. 444 (2018) 22–33. https://doi.org/10.1016/j.mcat.2017.05.022.

[29] J. Wang, B. Zhang, M. Shen, J. Wang, W. Wang, J. Ma, S. Liu, L. Jia, Effects of Fe-doping of ceria-based materials on their microstructural and dynamic oxygen storage and release properties, J. Sol-Gel Sci. Technol. 58 (2011) 259–268. https://doi.org/10.1007/s10971-010-2386-3.

[30] K. Polychronopoulou, A.A. AlKhoori, A.M. Efstathiou, M.A. Jaoude, C.M. Damaskinos, M.A. Baker, A. Almutawa, D.H. Anjum, M.A. Vasiliades, A. Belabbes, L.F. Vega, A.F. Zedan, S.J. Hinder, Design Aspects of Doped CeO2 for Low-Temperature Catalytic CO Oxidation: Transient Kinetics and DFT Approach, ACS Appl. Mater. Interfaces. 13 (2021) 22391–22415. https://doi.org/10.1021/acsami.1c02934.

[31] J. Wang, M. Shen, J. Wang, M. Cui, J. Gao, J. Ma, S. Liu, Preparation of FexCe1-xOy solid solution and its application in Pd-only three-way catalysts, J. Environ. Sci. 24 (2012) 757–764. https://doi.org/10.1016/S1001-0742(11)60816-4.

[32] O.H. Laguna, M.A. Centeno, G. Arzamendi, L.M. Gandía, F. Romero-Sarria, J.A. Odriozola, Iron-modified ceria and Au/ceria catalysts for Total and Preferential Oxidation of CO (TOX and PROX), Catal. Today. 157 (2010) 155–159. https://doi.org/10.1016/j.cattod.2010.04.011.

[33] O.H. Laguna, M.A. Centeno, M. Boutonnet, J.A. Odriozola, Fe-doped ceria solids synthesized by the microemulsion method for CO oxidation reactions, Appl. Catal. B Environ. 106 (2011) 621–629. https://doi.org/10.1016/j.apcatb.2011.06.025.

[34] L. Chen, P. Fleming, V. Morris, J.D. Holmes, M.A. Morris, Size-Related Lattice Parameter Changes and Surface Defects in Ceria Nanocrystals, J. Phys. Chem. C. 114 (2010) 12909–12919. https://doi.org/10.1021/jp1031465.

[35] S. Deshpande, S. Patil, S.V. Kuchibhatla, S. Seal, Size dependency variation in lattice parameter and valency states in nanocrystalline cerium oxide, Appl. Phys. Lett. 87 (2005) 133113. https://doi.org/10.1063/1.2061873.

[36] L. Spiridigliozzi, G. Dell'Agli, M. Biesuz, V.M. Sglavo, M. Pansini, Effect of the Precipitating Agent on the Synthesis and Sintering Behavior of 20 mol Sm-Doped Ceria, Adv. Mater. Sci. Eng. (2016). https://doi.org/10.1155/2016/6096123.

[37] L. Wang, H. Liu, Y. Liu, Y. Chen, S. Yang, Effect of precipitants on Ni-CeO2 catalysts prepared by a co-precipitation method for the reverse water-gas shift reaction, J. Rare Earths. 31 (2013) 969–974. https://doi.org/10.1016/S1002-0721(13)60014-9.

[38] C. Bueno-Ferrer, S. Parres-Esclapez, D. Lozano-Castelló, A. Bueno-López, Relationship between surface area and crystal size of pure and doped cerium oxides, J. Rare Earths. 28 (2010) 647–653. https://doi.org/10.1016/S1002-0721(09)60172-1.

[39] Q. Shen, G. Lu, C. Du, Y. Guo, Y. Wang, Y. Guo, X. Gong, Role and reduction of NOx in the catalytic combustion of soot over iron–ceria mixed oxide catalyst, Chem. Eng. J. 218 (2013) 164–172. https://doi.org/10.1016/j.cej.2012.12.010.

[40] B. Li, A. Raj, E. Croiset, J.Z. Wen, Reactive Fe-O-Ce Sites in Ceria Catalysts for Soot Oxidation, Catalysts. 9 (2019) 815. https://doi.org/10.3390/catal9100815.

[41] P.S. Barbato, S. Colussi, A. Di Benedetto, G. Landi, L. Lisi, J. Llorca, A. Trovarelli, CO preferential oxidation under H2-rich streams on copper oxide supported on Fe promoted CeO2, Appl. Catal. Gen. 506 (2015) 268–277. https://doi.org/10.1016/j.apcata.2015.09.018.

[42] G. Chai, W. Zhang, Y. Guo, J.L. Valverde, A. Giroir-Fendler, The Influence of Residual Sodium on the Catalytic Oxidation of Propane and Toluene over Co3O4 Catalysts, Catalysts. 10 (2020) 867. https://doi.org/10.3390/catal10080867.

[43] W. Tang, J. Weng, X. Lu, L. Wen, A. Suburamanian, C.-Y. Nam, P.-X. Gao, Alkali-metal poisoning effect of total CO and propane oxidation over Co3O4 nanocatalysts, Appl. Catal. B Environ. 256 (2019) 117859. https://doi.org/10.1016/j.apcatb.2019.117859.

[44] E. Paparazzo, Use and mis-use of x-ray photoemission spectroscopy Ce3d spectra of Ce2O3 and CeO2, J. Phys. Condens. Matter. 30 (2018) 343003. https://doi.org/10.1088/1361-648X/aad248.

[45] F. Zhang, P. Wang, J. Koberstein, S. Khalid, S.-W. Chan, Cerium oxidation state in ceria nanoparticles studied with X-ray photoelectron spectroscopy and absorption near edge spectroscopy, Surf. Sci. 563 (2004) 74–82. https://doi.org/10.1016/j.susc.2004.05.138.

[46] L. Torrente-Murciano, A. Gilbank, B. Puertolas, T. Garcia, B. Solsona, D. Chadwick, Shape-dependency activity of nanostructured CeO2 in the total oxidation of polycyclic aromatic hydrocarbons, Appl. Catal. B Environ. 132–133 (2013) 116–122. https://doi.org/10.1016/j.apcatb.2012.10.030.

[47] J.M. López, A.L. Gilbank, T. García, B. Solsona, S. Agouram, L. Torrente-Murciano, The prevalence of surface oxygen vacancies over the mobility of bulk oxygen in nanostructured ceria for the total toluene oxidation, Appl. Catal. B Environ. 174–175 (2015) 403–412. https://doi.org/10.1016/j.apcatb.2015.03.017.

[48] T. Tsoncheva, C. Rosmini, M. Dimitrov, G. Issa, J. Henych, Z. Němečková, D. Kovacheva, N. Velinov, G. Atanasova, I. Spassova, Formation of Catalytic Active Sites in Hydrothermally Obtained Binary Ceria–Iron Oxides: Composition and Preparation Effects, ACS Appl. Mater. Interfaces. 13 (2021) 1838–1852. https://doi.org/10.1021/acsami.0c16326.

[49] M. Yang, G. Shen, Q. Wang, K. Deng, M. Liu, Y. Chen, Y. Gong, Z. Wang, Roles of Oxygen Vacancies of CeO2 and Mn-Doped CeO2 with the Same Morphology in

Benzene Catalytic Oxidation, Molecules. 26 (2021) 6363. https://doi.org/10.3390/molecules26216363.

[50] H. Bao, X. Chen, J. Fang, Z. Jiang, W. Huang, Structure-activity Relation of Fe2O3–CeO2 Composite Catalysts in CO Oxidation, Catal. Lett. 125 (2008) 160–167. https://doi.org/10.1007/s10562-008-9540-3.

[51] J.P. Holgado, G. Munuera, J.P. Espinós, A.R. González-Elipe, XPS study of oxidation processes of CeOx defective layers, Appl. Surf. Sci. 158 (2000) 164–171. https://doi.org/10.1016/S0169-4332(99)00597-8.

[52] K. Wang, Y. Chang, L. Lv, Y. Long, Effect of annealing temperature on oxygen vacancy concentrations of nanocrystalline CeO2 film, Appl. Surf. Sci. 351 (2015) 164–168. https://doi.org/10.1016/j.apsusc.2015.05.122.

[53] D.R. Mullins, S.H. Overbury, D.R. Huntley, Electron spectroscopy of single crystal and polycrystalline cerium oxide surfaces, Surf. Sci. 409 (1998) 307–319. https://doi.org/10.1016/S0039-6028(98)00257-X.

[54] J. Yao, H. Lu, B. Hou, Y. Xiao, L. Jia, D. Li, J. Wang, The Promotional Effect of La Dopant on Co3O4 Catalytic Performance Towards C3H8 Combustion, Catal. Lett. 151 (2021) 1745–1754. https://doi.org/10.1007/s10562-020-03429-z.

[55] H. Liu, Y. Wu, L. Liu, B. Chu, Z. Qin, G. Jin, Z. Tong, L. Dong, B. Li, Three-dimensionally ordered macroporous Fe-doped ceria catalyst with enhanced activity at a wide operating temperature window for selective catalytic reduction of NOx, Appl. Surf. Sci. 498 (2019) 143780. https://doi.org/10.1016/j.apsusc.2019.143780.

[56] G.R. Rao, Influence of metal particles on the reduction properties of ceria-based materials studied by TPR, Bull. Mater. Sci. 22 (1999) 89–94. https://doi.org/10.1007/BF02745559.

[57] W.K. Jozwiak, E. Kaczmarek, T.P. Maniecki, W. Ignaczak, W. Maniukiewicz, Reduction behavior of iron oxides in hydrogen and carbon monoxide atmospheres, Appl. Catal. Gen. 326 (2007) 17–27. https://doi.org/10.1016/j.apcata.2007.03.021.

[58] C. Liang, Z. Ma, H. Lin, L. Ding, J. Qiu, W. Frandsen, D. Su, Template preparation of nanoscale CexFe1−xO2 solid solutions and their catalytic properties for ethanol steam reforming, J. Mater. Chem. 19 (2009) 1417–1424. https://doi.org/10.1039/B817942E.

[59] K. Li, H. Wang, Y. Wei, D. Yan, Syngas production from methane and air via a redox process using Ce–Fe mixed oxides as oxygen carriers, Appl. Catal. B Environ. 97 (2010) 361–372. https://doi.org/10.1016/j.apcatb.2010.04.018.

[60] B. Solsona, T. Garcia, E. Aylón, A.M. Dejoz, I. Vázquez, S. Agouram, T.E. Davies, S.H. Taylor, Promoting the activity and selectivity of high surface area Ni–Ce–O mixed oxides by gold deposition for VOC catalytic combustion, Chem. Eng. J. 175 (2011) 271–278. https://doi.org/10.1016/j.cej.2011.09.104.

[61] T. Garcia, S. Agouram, J.F. Sánchez-Royo, R. Murillo, A.M. Mastral, A. Aranda, I. Vázquez, A. Dejoz, B. Solsona, Deep oxidation of volatile organic compounds using ordered cobalt oxides prepared by a nanocasting route, Appl. Catal. Gen. 386 (2010) 16–27. https://doi.org/10.1016/j.apcata.2010.07.018.

[62] B. Solsona, R. Sanchis, A.M. Dejoz, T. García, L. Ruiz-Rodríguez, J.M. López Nieto, J.A. Cecilia, E. Rodríguez-Castellón, Total Oxidation of Propane Using CeO2 and CuO-CeO2 Catalysts Prepared Using Templates of Different Nature, Catalysts. 7 (2017) 96. https://doi.org/10.3390/catal7040096.

[63] P.M. Shah, J.W.H. Burnett, D.J. Morgan, T.E. Davies, S.H. Taylor, Ceria–Zirconia Mixed Metal Oxides Prepared via Mechanochemical Grinding of Carbonates for the Total

Oxidation of Propane and Naphthalene, Catalysts. 9 (2019) 475. https://doi.org/10.3390/catal9050475.

[64] P.M. Shah, A.N. Day, T.E. Davies, D.J. Morgan, S.H. Taylor, Mechanochemical preparation of ceria-zirconia catalysts for the total oxidation of propane and naphthalene Volatile Organic Compounds, Appl. Catal. B Environ. 253 (2019) 331–340. https://doi.org/10.1016/j.apcatb.2019.04.061.

[65] T. García, B. Solsona, S.H. Taylor, Naphthalene total oxidation over metal oxide catalysts, Appl. Catal. B Environ. 66 (2006) 92–99. https://doi.org/10.1016/j.apcatb.2006.03.003.

[66] S. Zhang, S. Liu, X. Zhu, Y. Yang, W. Hu, H. Zhao, R. Qu, C. Zheng, X. Gao, Low temperature catalytic oxidation of propane over cobalt-cerium spinel oxides catalysts, Appl. Surf. Sci. 479 (2019) 1132–1140. https://doi.org/10.1016/j.apsusc.2019.02.118.

[67] Z. Hu, S. Qiu, Y. You, Y. Guo, Y. Guo, L. Wang, W. Zhan, G. Lu, Hydrothermal synthesis of NiCeOx nanosheets and its application to the total oxidation of propane, Appl. Catal. B Environ. 225 (2018) 110–120. https://doi.org/10.1016/j.apcatb.2017.08.068.

[68] J.-Y. Luo, M. Meng, J.-S. Yao, X.-G. Li, Y.-Q. Zha, X. Wang, T.-Y. Zhang, One-step synthesis of nanostructured Pd-doped mixed oxides MOx-CeO2 (M=Mn, Fe, Co, Ni, Cu) for efficient CO and C3H8 total oxidation, Appl. Catal. B Environ. 87 (2009) 92–103. https://doi.org/10.1016/j.apcatb.2008.08.017.

[69] A. Aranda, B. Puértolas, B. Solsona, S. Agouram, R. Murillo, A.M. Mastral, S.H. Taylor, T. Garcia, Total Oxidation of Naphthalene Using Mesoporous CeO2 Catalysts Synthesized by Nanocasting from Two Dimensional SBA-15 and Three Dimensional KIT-6 and MCM-48 Silica Templates, Catal. Lett. 134 (2010) 110–117. https://doi.org/10.1007/s10562-009-0203-9.

[70] E.N. Ndifor, T. Garcia, B. Solsona, S.H. Taylor, Influence of preparation conditions of nano-crystalline ceria catalysts on the total oxidation of naphthalene, a model polycyclic aromatic hydrocarbon, Appl. Catal. B Environ. 76 (2007) 248–256. https://doi.org/10.1016/j.apcatb.2007.05.027.

[71] T. Garcia, D. Sellick, F. Varela, I. Vázquez, A. Dejoz, S. Agouram, S.H. Taylor, B. Solsona, Total oxidation of naphthalene using bulk manganese oxide catalysts, Appl. Catal. Gen. 450 (2013) 169–177. https://doi.org/10.1016/j.apcata.2012.10.029.

[72] A. Bampenrat, V. Meeyoo, B. Kitiyanan, P. Rangsunvigit, T. Rirksomboon, Catalytic oxidation of naphthalene over CeO2–ZrO2 mixed oxide catalysts, Catal. Commun. 9 (2008) 2349–2352. https://doi.org/10.1016/j.catcom.2008.05.029.

[73] R. Bonelli, S. Albonetti, V. Morandi, L. Ortolani, P.M. Riccobene, S. Scirè, S. Zacchini, Design of nano-sized FeOx and Au/FeOx catalysts supported on CeO2 for total oxidation of VOC, Appl. Catal. Gen. 395 (2011) 10–18. https://doi.org/10.1016/j.apcata.2011.01.017.

5. The modification of $CeZrO_x$ catalysts by the addition of transition metal dopants for propane and naphthalene total oxidation.

5.1 Introduction

As mentioned previously (Chapters 3 and 4), VOCs present concerns for human health and the environment due to the numerous adverse effects presented by this group of compounds [1,2]. Of the many VOCs, propane and naphthalene are excellent models for aliphatic and polyaromatic VOCs respectively. Short chain aliphatic VOCs are known to be difficult to remove from the atmosphere, with propane regularly studied as a suitable model compound for aliphatic VOC removal [3–5]. Whereas naphthalene, the simplest polyaromatic compound, has been studied as a suitable model for polyaromatic VOCs, which are carcinogenic in nature [6,7].

Catalytic oxidation has been identified as an effective method for VOC removal from dilute waste streams, as a result of the lower energy requirements and production of more environmentally benign products compared with standard thermal oxidation [8,9]. As discussed in Chapter 3, CeO_2 has been established as an effective oxidation catalyst. The beneficial characteristics relating to the redox properties, oxygen storage capacity (OSC) and oxygen mobility of CeO_2 have made it a prominent choice of catalyst for various oxidation reactions [10–12]. However, as with many metal oxide catalysts, CeO_2 can exhibit poor thermal stability and worse catalytic activity compared to supported metal catalysts.

Methods to improve the activity and stability of metal oxide catalysts have resulted in the development of mixed metal oxide catalysts, where two or more metals are incorporated into the final catalyst [13–15]. The incorporation of ZrO_2 into the CeO_2 structure has shown good activity for many oxidation reactions [16–18]. In particular, the replacement of CeO_2 with $CeZrO_x$ has been prevalent in the three-way catalyst, due to promotion of OSC and thermal stability of these catalysts [19]. The dissolution of ZrO_2 into the cubic fluorite CeO_2 structure has been shown to affect the catalyst properties, increasing the oxygen mobility which then improves catalytic activity for VOC oxidation [18,20]. Furthermore, the preparation of $CeZrO_x$ catalysts have been shown to improve catalyst stability as the incorporation of ZrO_2 into the lattice can reduce sintering of CeO_2 crystallites [21]. Whilst the use of mixed metal oxide catalysts have displayed improved catalytic activity, other methods; such as doping small amounts of metal into metal oxide catalysts, have also established improved catalytic activity for VOC oxidation [22–24]. Doping transition metals into $CeZrO_x$ catalysts has previously shown improved catalytic activity for soot oxidation and light hydrocarbon oxidation [25,26]. Therefore, the improvement of these frequently used catalysts, using small quantities of cheap and abundant transition metals, provides a promising area of research.

Previous research shows the incorporation of small amounts of ZrO_2 into the CeO_2 lattice results in the best activity for propane and naphthalene oxidation [27,28]. Hence, in this work, the preparation of a $Ce_{90}Zr_{10}O_x$ catalyst was carried out and compared to doped $Ce_{90}Zr_{10}M_1O_x$ catalysts for the total oxidation of propane and naphthalene VOCs. Cu, Co and Fe transition metals were chosen due to the cheap and abundant nature of the materials. Catalysts were prepared by co-precipitation and characterised by using Powder X-Ray Diffraction (XRD), Temperature Programmed Reduction (TPR), Scanning Electron Microscopy-Energy-Dispersive X-Ray analysis (SEM-EDX), X-Ray Photoelectron Spectroscopy (XPS), Laser Raman Spectroscopy, and Brunauer-Emmett-Teller (BET) surface area analysis.

5.2 Results

5.2.1 Catalyst characterisation

Table 1: Physiochemical properties of the calcined $Ce_{90}Zr_{10}M_1O_x$ catalysts.

Catalyst	Surface Area / $m^2 g^{-1}$	Position of Ce (111) reflection / °	Average Ce crystallite size / nm	Lattice Parameter / nm	A_{600}/A_{463}	FWHM
$Ce_{90}Zr_{10}O_x$	34	28.61	6.7	0.5400	0.053	24.9
$Ce_{90}Zr_{10}Fe_1Ox$	63	28.63	6.4	0.5396	0.077	34.5
$Ce_{90}Zr_{10}Cu_1O_x$	49	28.61	7.5	0.5399	0.129	24.2
$Ce_{90}Zr_{10}Co_1O_x$	40	28.59	8.6	0.5404	0.093	20.1

XRD patterns shown in Figure 1 indicate similar bulk structures for all catalysts. Only patterns representing the cubic fluorite CeO_2 structure were measured for all catalysts, with dominant reflections around 29°, 33°, 48° and 57°, corresponding to (111), (200), (220) and (311) lattice planes, respectively [29]. The absence of any reflections relating to ZrO_2 or transition metal species implies the dopant metals were highly dispersed within the cubic CeO_2 structure. Evidence of transition metal incorporation into the bulk structure could be determined by the changes seen in the lattice parameter (Table 1). When Fe was incorporated into the $Ce_{90}Zr_{10}O_x$ structure, contraction of the lattice parameter occurred, which was expected due to the smaller ionic radius compared with Ce^{4+} [30]. This effect was also observed for the $Ce_{90}Zr_{10}Cu_1O_x$ catalyst, but to a lesser extent. It has previously been proposed that Cu incorporation into the cubic CeO_2 structure can occur by a substitution mechanism, where similar sized Cu^+ ions replace Ce^{4+} ions and charge neutrality is maintained by the formation of oxygen vacancies [31]. The $Ce_{90}Zr_{10}Co_1O_x$ catalyst presented a larger lattice parameter, although the ionic radius of Co is smaller than Ce^{4+} [32]. This was unexpected and suggests the incorporation of Zr and Co into the cubic CeO_2 structure occurred by another mechanism, possibly as a result of an interstitial substitution [33]. On the other hand, the lattice expansion of the cubic structure could be related to the formation of more Ce^{3+} species as this has been shown to affect the CeO_2 lattice parameter in previous literature [34].

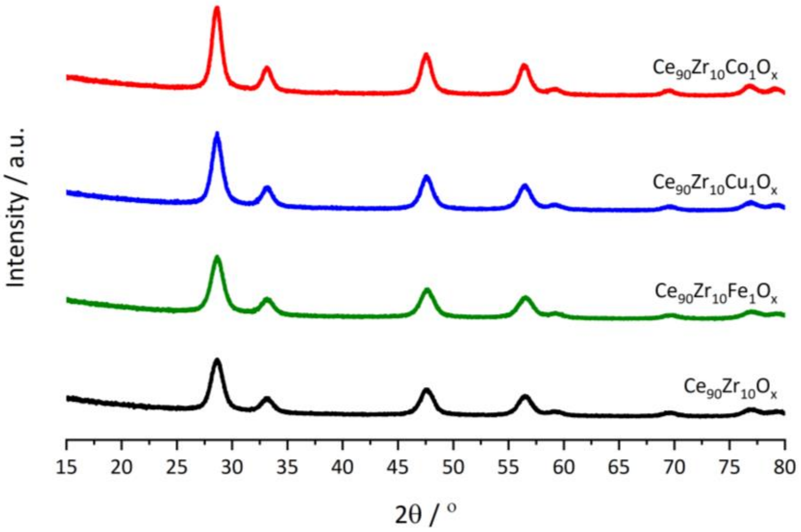

Figure 1: XRD patterns of the calcined $Ce_{90}Zr_{10}M_1O_x$ catalysts.

Ce crystallite sizes, determined by the Scherrer equation (Table 1), showed slight variation with the addition of transition metals. The incorporation of Cu and Co resulted in a larger crystallite size, whereas; the crystallite size was similar (error = ±0.3 nm) with the addition of Fe into the preparation method. The surface area (Table 1) of all doped catalysts increased with addition of dopants. An inverse relationship between crystallite size and surface area has been demonstrated for cerium oxide based catalysts in previous literature [35], and was mostly observed for the doped $Ce_{90}Zr_{10}M_1O_x$ catalysts. However, this trend was not consistent for the $Ce_{90}Zr_{10}O_x$ catalyst, suggesting the change in surface area was also affected by other factors, possibly relating to differing porosity or surface impurities of the catalysts [36].

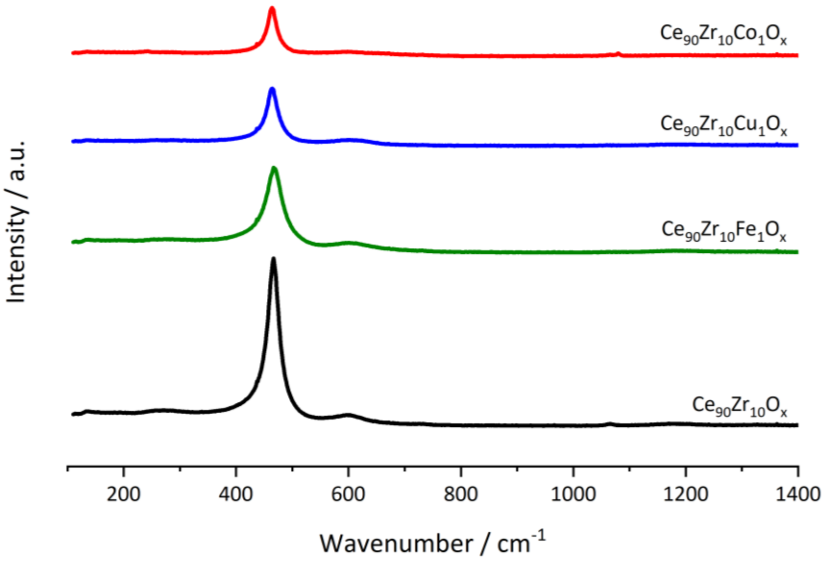

Figure 2: Laser Raman spectra of the calcined $Ce_{90}Zr_{10}M_1O_x$ catalysts.

Two main bands were displayed in the laser Raman spectra (Figure 2), one intense band at 463 cm^{-1} relating to the F_{2g} vibrational mode of CeO_2, and another less intense band centred around 600 cm^{-1}, which was associated with the presence of extrinsic bulk defect sites [37]. The defect band around 600 cm^{-1} is mainly attributed to Frenkel type defects in undoped CeO_2 materials, whereby oxygen anions are positioned in interstitial sites forming vacancies [38]. However, in doped materials, other components relating to extrinsic defects can become present in this region [39]. Hence, deconvolution of the broad band is difficult and can refer to multiple types of bulk defects within the catalysts. It has been previously demonstrated in the literature that the ratio between the bands at 463 cm^{-1} and 600 cm^{-1} (A_{600}/A_{463}) can be used to quantify the concentration of bulk lattice defect sites in these types of materials [29]. Table 1 shows that the incorporation of transition metals into the $Ce_{90}Zr_{10}O_x$ catalyst increased the concentration of defect sites, following the order:

$Ce_{90}Zr_{10}Cu_1O_x > Ce_{90}Zr_{10}Co_1O_x > Ce_{90}Zr_{10}Fe_1O_x > Ce_{90}Zr_{10}O_x$

These data further acknowledges conclusions drawn from the lattice parameters determined by XRD analysis, as the substitution of large Ce^{4+} ions for smaller aliovalent transition metal ions caused structural changes, resulting in the formation of oxygen defects occurring to maintain charge neutrality [39]. As discussed in Chapter 3, the FWHM of the F_{2g} band has previously been related to the defect concentration in CeO_2 based materials [40]. This showed a good correlation with the increased A_{600}/A_{463} ratio calculated for the $Ce_{90}Zr_{10}Fe_1O_x$ catalyst compared to the undoped $Ce_{90}Zr_{10}O_x$ catalyst. Although, the FWHM was similar to $Ce_{90}Zr_{10}O_x$ for the $Ce_{90}Zr_{10}Cu_1O_x$ and $Ce_{90}Zr_{10}Co_1O_x$ catalysts, an inverse relationship between crystallite size and FWHM has been demonstrated in the literature [41], suggesting that the combination of these competing factors occurred for these catalysts.

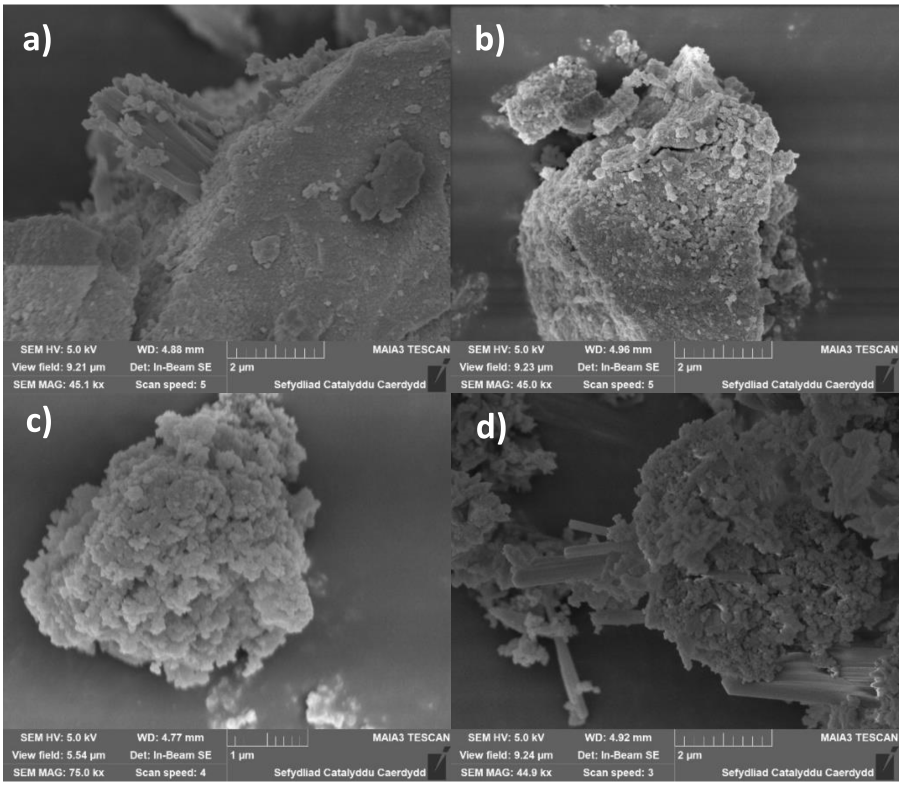

Figure 3: SEM images of a)$Ce_{90}Zr_{10}O_x$ b)$Ce_{90}Zr_{10}Fe_1O_x$ c)$Ce_{90}Zr_{10}Cu_1O_x$ d)$Ce_{90}Zr_{10}Co_1O_x$ catalysts.

SEM images shown in Figures 3a-d indicated varying morphologies for all catalysts. The $Ce_{90}Zr_{10}O_x$ and $Ce_{90}Zr_{10}Fe_1O_x$ catalysts showed well defined porous particles, whereas; the $Ce_{90}Zr_{10}Cu_1O_x$ and $Ce_{90}Zr_{10}Co_1O_x$ catalysts displayed a cauliflower type morphology. For the $Ce_{90}Zr_{10}O_x$ and $Ce_{90}Zr_{10}Co_1O_x$ catalysts (Figures 3a & 3d), significant needle growth could also be identified emanating from the main structures. EDX analysis of these needle growths (Figures 4a and 4b) showed a large accumulation of Na, suggesting residual Na was not removed effectively from these catalysts. Previous research by Tang *et al.* has demonstrated that alkali metals, such as Na, can act as a poison for the total oxidation of propane [42], hence it is important to quantify the amount of residual Na present on the catalysts. As shown by the EDX Ce:O:Na ratio (Table 3), both $Ce_{90}Zr_{10}O_x$ and $Ce_{90}Zr_{10}Co_1O_x$ had a much larger quantity of Na which is in agreement with the appearance of the needle-like growths shown in the SEM images. A homogeneous distribution of Ce and Zr was also identified by EDX analysis of the catalysts (Figure 5). However, all catalysts were shown to be Ce rich, with experimental Ce:Zr:M ratios not matching expected theoretically synthesised ratios (Table 3).

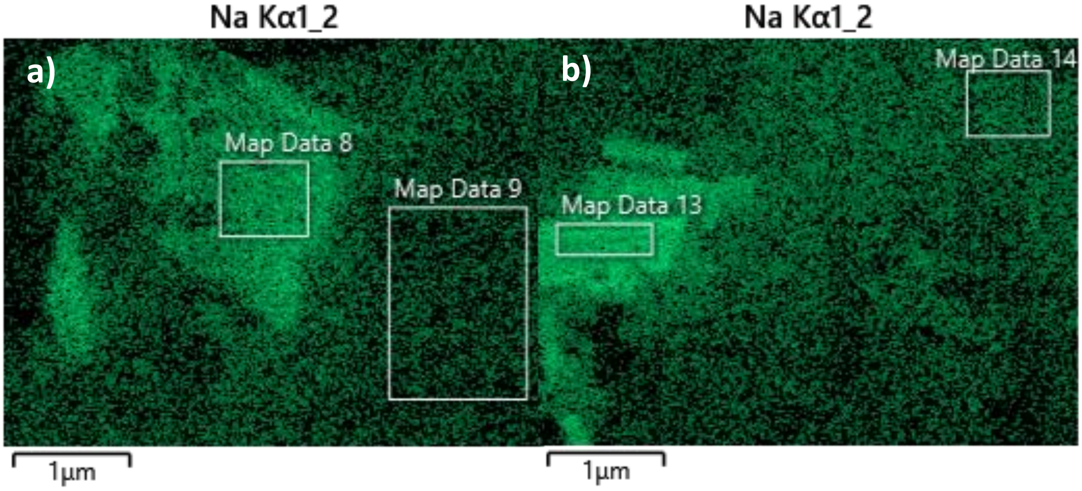

Figure 4: EDX mapping of Na for a) $Ce_{90}Zr_{10}O_x$ and b) $Ce_{90}Zr_{10}Co_1O_x$ catalysts.

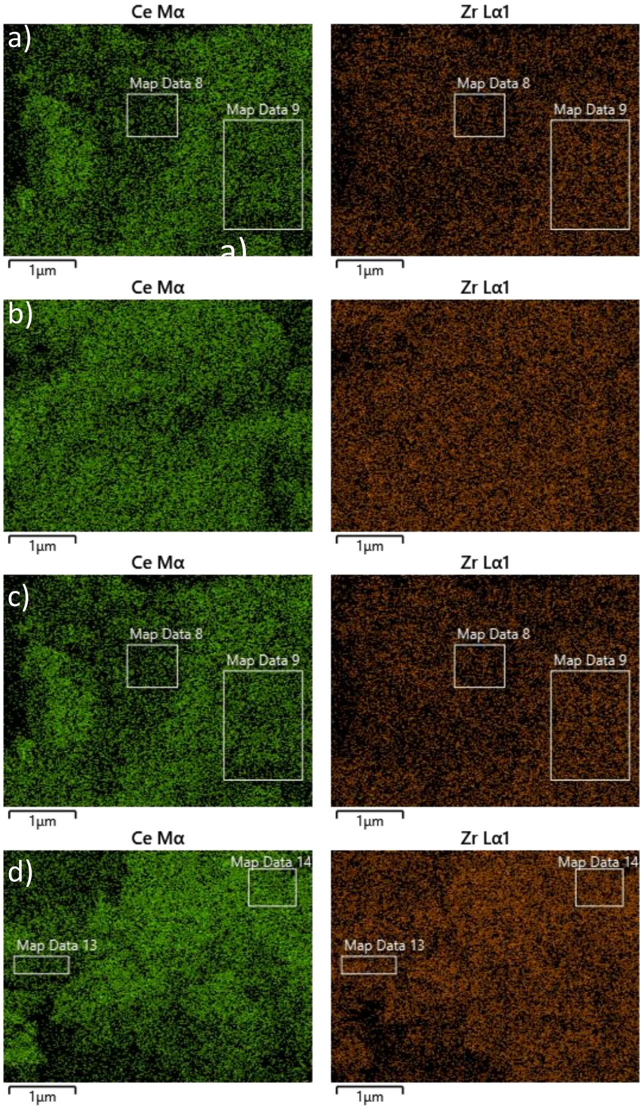

Figure 5: EDX mapping of Ce and Zr elements for a) $Ce_{90}Zr_{10}O_x$ b) $Ce_{90}Zr_{10}Fe_1O_x$ c) $Ce_{90}Zr_{10}Cu_1O_x$ d) $Ce_{90}Zr_{10}Co_1O_x$ catalysts.

Table 2: Reduction temperature and surface normalised H_2 consumption of the reduction peaks, determined by TPR analysis for the $Ce_{90}Zr_{10}M_1O_x$ catalysts.

Catalyst	TPR Peak Position / °C	H_2 Consumption per surface area /μmol m^{-2}
$Ce_{90}Zr_{10}O_x$	488	0.820
$Ce_{90}Zr_{10}Fe_1Ox$	482	0.555
$Ce_{90}Zr_{10}Cu_1O_x$	440	0.741
$Ce_{90}Zr_{10}Co_1O_x$	416	0.597

From the TPR profiles (Figure 6), only one main reduction peak was observed for all catalysts. For the $Ce_{90}Zr_{10}O_x$ catalyst, this peak occurred at 488°C and has previously been attributed to the bulk and surface reduction of the $CeZrO_x$ solid solution [18,43]. No additional peaks were present relating to the reduction of the transition metal dopants, indicating these species were limited on the catalyst surface. These data are in agreement with the XRD data showing the incorporation of the dopants into the $Ce_{90}Zr_{10}O_x$ lattice. Previous research has shown that the addition of aliovalent metal ions into $CeZrO_x$ allows for more facile reduction of the catalyst, as a result of improved oxygen mobility [44]. This trend is reciprocated by the data as the addition of the transition metals to the $Ce_{90}Zr_{10}O_x$ catalyst results in lower reduction temperatures for all catalysts (Table 2), with $Ce_{90}Zr_{10}Co_1O_x$ displaying the lowest reduction temperature. These data are also supported by the increased number of bulk defects, identified by Laser Raman spectroscopy, which have been stated to improve oxygen mobility and reducibility [45,46]. Interestingly, the surface normalised H_2 consumption (Table 2) does not follow the same trend as the ease of reducibility, with the undoped $Ce_{90}Zr_{10}O_x$ catalyst exhibiting the highest H_2 consumption.

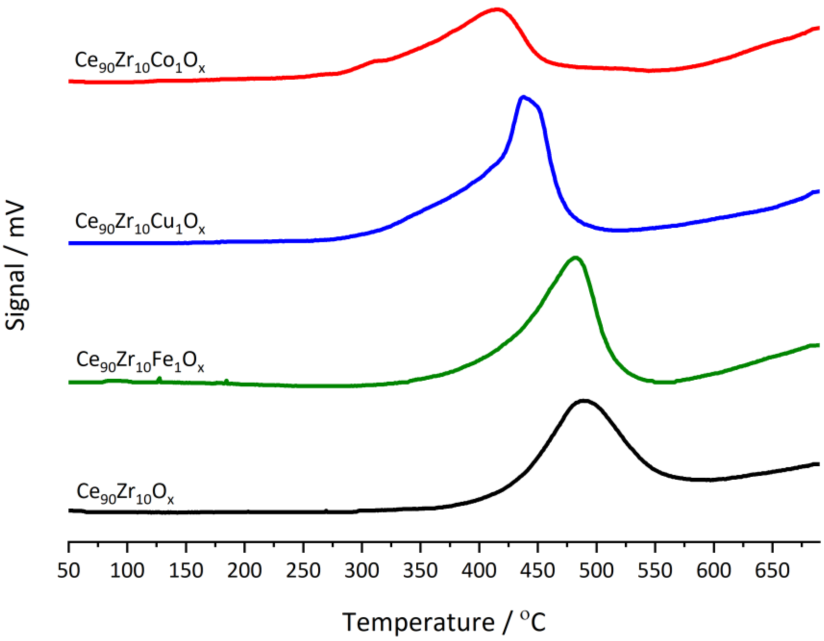

Figure 6: Reduction profiles of $Ce_{90}Zr_{10}M_1O_x$ catalysts, analysed by TPR.

Core-level Ce 3d photoelectron spectra for all catalysts are shown in Figure 7a. Fitting of these spectra was carried out as shown in previous chapters (Chapter 3, Figure 9), with peaks divided into the Ce^{3+} and Ce^{4+} oxidation states. Peaks denoted v_0, v’, u_0 and u’ were used to calculate the concentration of Ce^{3+} and v, v’’, v’’’, u, u’’ and u’’’ used to represent the Ce^{4+} oxidation state [47]. The ratio of Ce^{3+}/Ce^{4+} (Table 3) indicates slight increases in surface Ce^{3+} concentration on the $Ce_{90}Zr_{10}Fe_1O_x$ and $Ce_{90}Zr_{10}Co_1O_x$ catalysts, suggesting a more defective surface [48]. The defective surface caused by the Ce^{3+} species has been linked to the formation of surface oxygen vacancies [49], which is thought to promote more active oxygen species [50]. The increased Ce^{3+} concentration shown by the XPS data could also be used to rationalise the lower H_2 consumption obtained for the $Ce_{90}Zr_{10}Fe_1O_x$ and $Ce_{90}Zr_{10}Co_1O_x$ catalysts; as the surface would already be partially reduced, leading to decreased oxygen species available due to more surface vacancies. All catalysts displayed two low intensity peaks within the Zr 3d region (Figure 7b), highlighting the presence of Zr species on the catalyst surface. Peaks at 181.5 eV and 184.0 eV represented the Zr $3d_{5/2}$ and $3d_{3/2}$ splitting for Zr^{4+} species respectively [51]. However, no peaks relating to the transition metals were identified by XPS analysis. This is in contrast to EDX analysis where some metal species could be quantified (Table 3), indicating that the metals were limited on the catalyst surface and more likely well dispersed within the bulk of the catalyst, or below the detection limit of the surface.

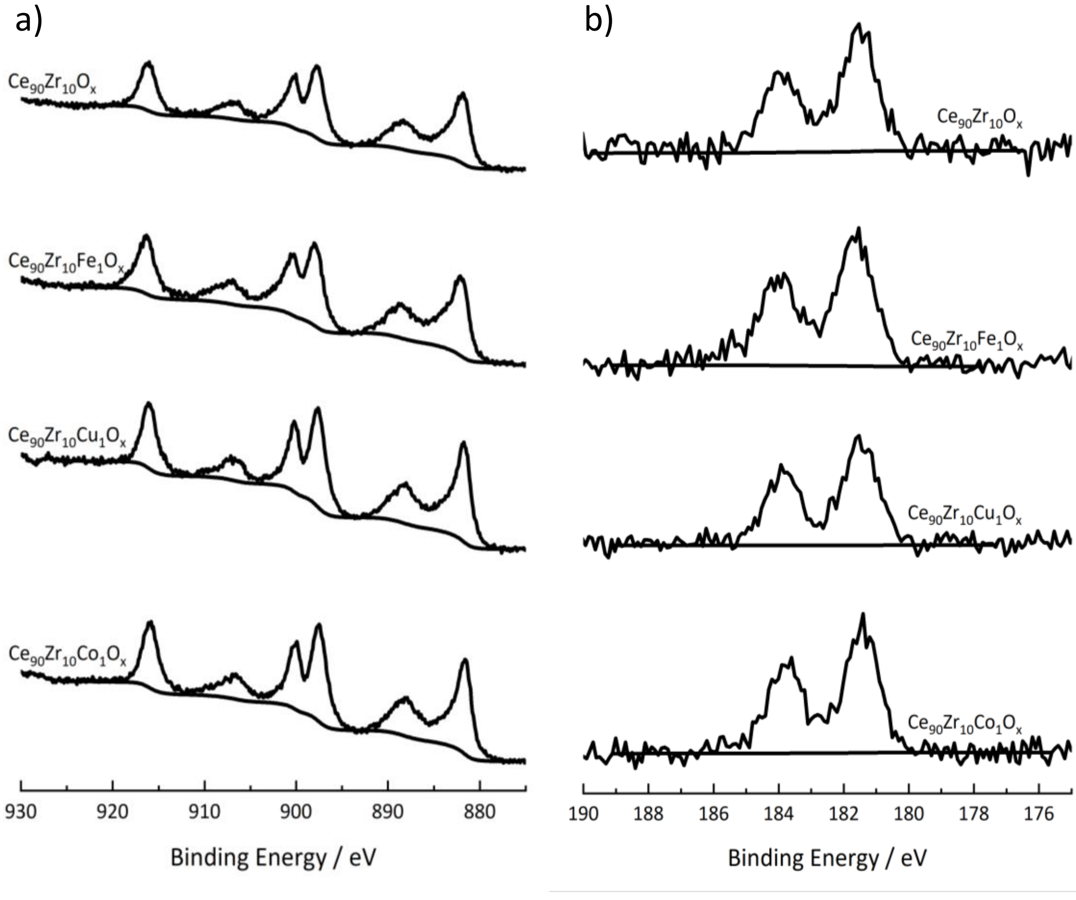

Figure 7: XPS spectra of the $Ce_{90}Zr_{10}M_1O_x$ catalysts for the a) Ce 3d region & b) Zr 3d region.

As discussed in previous chapters, oxygen surface species can influence the catalytic activity of metal oxide catalysts, hence analysis of the O 1s region was carried out for all catalysts (Figure 8). Two distinct oxygen environments were extracted from the spectra, which are ascribed as O^{β} (531 eV) and O^{α} (529 eV) states, reported to be characteristic of oxygen defect sites and lattice oxygen species respectively [29,52,53]. Previous chapters (Chapter 3) have discussed the controversy on the labelling of the O^{β}, hence this region has been referred to as surface oxygen defect sites. As previously mentioned, the presence of surface oxygen defect sites has been correlated with the formation of active oxygen species in previous literature [50,54]. The surface oxygen defect concentration (O^{β}/ O^{α}) shown in Table 3 indicated that the $Ce_{90}Zr_{10}O_x$ catalyst had the largest amount of surface defect sites compared with the doped catalysts. These data are in contrast with the defect concentrations calculated from Laser Raman spectroscopy, indicating that these defects are highly localised on the surface of the catalyst [29]. This further supports the evidence of the doped transition metals being well dispersed within the bulk structure rather than located at the catalyst surface, as a result of the higher bulk defects identified in these catalysts (A_{600}/A_{463}, Table 1). Furthermore, the higher concentration of surface oxygen defect sites on the $Ce_{90}Zr_{10}O_x$ catalyst was not consistent with the lower Ce^{3+} concentration also obtained by XPS analysis. This effect could be a result of defects formed from Zr species on the surface as opposed to just Ce^{3+} species, therefore providing the irregular trend.

Table 3: Surface compositions of $Ce_{90}Zr_{10}M_1O_x$ catalysts determined by XPS and EDX analysis.

Catalyst	EDX Ce:Zr:M Ratio	O^{β}/O^{α}	Ce^{3+}/Ce^{4+}	EDX Ce:O:Na Ratio	XPS Ce:O:Na Ratio
$Ce_{90}Zr_{10}O_x$	98:2:N/A	1.02	0.18	20:66:14	20:64:16
$Ce_{90}Zr_{10}Fe_1Ox$	95:0.6:4.4	0.78	0.21	32:66:2	27:67:6
$Ce_{90}Zr_{10}Cu_1O_x$	98:1.9:0.1	0.59	0.18	31:66:3	22:66:12
$Ce_{90}Zr_{10}Co_1O_x$	99.7:0.3:0	0.79	0.19	23:67:10	20:63:17

The deconvolution of the O 1s region also revealed two other peaks, which were fitted to species around 533 eV and 535eV. The peak around 533 eV has previously been related to the presence of water or hydroxyl species based on values in the literature [55–57] but this topic is highly contested so was excluded from further calculations. The fitting around 535 eV (green fitting, Figure 8) is representative of a Na Auger peak. As shown in Table 3, all catalysts presented Na on the catalyst surface when analysed by XPS, hence the appearance of the Na Auger peak in the O 1s region. Similarly to EDX analysis, the $Ce_{90}Zr_{10}O_x$ and $Ce_{90}Zr_{10}Co_1O_x$ catalysts showed high amounts of residual Na. However, in contrast to the EDX analysis, the $Ce_{90}Zr_{10}Cu_1O_x$ catalyst also showed a high amount of Na in comparison to the $Ce_{90}Zr_{10}Fe_1O_x$ catalyst, suggesting that the residual Na was localised at the catalyst surface for the $Ce_{90}Zr_{10}Cu_1O_x$ catalyst. As mentioned previously, Na content is important with regards to catalytic activity for propane total oxidation, as high quantities have been shown to poison the reaction [42].

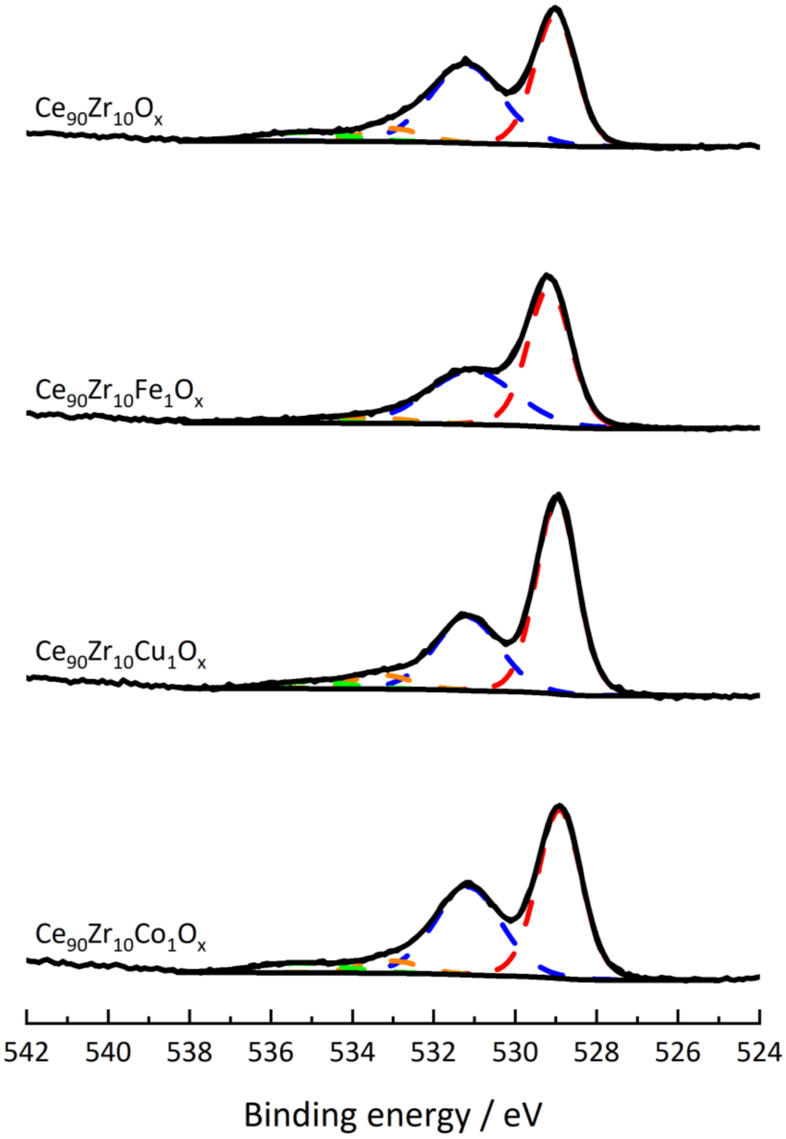

Figure 8: XPS spectra of the O 1s region for the $Ce_{90}Zr_{10}M_1O_x$ catalysts. Fitted peaks refer to O^{α} (red), O^{β} (blue) and hydroxyl (orange) species with overlapping Na Auger peak (green) as discussed in the main text.

5.2.2 Catalyst testing

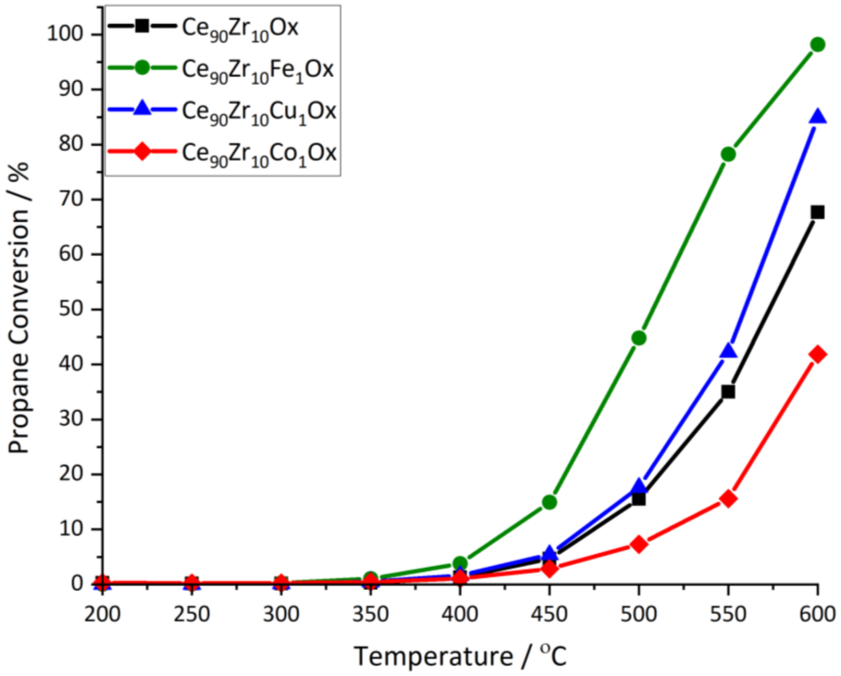

Figure 9: Catalyst activity for the total oxidation of propane using the $Ce_{90}Zr_{10}M_1O_x$ catalysts. Conditions: 5000 ppm propane in air, GHSV = 45000 h^{-1}. Legend refers to different dopants used.

Catalyst performance for propane total oxidation is shown in Figure 9. For all catalysts, the main reaction product detected was CO_2 and a carbon balance of >99% was maintained for all temperatures. The $Ce_{90}Zr_{10}O_x$, $Ce_{90}Zr_{10}Fe_1O_x$ and $Ce_{90}Zr_{10}Cu_1O_x$ catalysts presented a CO_2 selectivity of 100% below 450°C, with small amounts of propene detected above 450°C, resulting in a selectivity of >98%. The selectivity trend was the same for the $Ce_{90}Zr_{10}Co_1O_x$ catalyst, however the appearance of propene occurred at 400°C. The $Ce_{90}Zr_{10}Fe_1O_x$ catalyst was the most active for propane total oxidation across the temperature range (Figure 9), with activity decreasing in the order:

$$Ce_{90}Zr_{10}Cu_1O_x > Ce_{90}Zr_{10}O_x > Ce_{90}Zr_{10}Co_1O_x$$

However, when normalised for surface area, the $Ce_{90}Zr_{10}Fe_1O_x$ and $Ce_{90}Zr_{10}Cu_1O_x$ catalysts present similar activity (Table 4).

Table 4: Propane conversion and surface normalised catalytic activity for the $Ce_{90}Zr_{10}M_1O_x$ catalysts.

Catalyst	**Propane Conversion[a] / %**	**Catalyst Mass in Reaction / g**	**Active Catalyst Surface in Reaction / m²**	**Propane Surface Area Normalised Activity[a] / mols^{-1}m^{-2}**

$Ce_{90}Zr_{10}O_x$	16	0.31	10.5	2.78x10^{-3}
$Ce_{90}Zr_{10}Fe_1Ox$	45	0.29	18.3	4.60x10^{-3}
$Ce_{90}Zr_{10}Cu_1O_x$	18	0.15	7.4	4.43x10^{-3}
$Ce_{90}Zr_{10}Co_1O_x$	7	0.11	4.4	2.94x10^{-3}

a – Measured at 500°C

Previous research has highlighted the importance of oxygen defects or vacancies contributing to the total oxidation of aliphatic VOCs using metal oxide catalysts [57–60]. The oxidation of aliphatic VOCs, such as propane, are thought to occur through a Mars-van Krevelen type mechanism, where the VOC is adsorbed to the catalyst surface and oxidised by lattice oxygen *via* a redox cycle [61,62]. Bulk defects, calculated using Laser Raman spectroscopy, are thought to improve the catalytic activity for metal oxide catalysts by improving oxygen mobility through the lattice [45], therefore allowing faster re-oxidation of the surface [29,46,63,64]. Whereas surface oxygen defect sites, determined from XPS analysis, have been linked to the production of increased active oxygen species [64], which are able to activate C-H bonds, breaking them more easily [65,66]. The breaking of the C-H bond is also stated to be the rate determining step for propane oxidation [67]. When considering the data, no trends between bulk (A_{600}/A_{463}, Table 1) or surface oxygen defects (O^{β}/O^{α}, Table 3) could be associated with the results obtained for propane total oxidation, which is in contrast to previous literature [27].

Similarly to the effect of oxygen defect sites, catalyst reducibility has also been shown as an influential factor for propane oxidation [6,68]. The ease of reduction of the catalyst can be associated with the ease of removal of active oxygen species from the catalyst surface. The ability to easily remove these active oxygen species can then facilitate C-H bond activation, which as mentioned previously, is the rate determining step for propane oxidation. Hence, a direct relationship between these factors has been suggested in the literature [6,69]. As with the oxygen defect concentrations, no direct link can be acquired from this data set for improved reducibility directly relating to improved catalytic activity, suggesting other factors were more important for influencing activity.

Previous literature has shown that the increased surface area of metal oxide catalysts resulted in more available active sites, which then improved catalytic activity for VOC oxidation [58,70–72]. The surface area of the $Ce_{90}Zr_{10}M_1O_x$ catalysts has a very influential role on the catalytic activity for the total oxidation of propane. The $Ce_{90}Zr_{10}Fe_1O_x$ catalyst exhibited the highest catalytic activity, whilst exhibiting the largest surface area. Furthermore, as highlighted in Table 4, the $Ce_{90}Zr_{10}Cu_1O_x$ catalyst had a similar activity when normalised for surface area. This can be deduced as a linear relationship due to the “active catalyst surface” present in the reaction which occurred due to varying density of the catalyst samples. However, the surface normalised activity for the $Ce_{90}Zr_{10}O_x$ and $Ce_{90}Zr_{10}Co_1O_x$ catalysts were much lower which suggests another factor was also important when understanding the propane total oxidation trends.

As previously mentioned, Na is a known catalyst poison for propane total oxidation [42]. It has been indicated in previous studies that excess Na inhibits the oxygen mobility of the catalyst and promotes the adsorption of CO_2 on the surface, which then results in poor activity for propane oxidation [73]. From this, it can be concluded that the increased Na content on the $Ce_{90}Zr_{10}O_x$ and $Ce_{90}Zr_{10}Co_1O_x$ catalysts, identified by XPS and EDX analysis, was responsible for the lower catalytic activity. Another study has also proposed that increased Na loading on the catalyst surface results in decreased amounts of oxygen vacancies [74], which would then limit active oxygen species on the surface. This can be identified in the XPS analysis for the $Ce_{90}Zr_{10}Cu_1O_x$ catalyst, as the high surface Na content correlates with a low surface oxygen defect site concentration. This could also explain why the surface normalised activity for propane oxidation was slightly decreased for this catalyst, compared to $Ce_{90}Zr_{10}Fe_1O_x$. Finally, the residual Na on the surface of the catalysts poses a two-fold problem, as it could also hinder access to the active surface species available to partake in the propane oxidation reaction.

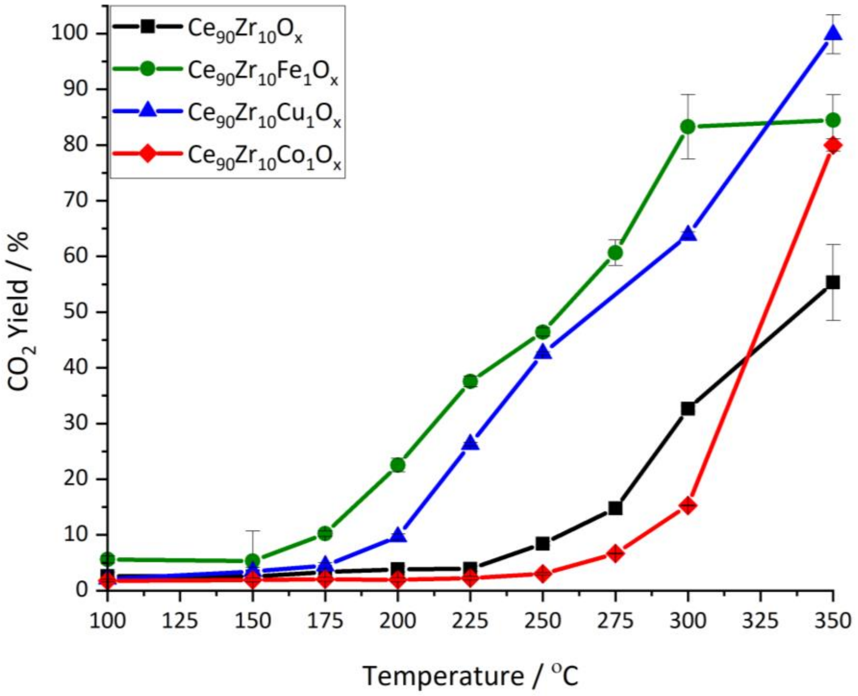

Figure 10: Catalyst activity for naphthalene total oxidation using the $Ce_{90}Zr_{10}M_1O_x$ catalysts. Conditions: 200 ppm naphthalene in 20% O_2/He, GHSV = 45000 h^{-1}. Legend refers to the different dopants used.

In addition to propane total oxidation, naphthalene was also used as a model VOC for polyaromatic VOC oxidation (Figure 10). Activity trends were similar to propane total oxidation, with the $Ce_{90}Zr_{10}Fe_1O_x$ and $Ce_{90}Zr_{10}Cu_1O_x$ catalysts being more active for naphthalene total oxidation. However, at higher temperatures the $Ce_{90}Zr_{10}Co_1O_x$ catalyst became more active than $Ce_{90}Zr_{10}O_x$ and deactivation of the $Ce_{90}Zr_{10}Fe_1O_x$ catalyst could be noticed. It is important to note for $Ce_{90}Zr_{10}Fe_1O_x$, full conversion of naphthalene was obtained at 350°C but CO_2 yield did not increase. This suggests that by-products were possibly formed over this catalyst at higher temperatures. By-product formation from the total oxidation of naphthalene has been reported previously at higher temperatures for Co/Al_2O_3 catalysts and most likely occurs from a partial decomposition pathway [75].

Table 5: CO_2 yield and surface normalised catalytic activity for naphthalene total oxidation using the $Ce_{90}Zr_{10}M_1O_x$ catalysts.

Catalyst	**Naphthalene Conversion^a / %**	**Catalyst Mass in Reaction / g**	**Active Catalyst Surface in Reaction / m^2**	**Naphthalene Surface Area Normalised Activity^a / mols^{-1}m^{-2}**
$Ce_{90}Zr_{10}O_x$	15	0.31	10.5	1.04×10^{-4}

$Ce_{90}Zr_{10}Fe_1Ox$	61	0.29	18.3	2.42×10^{-4}
$Ce_{90}Zr_{10}Cu_1O_x$	53	0.15	7.4	5.23×10^{-4}
$Ce_{90}Zr_{10}Co_1O_x$	7	0.11	4.4	1.28×10^{-4}

[a] Calculated at 275°C

Previous research has proposed catalyst surface area as a key factor when understanding the catalytic activity for naphthalene total oxidation, especially using CeO_2 based materials [6,48,70,71]. The high surface area promotes naphthalene accessibility on the active surface sites, leading to improved activity. Catalyst performance, shown in Figure 10, presented a slight agreement with this trend as the $Ce_{90}Zr_{10}Fe_1O_x$ and $Ce_{90}Zr_{10}Cu_1O_x$ catalysts, with higher surface areas, performed well for naphthalene oxidation. However, a direct relationship between surface area and activity could not be deduced which was also highlighted by the surface normalised activity shown in Table 5. Therefore, other catalyst characteristics must have also played an important role for naphthalene total oxidation.

As discussed for propane oxidation, naphthalene oxidation is also proposed to occur *via* a Mars-van Krevelen type mechanism [76]. Consequently, in addition to surface area, catalyst characteristics, such as lattice oxygen mobility [77] and redox properties [78] have also been shown to promote catalytic activity for naphthalene total oxidation. The $Ce_{90}Zr_{10}Cu_1O_x$ catalyst displayed the highest concentration of lattice oxygen defects (Table 1), which is thought to be indicative of oxygen mobility through the lattice [29,45], as well as presenting the highest surface normalised catalytic activity (Table 5). Therefore, it can be tentatively postulated that the improved oxygen mobility was an influential factor when determining catalytic activity. Furthermore, this trend is continued with the $Ce_{90}Zr_{10}Fe_1O_x$ and $Ce_{90}Zr_{10}O_x$ catalysts, with $Ce_{90}Zr_{10}Co_1O_x$ being the only exception. It could be argued that, similarly to the effect for propane oxidation, the high quantity of bulk Na present in this catalyst inhibited the oxygen mobility [73], which negatively impacted the activity for naphthalene oxidation. In contrast, no direct trends could be established from the reducibility of the catalysts, something that has been previously noted when using metal oxide catalysts for naphthalene oxidation [6]. Whilst it is accepted that redox properties are important for VOC oxidation reactions, it has been postulated that the rate-determining step for naphthalene total oxidation over $CeZrO_x$ catalysts is the re-oxidation of the catalyst

[76] making the reducibility of the catalyst less significant. This also further supports the importance of the oxygen mobility in the catalysts for naphthalene total oxidation.

5.3 Conclusions

A range of $Ce_{90}Zr_{10}M_1O_x$ (M = Fe, Cu, Co) were prepared by a co-precipitation method and assessed for the total oxidation of propane and naphthalene VOCs. The incorporation of small quantities of transition metals into the catalyst preparation resulted in changes to the bulk and surface structure of the catalysts. The doped catalysts presented distortions to the $Ce_{90}Zr_{10}O_x$ lattice, creating a higher quantity of bulk oxygen defects. Furthermore, the doped catalysts displayed higher surface areas and more facile surface reduction, but had less surface oxygen defect sites. For propane total oxidation, a linear relationship between surface area and catalytic activity was established, with the $Ce_{90}Zr_{10}Fe_1O_x$ catalyst demonstrating the best activity. In addition, the presence of excess Na identified in the catalyst was shown to result in poor catalytic activity, which was in agreement with previous research. Catalyst surface area and low Na content was also shown to be important factors with regard to naphthalene total oxidation. However, when normalised for surface area the $Ce_{90}Zr_{10}Cu_1O_x$ catalyst displayed the highest activity, which was related to the improved oxygen mobility of the catalyst as a result of the increased bulk oxygen defects.

5.4 References

[1] D.J. Wuebbles, S. Sanyal, Air Quality in a Cleaner Energy World, Curr. Pollut. Rep. 1 (2015) 117–129. https://doi.org/10.1007/s40726-015-0009-x.

[2] Y. Guo, M. Wen, G. Li, T. An, Recent advances in VOC elimination by catalytic oxidation technology onto various nanoparticles catalysts: a critical review, Appl. Catal. B Environ. 281 (2021) 119447. https://doi.org/10.1016/j.apcatb.2020.119447.

[3] P. Wang, Chenrui Cui, Kai Li, Jing Yi, Lili Lei, The Effect of Mn Content on Catalytic Activity of the Co–Mn–Ce Catalysts for Propane Oxidation: Importance of Lattice Defect and Surface Active Species, Catal. Lett. 150 (2020) 1505/1514. https://doi.org/10.1007/s10562-019-03061-6.

[4] Marie Taylor, Edwin Ntainjua Ndifor, Tomas Garcia, Benjamin Solsona, Albert F. Carley, Stuart H. Taylor, Deep oxidation of propane using palladium–titania catalysts modified by niobium, Appl. Catal. Gen. 350 (2008) 63–70. https://doi.org/10.1016/j.apcata.2008.07.045.

[5] Z. Hu, Z. Wang, Y. Guo, L. Wang, Y. Guo, J. Zhang, W. Zhan, Total Oxidation of Propane over a Ru/CeO2 Catalyst at Low Temperature, Environ. Sci. Technol. 52 (2018) 9531–9541. https://doi.org/10.1021/acs.est.8b03448.

[6] T. García, B. Solsona, S.H. Taylor, Naphthalene total oxidation over metal oxide catalysts, Appl. Catal. B Environ. 66 (2006) 92–99. https://doi.org/10.1016/j.apcatb.2006.03.003.

[7] D.R. Sellick, D.J. Morgan, S.H. Taylor, Silica Supported Platinum Catalysts for Total Oxidation of the Polyaromatic Hydrocarbon Naphthalene: An Investigation of Metal Loading and Calcination Temperature, Catalysts. 5 (2015) 690–702. https://doi.org/10.3390/catal5020690.

[8] C. Yang, G. Miao, Y. Pi, Q. Xia, J. Wu, Z. Li, J. Xiao, Abatement of various types of VOCs by adsorption/catalytic oxidation: A review, Chem. Eng. J. 370 (2019) 1128–1153. https://doi.org/10.1016/j.cej.2019.03.232.

[9] S.A.C. Carabineiro, X. Chen, O. Martynyuk, N. Bogdanchikova, M. Avalos-Borja, A. Pestryakov, P.B. Tavares, J.J.M. Órfão, M.F.R. Pereira, J.L. Figueiredo, Gold supported on metal oxides for volatile organic compounds total oxidation, Catal. Today. 244 (2015) 103–114. https://doi.org/10.1016/j.cattod.2014.06.034.

[10] A. Setiabudi, J. Chen, G. Mul, M. Makkee, J.A. Moulijn, CeO2 catalysed soot oxidation: The role of active oxygen to accelerate the oxidation conversion, Appl. Catal. B Environ. 51 (2004) 9–19. https://doi.org/10.1016/j.apcatb.2004.01.005.

[11] T. Garcia, B. Solsona, S.H. Taylor, Nano-crystalline Ceria Catalysts for the Abatement of Polycyclic Aromatic Hydrocarbons, Catal. Lett. 105 (2005) 183–189. https://doi.org/10.1007/s10562-005-8689-2.

[12] P. Yang, S. Yang, Z. Shi, Z. Meng, R. Zhou, Deep oxidation of chlorinated VOCs over CeO2-based transition metal mixed oxide catalysts, Appl. Catal. B Environ. 162 (2015) 227–235. https://doi.org/10.1016/j.apcatb.2014.06.048.

[13] H.J. Kim, D. Shin, H. Jeong, M.G. Jang, H. Lee, J.W. Han, Design of an Ultrastable and Highly Active Ceria Catalyst for CO Oxidation by Rare-Earth- and Transition-Metal Co-Doping, ACS Catal. 10 (2020) 14877–14886. https://doi.org/10.1021/acscatal.0c03386.

[14] S. Dey, D. Mohan, G.C. Dhal, R. Prasad, Copper based mixed oxide catalysts (CuMnCe, CuMnCo and CuCeZr) for the oxidation of CO at low temperature, Mater. Discov. 10 (2017) 1–14. https://doi.org/10.1016/j.md.2018.02.001.

[15] W. Deng, Q. Dai, Y. Lao, B. Shi, X. Wang, Low temperature catalytic combustion of 1,2-dichlorobenzene over CeO2–TiO2 mixed oxide catalysts, Appl. Catal. B Environ. 181 (2016) 848–861. https://doi.org/10.1016/j.apcatb.2015.07.053.

[16] M. Piumetti, S. Bensaid, D. Fino, N. Russo, Nanostructured ceria-zirconia catalysts for CO oxidation: Study on surface properties and reactivity, Appl. Catal. B Environ. 197 (2016) 35–46. https://doi.org/10.1016/j.apcatb.2016.02.023.

[17] B. de Rivas, J.I. Gutiérrez-Ortiz, R. López-Fonseca, J.R. González-Velasco, Analysis of the simultaneous catalytic combustion of chlorinated aliphatic pollutants and toluene over ceria-zirconia mixed oxides, Appl. Catal. Gen. 314 (2006) 54–63. https://doi.org/10.1016/j.apcata.2006.08.005.

[18] M. Piumetti, S. Bensaid, N. Russo, D. Fino, Investigations into nanostructured ceria–zirconia catalysts for soot combustion, Appl. Catal. B Environ. 180 (2016) 271–282. https://doi.org/10.1016/j.apcatb.2015.06.018.

[19] D. Devaiah, L.H. Reddy, S.-E. Park, B.M. Reddy, Ceria–zirconia mixed oxides: Synthetic methods and applications, Catal. Rev. 60 (2018) 177–277. https://doi.org/10.1080/01614940.2017.1415058.

[20] W.B. Li, J.X. Wang, H. Gong, Catalytic combustion of VOCs on non-noble metal catalysts, Catal. Today. 148 (2009) 81–87. https://doi.org/10.1016/j.cattod.2009.03.007.

[21] M. Ozawa, Role of cerium–zirconium mixed oxides as catalysts for car pollution: A short review1An invited paper.1, J. Alloys Compd. 275–277 (1998) 886–890. https://doi.org/10.1016/S0925-8388(98)00477-0.

[22] J. Pan, W. Du, Y. Liu, Y. Cheng, S. Yuan, Lanthanum-doped CuMn composite oxide catalysts for catalytic oxidation of toluene, J. Rare Earths. 37 (2019) 602–608. https://doi.org/10.1016/j.jre.2018.10.004.

[23] Z. Jiang, C. Chen, M. Ma, Z. Guo, Y. Yu, C. He, Rare-earth element doping-promoted toluene low-temperature combustion over mesostructured CuMCeO x (M = Y, Eu, Ho, and Sm) catalysts: the indispensable role of in situ generated oxygen vacancies, Catal. Sci. Technol. 8 (2018) 5933–5942. https://doi.org/10.1039/C8CY01849A.

[24] Z. Li, Q. Yan, Q. Jiang, Y. Gao, T. Xue, R. Li, Y. Liu, Q. Wang, Oxygen vacancy mediated CuyCo3-yFe1Ox mixed oxide as highly active and stable toluene oxidation catalyst by multiple phase interfaces formation and metal doping effect, Appl. Catal. B Environ. 269 (2020) 118827. https://doi.org/10.1016/j.apcatb.2020.118827.

[25] Q. Liang, X. Wu, D. Weng, Z. Lu, Selective oxidation of soot over Cu doped ceria/ceria–zirconia catalysts, Catal. Commun. 9 (2008) 202–206. https://doi.org/10.1016/j.catcom.2007.06.007.

[26] D. Terribile, A. Trovarelli, C. de Leitenburg, A. Primavera, G. Dolcetti, Catalytic combustion of hydrocarbons with Mn and Cu-doped ceria–zirconia solid solutions, Catal. Today. 47 (1999) 133–140. https://doi.org/10.1016/S0920-5861(98)00292-2.

[27] P.M. Shah, J.W.H. Burnett, D.J. Morgan, T.E. Davies, S.H. Taylor, Ceria–Zirconia Mixed Metal Oxides Prepared via Mechanochemical Grinding of Carbonates for the Total Oxidation of Propane and Naphthalene, Catalysts. 9 (2019) 475. https://doi.org/10.3390/catal9050475.

[28] P.M. Shah, A.N. Day, T.E. Davies, D.J. Morgan, S.H. Taylor, Mechanochemical preparation of ceria-zirconia catalysts for the total oxidation of propane and naphthalene Volatile Organic Compounds, Appl. Catal. B Environ. 253 (2019) 331–340. https://doi.org/10.1016/j.apcatb.2019.04.061.

[29] J.M. López, A.L. Gilbank, T. García, B. Solsona, S. Agouram, L. Torrente-Murciano, The prevalence of surface oxygen vacancies over the mobility of bulk oxygen in nanostructured ceria for the total toluene oxidation, Appl. Catal. B Environ. 174–175 (2015) 403–412. https://doi.org/10.1016/j.apcatb.2015.03.017.

[30] F.J. Perez-Alonso, I. Melián-Cabrera, M. López Granados, F. Kapteijn, J.L.G. Fierro, Synergy of FexCe1−xO2 mixed oxides for N2O decomposition, J. Catal. 239 (2006) 340–346. https://doi.org/10.1016/j.jcat.2006.02.008.

[31] S. Hočevar, U.O. Krašovec, B. Orel, A.S. Aricó, H. Kim, CWO of phenol on two differently prepared CuO–CeO2 catalysts, Appl. Catal. B Environ. 28 (2000) 113–125. https://doi.org/10.1016/S0926-3373(00)00167-3.

[32] L. Wang, H. Liu, Y. Chen, S. Yang, Reverse water–gas shift reaction over co-precipitated Co–CeO2 catalysts: Effect of Co content on selectivity and carbon formation, Int. J. Hydrog. Energy. 42 (2017) 3682–3689. https://doi.org/10.1016/j.ijhydene.2016.07.048.

[33] H. Bao, K. Qian, J. Fang, W. Huang, Fe-doped CeO2 solid solutions: Substituting-site doping versus interstitial-site doping, bulk doping versus surface doping, Appl. Surf. Sci. 414 (2017) 131–139. https://doi.org/10.1016/j.apsusc.2017.04.018.

[34] S. Deshpande, S. Patil, S.V. Kuchibhatla, S. Seal, Size dependency variation in lattice parameter and valency states in nanocrystalline cerium oxide, Appl. Phys. Lett. 87 (2005) 133113. https://doi.org/10.1063/1.2061873.

[35] C. Bueno-Ferrer, S. Parres-Esclapez, D. Lozano-Castelló, A. Bueno-López, Relationship between surface area and crystal size of pure and doped cerium oxides, J. Rare Earths. 28 (2010) 647–653. https://doi.org/10.1016/S1002-0721(09)60172-1.

[36] Y. Wang, H. Arandiyan, J. Scott, A. Bagheri, H. Dai, R. Amal, Recent advances in ordered meso/macroporous metal oxides for heterogeneous catalysis: a review, J. Mater. Chem. A. 5 (2017) 8825–8846. https://doi.org/10.1039/C6TA10896B.

[37] Z. Wu, M. Li, J. Howe, H.M. Meyer, S.H. Overbury, Probing Defect Sites on CeO2 Nanocrystals with Well-Defined Surface Planes by Raman Spectroscopy and O2 Adsorption, Langmuir. 26 (2010) 16595–16606. https://doi.org/10.1021/la101723w.

[38] E. Sartoretti, C. Novara, F. Giorgis, M. Piumetti, S. Bensaid, N. Russo, D. Fino, In situ Raman analyses of the soot oxidation reaction over nanostructured ceria-based catalysts, Sci. Rep. 9 (2019) 3875. https://doi.org/10.1038/s41598-019-39105-5.

[39] M. Dosa, M. Piumetti, S. Bensaid, T. Andana, C. Novara, F. Giorgis, D. Fino, N. Russo, Novel Mn–Cu-Containing CeO2 Nanopolyhedra for the Oxidation of CO and Diesel Soot: Effect of Dopants on the Nanostructure and Catalytic Activity, Catal. Lett. 148 (2018) 298–311. https://doi.org/10.1007/s10562-017-2226-y.

[40] K. Kappis, C. Papadopoulos, J. Papavasiliou, J. Vakros, Y. Georgiou, Y. Deligiannakis, G. Avgouropoulos, Tuning the Catalytic Properties of Copper-Promoted Nanoceria via a Hydrothermal Method, Catalysts. 9 (2019) 138. https://doi.org/10.3390/catal9020138.

[41] T. Hattori, K. Kobayashi, M. Ozawa, Size effect of Raman scattering on CeO2 nanocrystal by hydrothermal method, Jpn. J. Appl. Phys. 56 (2016) 01AE06. https://doi.org/10.7567/JJAP.56.01AE06.

[42] W. Tang, J. Weng, X. Lu, L. Wen, A. Suburamanian, C.-Y. Nam, P.-X. Gao, Alkali-metal poisoning effect of total CO and propane oxidation over Co3O4 nanocatalysts, Appl. Catal. B Environ. 256 (2019) 117859. https://doi.org/10.1016/j.apcatb.2019.117859.

[43] J. Wang, M. Shen, J. Wang, J. Gao, J. Ma, S. Liu, Effect of cobalt doping on ceria-zirconia mixed oxide: Structural characteristics, oxygen storage/release capacity and three-way catalytic performance, J. Rare Earths. 30 (2012) 878–883. https://doi.org/10.1016/S1002-0721(12)60149-5.

[44] O.O. Ajumobi, O. Muraza, I.A. Bakare, A.M. Al Amer, Iron- and Cobalt-Doped Ceria–Zirconia Nanocomposites for Catalytic Cracking of Naphtha with Regenerative Capability, Energy Fuels. 31 (2017) 12612–12623. https://doi.org/10.1021/acs.energyfuels.7b01376.

[45] K. Polychronopoulou, A.A. AlKhoori, A.M. Efstathiou, M.A. Jaoude, C.M. Damaskinos, M.A. Baker, A. Almutawa, D.H. Anjum, M.A. Vasiliades, A. Belabbes, L.F. Vega, A.F. Zedan, S.J. Hinder, Design Aspects of Doped CeO2 for Low-Temperature Catalytic CO Oxidation: Transient Kinetics and DFT Approach, ACS Appl. Mater. Interfaces. 13 (2021) 22391–22415. https://doi.org/10.1021/acsami.1c02934.

[46] Z. Su, W. Yang, C. Wang, S. Xiong, X. Cao, Y. Peng, W. Si, Y. Weng, M. Xue, J. Li, Roles of Oxygen Vacancies in the Bulk and Surface of CeO2 for Toluene Catalytic Combustion, Environ. Sci. Technol. 54 (2020) 12684–12692. https://doi.org/10.1021/acs.est.0c03981.

[47] F. Zhang, P. Wang, J. Koberstein, S. Khalid, S.-W. Chan, Cerium oxidation state in ceria nanoparticles studied with X-ray photoelectron spectroscopy and absorption near edge spectroscopy, Surf. Sci. 563 (2004) 74–82. https://doi.org/10.1016/j.susc.2004.05.138.

[48] L. Torrente-Murciano, A. Gilbank, B. Puertolas, T. Garcia, B. Solsona, D. Chadwick, Shape-dependency activity of nanostructured CeO2 in the total oxidation of

polycyclic aromatic hydrocarbons, Appl. Catal. B Environ. 132–133 (2013) 116–122. https://doi.org/10.1016/j.apcatb.2012.10.030.

[49] C.B. Gopal, F.E. Gabaly, A.H. McDaniel, W.C. Chueh, Origin and Tunability of Unusually Large Surface Capacitance in Doped Cerium Oxide Studied by Ambient-Pressure X-Ray Photoelectron Spectroscopy, Adv. Mater. 28 (2016) 4692–4697. https://doi.org/10.1002/adma.201506333.

[50] Q. Wang, K.L. Yeung, M.A. Bañares, Ceria and its related materials for VOC catalytic combustion: A review, Catal. Today. 356 (2020) 141–154. https://doi.org/10.1016/j.cattod.2019.05.016.

[51] A. Sinhamahapatra, J.-P. Jeon, J. Kang, B. Han, J.-S. Yu, Oxygen-Deficient Zirconia (ZrO2−x): A New Material for Solar Light Absorption, Sci. Rep. 6 (2016) 27218. https://doi.org/10.1038/srep27218.

[52] K. Wang, Y. Chang, L. Lv, Y. Long, Effect of annealing temperature on oxygen vacancy concentrations of nanocrystalline CeO2 film, Appl. Surf. Sci. 351 (2015) 164–168. https://doi.org/10.1016/j.apsusc.2015.05.122.

[53] J.P. Holgado, G. Munuera, J.P. Espinós, A.R. González-Elipe, XPS study of oxidation processes of CeOx defective layers, Appl. Surf. Sci. 158 (2000) 164–171. https://doi.org/10.1016/S0169-4332(99)00597-8.

[54] A. Trovarelli, J. Llorca, Ceria Catalysts at Nanoscale: How Do Crystal Shapes Shape Catalysis?, ACS Catal. 7 (2017) 4716–4735. https://doi.org/10.1021/acscatal.7b01246.

[55] D.R. Mullins, S.H. Overbury, D.R. Huntley, Electron spectroscopy of single crystal and polycrystalline cerium oxide surfaces, Surf. Sci. 409 (1998) 307–319. https://doi.org/10.1016/S0039-6028(98)00257-X.

[56] C. Barth, C. Laffon, R. Olbrich, A. Ranguis, P. Parent, M. Reichling, A perfectly stoichiometric and flat CeO2(111) surface on a bulk-like ceria film, Sci. Rep. 6 (2016) 21165. https://doi.org/10.1038/srep21165.

[57] J. Yao, H. Lu, B. Hou, Y. Xiao, L. Jia, D. Li, J. Wang, The Promotional Effect of La Dopant on Co3O4 Catalytic Performance Towards C3H8 Combustion, Catal. Lett. 151 (2021) 1745–1754. https://doi.org/10.1007/s10562-020-03429-z.

[58] T. Garcia, S. Agouram, J.F. Sánchez-Royo, R. Murillo, A.M. Mastral, A. Aranda, I. Vázquez, A. Dejoz, B. Solsona, Deep oxidation of volatile organic compounds using ordered cobalt oxides prepared by a nanocasting route, Appl. Catal. Gen. 386 (2010) 16–27. https://doi.org/10.1016/j.apcata.2010.07.018.

[59] S. Zhang, S. Liu, X. Zhu, Y. Yang, W. Hu, H. Zhao, R. Qu, C. Zheng, X. Gao, Low temperature catalytic oxidation of propane over cobalt-cerium spinel oxides catalysts, Appl. Surf. Sci. 479 (2019) 1132–1140. https://doi.org/10.1016/j.apsusc.2019.02.118.

[60] Y. Gao, S. Wang, L. Lv, D. Li, X. Yue, S. Wang, Insights into the Behaviors of the Catalytic Combustion of Propane over Spinel Catalysts, Catal. Lett. 150 (2020) 3617–3625. https://doi.org/10.1007/s10562-020-03239-3.

[61] V.R. Choudhary, G.M. Deshmukh, Kinetics of the complete combustion of dilute propane and methyl ethyl ketone over Cr-doped ZrO2 catalyst, Chem. Eng. Sci. 60 (2005) 1575–1581. https://doi.org/10.1016/j.ces.2004.10.028.

[62] V. R. Choudhary, G. M. Deshmukh, D. P. Mishra, Kinetics of the Complete Combustion of Dilute Propane and Toluene over Iron-Doped ZrO2 Catalyst, Energy Fuels. 19 (2005) 54–63. https://doi.org/10.1021/ef0498871.

[63] M. Yang, G. Shen, Q. Wang, K. Deng, M. Liu, Y. Chen, Y. Gong, Z. Wang, Roles of Oxygen Vacancies of CeO2 and Mn-Doped CeO2 with the Same Morphology in

Benzene Catalytic Oxidation, Molecules. 26 (2021) 6363. https://doi.org/10.3390/molecules26216363.

[64] Y. Jian, M. Tian, C. He, J. Xiong, Z. Jiang, H. Jin, L. Zheng, R. Albilali, J.-W. Shi, Efficient propane low-temperature destruction by Co3O4 crystal facets engineering: Unveiling the decisive role of lattice and oxygen defects and surface acid-base pairs, Appl. Catal. B Environ. 283 (2021) 119657. https://doi.org/10.1016/j.apcatb.2020.119657.

[65] Z. Liu, J. Li, R. Wang, CeO2 nanorods supported M–Co bimetallic oxides (M = Fe, Ni, Cu) for catalytic CO and C3H8 oxidation, J. Colloid Interface Sci. 560 (2020) 91–102. https://doi.org/10.1016/j.jcis.2019.10.046.

[66] W. Zhu, X. Chen, J. Jin, X. Di, C. Liang, Z. Liu, Insight into catalytic properties of Co3O4-CeO2 binary oxides for propane total oxidation, Chin. J. Catal. 41 (2020) 679–690. https://doi.org/10.1016/S1872-2067(19)63523-0.

[67] J.-Y. Luo, M. Meng, J.-S. Yao, X.-G. Li, Y.-Q. Zha, X. Wang, T.-Y. Zhang, One-step synthesis of nanostructured Pd-doped mixed oxides MOx-CeO2 (M=Mn, Fe, Co, Ni, Cu) for efficient CO and C3H8 total oxidation, Appl. Catal. B Environ. 87 (2009) 92–103. https://doi.org/10.1016/j.apcatb.2008.08.017.

[68] B. Solsona, T. García, R. Sanchis, M.D. Soriano, M. Moreno, E. Rodríguez-Castellón, S. Agouram, A. Dejoz, J.M. López Nieto, Total oxidation of VOCs on mesoporous iron oxide catalysts: Soft chemistry route versus hard template method, Chem. Eng. J. 290 (2016) 273–281. https://doi.org/10.1016/j.cej.2015.12.109.

[69] M.S. Leguizamón Aparicio, M.L. Ruiz, M.A. Ocsachoque, M.I. Ponzi, E. Rodríguez-Castellón, I.D. Lick, Propane and Naphthalene Oxidation over Gold-Promoted Cobalt Catalysts Supported on Zirconia, Catalysts. 10 (2020) 387. https://doi.org/10.3390/catal10040387.

[70] A. Aranda, B. Puértolas, B. Solsona, S. Agouram, R. Murillo, A.M. Mastral, S.H. Taylor, T. Garcia, Total Oxidation of Naphthalene Using Mesoporous CeO2 Catalysts Synthesized by Nanocasting from Two Dimensional SBA-15 and Three Dimensional KIT-6 and MCM-48 Silica Templates, Catal. Lett. 134 (2010) 110–117. https://doi.org/10.1007/s10562-009-0203-9.

[71] E.N. Ndifor, T. Garcia, B. Solsona, S.H. Taylor, Influence of preparation conditions of nano-crystalline ceria catalysts on the total oxidation of naphthalene, a model polycyclic aromatic hydrocarbon, Appl. Catal. B Environ. 76 (2007) 248–256. https://doi.org/10.1016/j.apcatb.2007.05.027.

[72] B. Solsona, T. Garcia, E. Aylón, A.M. Dejoz, I. Vázquez, S. Agouram, T.E. Davies, S.H. Taylor, Promoting the activity and selectivity of high surface area Ni–Ce–O mixed oxides by gold deposition for VOC catalytic combustion, Chem. Eng. J. 175 (2011) 271–278. https://doi.org/10.1016/j.cej.2011.09.104.

[73] G. Chai, W. Zhang, Y. Guo, J.L. Valverde, A. Giroir-Fendler, The Influence of Residual Sodium on the Catalytic Oxidation of Propane and Toluene over Co3O4 Catalysts, Catalysts. 10 (2020) 867. https://doi.org/10.3390/catal10080867.

[74] J. Haber, T. Machej, M. Derewiński, R. Janik, J. Kryściak, H. Sadowska, J. Janas, Catalytic oxidation of CH2Cl2 on sodium doped Al2O3, Catal. Today. 54 (1999) 47–55. https://doi.org/10.1016/S0920-5861(99)00167-4.

[75] X.-W. Zhang, S.-C. Shen, K. Hidajat, S. Kawi, L.E. Yu, K.Y. Simon Ng, Naphthalene Oxidation over 1%Pt and 5%Co/γ-Al2O3 Catalysts: Reaction Intermediates and Possible Pathways, Catal. Lett. 96 (2004) 87–96. https://doi.org/10.1023/B:CATL.0000029535.71343.7f.

[76] A. Bampenrat, V. Meeyoo, B. Kitiyanan, P. Rangsunvigit, T. Rirksomboon, Catalytic oxidation of naphthalene over CeO2–ZrO2 mixed oxide catalysts, Catal. Commun. 9 (2008) 2349–2352. https://doi.org/10.1016/j.catcom.2008.05.029.

[77] T. Garcia, D. Sellick, F. Varela, I. Vázquez, A. Dejoz, S. Agouram, S.H. Taylor, B. Solsona, Total oxidation of naphthalene using bulk manganese oxide catalysts, Appl. Catal. Gen. 450 (2013) 169–177. https://doi.org/10.1016/j.apcata.2012.10.029.

[78] M.S. Leguizamón Aparicio, M.A. Ocsachoque, D. Gazzoli, I.L. Botto, I.D. Lick, Total Oxidation of Naphthalene with Zirconia-Supported Cobalt, Copper and Nickel Catalysts, Catalysts. 7 (2017) 293. https://doi.org/10.3390/catal7100293.

6. Novel Au-Pt/ZrO_2/UVM-7 catalysts for the simultaneous total oxidation of CO, propene, and toluene pollutants.

6.1 Introduction

Volatile organic compounds (VOCs) are large contributors to air pollution because of their inherent toxicity and ability to react with NO_x species to form photochemical smog [1]. In addition, VOCs contribute to the growing issue of climate change and have been shown to promote adverse effects on human health [2]. The term VOC encompasses a wide variety of compounds, including compounds such as aliphatic and aromatic hydrocarbons. Major sources of VOC emissions can be linked to industrial combustion processes and automotive exhaust emissions [2,3]. Of the common VOCs emitted from these processes, propene and toluene are of particular interest due to their high Photochemical Ozone Creativity Potential (POCP) [4]. Toluene is also known to be a highly toxic compound [5], further highlighting the importance of removing VOCs to improve air quality. Another common product emitted by combustion processes is carbon monoxide (CO) [6]. Although CO is not defined as a VOC, it is known to be hazardous to human health under prolonged exposure [7]. The mixture of VOCs and CO has been utilised in research as an effective model to simulate emissions from vehicle engines.

The combination of chemically varying compounds, emitted from combustion processes, can prove challenging to remove from gas streams. The concentration of these compounds from automotive emissions are very low, making recovery methods an ineffective method of abatement [8]. Catalytic oxidation is a viable method of completely removing low concentrations of VOC and CO mixtures. Catalytic oxidation has the advantage of requiring less energy compared with standard thermal oxidation, as well as producing more environmentally benign products of CO_2 and H_2O [9].

Many studies have highlighted the notable catalytic activity of supported noble metals catalysts for VOC oxidation [10–14]. In particular, supported Pt catalysts have been extensively researched for VOC total oxidation, presenting significant activity for aliphatic and aromatic hydrocarbons [15–17]. Whereas, supported Au catalysts have previously shown remarkable activity for CO oxidation [15,18]. More recently studies have reported improvements of monometallic supported catalysts for total oxidation reactions by the addition of a second metal to the system [19–22]. It is reported that the use of bimetallic systems can manipulate metal dispersion, particle size, improve stability and form new active alloyed structures, which are beneficial for catalytic activity [20,23–25]. The use of mesoporous materials as supports for these types of catalysts has further enhanced the catalytic oxidation of VOCs, by improving metal nanoparticle dispersion and generating accessible pore networks for better diffusion of organic compounds [26].

With the increasing regulation around air pollutants, previous studies have used various single compounds to model VOC abatement by catalytic oxidation. However, focus has shifted to the simultaneous removal of a combination of VOCs with different chemical characteristics and CO [27]. It has been shown in the literature that the combination of different pollutants can inhibit the removal of VOCs at low temperature [28,29], requiring catalysts with improved performance for the simultaneous removal of a range of pollutants. In this work, a range of mono and bimetallic Pt/Au catalysts supported on a novel porous silica support, UVM-7 modified with ZrO_2, were evaluated for the simultaneous total oxidation of toluene, propene, and CO under oxygen lean conditions. Propene and toluene VOCs were used to model short chain alkenes and aromatic compounds respectively. Catalysts were prepared by a colloidal deposition method and characterised using Powder X-ray diffraction (XRD), Temperature programmed reduction (TPR), , X-ray photoelectron spectroscopy (XPS) and diffuse reflectance infrared Fourier transform spectroscopy (CO-DRIFTS). Electron microscopy (STEM-EDX) was carried out by researchers at the University of Zaragoza, in collaboration with this project.

6.2 Results

6.2.1 Catalyst characterisation

Table 1: Crystallite sizes of Au and Zr species, obtained by XRD analysis.

Catalyst	**Crystallite size / nm**	
	Au[a]	**ZrO_2**[b]
40% ZrO_2/UVM-7-C	N/A	11.4
40% ZrO_2/UVM-7-C 2% Au	9.9	10.0
40% ZrO_2/UVM-7-C 2% Pt	N/A	11.5
40% ZrO_2/UVM-7-C 2% Au-Pt	6.3	-
40% ZrO_2/UVM-7-C 1% Au + 1% Pt	6.2	6.3

40% ZrO_2/UVM-7-C 1% Pt + 1% Au	9.1	14.2

a – Scherrer equation applied to the Au (111) plane.

b – Scherrer equation applied to the Zr (111) plane.

XRD patterns of the catalysts shown in Figure 1 indicate a predominantly amorphous SiO_2 structure expected from the UVM-7 support [30]. However, some crystalline tetragonal ZrO_2 species were identified around 30.33°, representing the (111) lattice plane [31]. Au containing catalysts also exhibited a weak reflection around 38.90°, which was ascribed to the Au (111) lattice plane [32]. Table 1 shows the crystallite sizes identified by XRD analysis. For the support and monometallic catalysts, crystallite sizes of 10-11 nm were obtained for ZrO_2 incorporated onto the UVM-7 support. ZrO_2 crystallite size decreased for the 40% ZrO_2/UVM-7-C 1% Au + 1% Pt catalyst but increased for the 40% ZrO_2/UVM-7-C 1% Pt + 1% Au. The reflection at 30.33° observed on the 40% ZrO_2/UVM-7-C 2% Au-Pt catalyst was of low intensity and could not be reliably analysed by application of the Scherrer equation.

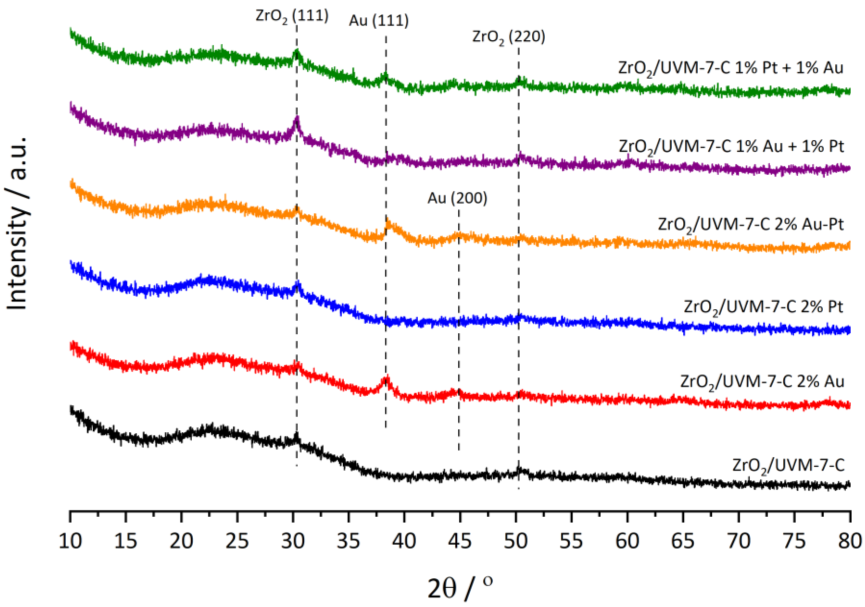

Figure 1: XRD patterns of calcined catalysts.

Also listed in Table 1 are the Au crystallite sizes for the Au containing catalysts. The monometallic 40% ZrO_2/UVM-7-C 2% Au displayed a crystallite size of 9.9 nm, whereas the 40% ZrO_2/UVM-7-C 2% Au-Pt and 40% ZrO_2/UVM-7-C 1% Au + 1% Pt bimetallic catalysts had slightly smaller crystallite sizes of 6.3 nm and 6.2 nm respectively. This trend of decreased crystallite size for the bimetallic catalysts was not reciprocated for the 40%

ZrO_2/UVM-7-C 1% Pt + 1% Au catalyst, having a crystallite size of 9.1 nm. The data shown highlights the importance of the preparation method, as a slight change in the order of metal deposition affected the metal particle size, which is thought to influence catalytic activity for certain reactions [33]. No reflections relating to bulk Pt particles could be identified for all Pt containing catalysts using XRD analysis.

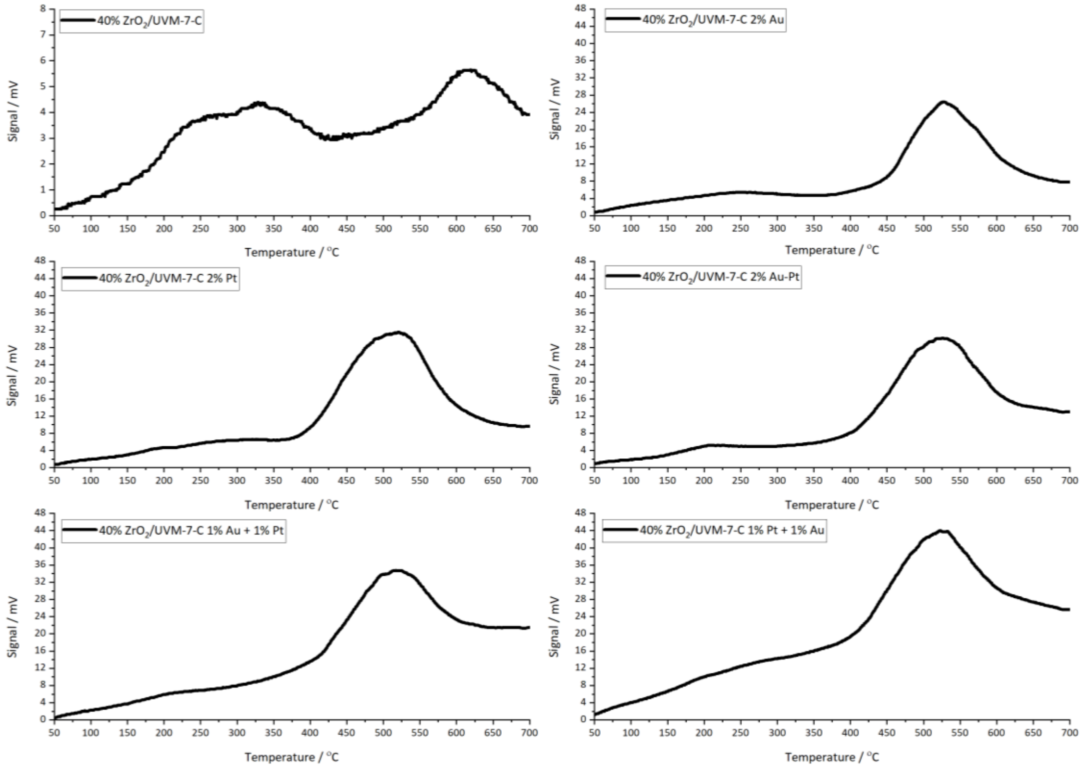

Figure 2: TPR profiles of the calcined catalysts.

TPR analysis, shown in Figure 2, displayed similar reduction profiles for each metal loaded catalyst. For the 40% ZrO_2/UVM-7-C support two weak reduction peaks are shown, one high temperature peak around 615 °C and another broad low temperature peak around 330 °C. These peaks were attributed to the reduction of coordinatively unsaturated Zr^{4+} surface species and bulk Zr^{4+} species, for the low temperature and high temperature peaks respectively [34]. Two reduction peaks can also be identified for the noble metal loaded catalysts, a large peak centred around 520 °C and a small broad peak centred around 200°C. The addition of Au or Pt metal nanoparticles to the support resulted in a shift to lower temperatures for the surface and bulk reduction of the Zr^{4+} species, which is in good agreement with previous literature [35–37].

Table 2: H_2 Consumption per gram of catalyst for both high temperature and low temperature peaks, determined by TPR analysis.

Catalyst	Low Temperature Peak Position / °C	High Temperature Peak Position / °C	Low Temperature H_2 Consumption / µmol g^{-1}	High Temperature H_2 Consumption / µmol g^{-1}
40% ZrO_2/UVM-7-C	329	619	4.25	2.33
40% ZrO_2/UVM-7-C 2% Au	236	525	5.35	28.05
40% ZrO_2/UVM-7-C 2% Pt	200	520	2.43	38.83
40% ZrO_2/UVM-7-C 2% Au-Pt	205	517	2.29	33.91
40% ZrO_2/UVM-7-C 1% Au + 1% Pt	204	514	1.16	29.25
40% ZrO_2/UVM-7-C 1% Pt + 1% Au	207	522	2.02	38.28

Table 2 shows the H_2 consumption per catalyst mass for both the low temperature and high temperature reduction features of ZrO_2. The addition of metal nanoparticles to the ZrO_2/UVM-7-C support increased the H_2 consumption for the high temperature peak, suggesting that the addition of either Au and/or Pt facilitated the reduction of bulk Zr^{4+} species. In contrast, only the addition of 2% Au was shown to improve the reduction of surface Zr^{4+} species, with all other catalysts presenting decreased H_2 consumption for the low temperature reduction peak.

CO-DRIFTS analysis (Figure 3) was used to identify the types of metal nanoparticles present on the catalyst surface. Only one distinctive band could be identified at 2075 cm^{-1} for catalysts 40% ZrO_2/UVM-7-C 2% Au-Pt and 40% ZrO_2/UVM-7-C 1% Au + 1% Pt. This band was attributed to CO linearly adsorbed on Pt surface sites [38,39]. Thus, it can be inferred from the presence of this band that the 40% ZrO_2/UVM-7-C 2% Au-Pt and 40% ZrO_2/UVM-7-C 1% Au + 1% Pt catalysts had accessible Pt surface species, which could participate in the oxidation reaction. Furthermore, the absence of this band from the 40% ZrO_2/UVM-7-C 2% Pt and 40% ZrO_2/UVM-7-C 1% Pt + 1% Au catalysts suggests there were limited Pt surface species available. Expected bands between 2120-2191 cm^{-1}, related to the adsorption of CO on Au species, were not present for all Au containing catalysts which implies weak bonding of these sites, suggesting there were limited available Au surface species [40]. A small residual band was identified at 1626 cm^{-1} for the support and monometallic catalysts, which has previously been linked to the formation of mono and bicarbonate species on the support surface [41].

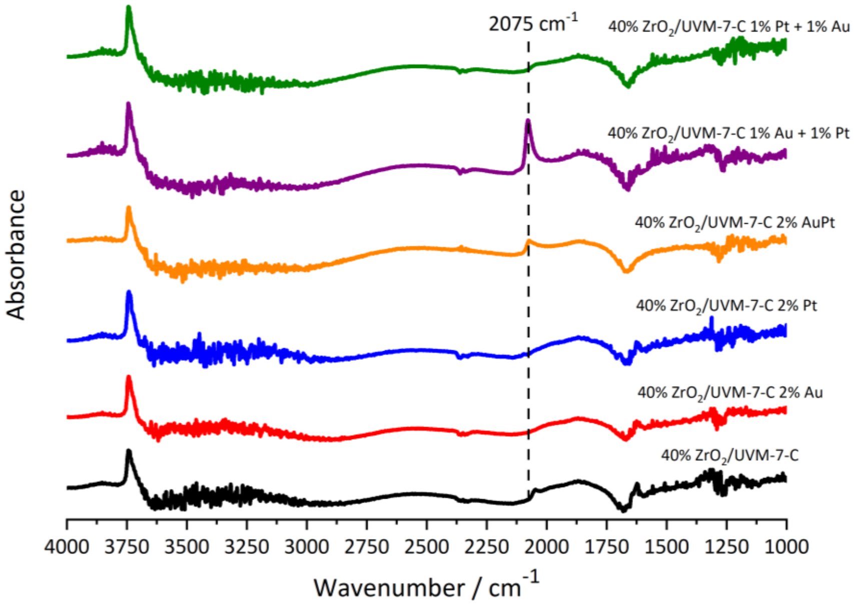

Figure 3: CO-DRIFTS spectra of the calcined catalysts.

XPS analysis (Figure 4) was used to determine metal nanoparticle species on the catalyst surface. All Au containing catalysts displayed one pair of Lorentzian curves at 84.3 eV and 87.9 eV, which are representative of metallic Au [42]. However, deconvolution of the Au bands for the 40% ZrO_2/UVM-7-C 2% Au-Pt catalyst showed some contribution from Au^I, with bands at 85.2 eV and 88.9 eV [43]. It has been previously stated that Au nanoparticles are resistant to oxidation, and the presence of Au^I in AuPt/SiO_2 catalysts suggested the interaction of the Pt and Au nanoparticles altered the electronic properties of the Au nanoparticles [43]. This implies strong interaction of the Pt and Au nanoparticles for the 40% ZrO_2/UVM-7-C 2% Au-Pt catalyst, suggesting alloying of the metal species.

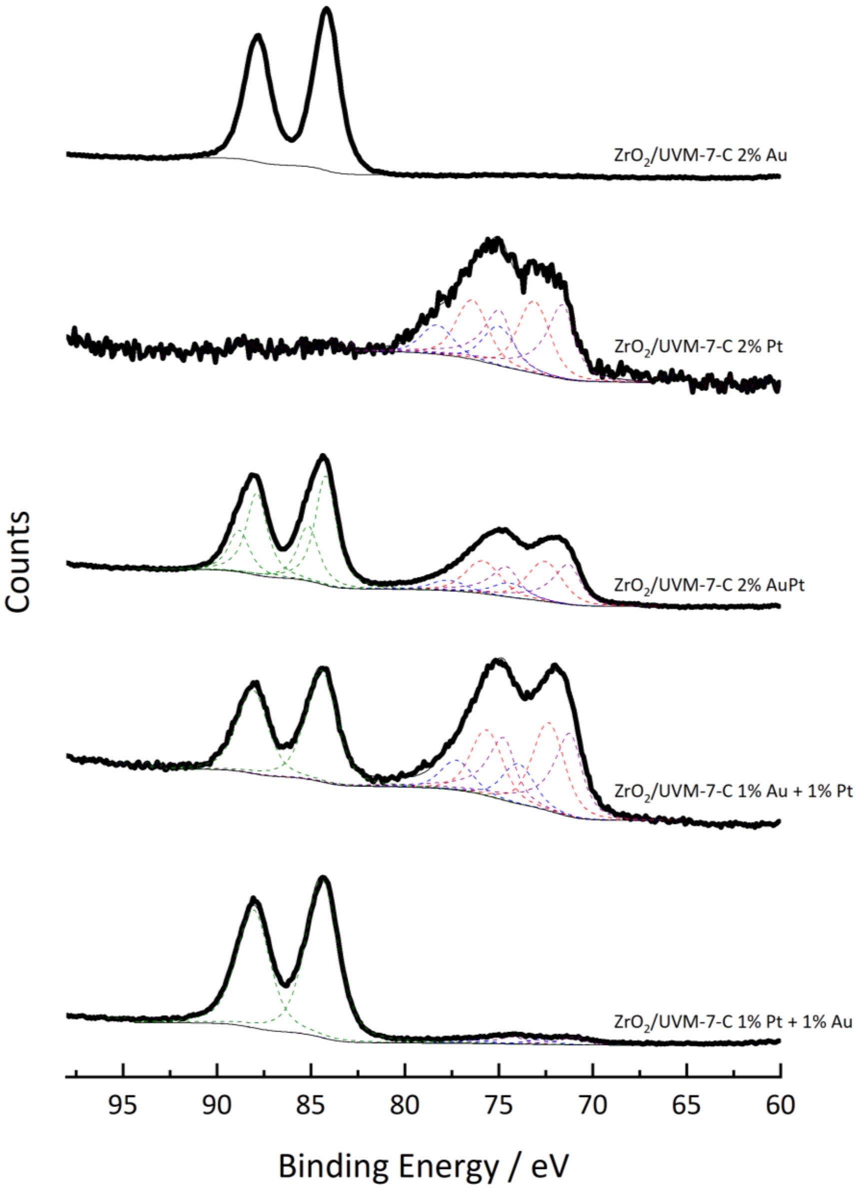

Figure 4: XPS spectra of the Au 4f and Pt 4f regions for the supported metal catalysts containing Au and Pt nanoparticles. Green curves represent the fitting of Au species. Purple, red and blue curves represent the fitting of Pt^0, Pt^{II} *and* Pt^{IV} *species respectively.*

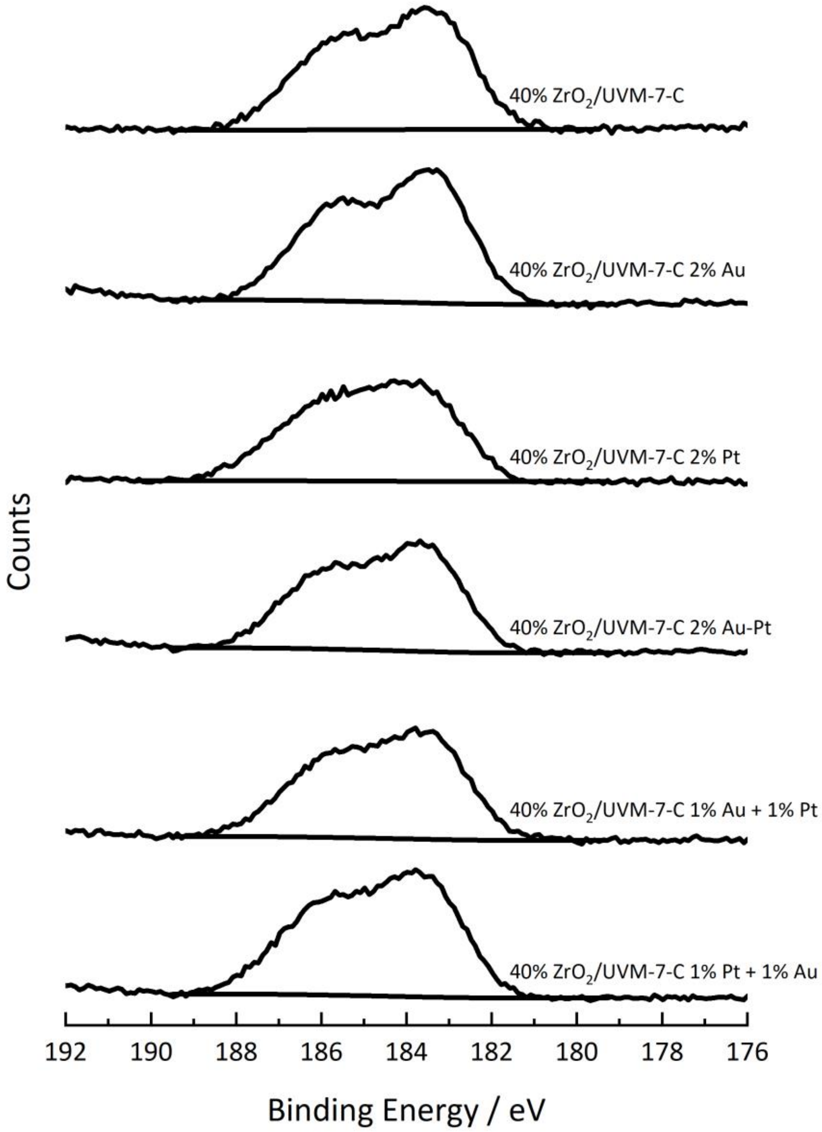

Figure 5: XPS spectra of the Zr 3d region for all catalysts.

For 40% ZrO_2/UVM-7-C 2% Pt, 40% ZrO_2/UVM-7-C 2% Au-Pt and 40% ZrO_2/UVM-7-C 1% Au + 1% Pt catalysts, three pairs of overlapping Lorentzian curves could be fitted, representing metallic Pt^0, Pt^{II} and Pt^{IV} species. These being the Pt $4f_{7/2}$ and Pt $4f_{5/2}$ pairs at 71.5 eV and 74.9 eV, 73.1 eV and 76.4 eV, 75 eV and 78.3 eV representing metallic Pt^0, Pt^{II} and Pt^{IV} respectively [44,45]. For the 40% ZrO_2/UVM-7-C 1% Pt + 1% Au catalyst, only two pairs of overlapping Lorentzian curves could be fitted, relating to metallic Pt^0 and Pt^{IV} species. A slight shift to lower binding energies for the Pt species could be noticed in the bimetallic catalysts, with an average shift of -0.5 eV for 40% ZrO_2/UVM-7-C 2% Au-Pt, -0.7 eV for 40% ZrO_2/UVM-7-C 1% Au + 1% Pt and -1.3 eV for 40% ZrO_2/UVM-7-C 1% Pt + 1% Au. This shift to lower binding energies occurred as a result of the charge transfer from the interaction of Pt with Au nanoparticles, as shown in previous literature [46,47].

Table 3: Surface species of Pt in at Pt containing catalysts, identified by XPS analysis.

Catalyst	Pt^0 / %	Pt^{II} / %	Pt^{IV} / %
40% ZrO_2/UVM-7-C 2% Pt	42.3	37.9	19.8
40% ZrO_2/UVM-7-C 2% Au-Pt	42.7	42.8	14.5
40% ZrO_2/UVM-7-C 1% Au + 1% Pt	42.4	39.6	18.0
40% ZrO_2/UVM-7-C 1% Pt + 1% Au	67.9	-	32.1

Deconvolution of the Lorentzian curves for the Pt $4f_{7/2}$ and Pt $4f_{5/2}$ pairs indicated little significant difference in the concentration of Pt surface species for most of the Pt containing catalysts (Table 3). Catalysts 40% ZrO_2/UVM-7-C 2% Pt, 40% ZrO_2/UVM-7-C 2% Au-Pt and 40% ZrO_2/UVM-7-C 1% Au + 1% Pt showed similar concentrations of metallic Pt^0, but had slight variations in Pt^{II} and Pt^{IV} concentrations. The 40% ZrO_2/UVM-7-C 1% Pt + 1% Au catalysts showed the largest difference in Pt surface species, indicating the absence of Pt^{II} but instead a much larger concentration of both Pt^0 and Pt^{IV} species.

Table 4: Catalyst surface composition, determined by XPS analysis.

Catalyst	Zr / At.%	Pt / At.%	Au / At.%
40% ZrO_2/UVM-7-C	2	-	-
40% ZrO_2/UVM-7-C 2% Au	2.58	-	0.94
40% ZrO_2/UVM-7-C 2% Pt	2.15	0.14	-
40% ZrO_2/UVM-7-C 2% Au-Pt	2.22	0.71	0.74
40% ZrO_2/UVM-7-C 1% Au + 1% Pt	2.35	0.52	0.24
40% ZrO_2/UVM-7-C 1% Pt + 1% Au	2.35	0.09	0.94

Catalyst surface compositions are shown in Table 4, determined by XPS analysis. All catalysts had a similar surface composition of Zr, ranging from 2-2.58 At.%, indicating good interaction with the UVM-7-C support. However, when identifying supported metal surface concentrations, variations were identified for all catalysts. For the monometallic catalysts, a much higher surface loading of Au was seen compared with the Pt loading on the 40% ZrO_2/UVM-7-C 2% Pt catalyst. The 40% ZrO_2/UVM-7-C 2% Au-Pt catalyst displayed the highest surface concentration of Pt and Au, with a near 1:1 ratio of Au-Pt which was in good agreement with the theoretical ratio expected. In contrast, the catalysts with differing orders of metal loading displayed varying surface concentrations of Au and Pt. The 40% ZrO_2/UVM-7-C 1% Au + 1% Pt catalyst showed a lower concentration of surface Au and Pt, but had a Pt rich surface with a Au-Pt ratio of 1:2; whereas, the 40% ZrO_2/UVM-7-C 1% Pt + 1% Au catalyst presented a much higher surface concentration of Au, similar to the monometallic Au catalyst, with a 10:1 Au-Pt ratio. These data suggests that the metal loaded last, during the synthesis, is deposited on the other metal, resulting in a surface enrichment and a higher surface ratio of the latter noble metal. Previous research has shown that, for the preparation of bimetallic catalysts with a different order of metal loading, the surface elemental composition was largely unaffected which is in contrast to XPS data shown in this work [19,48]. However, this could be a result of the different preparation methods used.

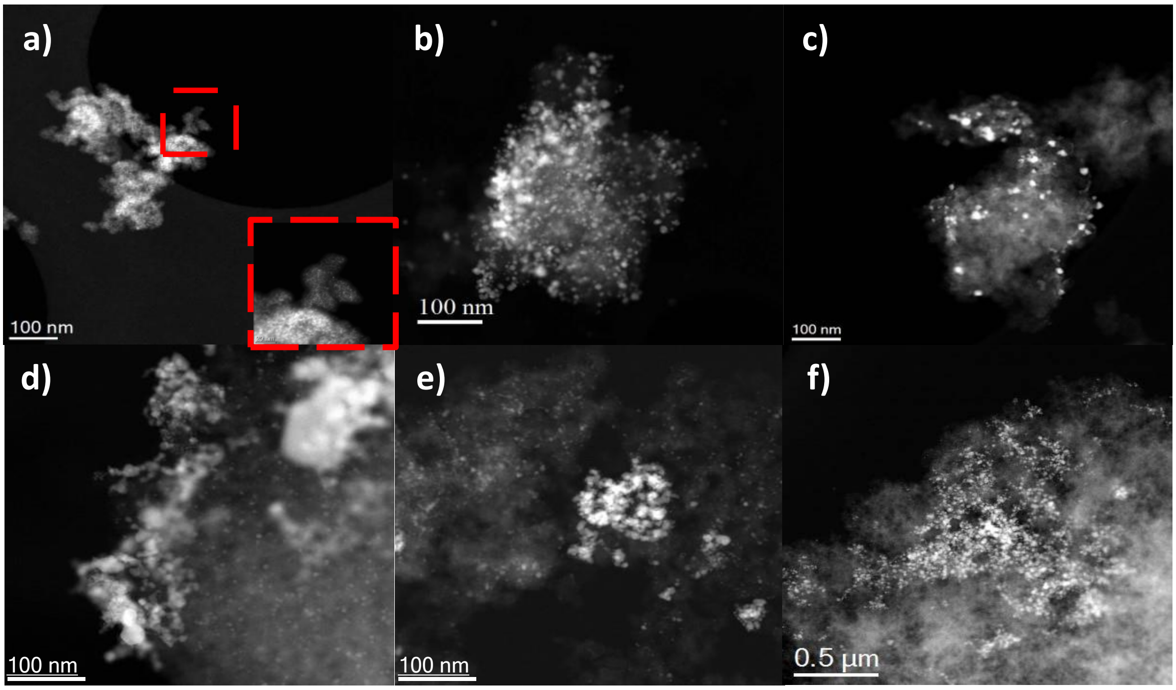

Figure 6: STEM images of the calcined catalysts. a) 40%ZrO_2/UVM-7-C b) 40%ZrO_2/UVM-7-C 2% Au c) 40%ZrO_2/UVM-7-C 2% Pt d) 40%ZrO_2/UVM-7-C 2% Au-Pt e) 40%ZrO_2/UVM-7-C 1% Au + 1% Pt f) 40%ZrO_2/UVM-7-C 1% Pt + 1% Au.

Images (Figures 6a-f) produced from STEM analysis, carried out by researchers at the University of Zaragoza, indicated heterogeneously distributed metal nanoparticles loaded on the 40%ZrO_2/UVM-7-C support for all catalysts. EDX analysis (Figure 7) showed a homogeneous distribution of ZrO_2 on the UVM-7-C support which is in good agreement with conclusions drawn from XPS analysis, indicating a strong interaction between the metal oxide and UVM-7-C. Au and Pt nanoparticles were identified for each of the monometallic catalysts respectively. The 40% ZrO_2/UVM-7-C 2% Au catalyst (Figure 6b) showed a large amount of Au nanoparticles with a size distribution between 2-10 nm and mean particle size of 5.3 nm, which is in good agreement with previous XRD data. For the 40% ZrO_2/UVM-7-C 2% Pt catalyst, fewer Pt nanoparticles could be identified, which was concurrent with the surface composition identified by XPS analysis. In addition, a combination of small and large clusters of Pt nanoparticles were identified by EDX analysis (Figure 8), resulting in a larger particle size distribution over the range 2-20 nm with a mean particle size of 6.7 nm.

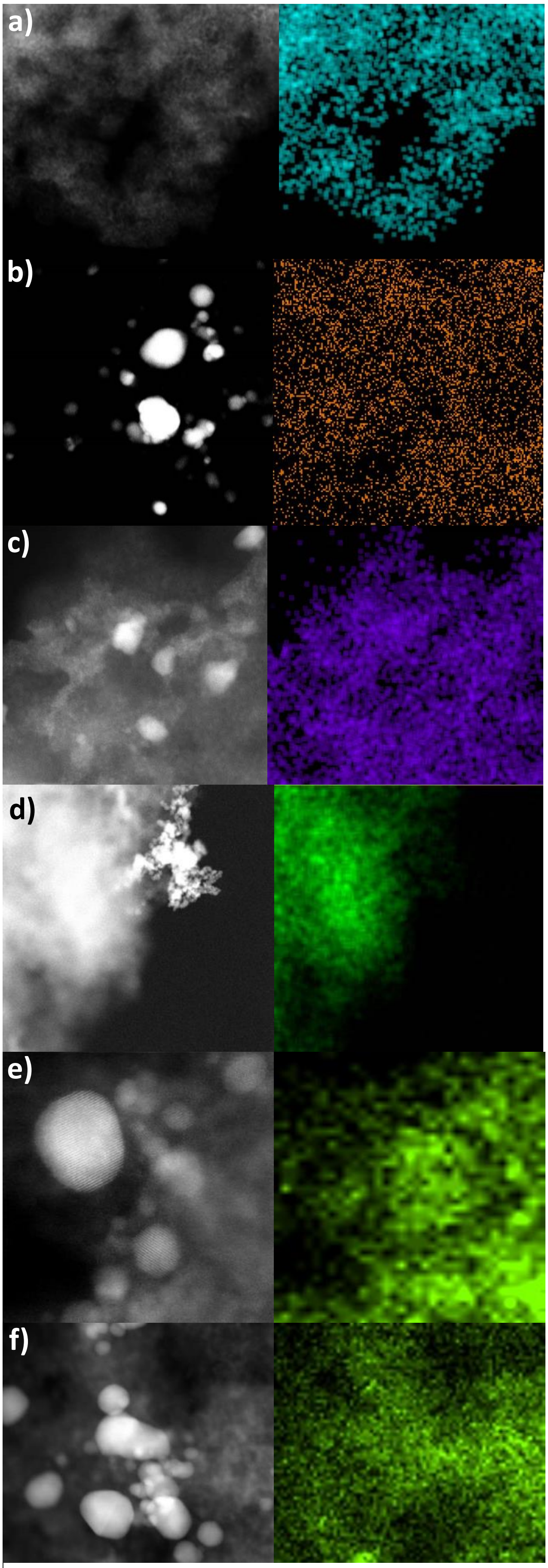

Figure 7: STEM images and corresponding EDX mapping of Zr Lα1 for catalysts: a) 40%ZrO_2/UVM-7-C b) 40%ZrO_2/UVM-7-C 2% Au c) 40%ZrO_2/UVM-7-C 2% Pt d) 40%ZrO_2/UVM-7-C 2% Au-Pt e) 40%ZrO_2/UVM-7-C 1% Au + 1% Pt f) 40%ZrO_2/UVM-7-C 1% Pt + 1% Au.

Table 5: Catalyst composition determined by EDX analysis.

Catalyst	Pt / At.%	Au / At.%
40% ZrO_2/UVM-7-C	N/A	N/A
40% ZrO_2/UVM-7-C 2% Au	N/A	2.70
40% ZrO_2/UVM-7-C 2% Pt	3.20	N/A
40% ZrO_2/UVM-7-C 2% Au-Pt	0.33	0.45
40% ZrO_2/UVM-7-C 1% Au + 1% Pt	1.12	0.26
40% ZrO_2/UVM-7-C 1% Pt + 1% Au	0.06	2.08

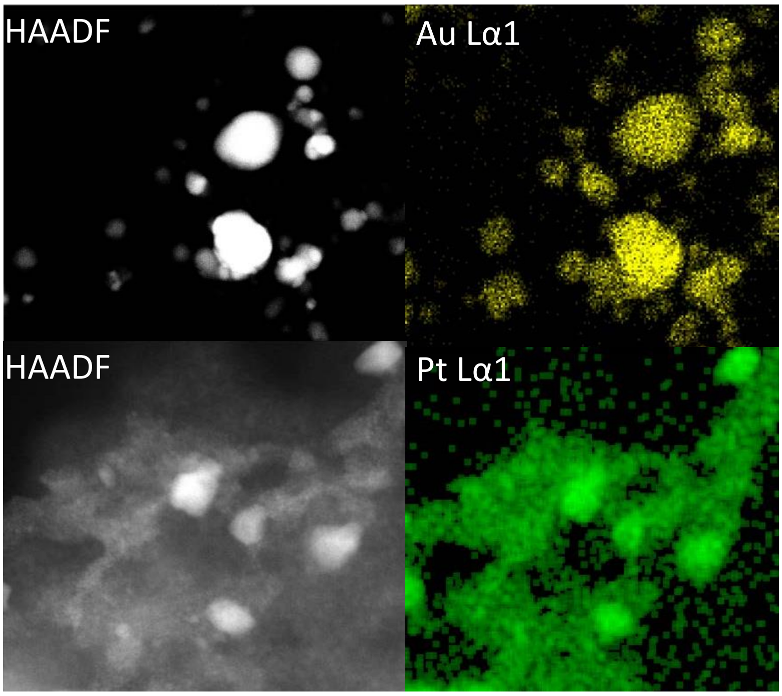

Figure 8: HAADF and corresponding EDX images of 40%ZrO_2/UVM-7-C 2% Au (Top) and 40%ZrO_2/UVM-7-C 2% Pt (Bottom) catalysts.

Both Au and Pt nanoparticles were assigned by STEM analysis for all the bimetallic catalysts. As shown by EDX analysis (Figure 9), all bimetallic catalysts showed Au and Pt co-located which suggests strong Au-Pt interaction. This was consistent with conclusions drawn from XPS analysis, regarding the strong metal nanoparticle interaction resulting in a shift to lower binding energies for Pt species. The 40% ZrO_2/UVM-7-C 2% Au-Pt catalyst only displayed alloyed metal nanoparticles with a large size distribution range of 3-100 nm and mean particle size of 6.5 nm. This further explains the appearance of Au^I species in the XPS data, confirming the strong electronic interaction of the alloyed Au-Pt species identified for this catalyst. Moreover, a similar concentration of both Pt and Au was identified (Table 5) which is comparable to the 1:1 ratio of Au and Pt obtained by XPS. For the 40% ZrO_2/UVM-

7-C 1% Au + 1% Pt catalyst, a heterogeneous particle size distribution was observed with a mean particle size of 5.9 nm. Both Au and Pt nanoparticles of >10 nm were formed, however, smaller nanoparticles (<5 nm), that were Pt rich, were also present. Similarly to the surface composition obtained from XPS analysis, a higher concentration of Pt was quantified by EDX for this catalyst. In contrast, the 40% ZrO_2/UVM-7-C 1% Pt + 1% Au catalyst, with a different order of metal loading, showed a higher concentration of Au by EDX analysis (Table 5). Again, this result is in good agreement with surface composition obtained by XPS analysis. Furthermore, the particle size distribution of the 40% ZrO_2/UVM-7-C 1% Pt + 1% Au catalyst was comparable to the 40% ZrO_2/UVM-7-C 1% Au + 1% Pt catalyst, but the smaller nanoparticles (<5 nm) were predominantly Au rich and the mean particle size was slightly larger at 7.4 nm.

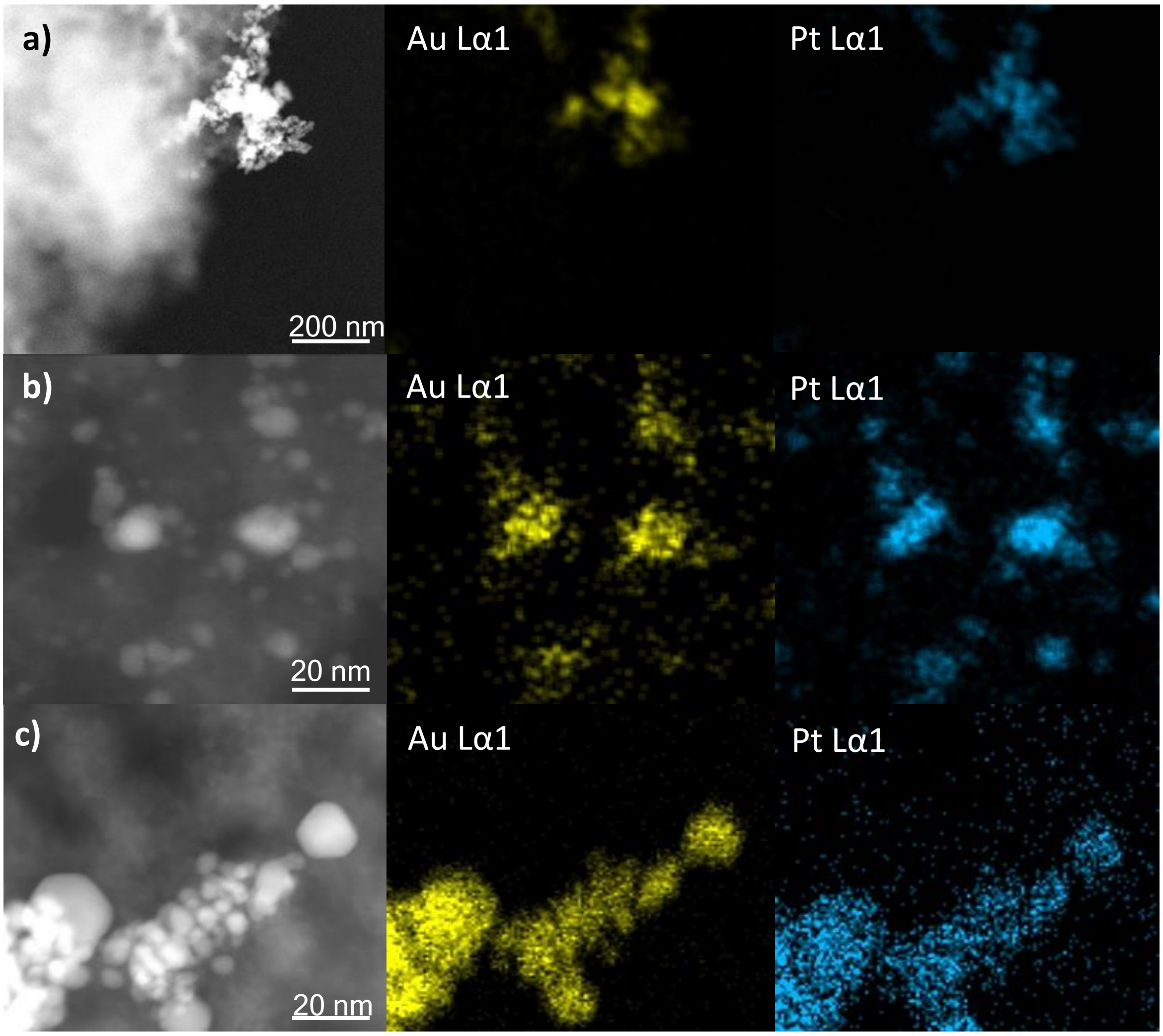

Figure 9: STEM images and corresponding EDX images of Pt and Au elements for the bimetallic catalyst: a) 40%ZrO_2/UVM-7-C 2% Au-Pt b) 40%ZrO_2/UVM-7-C 1% Au + 1% Pt c) 40%ZrO_2/UVM-7-C 1% Pt + 1% Au.

6.2.2 Catalyst testing

Catalytic performance for the simultaneous total oxidation of the VOC and CO mixture are shown in Figure 10 for all catalysts. CO_2 yield from all pollutants (propene, toluene and CO) was used to assess the overall catalytic activity for the combined total oxidation. CO_2 was the only product identified during the total oxidation of the gas mixture, with all catalysts obtaining a carbon balance >94 %. The 40% ZrO_2/UVM-7-C 1% Au + 1% Pt catalyst presented the highest catalytic activity, with all compounds fully oxidised at 250°C. The 40% ZrO_2/UVM-7-C 2% Au-Pt catalyst also showed appreciable activity, reaching full conversion at 250°C, but had a much lower CO_2 yield at temperatures under 250°C. Interestingly, the addition of Au to the support resulted in a negative effect on catalytic activity, with the 40% ZrO_2/UVM-7-C 2% Au catalyst being less active than the 40% ZrO_2/UVM-7-C support.

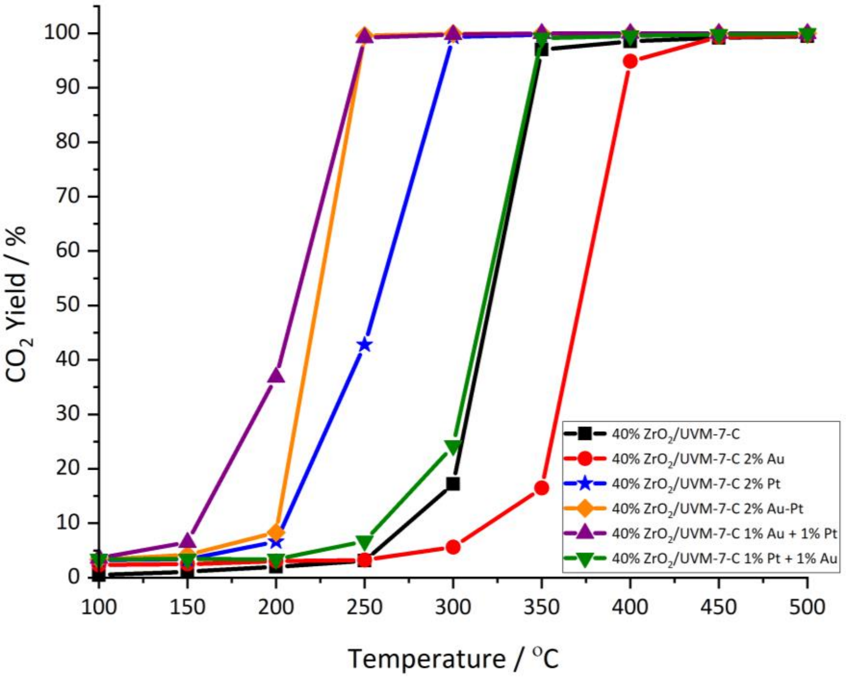

Figure 10: Combined CO_2 yield for the simultaneous total oxidation of toluene, propene, and CO gas mix. Conditions: 100 ppm toluene, 1000 ppm propene, 1000 ppm CO, 6% O_2/N_2, WHSV = 6000 h^{-1}. Legend refers to catalysts used.

The activity of the catalysts for the total oxidation of individual toluene, propene and CO components in the gas mix are shown in Figure 11. The general trend of catalyst activity is similar to the overall CO_2 yield presented, with the 40% ZrO_2/UVM-7-C 1% Au + 1% Pt catalyst being the most active for all compounds. Only a slight deviation from the overall trend can be noticed for CO oxidation and toluene oxidation, where the 40% ZrO_2/UVM-7-

C 2% Au catalyst showed slightly better conversion at low temperatures for CO oxidation and the 40% ZrO_2/UVM-7-C 1% Pt + 1% Au catalyst presented lower conversion than the support at 300°C for toluene oxidation.

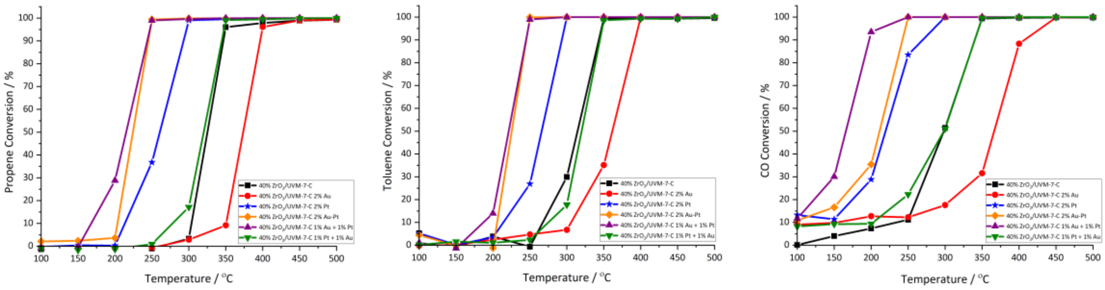

Figure 11: Individual breakdown of catalyst activity for the simultaneous oxidation of propene (Left), toluene (Middle) and CO (Right). Legend refers to catalysts used.

It is stated in the literature that the addition of a metal oxide onto a non-reducible support can improve the catalytic activity of supported metal catalysts for CO and VOCs oxidation [11,49,50]. The beneficial role of the metal oxide is to supply active oxygen species on the catalyst surface, which then enhances the activity of the metal nanoparticles [51,52]. The ability to promote active oxygen species can often be linked with surface reducibility of the catalyst, relating to the facile mobility of oxygen species [50,53,54]. However, in this work, no general trend was distinguished between catalyst reducibility and catalytic activity. In fact, the TPR data showed that the 40% ZrO_2/UVM-7-C 2% Au catalyst with the highest surface H_2 consumption relating to the Zr^{4+} bound oxygen species was the least active catalyst, suggesting other factors were important for controlling the activity. Furthermore, there seemed to be a negligible effect of the bulk crystallite size of the ZrO_2, identified by XRD analysis, improving the bulk oxygen mobility of the catalysts. Therefore, the influence of the metal nanoparticle loading had the largest impact on the overall catalytic activity compared with the reducibility of ZrO_2 species.

The role of metal nanoparticles in supported precious metal catalysts are widely reported as an important factor for VOC and CO oxidation [22,27,55,56]. From the data shown (Figure 10), catalysts containing a high surface concentration of Au nanoparticles, as determined by XPS and STEM, showed poor catalytic activity. Similar conclusions have been shown in previous studies for the oxidation of toluene and propene individually, with supported Au catalysts showing lower conversion compared with Pt or Pd counterparts [10,37,57]. This was proposed to occur due to the differing intrinsic dissociative chemisorption energies of oxygen for each noble metal, which is related to the role of oxygen adsorption in the oxidation mechanism [15]. Supported Au catalysts have been reported as effective catalysts for CO oxidation which is consistent with the CO oxidation performance at low temperatures in Figure 11. However, previous literature discussing the impact of simultaneous removal of VOCs and CO, showed that VOCs competitively bind to the catalyst surface, blocking active sites, which negatively impacted on the rate of CO oxidation [27,58]. Therefore, the efficiency of supported Au catalysts for CO oxidation was decreased under the reaction conditions used.

From the previous discussion, it can be assumed that Pt was the active species for the simultaneous total oxidation of CO, propene, and toluene. This fits well with surface compositions determined by XPS and EDX analysis. A structure sensitive relationship has been determined for toluene and propene oxidation using supported Pt catalysts [15,16,59,60]. It has been shown that increased Pt particle size results in oxygen being held on Pt atoms with a lower bond strength, facilitating improved catalytic activity for toluene oxidation [61]. Whereas for propene oxidation, this affect is slightly less direct and can also be somewhat related to higher concentrations of metallic Pt^0 species [59]. From the XPS data, no direct correlation between activity and Pt surface species could be identified for these catalysts. There was negligible difference in Pt^0 concentration and little significant difference in Pt^{II} and Pt^{IV} concentrations for the most active catalysts. Furthermore, the structure sensitive activity for VOC oxidation was also not exhibited by these catalysts, as the 40% ZrO_2/UVM-7-C 1% Au + 1% Pt catalyst contained more smaller Pt nanoparticles (<5 nm), determined by STEM analysis, compared with the 40% ZrO_2/UVM-7-C 2% Pt catalyst, which showed lower catalytic activity. Therefore, the predominant factor determining catalytic activity can be related to the relative concentration of Pt on the catalyst surface in relation to the quantity of the inactive Au nanoparticles. This trend is highlighted in Figure 12 by the linear correlation between decreasing temperature required to reach 50% conversion (T_{50}) and increasing relative Pt concentration. CO-DRIFTS analysis also confirms the importance of surface Pt as the data indicated available surface Pt species for the 40% ZrO_2/UVM-7-C 2% Au-Pt and 40% ZrO_2/UVM-7-C 1% Au + 1% Pt catalysts only. Whereas an absence of any Pt band was shown for the 40% ZrO_2/UVM-7-C 2% Pt catalyst, possibly as a result of the low surface Pt loading, measured by XPS analysis.

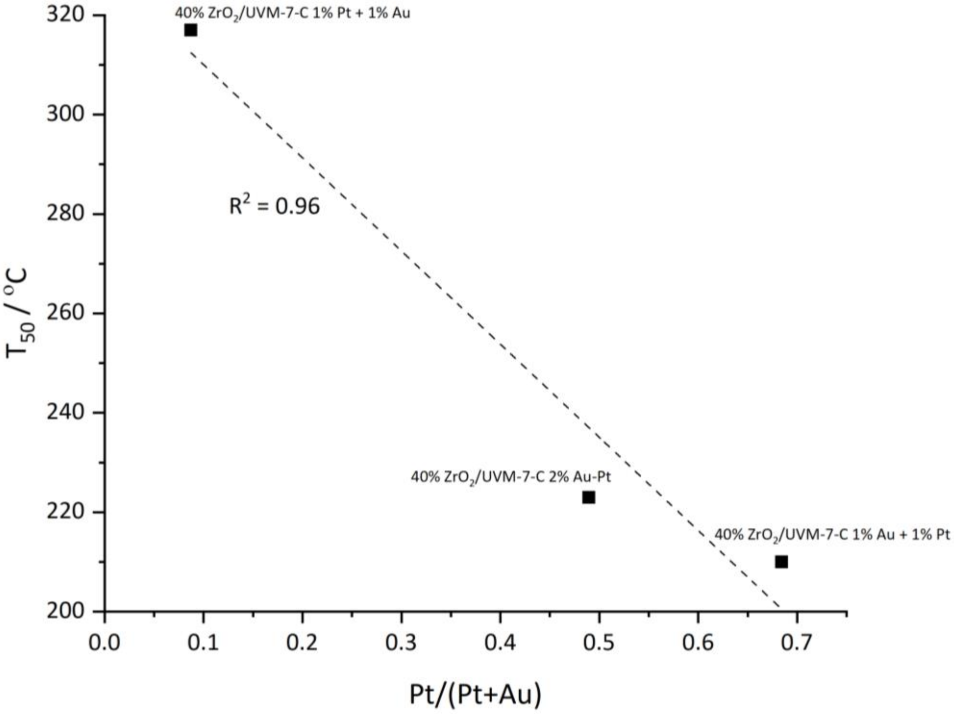

Figure 12: Relative Pt surface concentration identified by XPS analysis vs T_{50} for the bimetallic catalysts.

The bimetallic catalysts 40% ZrO_2/UVM-7-C 2% Au-Pt and 40% ZrO_2/UVM-7-C 1% Au + 1% Pt, with higher surface Pt concentrations, presented higher activity than the monometallic Pt catalyst, implying the incorporation of Au into the preparation method improved surface loading of Pt nanoparticles. Previous literature has stated that, in AuPt systems, Pt surface enrichment can occur due to the stronger affinity for adsorbates, forming stable oxides on the surface [62]. XPS data corroborated with this theory as the 40% ZrO_2/UVM-7-C 1% Pt + 1% Au catalyst had a larger quantity of Pt^0 species suggesting less stable Pt oxide species were formed, resulting in little surface migration. The order of metal loading was also significant to improve Pt loading on the surface. Depositing Pt or Au sequentially resulted in a drastic change in catalytic activity, mainly as a result of the improved surface concentration of Pt when it was deposited last (40% ZrO_2/UVM-7-C 1% Au + 1% Pt). However, when depositing Au and Pt simultaneously, both metal nanoparticles were evenly distributed on the surface, as demonstrated by the formation of alloyed nanoparticles in the STEM and XPS analysis. The formation of alloyed particles caused a 1:1 surface ratio of Au-Pt nanoparticles, which resulted in slightly lower activity compared with the Pt rich 1:2 Au-Pt surface ratio obtained for the 40% ZrO_2/UVM-7-C 1% Au + 1% Pt catalyst. This further highlights the negative impact caused by the increased amount of inactive Au nanoparticles on the simultaneous oxidation of CO, propene, and toluene.

6.2.3 Catalyst stability

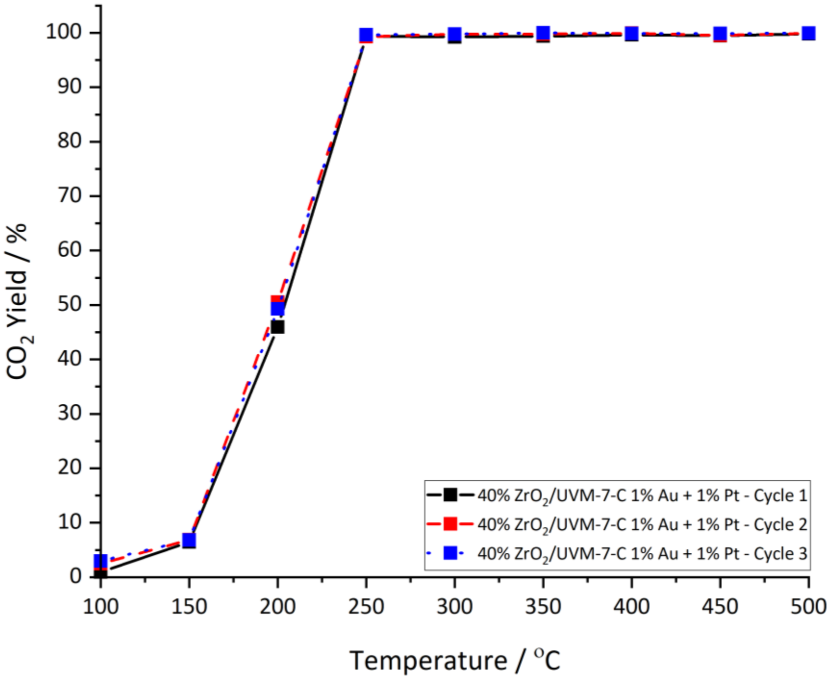

Figure 13: Stability test for the simultaneous total oxidation of toluene, propene and CO using the 40% ZrO_2/UVM-7-C 1% Au + 1% Pt catalyst.

In addition to catalytic activity and selectivity, catalyst stability is another important factor considered for many industrially relevant catalysts. Previously, modified UVM-7 catalysts have displayed good thermal stability towards Au sintering due to the confinement architecture of the silica structure and strong anchoring onto metal oxide, homogeneously dispersed within the structure [63]. To assess the stability of these catalysts cycle testing was carried out on the most active catalyst. As shown in Figure 13, the 40% ZrO_2/UVM-7-C 1% Au + 1% Pt catalyst remained active for the total oxidation of toluene, propene, and CO after three consecutive cycles. Further supporting the application of UVM-7 silica catalysts for industrial use.

6.3 Conclusions

Monometallic and bimetallic Au-Pt catalysts were prepared using a novel ZrO_2/UVM-7-C support and assessed for the simultaneous oxidation of toluene, propene, and CO pollutants under oxygen lean conditions. The 40% ZrO_2/UVM-7-C 1% Au + 1% Pt catalyst was found to be the most active for the total oxidation of all three compounds, obtaining full conversion by 250°C. The enhanced catalytic activity was related to the high relative surface concentration of Pt nanoparticles which were shown to be the active component for this reaction. The order of metal nanoparticle loading was also important for the bimetallic catalysts. Loading Pt and Au sequentially resulted in higher surface concentrations of either active Pt nanoparticles or inactive Au nanoparticles on the catalyst surface. Whereas simultaneous addition of metal nanoparticles resulted in alloyed nanoparticles with a 1:1 ratio on the catalyst surface. The alloyed nanoparticles displayed slightly lower catalytic activity as a result of the increased surface concentration of Au.

6.4 References

[1] Z.H. Ling, H. Guo, Contribution of VOC sources to photochemical ozone formation and its control policy implication in Hong Kong, Environ. Sci. Policy. 38 (2014) 180–191. https://doi.org/10.1016/j.envsci.2013.12.004.

[2] D.J. Wuebbles, S. Sanyal, Air Quality in a Cleaner Energy World, Curr. Pollut. Rep. 1 (2015) 117–129. https://doi.org/10.1007/s40726-015-0009-x.

[3] A. Ragothaman, W.A. Anderson, Air Quality Impacts of Petroleum Refining and Petrochemical Industries, Environments. 4 (2017) 66. https://doi.org/10.3390/environments4030066.

[4] M. Ousmane, L.F. Liotta, G.D. Carlo, G. Pantaleo, A.M. Venezia, G. Deganello, L. Retailleau, A. Boreave, A. Giroir-Fendler, Supported Au catalysts for low-temperature abatement of propene and toluene, as model VOCs: Support effect, Appl. Catal. B Environ. 101 (2011) 629–637. https://doi.org/10.1016/j.apcatb.2010.11.004.

[5] F. Pariselli, M.G. Sacco, J. Ponti, D. Rembges, Effects of toluene and benzene air mixtures on human lung cells (A549), Exp. Toxicol. Pathol. 61 (2009) 381–386. https://doi.org/10.1016/j.etp.2008.10.004.

[6] J.-O. Jo, H.Q. Trinh, S.H. Kim, Y.S. Mok, Simultaneous removal of hydrocarbon and CO using a nonthermal plasma-catalytic hybrid reactor system, Chem. Eng. J. 299 (2016) 93–103. https://doi.org/10.1016/j.cej.2016.04.070.

[7] A.L. Chiew, N.A. Buckley, Carbon monoxide poisoning in the 21st century, Crit. Care. 18 (2014) 221. https://doi.org/10.1186/cc13846.

[8] G.R. Parmar, N.N. Rao, Emerging Control Technologies for Volatile Organic Compounds, Crit. Rev. Environ. Sci. Technol. 39 (2008) 41–78. https://doi.org/10.1080/10643380701413658.

[9] A. Krishnamurthy, B. Adebayo, T. Gelles, A. Rownaghi, F. Rezaei, Abatement of gaseous volatile organic compounds: A process perspective, Catal. Today. 350 (2020) 100–119. https://doi.org/10.1016/j.cattod.2019.05.069.

[10] S. Scirè, L.F. Liotta, Supported gold catalysts for the total oxidation of volatile organic compounds, Appl. Catal. B Environ. 125 (2012) 222–246. https://doi.org/10.1016/j.apcatb.2012.05.047.

[11] A.C. Gluhoi, N. Bogdanchikova, B.E. Nieuwenhuys, The effect of different types of additives on the catalytic activity of Au/Al2O3 in propene total oxidation: transition metal oxides and ceria, J. Catal. 229 (2005) 154–162. https://doi.org/10.1016/j.jcat.2004.10.003.

[12] P. Gélin, M. Primet, Complete oxidation of methane at low temperature over noble metal based catalysts: a review, Appl. Catal. B Environ. 39 (2002) 1–37. https://doi.org/10.1016/S0926-3373(02)00076-0.

[13] T. Barakat, V. Idakiev, R. Cousin, G.-S. Shao, Z.-Y. Yuan, T. Tabakova, S. Siffert, Total oxidation of toluene over noble metal based Ce, Fe and Ni doped titanium oxides, Appl. Catal. B Environ. 146 (2014) 138–146. https://doi.org/10.1016/j.apcatb.2013.05.064.

[14] S. Huang, C. Zhang, H. He, Complete oxidation of o-xylene over Pd/Al2O3 catalyst at low temperature, Catal. Today. 139 (2008) 15–23. https://doi.org/10.1016/j.cattod.2008.08.020.

[15] V.P. Santos, S.A.C. Carabineiro, P.B. Tavares, M.F.R. Pereira, J.J.M. Órfão, J.L. Figueiredo, Oxidation of CO, ethanol and toluene over TiO2 supported noble metal catalysts, Appl. Catal. B Environ. 99 (2010) 198–205. https://doi.org/10.1016/j.apcatb.2010.06.020.

[16] Liotta, L.F, Catalytic oxidation of volatile organic compounds on supported noble metals, Appl. Catal. B Environ. 100 (2010) 403–412. https://doi.org/10.1016/j.apcatb.2010.08.023.

[17] A.C. Gluhoi, N. Bogdanchikova, B.E. Nieuwenhuys, Total oxidation of propene and propane over gold–copper oxide on alumina catalysts: Comparison with Pt/Al2O3, Catal. Today. 113 (2006) 178–181. https://doi.org/10.1016/j.cattod.2005.11.061.

[18] K.M. Saoud, M.S. El-Shall, Physical and Chemical Synthesis of Au/CeO2 Nanoparticle Catalysts for Room Temperature CO Oxidation: A Comparative Study, Catalysts. 10 (2020) 1351. https://doi.org/10.3390/catal10111351.

[19] M. Hosseini, T. Barakat, R. Cousin, A. Aboukaïs, B.-L. Su, G. De Weireld, S. Siffert, Catalytic performance of core–shell and alloy Pd–Au nanoparticles for total oxidation of VOC: The effect of metal deposition, Appl. Catal. B Environ. 111–112 (2012) 218–224. https://doi.org/10.1016/j.apcatb.2011.10.002.

[20] R. Fiorenza, Bimetallic Catalysts for Volatile Organic Compound Oxidation, Catalysts. 10 (2020) 661. https://doi.org/10.3390/catal10060661.

[21] T.K. Nevanperä, S. Ojala, T. Laitinen, S. Pitkäaho, S. Saukko, R.L. Keiski, Catalytic Oxidation of Dimethyl Disulfide over Bimetallic Cu–Au and Pt–Au Catalysts Supported on γ-Al2O3, CeO2, and CeO2–Al2O3, Catalysts. 9 (2019) 603. https://doi.org/10.3390/catal9070603.

[22] K.-J. Kim, H.-G. Ahn, Complete oxidation of toluene over bimetallic Pt–Au catalysts supported on ZnO/Al2O3, Appl. Catal. B Environ. 91 (2009) 308–318. https://doi.org/10.1016/j.apcatb.2009.05.037.

[23] A. Villa, D. Wang, D.S. Su, L. Prati, New challenges in gold catalysis: bimetallic systems, Catal. Sci. Technol. 5 (2014) 55–68. https://doi.org/10.1039/C4CY00976B.

[24] T. Barakat, J.C. Rooke, D. Chlala, R. Cousin, J.-F. Lamonier, J.-M. Giraudon, S. Casale, P. Massiani, B.-L. Su, S. Siffert, Oscillatory Behavior of Pd-Au Catalysts in Toluene Total Oxidation, Catalysts. 8 (2018) 574. https://doi.org/10.3390/catal8120574.

[25] X. Fu, Y. Liu, W. Yao, Z. Wu, One-step synthesis of bimetallic Pt-Pd/MCM-41 mesoporous materials with superior catalytic performance for toluene oxidation, Catal. Commun. 83 (2016) 22–26. https://doi.org/10.1016/j.catcom.2016.05.001.

[26] B. Solsona, M. Pérez-Cabero, I. Vázquez, A. Dejoz, T. García, J. Álvarez-Rodríguez, J. El-Haskouri, D. Beltrán, P. Amorós, Total oxidation of VOCs on Au nanoparticles anchored on Co doped mesoporous UVM-7 silica, Chem. Eng. J. 187 (2012) 391–400. https://doi.org/10.1016/j.cej.2012.01.132.

[27] P. Peng, J. Li, S. Mo, Q. Zhang, T. Shen, Q. Xie, Bimetallic Pt-Co Nanoparticle Deposited on Alumina for Simultaneous CO and Toluene Oxidation in the Presence of Moisture, Processes. 9 (2021) 230. https://doi.org/10.3390/pr9020230.

[28] R.K. Dadi, D. Luss, V. Balakotaiah, Bifurcation features of mixtures containing CO and hydrocarbons in diesel oxidation catalyst, Chem. Eng. J. 304 (2016) 941–952. https://doi.org/10.1016/j.cej.2016.06.119.

[29] Q. Zhang, S. Mo, J. Li, Y. Sun, M. Zhang, P. Chen, M. Fu, J. Wu, L. Chen, D. Ye, In situ DRIFT spectroscopy insights into the reaction mechanism of CO and toluene co-oxidation over Pt-based catalysts, Catal. Sci. Technol. 9 (2019) 4538–4551. https://doi.org/10.1039/C9CY00751B.

[30] M.M. Trandafir, A. Moragues, P. Amorós, V.I. Parvulescu, Selective hydrogenation of nitroderivatives over Au/TiO2/UVM-7 composite catalyst, Catal. Today. 355 (2020) 893–902. https://doi.org/10.1016/j.cattod.2019.02.053.

[31] C. Colbea, D. Avram, B. Cojocaru, R. Negrea, C. Ghica, V.G. Kessler, G.A. Seisenbaeva, V. Parvulescu, C. Tiseanu, Full Tetragonal Phase Stabilization in ZrO2 Nanoparticles Using Wet Impregnation: Interplay of Host Structure, Dopant Concentration and Sensitivity of Characterization Technique, Nanomaterials. 8 (2018) 988. https://doi.org/10.3390/nano8120988.

[32] L.-H. Chang, N. Sasirekha, Y.-W. Chen, W.-J. Wang, Preferential Oxidation of CO in H2 Stream over Au/MnO2−CeO2 Catalysts, Ind. Eng. Chem. Res. 45 (2006) 4927–4935. https://doi.org/10.1021/ie0514408.

[33] H. Wang, J. Lu, A Review on Particle Size Effect in Metal-Catalyzed Heterogeneous Reactions, Chin. J. Chem. 38 (2020) 1422–1444. https://doi.org/10.1002/cjoc.202000205.

[34] Z. Tang, P. Liu, H. Cao, S. Bals, H.J. Heeres, P.P. Pescarmona, Pt/ZrO2 Prepared by Atomic Trapping: An Efficient Catalyst for the Conversion of Glycerol to Lactic Acid with Concomitant Transfer Hydrogenation of Cyclohexene, ACS Catal. 9 (2019) 9953–9963. https://doi.org/10.1021/acscatal.9b02139.

[35] Y. Liu, H. Dai, J. Deng, S. Xie, H. Yang, W. Tan, W. Han, Y. Jiang, G. Guo, Mesoporous Co3O4-supported gold nanocatalysts: Highly active for the oxidation of carbon monoxide, benzene, toluene, and o-xylene, J. Catal. 309 (2014) 408–418. https://doi.org/10.1016/j.jcat.2013.10.019.

[36] Z. Han, L. Dai, Y. Liu, J. Deng, L. Jing, Y. Zhang, K. Zhang, X. Zhang, Z. Hou, W. Pei, H. Dai, AuPd/Co3O4/3DOM MnCo2O4: Highly active catalysts for methane combustion, Catal. Today. 376 (2021) 134–143. https://doi.org/10.1016/j.cattod.2020.06.068.

[37] H. Yang, J. Deng, Y. Liu, S. Xie, Z. Wu, H. Dai, Preparation and catalytic performance of Ag, Au, Pd or Pt nanoparticles supported on 3DOM CeO2–Al2O3 for toluene oxidation, J. Mol. Catal. Chem. 414 (2016) 9–18. https://doi.org/10.1016/j.molcata.2015.12.010.

[38] S. Oh, S. Back, W.H. Doh, S.Y. Moon, J. Kim, Y. Jung, J.Y. Park, Probing surface oxide formations on SiO2-supported platinum nanocatalysts under CO oxidation, RSC Adv. 7 (2017) 45003–45009. https://doi.org/10.1039/C7RA08952J.

[39] K. Balakrishnan, J. Schwank, FTIR study of bimetallic Pt-Sn/Al2O3 catalysts, J. Catal. 138 (1992) 491–499. https://doi.org/10.1016/0021-9517(92)90301-W.

[40] E.A. Redina, O.A. Kirichenko, A.A. Greish, A.V. Kucherov, O.P. Tkachenko, G.I. Kapustin, I.V. Mishin, L.M. Kustov, Preparation of bimetallic gold catalysts by redox reaction on oxide-supported metals for green chemistry applications, Catal. Today. 246 (2015) 216–231. https://doi.org/10.1016/j.cattod.2014.12.018.

[41] N.F.P. Ribeiro, F.M.T. Mendes, C.A.C. Perez, M.M.V.M. Souza, M. Schmal, Selective CO oxidation with nano gold particles-based catalysts over Al2O3 and ZrO2, Appl. Catal. Gen. 347 (2008) 62–71. https://doi.org/10.1016/j.apcata.2008.05.030.

[42] B. Koslowski, H.-G. Boyen, C. Wilderotter, G. Kästle, P. Ziemann, R. Wahrenberg, P. Oelhafen, Oxidation of preferentially (111)-oriented Au films in an oxygen plasma investigated by scanning tunneling microscopy and photoelectron spectroscopy, Surf. Sci. 475 (2001) 1–10. https://doi.org/10.1016/S0039-6028(00)00986-9.

[43] S. Zhou, G.S. Jackson, B. Eichhorn, AuPt Alloy Nanoparticles for CO-Tolerant Hydrogen Activation: Architectural Effects in Au-Pt Bimetallic Nanocatalysts, Adv. Funct. Mater. 17 (2007) 3099–3104. https://doi.org/10.1002/adfm.200700216.

[44] A.S. Aricò, A.K. Shukla, H. Kim, S. Park, M. Min, V. Antonucci, An XPS study on oxidation states of Pt and its alloys with Co and Cr and its relevance to electroreduction of oxygen, Appl. Surf. Sci. 172 (2001) 33–40. https://doi.org/10.1016/S0169-4332(00)00831-X.

[45] S. Viéitez-Calo, D.J. Morgan, S. Golunski, S.H. Taylor, M.V. Twigg, Structure Sensitivity and Hydration Effects in Pt/TiO2 and Pt/TiO2–SiO2 Catalysts for NO and Propane Oxidation, Top. Catal. (2021). https://doi.org/10.1007/s11244-021-01415-2.

[46] R.P. Doherty, J.-M. Krafft, C. Méthivier, S. Casale, H. Remita, C. Louis, C. Thomas, On the promoting effect of Au on CO oxidation kinetics of Au–Pt bimetallic nanoparticles supported on SiO2: An electronic effect?, J. Catal. 287 (2012) 102–113. https://doi.org/10.1016/j.jcat.2011.12.011.

[47] Y. Xu, Y. Dong, J. Shi, M. Xu, Z. Zhang, X. Yang, Au@Pt core-shell nanoparticles supported on multiwalled carbon nanotubes for methanol oxidation, Catal. Commun. 13 (2011) 54–58. https://doi.org/10.1016/j.catcom.2011.06.018.

[48] T. Garcia, S. Agouram, S.H. Taylor, D. Morgan, A. Dejoz, I. Vázquez, B. Solsona, Total oxidation of propane in vanadia-promoted platinum-alumina catalysts: Influence of the order of impregnation, Catal. Today. 254 (2015) 12–20. https://doi.org/10.1016/j.cattod.2015.01.038.

[49] M.-Y. Kim, J.-S. Choi, T.J. Toops, E.-S. Jeong, S.-W. Han, V. Schwartz, J. Chen, Coating SiO2 Support with TiO2 or ZrO2 and Effects on Structure and CO Oxidation Performance of Pt Catalysts, Catalysts. 3 (2013) 88–103. https://doi.org/10.3390/catal3010088.

[50] K.-J. Kim, S.-I. Boo, H.-G. Ahn, Preparation and characterization of the bimetallic Pt–Au/ZnO/Al2O3 catalysts: Influence of Pt–Au molar ratio on the catalytic activity for toluene oxidation, J. Ind. Eng. Chem. 15 (2009) 92–97. https://doi.org/10.1016/j.jiec.2008.09.005.

[51] H. Qin, X. Qian, T. Meng, Y. Lin, Z. Ma, Pt/MOx/SiO2, Pt/MOx/TiO2, and Pt/MOx/Al2O3 Catalysts for CO Oxidation, Catalysts. 5 (2015) 606–633. https://doi.org/10.3390/catal5020606.

[52] S.K. Jain, E.M. Crabb, L.E. Smart, D. Thompsett, A.M. Steele, Controlled modification of Pt/Al2O3 for the preferential oxidation of CO in hydrogen: A comparative study of modifying element, Appl. Catal. B Environ. 89 (2009) 349–355. https://doi.org/10.1016/j.apcatb.2008.12.013.

[53] L. Ilieva, A.M. Venezia, P. Petrova, G. Pantaleo, L.F. Liotta, R. Zanella, Z. Kaszkur, T. Tabakova, Effect of Y Modified Ceria Support in Mono and Bimetallic Pd–Au Catalysts for Complete Benzene Oxidation, Catalysts. 8 (2018) 283. https://doi.org/10.3390/catal8070283.

[54] T. Tabakova, L. Ilieva, P. Petrova, A.M. Venezia, Y. Karakirova, L.F. Liotta, G. Avdeev, Complete Benzene Oxidation over Mono and Bimetallic Pd—Au Catalysts on Alumina-Supported Y-Doped Ceria, Appl. Sci. 10 (2020) 1088. https://doi.org/10.3390/app10031088.

[55] S.W. Chee, J.M. Arce-Ramos, W. Li, A. Genest, U. Mirsaidov, Structural changes in noble metal nanoparticles during CO oxidation and their impact on catalyst activity, Nat. Commun. 11 (2020) 2133. https://doi.org/10.1038/s41467-020-16027-9.

[56] Y.-F.Y. Yao, The oxidation of CO and hydrocarbons over noble metal catalysts, J. Catal. 87 (1984) 152–162. https://doi.org/10.1016/0021-9517(84)90178-7.

[57] D. Chlala, M. Labaki, J.-M. Giraudon, O. Gardoll, A. Denicourt-Nowicki, A. Roucoux, J.-F. Lamonier, Toluene total oxidation over Pd and Au nanoparticles supported on hydroxyapatite, Comptes Rendus Chim. 19 (2016) 525–537. https://doi.org/10.1016/j.crci.2015.07.015.

[58] A. Buzková Arvajová, J. Březina, R. Pečinka, P. Kočí, Modeling of two-step CO oxidation light-off on Pt/γ-Al2O3 in the presence of C3H6 and NOx, Appl. Catal. B Environ. 233 (2018) 167–174. https://doi.org/10.1016/j.apcatb.2018.03.081.

[59] A.-C. Yang, V. Streibel, T.S. Choksi, H. Aljama, B. Werghi, S.R. Bare, R.S. Sánchez-Carrera, A. Schäfer, Y. Li, F. Abild-Pedersen, M. Cargnello, Insights and comparison of structure–property relationships in propane and propene catalytic combustion on Pd- and Pt-based catalysts, J. Catal. 401 (2021) 89–101. https://doi.org/10.1016/j.jcat.2021.06.018.

[60] A. Aznárez, A. Gil, S. A. Korili, Performance of palladium and platinum supported on alumina pillared clays in the catalytic combustion of propene, RSC Adv. 5 (2015) 82296–82309. https://doi.org/10.1039/C5RA15675K.

[61] N. Radic, B. Grbic, A. Terlecki-Baricevic, Kinetics of deep oxidation of n-hexane and toluene over Pt/Al2O3 catalysts: Platinum crystallite size effect, Appl. Catal. B Environ. 50 (2004) 153–159. https://doi.org/10.1016/j.apcatb.2004.01.011.

[62] L. Lu, Y. Nie, Y. Wang, G. Wu, L. Li, J. Li, X. Qi, Z. Wei, Preparation of highly dispersed carbon supported AuPt nanoparticles via a capping agent-free route for efficient methanol oxidation, J. Mater. Chem. A. 6 (2018) 104–109. https://doi.org/10.1039/C7TA08343B.

[63] B. Puértolas, Á. Mayoral, R. Arenal, B. Solsona, A. Moragues, S. Murcia-Mascaros, P. Amorós, A.B. Hungría, S.H. Taylor, T. García, High-Temperature Stable Gold Nanoparticle Catalysts for Application under Severe Conditions: The Role of TiO2 Nanodomains in Structure and Activity, ACS Catal. 5 (2015) 1078–1086. https://doi.org/10.1021/cs501741u.

7. Conclusions and Future Work

7.1 Conclusions

7.1.1 Thesis aim

The overall objective of this work was the design of novel catalysts for the abatement of various atmospheric pollutants. As discussed in the Introduction, the control of VOC pollutants is of growing importance, with many negative impacts related to their emission. In addition, the application of more stringent restrictions upon industries, relating to the emission of VOCs, provides further encouragement to improve abatement processes. The use of catalytic total oxidation for controlling the emission of VOCs has been widely studied, with industries already employing this strategy [1]. More recently, developments in the catalysts used have been the focus of research, where cheaper and more environmentally benign alternatives provide enticing prospects. Improvements in VOC conversion, selectivity and catalyst stability are constantly required to enhance abatement technology, whilst limiting costs and the impact generating these materials has on the environment. Therefore, the synthesis of novel effective catalysts using cheap and abundant materials, with application for industrial uses, is at the forefront of this area of research.

7.1.2 Chapter 3: Comparison of cerium (III) & (IV) precursors for the synthesis of CeO_2 catalysts for propane and naphthalene total oxidation

The work conducted in Chapter 3 focused on the synthesis design for a widely regarded effective oxidation catalyst. CeO_2 catalysts were prepared by a simple and reproducible precipitation method, where the impact of using cerium precursors with different oxidation states was assessed. The influence of the cerium precursor was evaluated by comparing the activity for the total oxidation of two model VOCs, propane and naphthalene, and how this was related to the different characteristics present for the catalysts.

For both propane and naphthalene total oxidation, the final CeO_2 catalyst prepared using the Ce^{IV} precursor was more active. It was determined that factors such as redox properties, surface defects and poison concentration affected catalytic activity, however; the most influential factor relating to the catalytic activity was the surface area of the final catalyst. The increased surface area of the CeO_2 (IV) catalyst was thought to be a result of the different precipitates formed during synthesis, when using the different precursors.

Synthesis using the Ce^{IV} precursor formed hydrated $CeO_2.H_2O$ nanoparticles in solution which was determined by TG-DTA and XRD analysis. Whereas, the Ce^{III} precursor formed a $Ce_2(OH)_2(CO_3)_2.H_2O$ precipitate under the same synthesis conditions. The transformation to bulk CeO_2 for the Ce^{IV} precipitate was thought to be topotactic compared to a more disruptive transformation of the $Ce_2(OH)_2(CO_3)_2.H_2O$ precipitate, which was proposed to result in the different surface areas measured. The analysis of the CeO_2 catalysts showed similarities in the bulk structure from XRD and Laser Raman spectroscopy. In contrast, differences were observed in the SEM images of the particles, as well as on the catalyst surface from XPS analysis. This was again suggested to relate to the transformation of the different precipitates formed. The chemical properties of the two different CeO_2 catalysts also varied as CeO_2 (III) presented improved redox properties compared to CeO_2 (IV).

A 50:50 mixture of the two precursors was used in the synthesis method to assess whether the trends observed for the CeO_2 (IV) and CeO_2 (III) catalysts showed a linear relationship. This was found to be true for the surface area of the catalysts, with increasing Ce^{IV} content relating to increased catalyst surface area. However, other characteristics identified had little direct correlation with varying precursor ratio. This was also observed for the catalytic activity of both propane and naphthalene total oxidation as the improved surface area did relate to improved activity but this was not directly linear. Instead, it was suggested competing factors of increased defect concentration and Na retention led to more complex activity trends. The increased retention of Na as a catalyst poison was proposed to inhibit oxygen mobility of the catalyst, affecting the overall catalytic activity of CeO_2 (III+IV).

A CeO_2 catalyst was prepared using the Ce^{III} precursor, but NaOH was used as the precipitating agent to ensure the formation of the $CeO_2.H_2O$ precipitate. The formation of this precipitate using the Ce^{III} precursor resulted in similar characteristics to the CeO_2 (IV) catalyst, supporting previous conclusions drawn from the formation and subsequent transformation of the precipitates into the final catalysts. Of note, an increased surface area was obtained for the CeO_2 (III) NaOH catalyst, which was consistent with the proposed transformation of the $CeO_2.H_2O$ precipitate. Furthermore, it was also noticed from this work that the formation of the $CeO_2.H_2O$ precipitate resulted in limited Na retention which was previously shown to affect catalytic activity. The CeO_2 (III) NaOH catalyst showed a similar performance to CeO_2 (IV) for propane and naphthalene total oxidation, with slight improvement attributed to the increased bulk defect concentration measured by Laser Raman spectroscopy.

Finally, the impact on testing conditions was assessed for the CeO_2 catalysts, where water vapour was added into the VOC feed. Both CeO_2 catalysts, prepared using the different precursors, showed suppressed activity when compared with VOC total oxidation under dry conditions, which was in good agreement with previous literature [2,3]. The inhibition of catalytic activity by water vapour was more pronounced for naphthalene total oxidation compared with propane total oxidation. For both reactions it was stated that the decreased activity was caused by competitive adsorption of VOC and water molecules on the catalyst surface, with water blocking active surface sites. This work highlights the wider impact on the importance of conditions used for catalyst testing, as catalytic activity was significantly affected irrespective of the preparation conditions used.

7.1.3 Chapter 4: Ceria-Iron mixed oxides for the total oxidation of propane and naphthalene VOCs: Effect of molar ratios and cerium precursor

Work in Chapter 4 expanded on themes addressed in Chapter 3 but in the context of mixed metal oxide catalysts. Similar results were found for the preparation of $CeFeO_x$ mixed oxide catalysts when synthesised using different cerium precursors, with factors such as surface area, Na retention and catalyst morphology closely related to the precipitate formed. Furthermore, it was shown that, in general, the catalysts prepared using the Ce^{IV} precursor were more active for propane and naphthalene total oxidation as a result of the varied characteristics mentioned. The importance of understanding the basic principles of catalyst preparation can be shown here and how that can be expanded upon for more complex systems, allowing for more productive research to be conducted.

Although the mixed $CeFeO_x$ (IV) catalysts showed good performance for propane total oxidation, it was determined that the Fe_2O_3 catalyst was the most active when normalised for surface area. These data were in good agreement with previous research on the total oxidation of propane using metal oxide catalysts [4] and was proposed to be strongly associated with the redox properties of the different metal oxides. TPR data suggested the mixture of Ce and Fe oxides suppressed the low temperature reduction of Fe_2O_3 species, which were thought to be important for the reaction. The presence of bulk Fe_2O_3 species was suggested to be the most significant factor relating to the catalytic activity for propane total oxidation, however; other factors such as catalyst surface area and residual Na concentration were also shown to influence catalytic activity. To assess the impact of Fe_2O_3 segregation on the mixed catalyst, a supported Fe/CeO_2 catalyst was prepared by a wet impregnation synthesis method. It was theorised that the intimate mixing of the Ce and Fe species by co-precipitation suppressed the low temperature reducibility of the Fe_2O_3. However, the supported Fe/CeO_2 (IV) catalyst also exhibited inferior reduction of the Fe_2O_3 species and consequently worse catalytic activity when compared to bulk Fe_2O_3.

Contrasting trends were established for the total oxidation of naphthalene, with the CeO_2 (IV) catalyst achieving the best catalytic activity. This was again consistent with previous research highlighting the impressive activity of CeO_2 for naphthalene total oxidation when compared with other metal oxide catalysts [4]. It was proposed that the improved activity of CeO_2 originated from the weaker surface interaction with naphthalene molecules. A linear trend of increasing Fe content with decreasing activity was established for the $CeFeO_x$ (IV) range of catalysts. Whereas, for the $CeFeO_x$ (III) range of catalysts, the catalytic activity was related to the catalyst surface area and concentration of residual Na species. The insufficient catalytic activity of the mixed $CeFeO_x$ catalysts further demonstrates the challenge presented when considering more efficient ways to remove VOCs of a different nature, where the oxidation mechanism is dependent on different rate-determining factors.

7.1.4 Chapter 5: The modification of $CeZrO_x$ catalysts by the addition of transition metal dopants for propane and naphthalene total oxidation.

The focus of catalyst dopants in Chapter 5 highlighted that incorporating small amounts of metals into a $CeZrO_x$ catalyst could improve activity for the total oxidation of propane and naphthalene VOCs. The enhanced activity for the total oxidation of propane occurred as a result of increased catalyst surface area from the incorporation of Fe and Cu dopants, with the $Ce_{90}Zr_{10}Fe_1O_x$ catalyst performing the best. However, this was not the only factor found to be influential for catalytic activity as the residual Na concentration was also proposed to impact activity, which was in good agreement with previous literature [5].

For the total oxidation of naphthalene, these factors were also proposed to influence catalytic activity. The increased surface area has previously been attributed to improved catalytic activity as a result of the improved surface coverage of naphthalene on the catalyst [6]. However, in contrast to propane total oxidation, a direct relationship was not identified with these catalysts but rather the surface normalised activity indicated a strong correlation with the bulk defects observed by Laser Raman spectroscopy. It was proposed that the improved oxygen mobility from the bulk defects facilitated naphthalene total oxidation, which was consistent with previous research identifying the re-oxidation of $CeZrO_x$ catalysts as the rate determining step for naphthalene total oxidation [7]. This also linked with the varying concentration of residual Na on the catalysts, as this has been shown to affect oxygen mobility, hence inhibiting naphthalene oxidation. Overall, the doping of well-known $CeZrO_x$ catalysts, which are commonly used in industrial processes such as in three-way catalysts [1], with cheap and abundant transition metals opens up an avenue to easily promote catalytic activity for VOC oxidation. Furthermore, this work has emphasised the need for only small quantities of these dopants, near 1 at.%, required to enhance catalytic activity.

7.1.5 Chapter 6: Novel Au-Pt/ZrO_2/UVM-7 catalysts for the simultaneous total oxidation of CO, propene, and toluene pollutants

Research into the simultaneous removal of VOCs, discussed in Chapter 6, is an important and growing area of research that focuses on the more "real-world" conditions of heterogeneous catalysis for industrial application. Many studies for VOC oxidation use conditions where either poisons are omitted or competing compounds are excluded, resulting in only one compound used as a model, providing limited reaction information. Hence the use of a model mixture of VOCs, where compounds with varying functional groups can interact differently with the catalysts used, is important when understanding competing factors affecting catalytic activity.

The mono and bimetallic Au-Pt catalysts supported on novel ZrO_2/UVM-7-C showed good activity for the simultaneous total oxidation of propene, toluene and CO. It was found that catalysts containing a higher concentration of surface Au nanoparticles exhibited worse catalytic activity, with the 40% ZrO_2/UVM-7-C 2% Au catalyst being the least active. This was proposed to be caused by the lower intrinsic dissociative chemisorption energy of oxygen associated with Au nanoparticles [8], which negatively impacted VOC oxidation. Whilst supported Au catalysts have shown good activity for CO oxidation, this was generally inhibited by the combination of the other pollutants. Previous literature suggested the competitive binding of the VOCs and CO on the catalyst surface negatively influenced CO oxidation [9], which was consistent with the Au catalysts tested in Chapter 6.

Pt species were therefore suggested to be the active species for these catalysts. No direct correlation between the particle size or oxidation state of Pt nanoparticles could be determined for the simultaneous oxidation of propene, toluene and CO. Rather, catalytic activity was more closely linked to the concentration of Pt on the surface in relation to Au. The 40% ZrO_2/UVM-7-C 2% Pt catalyst showed a limited amount of Pt nanoparticles on the surface which was suggested to explain the worse activity of this catalyst compared with some of the bimetallic catalysts containing inactive Au species. For the bimetallic catalysts, a linear trend was established where increased Pt surface concentration related to improved catalytic activity. This was influenced by the order of metal nanoparticle deposition on the support, where sequentially adding either Au or Pt resulted in surface enrichment of the metal added last. In contrast, the simultaneous addition of the metals formed alloyed nanoparticles but this negatively impacted activity due to increased Au content. In addition to the 40% ZrO_2/UVM-7-C 1% Au + 1% Pt catalyst presenting the highest activity for the simultaneous total oxidation of propene, toluene and CO, it also showed good stability for consecutive reaction cycles.

7.2 Future Work

7.2.1 Chapter 3: Comparison of cerium (III) & (IV) precursors for the synthesis of CeO_2 catalysts for propane and naphthalene total oxidation

Further work on the preparation of CeO_2 catalysts using the different precursors should consist of isolating key factors identified for improved catalytic activity. The use of Na free precipitating agents should be considered, with $(NH_4)_2CO_3$ and NH_4OH prime candidates, to eliminate residual Na content on the catalyst, which is known to affect oxygen mobility and therefore catalytic activity. In addition, the preparation of high surface area CeO_2 was shown to be advantageous for the total oxidation of both propane and naphthalene. Hence, synthesis routes to produce CeO_2 catalysts with high surface area, such as previously proposed urea preparation [10], should be pursued. This would allow for better correlation of the physiochemical properties with catalyst activity and remove any limiting factors. For example the low surface area of CeO_2 (III) was thought to limit the redox properties of the catalyst, which impacted the activity for propane total oxidation as seen from the surface normalised activity, so a higher surface area catalyst may negate these effects to provide a more direct comparison with the CeO_2 (IV) catalyst. Furthermore, the mechanism of VOC oxidation, where water vapour is present in the feed, should be studied to understand the inhibiting nature of the water on the catalysts surface. This could be achieved by using *in-situ* FTIR analysis techniques.

7.2.2 Chapter 4: Ceria-Iron mixed oxides for the total oxidation of propane and naphthalene VOCs: Effect of molar ratios and cerium precursor

The analysis of the $CeFeO_x$ catalysts is somewhat limited, which leads to an unclear understanding of the catalyst properties impacting activity for VOC oxidation. An improved understanding of the species present on the catalyst surface could be studied, as the XPS analysis conducted was not able to identify Fe species clearly, due to the overlapping Ce Auger peak present in the spectra. Moreover, a better understanding of how the Ce and Fe species interact with each other would provide useful information. An in-depth characterisation, using techniques such as TEM and Mössbauer spectroscopy, would help to identify the active Fe species present for the total oxidation of propane. Bulk analysis was also slightly limited in this work and techniques such as Laser Raman spectroscopy would provide more useful information. This would have to be conducted using an enhanced Raman spectroscopy due to the difficulties with analysing Fe species by this method.

7.2.3 Chapter 5: The modification of $CeZrO_x$ catalysts by the addition of transition metal dopants for propane and naphthalene total oxidation.

The method of incorporating the dopants into the $CeZrO_x$ catalysts could be interesting to expand on. Either different synthesis techniques could be pursued, where the dopant is incorporated into the bulk structure, or where the dopants are deposited directly on the surface to compare the effect they have on VOC total oxidation. The testing conditions could also be further studied, with the inclusion of water vapour used, as seen in Chapter 3, or with a mixture of VOCs studied similarly to Chapter 6. However, it is clear that these conditions could be implemented in multiple chapters to gain a better understanding of these competing factors for more industrial catalytic uses.

7.2.4 Chapter 6: Novel Au-Pt/ZrO_2/UVM-7 catalysts for the simultaneous total oxidation of CO, propene, and toluene pollutants

The most interesting aspect of this research that could be conducted is to probe the reaction mechanism for the simultaneous total oxidation of the propene, toluene and CO mixture. This would be a complex task due to the competing binding of the different species on the catalyst surface but would provide useful information to better understand the important catalyst characteristics. Techniques such as Temporal analysis of products (TAP) and *in-situ* FTIR analysis could be used to carry out this research. In addition, to mechanistic studies, the importance of the metal oxide loaded onto the UVM-7-C support could be considered. A range of metal oxides have been studied for VOC oxidation, each presenting varying characteristics that can promote or inhibit certain aspects of the catalyst. A comparison between these and how they interact with the metal nanoparticles could greatly improve understanding of these catalysts.

7.3 References

[1] S. Rood, S. Eslava, A. Manigrasso, C. Bannister, Recent advances in gasoline three-way catalyst formulation: A review, Proc. Inst. Mech. Eng. Part J. Automob. Eng. 234 (2020) 936–949. https://doi.org/10.1177/0954407019859822.

[2] W. Zhu, X. Chen, J. Jin, X. Di, C. Liang, Z. Liu, Insight into catalytic properties of Co3O4-CeO2 binary oxides for propane total oxidation, Chin. J. Catal. 41 (2020) 679–690. https://doi.org/10.1016/S1872-2067(19)63523-0.

[3] J. Fang, X. Chen, Q. Xia, H. Xi, Z. Li, Effect of Relative Humidity on Catalytic Combustion of Toluene over Copper Based Catalysts with Different Supports, Chin. J. Chem. Eng. 17 (2009) 767–772. https://doi.org/10.1016/S1004-9541(08)60275-X.

[4] T. García, B. Solsona, S.H. Taylor, Naphthalene total oxidation over metal oxide catalysts, Appl. Catal. B Environ. 66 (2006) 92–99. https://doi.org/10.1016/j.apcatb.2006.03.003.

[5] W. Tang, J. Weng, X. Lu, L. Wen, A. Suburamanian, C.-Y. Nam, P.-X. Gao, Alkali-metal poisoning effect of total CO and propane oxidation over Co3O4 nanocatalysts, Appl. Catal. B Environ. 256 (2019) 117859. https://doi.org/10.1016/j.apcatb.2019.117859.

[6] A. Aranda, B. Puértolas, B. Solsona, S. Agouram, R. Murillo, A.M. Mastral, S.H. Taylor, T. Garcia, Total Oxidation of Naphthalene Using Mesoporous CeO2 Catalysts Synthesized by Nanocasting from Two Dimensional SBA-15 and Three Dimensional KIT-6 and MCM-48 Silica Templates, Catal. Lett. 134 (2010) 110–117. https://doi.org/10.1007/s10562-009-0203-9.

[7] A. Bampenrat, V. Meeyoo, B. Kitiyanan, P. Rangsunvigit, T. Rirksomboon, Catalytic oxidation of naphthalene over CeO2–ZrO2 mixed oxide catalysts, Catal. Commun. 9 (2008) 2349–2352. https://doi.org/10.1016/j.catcom.2008.05.029.

[8] V.P. Santos, S.A.C. Carabineiro, P.B. Tavares, M.F.R. Pereira, J.J.M. Órfão, J.L. Figueiredo, Oxidation of CO, ethanol and toluene over TiO2 supported noble metal catalysts, Appl. Catal. B Environ. 99 (2010) 198–205. https://doi.org/10.1016/j.apcatb.2010.06.020.

[9] P. Peng, J. Li, S. Mo, Q. Zhang, T. Shen, Q. Xie, Bimetallic Pt-Co Nanoparticle Deposited on Alumina for Simultaneous CO and Toluene Oxidation in the Presence of Moisture, Processes. 9 (2021) 230. https://doi.org/10.3390/pr9020230.

[10] E.N. Ndifor, T. Garcia, B. Solsona, S.H. Taylor, Influence of preparation conditions of nano-crystalline ceria catalysts on the total oxidation of naphthalene, a model polycyclic aromatic hydrocarbon, Appl. Catal. B Environ. 76 (2007) 248–256. https://doi.org/10.1016/j.apcatb.2007.05.027.